Development of Metal-supported Solid Oxide Fuel Cell (MS-SOFC) by Atmospheric Plasma Spraying and Reactive Magnetron Sputtering Technique

Xiaolei Ye

THESE DE DOCTORAT DE L'ETABLISSEMENT UNIVERSITE BOURGOGNE FRANCHE-COMTE
PREPAREE A UNIVERSITE DE TECHNOLOGIE DE BELFORT-MONTBELIARD

Ecole doctorale n°37
École Doctorale Sciences Pour l'Ingénieur et Microtechniques

Doctorat de Matériaux

Par
Xiaolei YE

Development of Metal-supported Solid Oxide Fuel Cell (MS-SOFC) by Atmospheric Plasma Spraying (APS) and Reactive Magnetron Sputtering (RMS) Technique

Thèse présentée et soutenue à Montbéliard, le 22/06/2023

Composition du Jury:

Mme, RINGUEDE Armelle	Principal Researcher, Chimie Paris Tech France, Présidente
Mme THOMANN Anne-Lise	Principal Researcher, GREMI-Université d'Orleans France, Rapporteur
M. MAUVY Fabrice	Full Professor, Université de Bordeaux France, Rapporteur
M. COSTA Remi	Head of High Temperature-Fuel Cell Team, DLR Stuttgart Allemaqgne Examinateur
M. BRIOIS Pascal	Associate Professor Université de Technologie de Belfort, France Directeur de thèse
M. BERTRAND Pierre	Engineer, Université de Technologie de Belfort Montbéliard, France Co-Encadrant de thèse

Acknowledgment

I did all the works on my PhD thesis in the team of Micro Nano Materials and Surfaces (MINAMAS), department of Micro Nano Sciences and Systems (MN2S), Franche-Comté Electronic Mechanic Thermic and Optic-Sciences and Technologies (FEMTO-ST), at University Bourgogne Franche-Comté, UTBM, CNRS. In retrospect on the years, I am full of gratitude to many people.

I would like to firstly express my most sincere gratitude to my supervisor, Prof. Pascal BRIOIS, who gave me meticulous guidance and help in my research work. Whenever I get stuck in research work, he always gives me professional guidance. He also provides me with a very good research platform so that I can carry out my research work smoothly. I would also like to express my most sincere thanks to my co-supervisor, Prof. Pierre BERTRAND, who always patiently guided me to carry out related experiments. His rich professional knowledge has helped me a lot. In addition, I would also like to sincerely thank Prof. Alain BILLARD, who gave me professional training, which enabled me to master the relevant experimental skills proficiently.

I would like to express my sincere thanks to Dr. Mohammad Arab Pour Yazdi, and Dr. Eric AUBRY for their advice and encouragement in my research work. I would also like to express my sincere thanks to Mr. Khalid NEFFA Aand Mr. Christian PETITOT for their timely maintenance of experimental equipment so that I can carry out the experiment more smoothly. I would also like to thank my friends and colleagues who work in the lab and put me in a pleasant working environment, they are Ms Huan LUO, Ms. Shutong LAI, Ms. Emmanuelle ARCENS, Ms. Mahsasadat SAFAVI.

I would like to thank my friends who work in Belfort and Sévenans, they gave me a lot of support in life. We have spent more than three years of happy time together, there are Mr. Rui YANG, Mr. Xinyang HAO, Dr. Zhiguang HUA, Mr. Yingjie LI, Dr. Cheng Chang. I would like to express my sincere thanks to my friends work in China Prof. Li YANG and Dr. Ming Hou for their support in the research work. I would also like to thank Prof. Lichao JIA and Dr. Bo LIU who work in the School of Materials Science and Engineering of Huazhong University of Science and Technology for

conducting single cells and symmetrical cells measurements for me.

I am very grateful to China Scholarship Council (CSC) for providing me with funding to do my doctoral research work in France.

I especially want to extend my deepest love to my family. My parents, sisters, and girlfriend have given me great encouragement and support. They have given me a source of strength to continue my research work.

Abstract

In recent decades, to cope with the global energy shortage and environmental pollution challenges, the development of renewable clean energy has become imminent. As a device that can directly convert chemical energy into electrical energy, Solid oxide fuel cell (SOFC) plays an important role in clean energy production due to the advantages of high energy conversion efficiency, fuel flexibility, and the significant environmental benefits. It is well-suited for infrastructure support from distributed generation to combined heat and power to automotive auxiliary power systems. Initially, SOFC is designed to operate at high temperature (800-1000°C), which facilitates efficient energy conversion while avoiding the use of precious metal electrodes. However, the high temperature also causes a series of disadvantages in terms of material selection, fabricating cost, and cell life, etc. Lowering the operating temperature to intermediate/low temperature (600-800°C, IT-SOFC; ~600°C, LT-SOFC) can effectively overcome these disadvantages but will lead to a decline in cell performance. Maintaining even improving the cell performance working at lower temperature is a development trend of SOFC. A significant benefit brought by the lower operating temperature is that relatively cheap metal materials can be used as support material for SOFC (MS-SOFC). The fundamental concept of MS-SOFC is to support thin ceramic electrode/electrolyte layers on low-cost, robust metal support. In this way, the use of expensive ceramic materials is greatly reduced, which minimizes cell costs and maximizes cell strength. However, for MS-SOFC, higher cell fabrication and component material performance requirements are proposed.

In this thesis, the complete single MS-SFCs are fabricated using physical deposition techniques. In Chapter 1, the development from fuel cell to MS-SOFC is first described. Then the support materials, electrode (anode/cathode) materials, and electrolyte materials that can be used in MS-SOFC are reviewed in detail. Various fabrication technologies for MS-SOFC are compared. Finally, the research purpose and significance of this thesis are presented. In Chapter 2, the deposition principle and deposition devices of Atmospheric Plasma Spray (APS) and Reactive Magnetron

Sputtering (RMS) are first introduced in detail. Then a series of material and cell characterization techniques are introduced. In Chapter 3, the oxidation behavior of a so-called intermediate temperature alloy (ITM) in air is first investigated, which provides a basis for the annealing treatment of the complete single cell. Then the APS deposition parameters are optimized for the deposition of NiO-YSZ bilayer anode. After reduction, its upper and lower layers have low porosity of 17.2 ± 0.4 Vol.% and high porosity of 33.1 ± 0.6 Vol.%, respectively. Subsequently, a thin 8YSZ/GDC10 bilayer electrolyte (about 10.8 μm) is deposited on the polished NiO-YSZ anode layer by RMS. Finally, the beneficial effect of the GDC10 buffer layer deposited between the ITM and the NiO-YSZ anode layer to prevent the interdiffusion between Fe, Cr, and Ni is clarified. The interesting of Chapter 4 is the successful synthesis of porous Pr_2NiO_4@Pr_6O_{11} (PPNO) composite and Pr_2NiO_4 (PNO) for cathode by RMS. A series of characterizations are carried out on PPNO and PNO coatings, including morphology, structure, electrical and electrochemical properties. Finally, the performance of complete single cells with the configurations of ITM/GDC10/NiO-YSZ/8YSZ/GDC10/PPNO2 (MS/PPNO2) and ITM/GDC10/NiO-YSZ/8YSZ/GDC10/PNO (MS/PNO) is measured, where the long-term performance test of MS/PPNO2 single cell is performed.

Keywords: MS-SOFC, APS, RMS, NiO-YSZ anode, PPNO composite cathode

Résumé

Au cours des dernières décennies, afin de faire face à la pénurie mondiale d'énergie et aux défis de la pollution environnementale, le développement des énergies renouvelables est devenu imminent. En tant qu'appareil capable de convertir directement l'énergie chimique en énergie électrique, les piles à combustible à oxyde solide (SOFC) jouent un rôle important dans la production d'énergie propre. Cette technologie est bien adaptée à la production combinée de chaleur et d'électricité dans le stationnaire mais également dans l'alimentation auxiliaire pour la production mobile. Initialement, la SOFC est conçue pour fonctionner à haute température (800-1000°C), ce qui facilite une conversion efficace de l'énergie. Cependant, l'environnement de travail à haute température entraîne également une série d'inconvénients en termes de sélection des matériaux, de coût de fabrication et de durée de vie des cellules, etc. L'abaissement de la température de fonctionnement à une température intermédiaire/basse (600-800°C, IT-SOFC; ~600°C, LT-SOFC) peut efficacement surmonter ces inconvénients mais entraînera une baisse des performances de la cellule. Le maintien ou l'amélioration des performances des cellules travaillant à plus basse température est une tendance de développement des SOFC. Un avantage significatif apporté par la température de fonctionnement plus basse est que les matériaux métalliques peuvent être utilisés comme matériaux de support pour SOFC (MS-SOFC). Le concept fondamental de MS-SOFC est de supporter de fines couches d'électrodes/électrolytes en céramique sur des matériaux métalliques robustes et peu coûteux. De cette manière, l'utilisation de matériaux céramiques coûteux est considérablement réduite, ce qui minimise les coûts des cellules et maximise la résistance des cellules. Cependant, pour les MS-SOFC, des exigences plus élevées en matière de fabrication de cellule et de performance du matériau composant sont nécessaires.

Dans cette thèse, les MS-SOFC sont fabriqués à l'aide de techniques de dépôt physique. Dans le chapitre 1, le développement des piles à combustible de type MS-SOFC est d'abord décrit. Ensuite, les matériaux de support, les matériaux d'électrode

(anode/cathode) et les matériaux d'électrolyte qui peuvent être utilisés dans les MS-SOFC sont revus en détail. Différentes technologies de fabrication utilisées pour fabriquer les MS-SOFC sont comparées. Dans le chapitre 2, les principes de dépôt et les équipements de synthèse : APS et RMS sont d'abord présentés en détail. Ensuite, les techniques de caractérisation des matériaux et des cellules sont décrites. Dans le chapitre 3, le comportement d'oxydation dans l'air d'un alliage dit à température intermédiaire (ITM) est d'abord étudié, ce qui fournit une base pour le traitement de recuit ultérieur de la cellule unique complète. Ensuite, les paramètres de dépôt APS sont optimisés pour le dépôt de la couche d'anode bicouche NiO-YSZ. Après réduction, ses couches supérieure et inférieure ont une faible porosité de 17,2 ± 0,4 % en volume et une porosité élevée de 33,1 ± 0,6 % en volume, respectivement. Par la suite, un électrolyte bicouche mince 8YSZ/GDC10 (environ 10,8 μm) est déposé sur la couche d'anode NiO-YSZ polie par RMS. Enfin, l'effet bénéfique de la couche barrière en GDC10 déposée entre l'ITM et la couche d'anode NiO-YSZ pour empêcher l'interdiffusion entre Fe, Cr et Ni est clarifié. L'intérêt du chapitre 4 est la synthèse réussie du matériau cathodique composite poreux Pr_2NiO_4@Pr_6O_{11} (PPNO) et Pr_2NiO_4 (PNO) par RMS. Une série de caractérisations sont réalisées sur les revêtements PPNO et PNO, incluant la morphologie, la structure, les propriétés électriques et électrochimiques. Enfin, les performances des cellules individuelles complètes avec les configurations ITM/GDC10/NiO-YSZ/8YSZ/GDC10/PPNO2 (MS/PPNO2) et ITM/GDC10/NiO-YSZ/8YSZ/GDC10/PNO (MS/PNO) sont mesurées. Un test de performance à long terme de la cellule unique MS/PPNO2 est effectué.

Mots clés : MS-SOFC, APS, RMS, anode NiO-YSZ, cathode composite PPNO

Nomenclature

Abbreviations

AC EIS	Alternative Current EIS
AFC	Alkaline Acid Fuel Cell
APS	Atmospheric Plasma Spray
AS-SOFC	Anode Supported SOFC
ASS	Austenitic Stainless Steels
BED	Backscatter Electron Detector
CHP	Combined Heat and Power
CS-SOFC	Cathode Supported SOFC
CTE	Coefficient of Thermal Expansion
D50	Median grain size
D_δ	Oxygen bulk diffusion coefficients
DC	Direct Current
D*t-s*	Distance between target and substrate
EDS	Energy Dispersive X-ray Spectroscopy
EIS	Electrochemical Impedance Spectroscopy
ES-SOFC	Electrolyte Supported SOFC
FeBSA	Fe-Ni-based superalloys
FSS	Ferritic Stainless Steels
FWHM	Full Width at Half Maximum
GDC	Gadolinia Doped Ceria
GDC10	10 mol% Gadolinia Doped Ceria
H-SOFC	Proton Conduction Solid Oxide Fuel Cell
HT-SOFC	High Temperature SOFC
IT-SOFC	Intermediate Temperature SOFC
ITM	Intermediate Temperature Metal
k	Oxygen surface exchange coefficients
LNO	La_2NiO_4
LSCF	Sr and Co co-doped $LaFeO_3$
LSFSc	Sr and Fe co-doped $LaScO_3$
LSM	$(La,Sr)MnO_3$
LT-SOFC	Low Temperature SOFC
MCFC	Molten Carbonate Fuel Cell
MIEC	Mixed Ionic and Electronic Conductor
MS-SOFC	Metal Supported SOFC
MS/PNO	ITM/GDC10/NiO-YSZ/8YSZ/GDC10/PNO
MS/PPNO2	ITM/GDC10/NiO-YSZ/8YSZ/GDC10/PPNO2
Ni-ScSZ	Ni mixed ScSZ cermet
Ni-SDC	Ni mixed SDC cermet
Ni-YSZ	Ni mixed YSZ cermet

NiBSA	Ni-Fe-based superalloys
O-SOFC	Oxygen Ion Conduction Solid Oxide Fuel Cell
OCV	Open Circuit Voltage
ORR	Oxygen Reduction Reaction
PAFC	Phosphoric Acid Fuel Cell
PCFC	Proton Conductor Fuel Cell
PEM	Plasma Emission Monitoring
PEMFC	Proton Exchange Membrane Fuel Cell
P_{max}	Maximum Output Power Density
PNO	Pr_2NiO_4
PPNO	Pr_2NiO_4@Pr_6O_{11}
PVD	Physical Vapour Deposition
RF	Radio Frequency
RMS	Reactive Magnetron Sputtering
Ra	Arithmetical mean deviation of profile
R_p	Polarization Resistance
Rsk	Skewness (asymmetry) of the assessed profile
Rz	Maximum height of the profile within a sampling length
sccm	Standard Cubic Centimeter per Minute
ScSZ	Scandia Stabilized Zirconia
ScYSZ	ZrO_2 co-doped with Sc_2O_3 and Y_2O_3
SDC	Samaria Doped Ceria
SEM	Scanning Electron Microscope
SOFC	Solid Oxide Fuel Cell
TG	Thermogravimetry Analysis
TPB	Triple Phase Boundary
XPS	X-ray Photoelectron Spectroscopy
XRD	X-ray Diffraction
YSZ	Yttria Stabilized Zirconia
8YSZ	8 mol% Yttria Stabilized Zirconia

Content

Chapter 1: Introduction

1.1 Fuel Cell

As an energy conversion device, a fuel cell can directly convert the chemical energy of fuel into electricity and heat without going through intermediate steps (Figure 1.1). This provides higher conversion efficiencies than conventional thermal conversion methods. In a fuel cell, oxidizing gas (oxygen or air) and gaseous fuel (hydrogen or hydrocarbons) pass through the cathode and anode, respectively. The half-cell reactions occur at the electrodes, where the charge carrier species pass through the ionically conductive solid electrolyte layer while electrons flow through the external circuit to generate electricity. Unlike traditional batteries, as show in figure 1.2, a fuel cell is like an energy factory that can continuously produce electricity as long as the fuel and oxidants are constantly replenished [1]. More importantly, it is an environmentally friendly power generation method if only hydrogen is used as fuel because the only emission is water.

Generally, fuel cell can be classified into six typical types of Alkaline Fuel Cell (AFC), Proton Exchange Membrane Fuel Cell (PEMFC), Phosphoric Acid Fuel Cell (PAFC), Proton Conductor Fuel Cell (PCFC), Molten Carbonate Fuel Cell (MCFC), and Solid Oxide Fuel Cell (SOFC) according to the properties of the ionic conductors used as electrolyte and their operating temperature. Some characteristics of these fuel cells have been listed in Table 1.1. In recent years, more researchers have paid attention to SOFC because of its high energy conversion efficiency, fuel flexibility, and no need for precious metal electrodes.

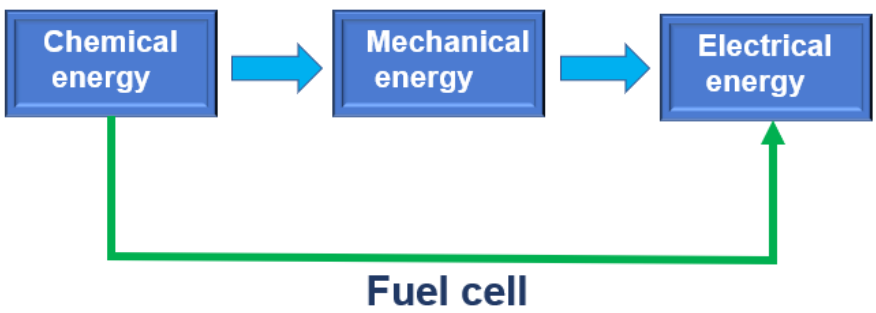

Figure 1.1: A comparison schematic diagram of direct energy conversion a fuel cell and

conventional thermal conversion

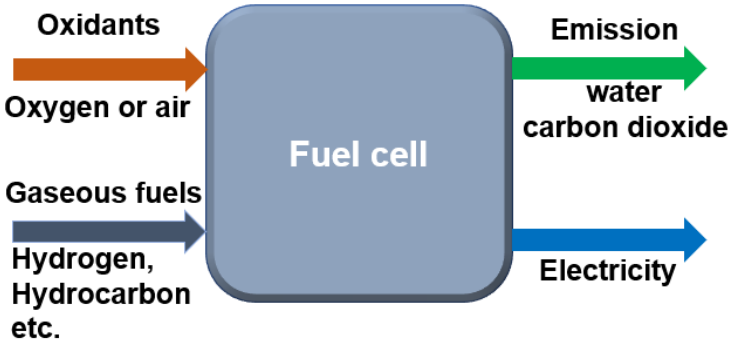

Figure 1.2: General concept of a fuel cell

Table.1.1: Some relevant characteristics of the different type of fuel cell [2, 3]

Type of cell	Electrolyte	Fuel	Charge carrier	Operating temperature (°C)	Conversion efficiency (%)	Application
AFC	KOH (Liquid)	H_2	OH^-	60-90	35	Spatial, transport
PEMFC	Proton exchange membrane	H_2, methanol	H^+	50-90	35	Portable, transport, stationary
PAFC	H_3PO_4 (Liquid)	H_2	H^+	160-220	45	Transport, stationary
PCFC	Ceramic (solid)	H_2	H^+	400-600	65	Transport, stationary
MCFC	Molten carbonate	H_2, CO	CO_3^{2-}	580-660	50	stationary
SOFC	Ceramic (solid)	H_2, hydrocarbon	O^{2-}/ H^+	600-1000	60-92 (Cogeneration)	Stationary, mobile

1.2 Solid Oxide Fuel Cell (SOFC)

SOFC is a kind of high temperature fuel cells which usually works at 600-1000°C. The by-products of SOFC are heat and water vapor when hydrogen is supplied as fuel, and the energy conversion efficiency is as high as 92 % when performing Combined Heat and Power (CHP) [3]. Compared with MCFC working at relatively high temperature, SOFC has higher power density and no liquid molten salt, which effectively avoids the problem of thermal corrosion of components. Compared with PEMFC, which works at low temperature, SOFC does not require precious metal

electrode materials, which reduces the requirements for fuel quality, thus making the choice of fuel more flexible. Moreover, as an independent power generation system, SOFC can be freely applied to places that need electricity without expensive power transmission system. This distributed power generation is especially convenient for mobile facilities and remote areas. It is foreseeable that the successful application of SOFC can help meet human energy needs, alleviate energy crises, and protect the environment.

1.2.1 The basic principle of SOFC

A single SOFC usually consists of porous electrodes (anode anode cathode) and a dense electrolyte in a sandwich configuration. Gas catalytic reactions and current transport take place on the porous electrodes, while the dense electrolyte is responsible for ion conduction and isolation of fuel and oxidizing gases. As shown in Figure 1.3, SOFC can be divided into oxygen ion conduction type (O-SOFC) and proton conduction type (H-SOFC) according to different electrolyte conduction types.

For O-SOFC, oxygen is decomposed into oxygen ions by a catalytic reduction reaction at the cathode, and then the oxygen ions migrate to the anode through the electrolyte. Finally, the electrons released by the reaction between the oxygen ions and the fuel return to the cathode through the external circuit, and the formed current drives load work. The electrode reactions are as follows:

Anode: $H_2 + O^{2-} = H_2O + 2e^-$ 1.1

Cathode: $\frac{1}{2}O_2 + 2e^- = O^{2-}$ 1.2

Unlike O-SOFC, for H-SOFC, protons migrate from the anode to the cathode through the electrolyte and react with oxygen at the cathode. The electrode reactions are as follows:

Anode: $H_2 = 2H^+ + 2e^-$ 1.3

Cathode: $2H^+ + \frac{1}{2}O_2 + 2e^- = H_2O$ 1.4

Although, different ionic conduction leads to different the electrochemical half reactions, the overall electrochemical reaction is the same as follows:

$$H_2 + \frac{1}{2}O_2 = H_2O \qquad 1.5$$

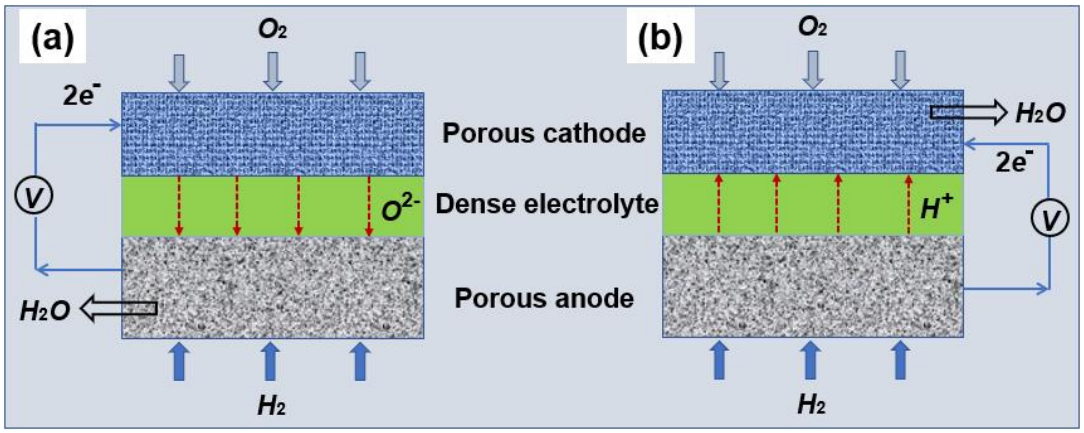

Figure 1.3: Operating principles of SOFC: (a) O-SOFC, (b) H-SOFC

1.2.2 Technical challenges and development trends of SOFC

For SOFC, the ionic conductivity of the electrolyte is an important factor affecting the performance of the cell. The ionic conductivity of the electrolyte is mainly affected by the properties of the material and the temperature. Initial SOFC generally operate at high temperature (~800-1000°C) to increase the ionic conductivity of the electrolyte to reduce the polarization loss [4]. The SOFC system also produces heat at high temperature that can be recycled. However, SOFC operating at high temperature are challenged by various material problems such as electrode sintering, catalyst poisoning, interfacial diffusion between electrolyte and electrodes, thermal instability and mechanical (or thermal) stress due to different coefficient of thermal expansion (CTE) of cell components [5]. The above problems will lead to failure of cell components and reduce cell life, which seriously restricts the development of SOFC. Reducing the working temperature of SOFC can effectively alleviate the above problems. In addition, lowering the working temperature can also solve the packaging problem of the cell stack at high temperature and reduce the cost because cheap stainless steel can be considered as the connector instead of ceramics in SOFC technology. Therefore, it is an important development trend to make SOFC work efficiently at intermediate temperature.

However, lowering the temperature will lead to a sharp decrease in the conductivity of the electrolyte. Reducing the thickness of the electrolyte layer is one of the effective ways to solve this problem. To reduce the thickness of the electrolyte as much as possible (make the electrolyte thin), the configuration design of SOFC must be carefully considered. As shown in Figure 1.4, there are four basic SOFC configuration designs, which are ES-SOFC, AS-SOFC, CS-SOFC, and externally supported SOFC [6]. Conventional ES-SOFC generally operates at high temperature (850-1000°C) to avoid high electrolyte ohmic impedance and obtain considerable cell performance due to thicker electrolyte layer (100 μm-1 mm). For AS-SOFC and CS-SOFC, a thin electrolyte layer (< 50 μm) can be designed to facilitate operation at lower temperature (< 800°C). However, the above three designs all use relatively expensive, brittle ceramics or cermets as mechanical supports, in which leads to increased manufacturing costs. Besides, it also faces problems such as structural damage caused by rapid thermal cycles and mechanical vibrations, and limitations in processing complex ceramic components. With the research on the operation of SOFC at intermediate temperature (600-800°C), more attention has been paid to the external support strategy using metal materials as support. In contrast, metal-supported SOFC (MS-SOFC) is an attractive design because of its high electrical conductivity, high strength, and good thermal shock resistance. Especially with the application of cheaper stainless-steel supports, there is a huge advantage in saving the fabrication cost of SOFC. Therefore, it can be predicted that MS-SOFC will be an important development direction of SOFC commercialization.

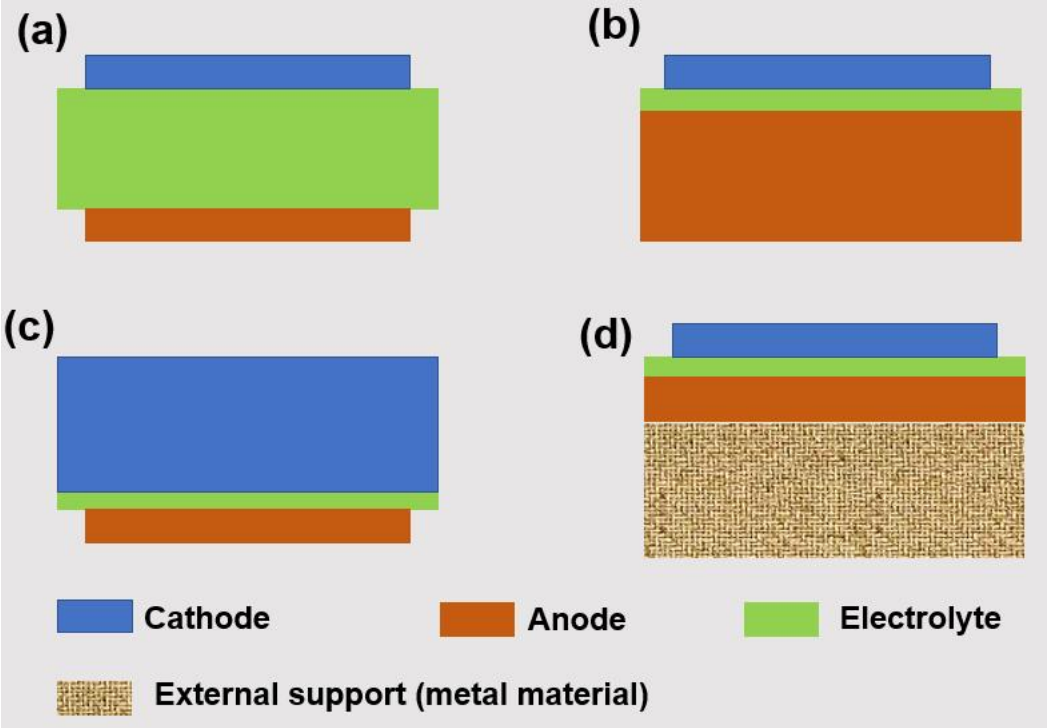

Figure 1.4: Single cell configurations of SOFC: (a) electrolyte-supported cell (b) anode-supported cell (c) cathode-supported cell and (d) external supported cell (metal supported)

1.3 Metal Supported Solid Oxide Fuel Cell (MS-SOFC)

Figure 1.5 shows the schematic configuration of typical AS-SOFC and MS-SOFC. The porous metal support can provide gas transmission channels, while greatly reducing the thickness of the anode layer and only retaining a thin anode layer as the function layer. Improving mechanical strength using metal supports allows cells and cell stacks to withstand stronger shock, vibration, and mechanical loads. The increase in mechanical strength is also beneficial for improving the processability of cells. In addition, the metal support can improve the rapid thermal cycling tolerance of the cell, allowing the cell to work in complex environments.

MS-SOFC is first reported in the 1960s. Williams et al. [7] deposited a ZrO_2-based electrolyte on pre-sintered austenitic stainless steel using flame spray technique. The cell produced a power density of 115 mW/cm^2 at 750°C. However, this work did not receive enough attention at that time. Until the 1990s, MS-SOFC regained attention. Momma et al. [8] and Schiller et al. [9] deposited zirconia electrolytes by plasma spraying on prefabricated tubular NiCrAlY alloy and planar $CrFe_5Y_2O_3$ supports, respectively. The power density of the cells reaches close to 1 W/cm^2 at 900°C. Since

the beginning of the new century, the application of colloidal and wet chemical methods in the preparation of thin film electrolytes has greatly promoted the development of MS-SOFC. Nowadays, many research teams have made many useful explorations in the development of MS-SOFC. This thesis will then introduce the development of MS-SOFC in detail in recent years.

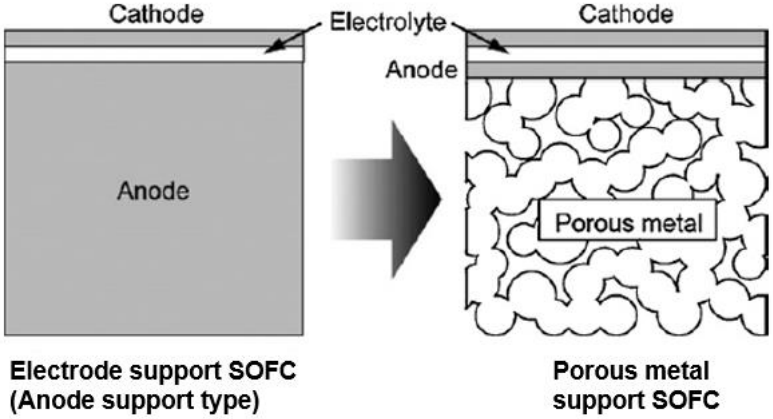

Figure 1.5: Schematic representation of anode-supported SOFC (AS-SOFC) and metal supported SOFC (MS-SOFC) [10].

1.3.1 Materials for MS-SOFC

The selection of materials for cell is a key factor in determining the performance of MS-SOFC. The electrochemical activity of materials and the possible impact by physical and chemical properties of materials on cell performance must be considered when selecting key materials for MS-SOFC.

1.3.1.1 Support materials

A suitable metal support for MS-SOFC should have these characteristics, that is, high electrical conductivity, high mechanical strength, good chemical stability, low volatility, and corrosion rate, CTE matching with commonly used component materials such as YSZ, GDC, etc., sufficient porosity and low cost. After many explorations on the selection of metal supports for MS-SOFC, the research focus is mainly on Fe-Cr-Ni system.

Figure 1.6 shows the schematic phase diagram of Fe-Cr-Ni system. Wu et al. summarized the properties of some alloys mentioned in the phase diagram (Table 1.2). ASS [11], FeBSA [12], and NiBSA [13] can be considered as candidate support materials due to their interesting oxidation resistance and high mechanical strength.

However, the CTE of these alloys are quite different from those of commonly used SOFC component materials, so they should be further explored. Porous pure nickel is also considered to be used as a support [14], but its CTE (16.5 $\times 10^{-6}$/K) is poorly matched with other SOFC component materials (10-13 $\times 10^{-6}$/K). The addition of iron to nickel can effectively reduce the CTE [15], but it still has problems such as weak oxidation resistance and weak mechanical strength.

Ferritic stainless steels (FSS) are considered as the preferred support material due to its interesting oxidation resistance and suitable CTE for MS-SOFC. FSS has oxidation resistance because the Cr forms a continuous Cr_2O_3 scale on the surface of stainless steel to prevent further oxidation. Yang et al. [16] summarized that the critical minimum Cr content is approximately 20-25 % to ensure the formation of a continuous, protective Cr_2O_3 scale. However, the oxidation resistance of FSS decreased sharply when the Cr content was reduced [17]. Excessive Cr content will lead to the formation of brittle phases, and the presence of excessive Cr_2O_3 scale is easy to detach from the matrix, which affects the adhesion between other component material and support. The minor addition of Ti, La, Ce, Y, Nb, Ta, Mo, and Si can effectively improve the adhesion between the Cr_2O_3 scale and the matrix [18]. However, compared with the FSS matrix, the conductivity of Cr_2O_3 scale is lower. The addition of Ti and Mn can effectively improve the conductivity of oxide scale [19]. An additional $(Cr, Mn)_3O_4$ protective layer can be formed when the Mn content is sufficient [20]. Therefore, usually a minor amount of the elements mentioned above will be added to FSS to improve performance. Table 1.3 lists several typical FSS that can be used as supports.

In addition, Fe and Cr will interdiffuse with Ni in the anode during cell operation when FSS is used as the support. As the Ni in the anode diffuses into the support, the FSS will transform into ASS and increase the CTE. The diffusion of Fe and Cr into the anode layer will lead to deactivation of the anode and cause a sharp decline in cell performance due to the formation of oxides on Ni particles [21-23]. Depositing a buffer layer between the metal support and the anode is a common strategy to prevent element diffusion. In this regard, researchers have done many useful explorations, such as GDC [21], La_2O_3 [22], $(Cr, Mn)_3O_4$ [20, 23], $(Co, Mn)_3O_4$ [24-25], $(Cr, Mn, Co)_3O_4$ [26], and

$CuMn_2O_4$ [27] have been widely studied as buffer layer.

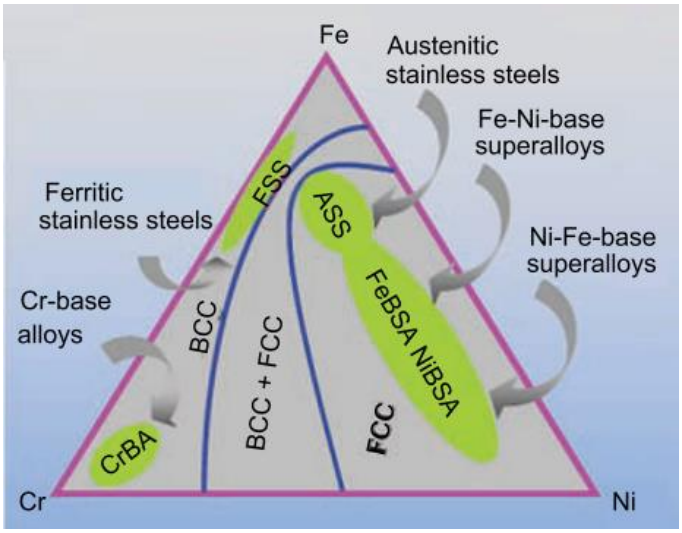

Figure 1.6: Schematic phase diagram of Fe-Cr-Ni system [28]

Table 1.2: Comparison of key properties of alloys as candidate metal supports [28-31]

Alloys	Main structure	CTE (RT-800°C, $10^{-6}K^{-1}$)	Oxidation resistance	Mechanical strength	Manufacturability	Cost
Cr based	BCC	11.0-12.5	Good	High	Difficult	Very expensive
FSS	BCC	11.5-14.0	Good	Low	Fairly readily	Cheap
ASS	FCC	18.0-20.0	Good	Fairly high	Readily	Cheap
FeBSA	FCC	15.0-20.0	Good	High	Readily	Fairly cheap
NiBSA	FCC	14.0-19.0	Good	High	Readily	Expensive
Ni	FCC	16.0-17.0	Low	Low	Readily	Expensive
Ni-Fe (1:1)	FCC	13.0-14.0	Low	Low	Readily	Fairly expensive

Table 1.3: Nominal compositions and CTE of FSS alloys [18, 32]

Alloys	Composition (wt %)	Additives (wt %)	CTE[a] (10^{-6}/K)
SS430	17Cr-Bal.Fe	1(Mn,Si)0.3(P,S)	11.4
SS441	18Cr-Bal.Fe	0.35Mn0.34Si0.22Ti0.5Nb0.3Ni	13.1
Crofer 22APU	20-24Cr-Bal.Fe	0.5(Si,Cu,Al)0.2(Ti,La)	12.5
Sandvik sanergy	22Cr-Bal.Fe	1Mo0.5Mn0.3Si0.75Nb	12.0
ITM	26Cr-Bal.Fe	Mo,Mn,Ti,Y_2O_3	11.3

[a] average between 25-900°C

1.3.1.2 Anode materials

The anode material should possess such properties as stability in reducing atmosphere, high electrical conductivity, and sufficient porosity for gas transport. Currently, Ni-based composite anodes are the most widely used. Ni has been used as an anode for many years because of its excellent catalytic activity for hydrogen oxidation and reforming of hydrocarbon fuels at relatively low cost. However, the CTE of Ni (16.0×10^{-6}/K) is quite different from commonly used electrolyte materials such as YSZ (10.5×10^{-6}/K), which will lead to thermal mismatch between the anode and the electrolyte. Therefore, Ni-based composite anodes, which are obtained by mixing metallic Ni and corresponding electrolyte materials, are widely used. The CTE of the composite anode can be adjusted by controlling the content of Ni. In addition, this composite anode has both ionic and electrical conductivity properties. Moreover, the Triple Phase Boundary (TPB) where the electrochemical reaction occurs is also increased [33].

Among Ni-based composite anodes, Ni-YSZ is the most widely used. The relative content of Ni and YSZ in the Ni-YSZ cermet anode affects the CTE, conductivity, porosity, and TPB density of the anode. As shown in Figure 1.7, Dees et al. [34] found that the conductivity of Ni-YSZ suddenly increased sharply when the volume content of Ni is 30 % in volume. This indicates that there is a threshold for the Ni content. The Ni-YSZ composite anode has better electrical conductivity due to the interconnection between Ni particles when the Ni content exceeds this threshold. However, when the Ni content is too high, the Ni particles will block the interconnection of the YSZ

particles, which increases the CTE and reduces the TPB concentration accordingly.

In addition to common Ni-YSZ composite anodes, other Ni-based anodes have also been widely studied, such as Ni-GDC, Ni-ScSZ, Ni-SDC, etc. Table 1.4 lists the power output performance of some single cells using Ni-based composite anodes. Other Ni-based composite anodes also have better performance and meet the requirements of MS-SOFC for anode materials.

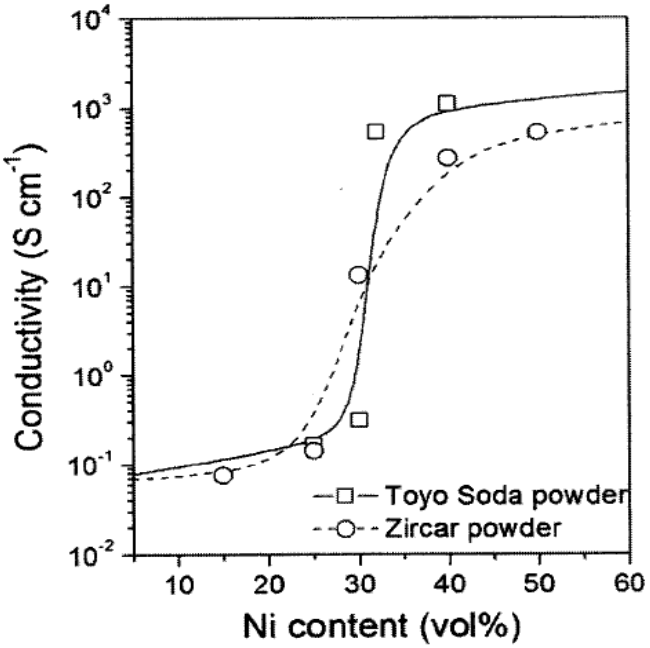

Figure 1.7: The conductivity of the Ni-YSZ composite anode as a function of Ni volume content at 1000°C [34]

Table 1.4: Comparison of maximum power densities of MS-SOFCs with different Ni-based composite anodes

Support/Anode	Electrolyte/Cathode	Temperature (°C)	Fuel	P_{max} (mW/cm^2)
22Cr-Bal.Fe/Ni-YSZ	ScYSZ/ LSCF	749	H_2	1200 [35]
FeCr/Ni-YSZ	YSZ/LSM/	700	H_2	993 [36]
ITM/Ni-YSZ/Ni-GDC	YSZ-GDC/LSCF	750	H_2	760 [37]
$Ni_{0.9}Fe_{0.1}$/Ni-GDC	GDC/LSCF	650	Wet CH_4	400 [38]
430L-SDC	SSZ/LSFSc-SSZ	750	Wet H_2	1000 [39]
430L/Ni-ScSZ	ScSZ/LSCF	700	Wet H_2	1079 [40]

ScYSZ: ZrO_2 co-doped with $Sc2O_3$ and Y_2O_3; LSCF: Sr, Co co-doped $LaFeO_3$; LSM: $(La,Sr)MnO_3$
SSZ: scandia stabilized zirconia; SDC: Samaria Doped Ceria; LSFSc: Sr, Fe co-doped $LaScO_3$

1.3.1.3 Electrolyte materials

As a key component of SOFC, the electrolyte layer determines the operating temperature, and affects the selection of electrode materials and preparation techniques. Commonly used electrolyte materials are oxide ceramics, including oxygen ion conducting and proton conducting. Only oxygen ion conducting is discussed in this thesis. For MS-SOFC, the electrolyte layer with the properties of high oxygen ion conductivity, chemical stability in oxidizing and reducing atmospheres, high density for gas tight, chemical compatibility, and thermal matching with other components of the cell, high strength, toughness, and low cost are ideal choices. At present, there are two main types of materials that are considered suitable for MS-SOFC operating at intermediate temperatures, including fluorite structure materials (ZrO_2-based, CeO_2-based, and Bi_2O_3-based materials), and perovskite structure material ($LaGaO_3$-based materials). Figure 1.8 shows the ionic conductivity of several typical oxygen ion conduction solid electrolytes as function as temperature.

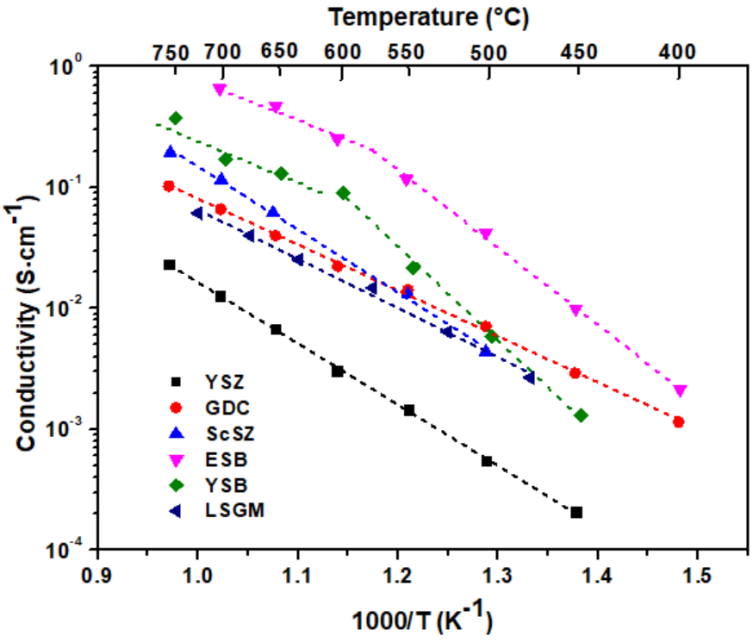

Figure 1.8: Ionic conductivity of several typical oxygen ion conducting solid electrolytes versus reciprocal temperatures [43, 44]

(a) ZrO_2-based electrolyte:

ZrO_2-based materials are the most used as electrolyte for the HT-SOFC. However, with the in-depth research of researchers and the development of material preparation

technology, it has also been used in IT-SOFC. Pure ZrO_2 exists in three distinct crystal structures, including monoclinic (< 1170°C), tetragonal (1170-2370°C) and cubic (> 2370°C) [5]. The change of crystal volume is accompanied by a crystal structure transformation, which makes the thermal stability of pure ZrO_2 material very poor. Researchers tried to partially replace Zr with suitable trivalent or divalent cations and found two beneficial results: the introduction of oxygen vacancies promotes oxygen ion conduction and stabilizes the cubic structure in a wide temperature range. Besides, the mechanical properties and thermal stability are also improved. Figure 1.9 shows the change of ionic conductivity and activation energy of ZrO_2-based electrolytes with the radius of doped ions. The ionic conductivity of ZrO_2-based electrolyte decreases with the increase of dopant ion radius, while the activation energy increases. The main reason is that the increase of the dopant ion radius leads to greater lattice distortion, which hinders the conduction of oxygen ions.

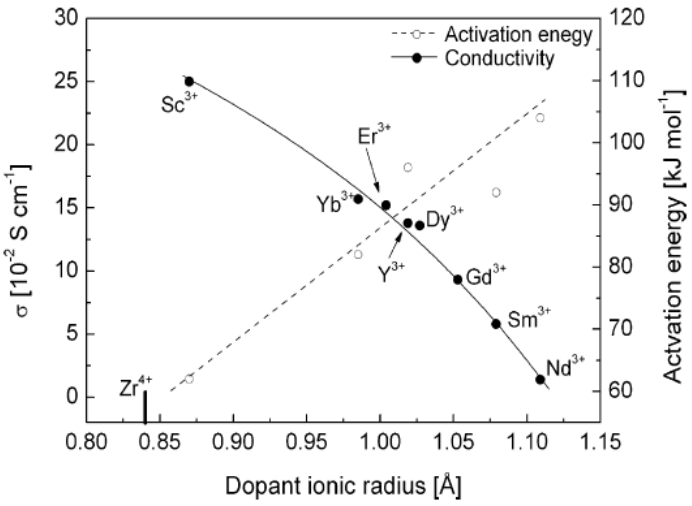

Figure 1.9: Effect of doping ionic radius on ionic conductivity (1000°C) and activation energy of ZrO_2-based electrolytes [45]

Y is the most commonly used dopant for ZrO_2. As shown in Figure 1.10, oxygen vacancies are correspondingly generated in the crystal to compensate for the charge change caused by doping Y^{3+}, which provides a channel for oxygen ion conduction. As the most used for SOFC electrolyte, the properties of YSZ have been well studied, including optimal doping amount and structural stability. At present, HT-SOFC stacks with YSZ electrolyte have been commercialized in the power range from 1 KW to 1

MW [41]. According to the research results from Badwal [42], 8YSZ has the highest oxygen ionic conductivity for YSZ. However, the ionic conductivity decreases rapidly with decreasing temperature even for 8YSZ. Therefore, the electrolyte layer should be thin enough to maintain low ohmic resistance when using YSZ as the electrolyte of MS-SOFC. In addition, ScSZ is also a commonly used electrolyte, and its ionic conductivity is generally higher than that of YSZ [42]. The main reason is that the radius of Sc^{3+} matches the Zr^{4+} better than that of Y^{3+}, which improve oxygen ion conduction. However, the smaller radius of Sc^{3+} leads to worse thermal stability of ScSZ than YSZ [42].

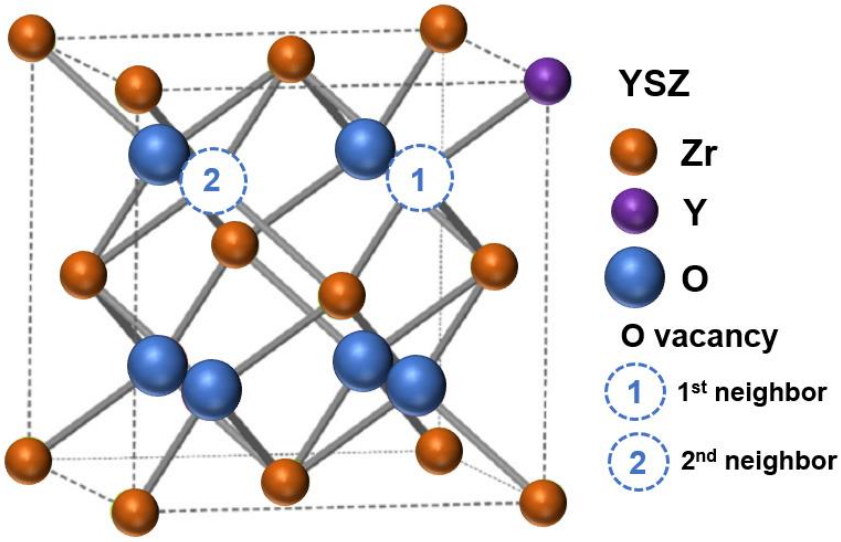

Figure 1.10: Schematic of the YSZ with defect fluorite structure [43]

(b) CeO_2-based electrolyte:

CeO_2 with cubic fluorite structure is stable from room temperature to its melting point. However, the ionic conductivity of pure CeO_2 is very low due to negligible oxygen vacancies in its crystal structure. As show in Figure 1.11, Yahiro et al. [46-48] have extensively investigated the partial substituent of Ce^{4+} in the crystal with trivalent or divalent cations to induce more oxygen vacancies to promote oxygen ion conduction. They found that when trivalent cations or divalent oxygen ions are doped into CeO_2, the conductivity shows a "volcano-type" change law with the increase of the doped ion radius. In addition, the conductivity of CeO_2 doped with trivalent cations is generally higher than that of divalent cations. Among them, $Gd_{0.1}Ce_{0.9}O_{1.95}$ (GDC10) and

$Sm_{0.2}Ce_{0.8}O_{1.9}$ (SDC20) have the highest conductivity.

Compared with ZrO_2-based electrolytes, CeO_2-based electrolytes generally have higher oxygen ion conductivity, especially at low temperatures. However, as the temperature increases (> 600°C), Ce^{4+} in CeO_2 will be reduced to Ce^{3+}, resulting in electronic conduction and lattice volume change. The existence of electrical conduction in the electrolyte will lead to the formation of internal short-circuit current during cell operation, which will reduce the OCV of the cell. Therefore, a single CeO_2-based electrolyte is suitable for working at low temperatures (< 600°C) [49]. Another advantage of the CeO_2-based electrolyte is that it has good thermal compatibility and chemical stability with commonly used component materials (FSS, Nickel based anode, LSF, LSM, LSCF, LNO, etc.) of MS-SOFC [50].

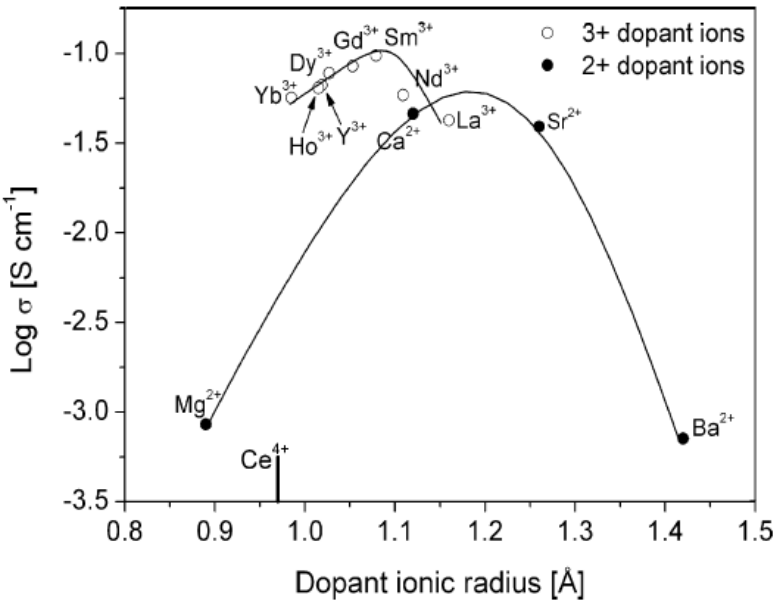

Figure 1.11: Effect of doping ionic radius on ionic conductivity (1000°C) and activation energy of CeO_2-based electrolytes [45-48]

(c) Bi_2O_3-based electrolyte:

Cubic δ-Bi_2O_3 with fluorite structure perhaps be the best oxygen ion conductor among such a category of materials (1 S/cm at 730°C), and it exhibits both high oxygen ion conductivity and electrocatalytic activity to transform O_2 into O^{2-} [51]. The oxygen ion conductivity of cubic δ-Bi_2O_3 is 1-2 orders of magnitude higher than that of YSZ. However, cubic δ-Bi_2O_3 has a limited in operating temperature range for SOFC

applications. Cubic δ-Bi_2O_3 is melted above 823°C and transitions to monoclinic α-phase below 730°C, resulting in significantly reduced conductivity [52]. Numerous studies have shown that the stable temperature of cubic δ-Bi_2O_3 can be extended to room temperature by doping with specific elements, mainly trivalent lanthanides, but at the expense of reduced ionic conductivity. However, the chemical stability of the stabilized bismuth oxide is still relatively poor, and it is easily reduced to metallic bismuth in a reducing atmosphere. In addition, the stabilized bismuth oxide electrolytes are usually difficult to densify and have poor mechanical strength, which is attributed to the volatile nature of Bi_2O_3 at high temperature [53]. Therefore, stabilized bismuth oxide is usually combined with YSZ, GDC, and SDC to form a bilayer electrolyte for LT/IT-SOFC (including MS-SOFC) applications [54].

(d) $LaGaO_3$-based electrolyte:

Some perovskite-type or related materials, such as $LnBO_3$ (Ln = lanthanum or alkaline earth element; B = Al, In, Sc, Y) perovskites, doped $LaGaO_3$ perovskites, $La_2Mo_2O_9$, and brownmillerite-like phases (chemical formula $A_2B_2O_5$), show high pure oxygen ion conductivity at intermediate temperatures. Among them, $LaGaO_3$-based perovskite materials have been intensively studied for MS-SOFC. It has been reported that partial substitution of the La site in $LaGaO_3$ with divalent alkaline earth metal ions, such as Sr^{2+}, Ba^{2+}, and Ca^{2+}, increases the ionic conductivity due to the generation of oxygen vacancies. In particular, the highest conductivity will be obtained in the doped $LaGaO_3$ series materials after partial substitution of Sr^{2+} with the closest ionic radius to La^{3+}. Theoretically, more oxygen vacancies will be generated to facilitate oxygen ion conduction as the doping amount of La site in $LaGdO_3$ increases. In fact, when the doping amount in the La site exceeds a value, $SrGaO_3$ or La_4SrO_7 impurity phases are generated, which will hinder the conduction of oxygen ions. In addition, the partial substitution of Ga site by divalent cations such as Mg^{2+} will also promote the generation of oxygen vacancies and increase the doping limit on La site. Ishihara et al. [55] reported that $La_{0.8}Sr_{0.2}Ga_{0.8}Mg_{0.2}O_{3-\delta}$ (LSGM) has the best oxygen ion conductivity in the $La_{1-x}Sr_xGa_{1-y}Mg_yO_{3-\delta}$ (x = 0.10-0.20, y = 0.15-0.20) series. Its oxygen ion

conductivity is higher than that of stabilized ZrO_2 and comparable to that of doped CeO_2 at intermediate temperatures. It should be noted that in MS-SOFC, LSGM will react with Cr_2O_3 or Cr-containing vapor, which will affect the long-term stability of the cell. In addition, LSGM also has serious chemical compatibility issues with Ni in Ni-based anodes and metal supports [56, 57]. Therefore, it is necessary to add a buffer layer such as GDC, SDC on the side of the LSGM electrolyte layer close to the anode and the metal support in MS-SOFC [50, 58].

1.3.1.4 Cathode materials

As an important component of SOFC, the cathode has a great influence on the overall performance of the cell, especially for MS-SOFC operating at intermediate temperature. Because the ORR that takes place at the cathode is directly affected by the decrease in temperature [59]. The ORR is a complex process involving several steps such as O_2 diffusion, surface exchange (oxygen adsorption, dissociation, and charge transfer), diffusion of oxygen ions on the surface or in the bulk, and oxygen ions transfer across the electrode/electrolyte interface, oxygen surface exchange and volume/surface diffusion [60]. Therefore, a good cathode material should first possess high electronic conductivity, usually greater than 100 S/cm, at operating temperature. The most ideal cathodes are Mixed Ionic and Electronic Conducting (MIEC) materials with high oxygen surface exchange coefficients (k) and oxygen bulk diffusion coefficients (D_δ) for MS-SOFC. In addition, the porous design of cathode materials can provide channels for oxygen transport to promote ORR. The CTE matching with the relevant cell components (typically electrolyte, 10-13 $\times$ 10^{-6}/K) also needs to be considered in the selection of cathode materials.

To reduce the cost of SOFC for wider commercial promotion, the selection of cathode materials has undergone a shift from precious metals such as (Pt, Au) to certain oxide families. Perovskites oxides with general formula ABO_3 are first widely investigated. Among them, $LaMnO_3$-based perovskite materials have attracted extensive attention. For $LaMnO_3$, which is an intrinsic p-type conductor, it can be doped with divalent alkaline earth to obtain a perovskite material with high p-type conductivity and stable in oxidizing atmosphere [61]. Sr^{2+} is the most widely used

dopant cation because the ion sizes between Sr^{2+} ($r_{Sr}^{2+} = 1.44$ Å) and La^{3+} ($r_{Sr}^{3+} = 1.36$ Å) are close [62]. In addition, an appropriate amount of Sr^{2+} (30 mol.%) doping into $LaMnO_3$ can inhibit the formation of the non-conductive phase $La_2Zr_2O_7$ when YSZ is used as the electrolyte. However, too high Sr^{2+} doping amount (> 30 mol%) in $La_{1-x}Sr_xMnO_{3-\delta}$ (LSM) will also form the non-conductive phase $SrZrO_3$. Unlike some other perovskite materials, when Sr^{2+} cations are used to substitute La^{3+} in $LaMnO_3$, this is not compensated by the formation of positively charged oxygen vacancies, but by the oxidation of manganese cations to increase the electron-hole concentration and thus improve the electronic conductivity [63]. Therefore, LSM is generally regarded as a purely electronic conductor and is used as the cathode in classical SOFCs with ZrO_2-based electrolytes operating at 1000°C. The reaction process on the LSM cathode is shown in Figure 1.12(a) and can be divided into three elementary stages: the adsorption of oxygen on the active center of the cathode material surface, the diffusion of adsorbed oxygen to TPB (electrolyte/cathode/oxygen), and the reduction of adsorbed oxygen to lattice oxygen ions. Apparently, for a purely electronic conductive cathode, TPB exists only between the interface of the cathode and the electrolyte, which constrains the ORR process on the cathode. To obtain acceptable cathode performance even for MS-SOFC, several approaches are taken. Mixing LSM with common electrolyte materials such as YSZ [64-68], GDC [69-72], etc. to form a composite cathode with MIEC property has been proved to be an effective method. For the reaction process of this type of composite material in the cathode as shown in Figure 1.12(b), it can be considered that the TPB is extended to the bulk of cathode, thereby enhancing the ORR reaction. For ABO_3 perovskite materials, another idea that can improve the electrochemical performance is to dope the A-site and B-site with cations. Usually, oxygen vacancies will be generated when the A-site of ABO_3 is doped with low-valent cations due to the charge compensation mechanism (except LSM). After doping modification, the material has MEIC properties. As shown in Figure 1.12(c), when the cathode material has MEIC properties, the reaction process at the cathode is not only on the TPB, but more on each microscopic surface of the cathode, which further strengthens the ORR on the cathode. There are mainly these materials with ABO_3 perovskite structure, La_{1-}

$_x$Sr$_x$Co$_{1-y}$Fe$_y$O$_{3-\delta}$ (LSCF) [73-75], Ba$_{1-x}$Sr$_x$Co$_{1-y}$Fe$_y$O$_{3-\delta}$ (BSCF) [76], Sm$_{1-x}$Sr$_x$CoO$_{3-\delta}$ (SSC) [77], La$_{1-x}$Sr$_x$Ni$_{1-y}$Fe$_y$O$_{3-\delta}$ (LSNF) [78], and LaNi$_{1-y}$Fe$_y$O$_{3-\delta}$ (LNF) [79] etc. which are considered to have potential application in MS-SOFC. Among these materials, LSCF is the most widely used. For LSCF, the CTE is usually reduced by increasing the doping amount of Fe to match the other component materials CTE (such as YSZ, GDC, etc.), but this also weakens the MIEC properties of the material. With the promotion of Co-free cathode materials to combine the current environmental protection concept, LSNF and LNF have attracted more attention. However, the influence of Ni on the MIEC properties of materials needs to be further investigated.

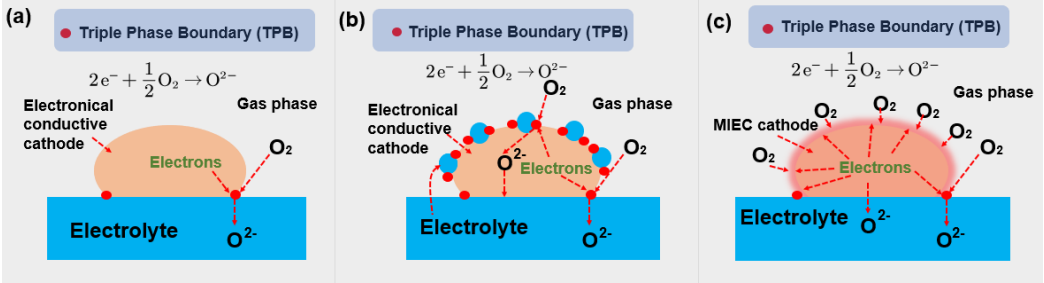

Figure 1.12: Schematic diagram of the cathode processes: (a) pure electronically conductive cathode material; (b) MIEC composite cathode material; (c) MIEC cathode material

In recent years, a kind of A_2BO_4 (where A = La, Pr, Nd; B = Cu, Ni, Co) oxides with K_2NiF_4-type structure has gained more attention for application on MS-SOFC due to its excellent ability to promote ORR at cathode. A typical K_2NiF_4 type structure is formed by ABO_3 perovskite structure and A_2O_2 rock layers arranged layer by layer along the *c*-axis, as shown in Figure 1.13. This structure can accommodate interstitial oxygen (in the rock layers) and oxygen vacancies (in the perovskite layers), which indicates that the conduction of oxygen ions in this type of material is not only through oxygen vacancies but also interstitial oxygen. These materials also have high electronic conductivity. Although the electronic conductivity of A_2BO_4 is not excellent compared to other doped perovskite materials (such as LSCF) at low/intermediate temperature, their CTE can match well with commonly used electrolyte materials. Current research on this type materials has mainly focused on nickelates considering the avoidance of Co. Cuprates are also investigated, but only Pr_2CuO_4 is found to have sufficient electronic conductivity, k, and D_δ for potential applications in IT/LT-SOFC [80].

Through the research on Ln_2NiO_4 (Ln = La, Pr, Nd), it is found that although they all show interesting performance at low/intermediate temperature, some issues should still be noticed. Mauvy et al. [81] found that La_2NiO_4 and Nd_2NiO_4 possess sufficient chemical stability not to decompose in a wide temperature range. The deficient Nd compound, $Nd_{1.95}NiO_4$, remained stable even at 1000°C when in contact with YSZ. However, when the well-mixed $Nd_{1.95}NiO_4$ and YSZ powders are sintered at 1100°C for 4 h, trace amount of the non-conductive pyrochlore phase $Nd_2Zr_2O_7$ formed. Hernández et al. [82] found that when La_2NiO_4 powder is directly deposited on the surface of YSZ or GDC pellets, no chemical reaction occurred at 900°C for 1 h. However, some $La_2Zr_2O_7$ and $La_3Ni_2O_7$ phases are observed after sintering for long time of 72 h. Syers et al. [83] investigated the chemical compatibility of La_2NiO_4 with YSZ and LSGM. They found that serious reactions occurred at 900°C for 4 h when La_2NiO_4 powders are mixed with YSZ, but not with LSGM. In addition, there is still a lack of favorable evidence on whether GDC, SDC electrolytes react with La_2NiO_4 and Nd_2NiO_4. From the above reports, the use of a buffer layer (such as GDC, LSGM) between the cathode and the electrolyte is necessary when Ln_2NiO_4 (Ln = La, Nd) and the commonly used electrolyte YSZ are used in SOFC. In addition, care should also be taken to minimize the sintering time when using the sintering method to prepare the cathode.

Pr_2NiO_4 is considered to have chemical stability issues, it will be decomposed to $Pr_4Ni_3O_{10}$ and Pr_6O_{11} below 1000°C, and the decomposition rate seems to be related to the electrolyte used [84, 85]. The decomposition of Pr_2NiO_4 as the cathode will cause the lattice change of the material, which may lead to the structural damage to the cell. Doping with La, Cu, Gd, etc. may stabilize this material against decomposition [86-88]. Additionally, it has been reported that $Pr_4Ni_3O_{10}$ with higher order Ruddlesden-Popper phase $(AO)(ABO_3)_m$ (m = 3) also has useful MIEC properties and is more stable at the operating temperature of SOFC [89, 90]. Unlike Pr_2NiO_4, $Pr_4Ni_3O_{10}$ has higher electronic conductivity and oxygen diffusion dominated by oxygen vacancies, but higher CTE [90-92]. Interestingly, it is shown that composite cathodes containing Pr_6O_{11} exhibited good ORR properties since Pr_6O_{11} can significantly accelerate the

oxygen surface exchange [93, 94].

Tables 1.5 and 1.6 list the CTE and performance (characterized by R_p of cathode) of the cathode materials reviewed above, respectively, providing a direct reference for the selection of cathode materials.

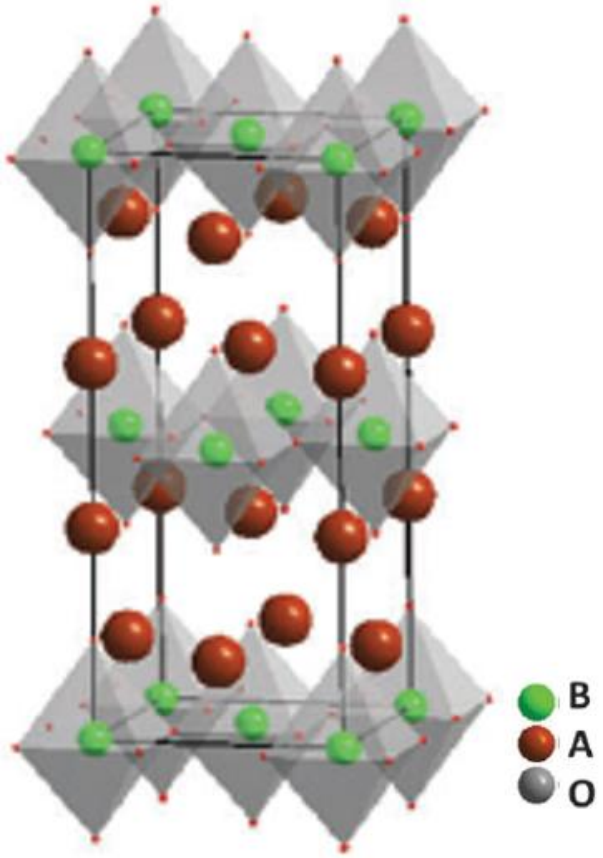

Figure 1.13: Crystal structure of A_2BO_4 with Ruddlesden-Popper phases cathode material [60]

Table 1.5: The average CTE of different cathode materials (300-1000°C) in air [86, 95, 96]

Composition	CTE×10^{-6}(K^{-1})	Composition	CTE×10^{-6}(K^{-1})
A_2BO_4		ABO_3	
La_2NiO_4	13.0	$La_{0.8}Sr_{0.2}MnO_3$	12.3
Nd_2NiO_4	12.7	$La_{0.6}Sr_{0.4}CoO_3$	20.5
Pr_2CuO_4	10.2	$La_{0.6}Sr_{0.4}FeO_3$	16.3
Pr_2NiO_4	13.6	$La_{0.6}Sr_{0.4}Co_{0.2}Fe_{0.8}O_3$	17.5
$La_{2-x}Pr_xNiO_4$ (x = 0-2)	13-13.5	$LaNi_{0.6}Fe_{0.4}O_3$	13.75
Electrolytes		$Ba_{0.5}Sr_{0.5}Co_{0.8}Fe_{0.2}O_3$	19.8
YSZ	10.8		
SDC	12.3		
GDC	13.5		
LSGM	11.1		

Table 1.6: The polarization resistance R_p of different cathode materials in air

	Composition	R_p (Ω cm^2)	Ref.
LSM	$La_{0.8}Sr_{0.2}MnO_3$	3.5[a,e] (750°C)	
LSM/GDC	$La_{0.8}Sr_{0.2}MnO_3/Ce_{0.8}Gd_{0.2}O_2$	0.49[a,e] (750°C)	[72]
LSM/YSZ	$La_{0.8}Sr_{0.2}MnO_3/Zr_{0.84}Y_{0.16}O_2$	1.31[a,e] (750°C)	
LSM/YSZ	$La_{0.8}Sr_{0.2}MnO_3/Zr_{0.84}Y_{0.16}O_2$	0.3[a,d] (700°C)	[97]
LSM/SDC	$La_{0.8}Sr_{0.2}MnO_3$ /$Ce_{0.8}Sm_{0.2}O_{1.9}$	1.034[b,e] (650°C)	[98]
LSCF	$La_{0.6}Sr_{0.4}Co_{0.2}Fe_{0.8}O_{3-\delta}$	0.67[a,d] (600 °C)	[99]
	$La_{0.8}Sr_{0.2}Co_{0.8}Fe_{0.2}O_{3-\delta}$	0.3[c,e] (700 °C)	[100]
BSCF	$Ba_{0.5}Sr_{0.5}Co_{0.2}Fe_{0.8}O_{3-\delta}$	0.26[c,e] (700 °C)	[101]
LNF	$LaNi_{0.6}Fe_{0.4}O_3$	2.78[b,e](750 °C)	[96]
	$La_{0.94}Ni_{0.6}Fe_{0.4}O_3$	0.61[b,e] (700 °C)	
LNO	La_2NiO_4	0.93[a,b,e] (600 °C)	[102]
LPNO	$La_{0.5}Pr_{1.5}NiO_4$	0.23[a,b,e] (600 °C)	
PNO	Pr_2NiO_4	0.15 [a,b,e] (600 °C)	
LNO	La_2NiO_4	0.42[b,e] (700 °C)	[85]
PNO	Pr_2NiO_4	0.36[b,e] (700 °C)	
NNO	Nd_2NiO_4	4.1 [b,e] (700 °C)	
20PPCO	Pr_2CuO_4-20%Pr_6O_{11}	0.07[b,e] (700 °C)	[103]

[a]YSZ support electrolyte; [b]GDC support electrolyte; [c]SDC support electrolyte; [d]Infiltrated; [e]Co-fire

1.3.2 Fabrication of MS-SOFC

Since the invention of SOFC, researchers have started from material development and preparation technology improvement with the goal of improving cell performance and reducing fabrication costs. Metal Support Strategy (MS-SOFC) is responsible for reducing the fabrication cost of SOFC to be more widely commercialized. However, the introduction of metal supports into SOFC also puts forward higher requirements on the fabrication of SOFC because the properties of metal materials are different from ceramic materials commonly used in SOFC. Therefore, the fabrication process should be carefully selected for MS-SOC. As regard, researchers have developed a series of fabrication technologies as shown in Figure 1.14 and Table 1.7. At present, the following two routes are mainly used to manufacture MS-SOFC:

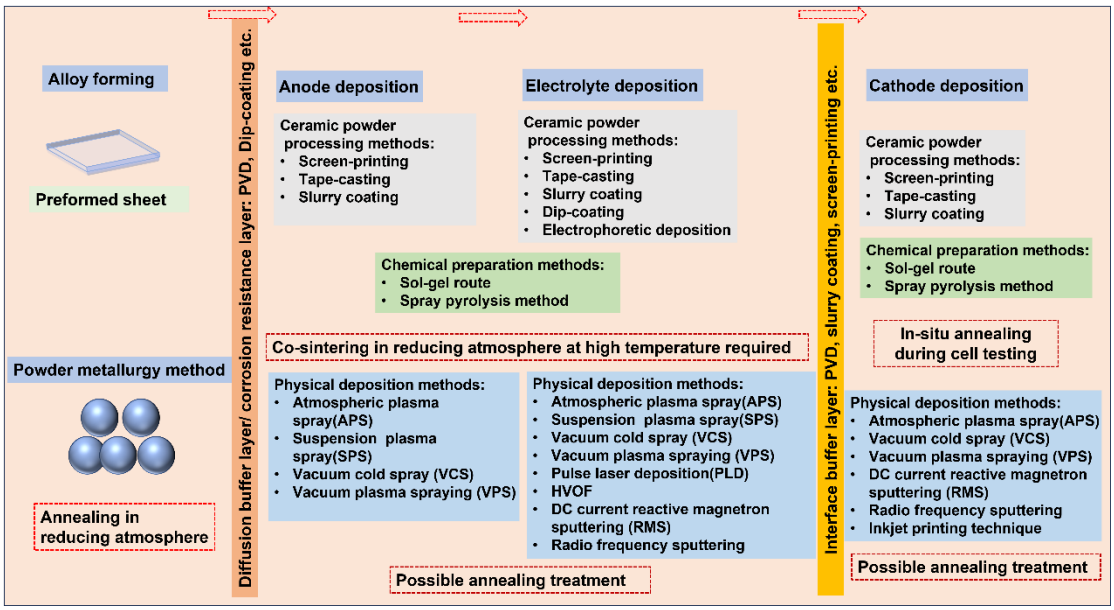

Figure 1.14: Technologies currently used to fabricate MS-SOFC [18]

(a) Mixed fabrication method

In mixed fabrication, ceramic powder processing technology combined with chemical preparation technology is most adopted due to significant cost advantages and good structural integrity. Metal supports, anode functional layers and electrolyte layers can be prepared by this method. However, one or more high-temperature co-sintering processes are required to obtain a sufficiently dense electrolyte layer and a support with sufficient strength in a reducing atmosphere. The cathode layer can be prepared by screen-printing and in-situ sintering (during cell testing) to avoid the decomposition of cathode material under low oxygen partial pressure. The disadvantage of this method is that it is difficult to establish a suitable co-sintering schedule due to the temperature requirements are often contradictory for the densification of the electrolyte, the sintering shrinkage of the metal support, and the oxidation of the metal. In addition, it has been reported that cathodes obtained by in-situ sintering have greater polarization resistance than those obtained by co-sintering [49, 76]. However, common cathode materials such as LSM, LSCF, etc. are not suitable for co-sintering with other components because they are easily decomposed in a high temperature reducing atmosphere.

For the mixed fabrication method, another approach is to comprehensively

consider the physical deposition method, chemical preparation method, and powder ceramic processing method to design a more suitable technical route for the fabrication of MS-SOFC. In this mixed fabrication method, the electrodes are prepared by powder ceramics preparation method or chemical preparation method, while the electrolyte is deposited by physical deposition method, especially magnetron sputtering technology, to avoid high temperature sintering process. As regard, researchers have carried out a lot of beneficial exploration.

(b) Physical deposition method

The physical deposition method usually deposits the coating at low temperature to avoid the long-term high-temperature sintering process. If necessary, annealing treatment can be used to release the stress of the coating and improve the crystallinity. This method makes it possible to sequentially deposit different functional layers on metal supports to obtain single cells in one step. Moreover, the complete single cell can be obtained at a lower temperature to avoid interdiffusion among Fr, Cr, and Ni. At present, the drawbacks of preparing MS-SOFC by physical deposition method are generally high cost and limited flexibility.

Although MS-SOFC has shown great potential due to its potential cost and performance advantages, the most mature commercialization is AS-SOFC. The main reason for this is that the fabrication process of MS-SOFC is not mature enough. The fabrication of MS-SOFC should be considered comprehensively, because it involves the realization of different component layers of the cell. Especially for metal supports, its compatibility with other component materials and high temperature oxidation tolerance must be considered. The comparison of some existing technologies that can be used to prepare MS-SOFC is listed in Table 1.7. It can be seen that the obvious disadvantage of the technologies widely used to prepare electrolyte, anode and cathode layers for a complete MS-SOFC, such as ceramic powder processing and chemical preparation, is that they usually need to undergo sintering at high temperature for a long time, which is unfavorable for metal supports. An obvious advantage of physical deposition is that the component layers can be deposited at low temperature, which is

very attractive for the fabrication of MS-SOFC. Low-temperature deposition can avoid element diffusion between component layers, especially metal elements in the metal support diffuse to the anode layer, during the deposition process. However, the current application of physical deposition techniques in MS-SOFC fabrication is limited. Therefore, the fabrication of MS-SOFC needs to be further developed.

The cell performance of MS-SOFC supported by ferritic stainless steel using different manufacturing methods is summarized in Table 1.8. From the table, it seems impossible to determine which fabrication process is the best but is directly related to the specific fabricating process.

Table 1.7: Advantages and drawbacks of various technologies for MS-SOFC fabrication [18, 104-106]

Fabrication methods		Estimated costs	Advantages	Drawbacks
Ceramic powder processing methods	Screen-printing Tape-casting	Low	Preparation of dense or porous layers with a thickness down to 5 μm with good uniformity; easy control of porosity; reproducibility; reliable multi-layer deposition technique; Scalable	High temperature sintering step for electrolyte densification; substrate uniformity required for deposition; size of the screen and resolution given by the mesh opening; Minimum coated layer 5 μm High temperature sintering step for electrolyte densification; bending issues; difficult to prepare coatings below 30 μm; need to burn out organic compounds in air to avoid formation of nitrides or carbides in reducing atmosphere
	Slurry coating Dip-coating	Low	Preparation of dense or porous layers with a thickness down to hundred nanometers; flexibility of size and shape of supports to be coated; multi-layer deposition technique; scalable	High temperature sintering step for electrolyte densification; often requires multiple steps of coating and annealing to achieve sufficient density
	Electrophoretic deposition	Moderate	Fast deposition speed; fewer restrictions on substrate shape and roughness; controllable film thickness; high powder packing density in the deposited layer, which is beneficial to reduce sintering temperature; good manufacturability	High temperature sintering step for electrolyte densification; cracks are formed when the thickness exceeds 50 μm; the substrate should be a conductor or a conductive backing such as carbon or platinum should be used; not easy to control the porosity of the electrode
Chemical	Sol-gel	Low	No shape required, can be sintered at intermediate and low temperature	Long duration (days or even a week); precursors are expensive (some are highly toxic)

preparation methods	Spray pyrolysis	Low	Possibility of multi-layer deposition; fast deposition; high purity and uniform film; simple device	Decomposition of precursors at high temperature; adhesion issues between film and substrate; large-Scale spray pyrolysis limited
Physical deposition methods	APS SPS VCS VPS HVOF	Moderate to high	Possibility of multi-layer deposition; fast deposition, deposition at low temperature avoids chemical reactions between different layers; flexibility in automated production; VPS has higher particle velocity than APS, resulting in higher density films	low P_{O2} during deposition leads to strain relaxation and formation of microcracks during post-annealing; electrodes with low porosity; anisotropy in electrolyte layer
	Magnetron sputtering	High	Preparation of high-dense or porous layers with a thickness down to hundred nanometers; high deposition rates; deposition at low temperature avoids chemical reactions between different layers; possibility of multi-layer deposition; high-purity films; extremely high adhesion of films; ability to coat heat-sensitive substrates; ease of automation; excellent uniformity on large-area substrates	Post-annealing may be required to obtain crystalline material; low P_{O2} during deposition leads to strain relaxation and formation of microcracks during post-annealing; anisotropy in electrolyte layer
	PLD	High	Ability to deposit layers with controlled microstructure at intermediate temperatures; multilayer films of different materials can be produced by sequentially ablating various targets	Post-annealing may be required to obtain crystalline material; low P_{O2} during deposition leads to strain relaxation and formation of microcracks during post-annealing; inhomogeneous deposition of large samples

Table 1.8 Performance of MS-SOFC use ferritic stainless steel as support prepared by different fabrication methods measured under H_2

Fabrication methods	Support	Diffusion buffer layer	Anode layer	Electrolyte layer	Interface buffer layer	Cathode layer	Maximum Power density(mW/cm^2)	Ref.
Ceramic powder processing and Chemical preparation	ITM	GDC20	Ni-YSZ /Ni-GDC	8YSZ/GDC	GDC20	LSCF	550 at 700°C	[37]
	STS430	−	Ni-YSZ	8YSZ	GDC	BSCF	310 at 700 °C	[76]
	STS430	−	Ni-YSZ	8YSZ	−	LSCM	30 at 700 °C	[107]
Ceramic powder processing and physical deposition methods	ITM	GDC20	Ni-YSZ /Ni-GDC10	8YSZ	GDC20	LSCF	910 at 700°C	[108]
	SS430	−	Ni-SDC	ScSZ/GDC	−	SSC-SDC	140 at 600 °C	[109]
	CroFer22APU	−	Ni-YSZ	YSZ	CeO_2	LSCF	430 at 800 °C	[73]
Physical deposition methods	Hastelloy X	−	NiO-SDC	ScSZ/GDC	−	SSC-SDC	110 at 600°C	[109]
	Hastelloy X	−	NiO-SDC	ScSZ/GDC	−	SDC-SSC	530 at 650°C	[110]
	ITM	LSG	NiO-YSZ	YSZ	LSG	LSM/LSCF	610 at 800°C	[111]
	ITM	GDC20	NiO-YSZ	8YSZ	GDC20	LNO	76 at 700°C	[2]

1.4 The research purpose and significance of this thesis

From Table 1.7, there are pros and cons to the different fabricating methods for MS-SOFC. From the cost point of view, ceramic powder processing methods and chemical preparation methods are advantageous, but the establishment of a reasonable sintering schedule is not easy. At present, the common disadvantage of the physical deposition methods is the relatively high cost. Interestingly, physical deposition methods allow possible multi-layer deposition as well as low-temperature deposition, which is attractive for the fabrication of MS-SOFC. The porous anode layer of MS-SOFC can be rapidly deposited by APS at low temperature, which avoids the reaction or diffusion between the anode layer and the metal support during the fabrication process. Magnetron sputtering can be used to deposit the dense and thin electrolyte layer, which avoids the prolonged high temperature sintering process for densification of the electrolyte layer.

Dr. J. FONDARD explored the fabrication of MS-SOFC single cell with configuration of ITM/GDC/Ni-YSZ/8YSZ/GDC/LNO under the guidance of Associate Prof. P. BRIOIS and Prof. G. BERTRAND during his doctoral studies. However, the P_{max} is only 76 mW/cm^2, which is far from meeting expectations [2]. This thesis is another attempt to fabricate MS-SOFC by combining APS and RMS technology, expecting to obtain interesting cell performance, based on the research results of Dr. J. FONDARD. Here, a novel composite cathode Pr_2NiO_4@Pr_6O_{11} (PPNO) is explored. The fabrication strategy of the complete single cell has changed. Annealing treatment is performed in air before the cell performance test in order to obtain a PPNO cathode with excellent electrochemical activity. The thickness of the GDC10 layer on the 8YSZ layer has been increased to form an 8YSZ/GDC10 bilayer electrolyte. The configuration of the MS-SOFC to be developed is shown in Fig. 1.15. Specifically, a bilayer NiO-YSZ anode is deposited by APS. The buffer, electrolyte, and cathode layer are deposited by RMS. The specific research content of this thesis is as follows:

(a) The deposition of NiO-YSZ anode on commercial ITM by APS and the evolution of the oxidation resistance of commercial ITM in air as temperature

are investigated in detail.

(b) The deposition of 8YSZ and GDC10 by RMS coupled with Plasma Emission Monitor (PEM) is investigated.

(c) A novel porous PPNO composite cathodes synthesized by RMS is explored.

(d) The fabrication process of MS-SOFC with ITM/GDC10/NiO-YSZ/8YSZ/GDC10/PPNO2 configuration is explored by APS and RMS. The performance of single cell is evaluated by electrochemical impedance spectroscopy (EIS), I-V curve and long-term constant current discharge test.

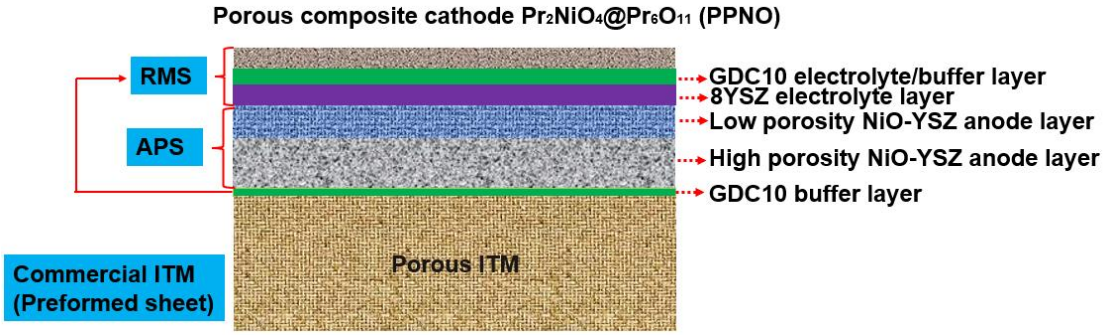

Figure 1.15: A brief schematic diagram of the MS-SOFC to be developed in this thesis

1.5 References

[1] O'hayre, R., Cha, S. W., Colella, W., & Prinz, F. B. (2016). Fuel cell fundamentals. John Wiley & Sons.

[2] Fondard, J. (2015) Elaboration et test d'une pile à combustible IT-SOFC à support métallique poreux par l'intermédiaire de techniques de dépôt en voie sèche: projection thermique et pulvérisation cathodique magnétron. (Doctoral dissertation, Université de Technologie de Belfort-Montbeliard).

[3] Buccheri, M. A., Singh, A., & Hill, J. M. (2011). Anode-versus electrolyte-supported Ni-YSZ/YSZ/Pt SOFCs: Effect of cell design on OCV, performance and carbon formation for the direct utilization of dry methane. Journal of Power Sources, 196(3), 968-976.

[4] Stambouli, A. B., & Traversa, E. (2002). Solid oxide fuel cells (SOFCs): a review of an environmentally clean and efficient source of energy. Renewable and sustainable energy reviews, 6(5), 433-455.

[5] Mahato, N., Banerjee, A., Gupta, A., Omar, S., & Balani, K. (2015). Progress in material selection for solid oxide fuel cell technology: A review. Progress in Materials Science, 72, 141-337.

[6] Badwal, S. P. S., Giddey, S., Munnings, C., & Kulkarni, A. (2015). Review of progress in high temperature solid oxide fuel cells. ChemInform, 46(31), no-no.

[7] Williams, K. R., & Smith, J. G. (1969). Fuel Cell with Solid State Electrolytes. US Pattent, 3(464), 861.

[8] Momma, A., Kaga, Y., Okuo, T., Fujii, K., Hohjyo, K. (1999) Improvement of the Electrode Performance of Alloy Substrate-type Tubular SOFC, 63, 103-113.

[9] Schiller, G., Henne, R., Lang, M., & Schaper, S. (2000). Development of Thin-Film SOFC for Reduced Operating Temperature. Functional Materials, 13, 170-174.

[10] Kurokawa, H., Lau, G. Y., Jacobson, C. P., De Jonghe, L. C., & Visco, S. J. (2007). Water-based binder system for SOFC porous steel substrates. Journal of materials processing technology, 182(1-3), 469-476.

[11] Molin, S., Gazda, M., & Jasinski, P. (2010). High temperature oxidation of porous alloys for solid oxide fuel cell applications. Solid State Ionics, 181(25-26), 1214-1220.

[12] Radhika, D., & Nesaraj, A. S. (2013). Materials and components for low temperature solid oxide fuel cells-an overview. International Journal of Renewable Energy Development, 2(2), 87.

[13] Yeh, A. C., Chen, Y. M., Liu, C. K., & Shong, W. J. (2015). Development of an advanced bond coat for solid oxide fuel cell interconnector applications. Journal of Power Sources, 296, 426-432.

[14] Kong, Y., Hua, B., Pu, J., Chi, B., & Jian, L. (2010). A cost-effective process for fabrication of metal-supported solid oxide fuel cells. International journal of hydrogen energy, 35(10), 4592-4596.

[15] Kim, K. H., Park, Y. M., & Kim, H. (2010). Fabrication and evaluation of the thin NiFe supported solid oxide fuel cell by co-firing method. Energy, 35(12), 5385-5390.

[16] Yang, Z., Weil, K. S., Paxton, D. M., & Stevenson, J. W. (2003). Selection and evaluation of heat-resistant alloys for SOFC interconnect applications. Journal of the Electrochemical Society, 150(9), A1188.

[17] Geng, S., Zhu, J., Brady, M. P., Anderson, H. U., Zhou, X. D., & Yang, Z. (2007). A low-Cr metallic interconnect for intermediate-temperature solid oxide fuel cells. Journal of Power Sources, 172(2), 775-781.

[18] Larring, Y., & Fontaine, M. L. (2013). Critical issues of metal-supported fuel cell. Solid Oxide Fuels Cells: Facts and Figures: Past Present and Future Perspectives for SOFC Technologies, 71-93.

[19] Ebrahimifar, H., & Zandrahimi, M. (2011). Mn coating on AISI 430 ferritic stainless steel by pack cementation method for SOFC interconnect applications. Solid State Ionics, 183(1), 71-79.

[20] Mah, J. C., Muchtar, A., Somalu, M. R., & Ghazali, M. J. (2017). Metallic interconnects for solid oxide fuel cell: A review on protective coating and deposition techniques. International Journal of Hydrogen Energy, 42(14), 9219-9229.

[21] Solovyev, A. A., Rabotkin, S. V., Shipilova, A. V., Kirdyashkin, A. I., Ionov, I. V., Kovalchuk, A. N., ... & Borduleva, A. O. (2015). Solid oxide fuel cell with Ni-Al support. International Journal of Hydrogen Energy, 40(40), 14077-14084.

[22] Fan, E. S. C., Kuhn, J., & Kesler, O. (2016). Suspension plasma spraying of $La_{0.6}Sr_{0.4}Co_{0.2}Fe_{0.8}O_{3-\delta}$ cathodes: Influence of carbon black pore former on performance and degradation. Journal of Power Sources, 316, 72-84.

[23] Yang, Z., Xia, G. G., Maupin, G. D., & Stevenson, J. W. (2006). Conductive protection layers on oxidation resistant alloys for SOFC interconnect applications. Surface and Coatings Technology, 201(7), 4476-4483.

[24] Jin, Y., Sheng, J., Hao, G., Guo, M., Hao, W., Yang, Z., & Peng, S. (2022). Highly dense (Mn, Co) 3O4 spinel protective coating derived from Mn–Co metal precursors for SOFC interconnect applications. International Journal of Hydrogen Energy, 47(29), 13960-13968.

[25] Zhu, J. H., Chesson, D. A., & Yu, Y. T. (2021). $(Mn, Co)_3O_4$-Based Spinels for SOFC Interconnect Coating Application. Journal of The Electrochemical Society, 168(11), 114519.

[26] Wei, W., Chen, W., & Ivey, D. G. (2009). Oxidation resistance and electrical properties of anodically electrodeposited Mn-Co oxide coatings for solid oxide fuel cell

interconnect applications. Journal of Power Sources, 186(2), 428-434.

[27] Acharya, N., Chaitra, U., Vijeth, H., & Sagar, R. (2022). Highly dense Mn3O4 and $CuMn_2O_4$ spinels as efficient protective coatings on solid oxide fuel cell interconnect and their chromium diffusion studies. Journal of Alloys and Compounds, 918, 165377.

[28] Wu, J., & Liu, X. (2010). Recent development of SOFC metallic interconnect. Journal of materials science & technology, 26(4), 293-305.

[29] Kong, Y., Hua, B., Pu, J., Chi, B., & Jian, L. (2010). A cost-effective process for fabrication of metal-supported solid oxide fuel cells. International journal of hydrogen energy, 35(10), 4592-4596.

[30] Kim, K. H., Park, Y. M., & Kim, H. (2010). Fabrication and evaluation of the thin NiFe supported solid oxide fuel cell by co-firing method. Energy, 35(12), 5385-5390.

[31] Yang, Z., Xia, G. G., & Stevenson, J. W. (2006). Evaluation of Ni-Cr-base alloys for SOFC interconnect applications. Journal of Power Sources, 160(2), 1104-1110.

[32] Shong, W. J., Liu, C. K., Kao, W. X., Cheng, Y. N., & Lee, R. Y. (2022). High temperature (800°C) oxidation of AISI 441 stainless steel with Mn-Co contact layers for SOFC stacks. International Journal of Hydrogen Energy, 47(10), 6811-6826.

[33] Zhang, Y., & Xia, C. (2011). Film percolation for composite electrodes of solid oxide fuel cells. Electrochimica acta, 56(13), 4763-4769.

[34] Dees, D. W., Claar, T. D., Easler, T. E., Fee, D. C., & Mrazek, F. C. (1987). Conductivity of Porous Ni/ZrO2-Y_2O_3 Cermets. Journal of the Electrochemical Society, 134(9), 2141.

[35] Blennow, P., Hjelm, J., Klemensø, T., Persson, Å. H., Ramousse, S., & Mogensen, M. (2011). Planar metal-supported SOFC with novel cermet anode. Fuel Cells, 11(5), 661-668.

[36] Tucker, M. C., Lau, G. Y., Jacobson, C. P., DeJonghe, L. C., & Visco, S. J. (2007). Performance of metal-supported SOFCs with infiltrated electrodes. Journal of Power Sources, 171(2), 477-482.

[37] Rojek-Wöckner, V. A., Opitz, A. K., Brandner, M., Mathé, J., & Bram, M. (2016). A novel Ni/ceria-based anode for metal-supported solid oxide fuel cells. Journal of Power Sources, 328, 65-74.

[38] Li, Q., Wang, X., Liu, C., Yang, X., Li, C., Jia, L., & Li, J. (2022). A direct-methane solid oxide fuel cell with a functionally engineered Ni–Fe metal support. Journal of Power Sources, 537, 231533.

[39] Zhou, Y., Chen, T., Li, J., Yuan, C., Xin, X., Chen, G., & Wang, S. (2015). Long-term stability of metal-supported solid oxide fuel cells employing infiltrated electrodes. Journal of Power Sources, 295, 67-73.

[40] Lin, J., Li, H., Wang, W., Qiu, P., Tao, G., Huang, K., & Chen, F. (2023). Atmospheric plasma spraying to fabricate metal-supported solid oxide fuel cells with open-channel porous metal support. Journal of the American Ceramic Society, 106(1), 68-78.

[41] Yan, D., Liang, L., Yang, J., Zhang, T., Pu, J., Chi, B., & Li, J. (2017). Performance degradation and analysis of 10-cell anode-supported SOFC stack with external manifold structure. Energy, 125, 663-670.

[42] Badwal, S. P. S. (1992). Zirconia-based solid electrolytes: microstructure, stability and ionic conductivity. Solid State Ionics, 52(1-3), 23-32.

[43] Shi, H., Su, C., Ran, R., Cao, J., & Shao, Z. (2020). Electrolyte materials for intermediate-temperature solid oxide fuel cells. Progress in Natural Science: Materials International, 30(6), 764-774.

[44] Ye, X., Yang, L., Luo, H., Bertrand, P., Billard, A., & Briois, P. (2022). Synthesis of Yttria Stabilized Bismuth Oxide by DC Reactive Magnetron Sputtering (RMS) for SOFC Electrolyte. Crystals, 12(11), 1585.

[45] Molenda, J., Świerczek, K., & Zając, W. (2007). Functional materials for the IT-SOFC. Journal of Power Sources, 173(2), 657-670.

[46] Eguchi, K., Setoguchi, T., Inoue, T., Arai, H.J.S.S.I. (1992) Electrical properties of ceria-based oxides and their application to solid oxide fuel cells, 52, 165-172.

[47] Yahiro, H., Eguchi, K., & Arai, H. (1989). Electrical properties and reducibilities of ceria-rare earth oxide systems and their application to solid oxide fuel cell. Solid State Ionics, 36(1-2), 71-75.

[48] Yahiro, H., Ohuchi, T., Eguchi, K., & Arai, H. (1988). Electrical properties and microstructure in the system ceria-alkaline earth oxide. Journal of Materials Science,

23, 1036-1041.

[49] Huang, Q. A., Wang, B., Qu, W., & Hui, R. (2009). Impedance diagnosis of metal-supported SOFCs with SDC as electrolyte. Journal of Power Sources, 191(2), 297-303.

[50] Ishihara, T., Yan, J., Shinagawa, M., & Matsumoto, H. (2006). Ni–Fe bimetallic anode as an active anode for intermediate temperature SOFC using $LaGaO_3$ based electrolyte film. Electrochimica Acta, 52(4), 1645-1650.

[51] Lovett, A. J., Wells, M. P., He, Z., Lu, J., Wang, H., & MacManus-Driscoll, J. L. (2022). High ionic conductivity in fluorite δ-bismuth oxide-based vertically aligned nanocomposite thin films. Journal of Materials Chemistry A, 10(7), 3478-3484.

[52] Sammes, N. M., Tompsett, G. A., Näfe, H., & Aldinger, F. (1999). Bismuth based oxide electrolytes-structure and ionic conductivity. Journal of the European Ceramic Society, 19(10), 1801-1826.

[53] Ayhan, Y. S., & Buyukaksoy, A. (2019). Impact of fabrication temperature on the stability of yttria doped bismuth oxide ceramics. Solid State Ionics, 338, 66-73.

[54] Pesaran, A., Jaiswal, A., & Wachsman, E. D. (2019). Bilayer electrolytes for low temperature and intermediate temperature solid oxide fuel cells-a review.

[55] Ishihara, T., Matsuda, H., & Takita, Y. (1995). Effects of rare earth cations doped for La site on the oxide ionic conductivity of $LaGaO_3$-based perovskite type oxide. Solid State Ionics, 79, 147-151.

[56] Huang, P., Horky, A., & Petric, A. (1999). Interfacial reaction between nickel oxide and lanthanum gallate during sintering and its effect on conductivity. Journal of the American Ceramic Society, 82(9), 2402-2406.

[57] Zhang, X., Ohara, S., Okawa, H., Maric, R., & Fukui, T. (2001). Interactions of a $La_{0.9}Sr_{0.1}Ga_{0.8}Mg_{0.2}O_{3-\delta}$ electrolyte with Fe_2O_3, Co_2O_3 and NiO anode materials. Solid State Ionics, 139(1-2), 145-152.

[58] Ju, Y. W., Eto, H., Inagaki, T., & Ishihara, T. (2009). High power SOFC using LSGM film on NiFe porous bi-metal substrate. ECS transactions, 25(2), 719.

[59] Steele, B. C., & Heinzel, A. (2001). Materials for fuel-cell technologies. Nature, 414(6861), 345-352.

[60] Gao, Z., Mogni, L. V., Miller, E. C., Railsback, J. G., & Barnett, S. A. (2016). A

perspective on low-temperature solid oxide fuel cells. Energy & Environmental Science, 9(5), 1602-1644.

[61] Kuo, J. H., Anderson, H. U., & Sparlin, D. M. (1989). Oxidation-reduction behavior of undoped and Sr-doped $LaMnO_3$ nonstoichiometry and defect structure. Journal of Solid State Chemistry, 83(1), 52-60.

[62] Shannon, R. D. (1976). Revised effective ionic radii and systematic studies of interatomic distances in halides and chalcogenides. Acta crystallographica section A: crystal physics, diffraction, theoretical and general crystallography, 32(5), 751-767.

[63] Sun, C., Hui, R., & Roller, J. (2010). Cathode materials for solid oxide fuel cells: a review. Journal of Solid State Electrochemistry, 14, 1125-1144.

[64] Rehman, S. U., Song, R. H., Lee, J. W., Lim, T. H., Park, S. J., & Lee, S. B. (2016). Effect of GDC addition method on the properties of LSM-YSZ composite cathode support for solid oxide fuel cells. Ceramics International, 42(10), 11772-11779.

[65] Liu, Y. L., Hagen, A., Barfod, R., Chen, M., Wang, H. J., Poulsen, F. W., & Hendriksen, P. V. (2009). Microstructural studies on degradation of interface between LSM-YSZ cathode and YSZ electrolyte in SOFCs. Solid State Ionics, 180(23-25), 1298-1304.

[66] McIntosh, S., Adler, S. B., Vohs, J. M., & Gorte, R. J. (2004). Effect of polarization on and implications for characterization of LSM-YSZ composite cathodes. Electrochemical and solid-state letters, 7(5), A111.

[67] Agbede, O. O., Hellgardt, K., & Kelsall, G. H. (2020). Electrical conductivities and microstructures of LSM, LSM-YSZ and LSM-YSZ/LSM cathodes fabricated on YSZ electrolyte hollow fibres by dip-coating. Materials Today Chemistry, 16, 100252.

[68] Lee, E., Jeong, H., Shin, T. H., & Myung, J. H. (2021). Determination of the rate-determining step of the oxygen reduction reaction of $La_{0.8}Sr_{0.2}MnO_3$ (LSM)-8mol% yttria-stabilized zirconia (YSZ): Composition and microstructure. Ceramics International, 47(2), 1792-1797.

[69] Ahmed, B., Lee, S. B., Song, R. H., Lee, J. W., Lim, T. H., & Park, S. J. (2014). Development of novel LSM/GDC composite and electrochemical characterization of LSM/GDC based cathode-supported direct carbon fuel cells. Journal of Solid State

Electrochemistry, 18, 435-443.

[70] Xia, C., Zhang, Y., & Liu, M. (2003). LSM-GDC composite cathodes derived from a sol-gel process: Effect of microstructure on interfacial polarization resistance. Electrochemical and Solid-State Letters, 6(12), A290.

[71] Wang, W. (2005). Fabrication and performance of GDC-impregnated (La, Sr) MnO3 cathodes for intermediate temperature solid oxide fuel cells. Journal of the Electrochemical Society, 152(7), A1398.

[72] Murray, E. P., & Barnett, S. A. (2001). (La, Sr) MnO_3-(Ce, Gd) O_{2-x} composite cathodes for solid oxide fuel cells. Solid State Ionics, 143(3-4), 265-273.

[73] Brandner, M., Bram, M., Froitzheim, J., Buchkremer, H. P., & Stöver, D. (2008). Electrically conductive diffusion barrier layers for metal-supported SOFC. Solid state ionics, 179(27-32), 1501-1504.

[74] Hwang, C., Tsai, C. H., Lo, C. H., & Sun, C. H. (2008). Plasma sprayed metal supported YSZ/Ni-LSGM-LSCF ITSOFC with nanostructured anode. Journal of Power Sources, 180(1), 132-142.

[75] Zhu, T., Du, X., Bu, Y., Zhong, Q., Sun, Z., & Han, M. (2017). Validation and electrochemical characterization of LSCF cathode deposition on metal supported SOFC. Journal of The Electrochemical Society, 164(13), F1489.

[76] Kim, Y. M., Kim-Lohsoontorn, P., & Bae, J. (2010). Effect of unsintered gadolinium-doped ceria buffer layer on performance of metal-supported solid oxide fuel cells using unsintered barium strontium cobalt ferrite cathode. Journal of Power Sources, 195(19), 6420-6427.

[77] Harris, J., & Kesler, O. (2011). Performance of metal-supported composite and single-phase cathodes based on LSCF and SSC. ECS Transactions, 35(1), 1927.

[78] Smirnova, A., Sadykov, V., Mezentseva, N., Usoltsev, V., Smorygo, O., Bobrenok, O., & Uvarov, N. (2010, January). Metal-supported SOFC on compressed Ni-Al foam substrates. In International Conference on Fuel Cell Science, Engineering and Technology (Vol. 44052, pp. 411-416).

[79] Komatsu, T., Arai, H., Chiba, R., Nozawa, K., Arakawa, M., & Sato, K. (2007). Long-term chemical stability of $LaNi(Fe)O_3$ as a cathode material in solid oxide fuel

cells. Journal of The Electrochemical Society, 154(4), B379.

[80] Zheng, K., Gorzkowska-Sobaś, A., & Świerczek, K. (2012). Evaluation of Ln_2CuO_4 (Ln: La, Pr, Nd) oxides as cathode materials for IT-SOFCs. Materials Research Bulletin, 47(12), 4089-4095.

[81] Mauvy, F., Lalanne, C., Bassat, J. M., Grenier, J. C., Zhao, H., Huo, L., & Stevens, P. (2006). Electrode properties of $Ln_2NiO_{4+\delta}$ (Ln= La, Nd, Pr): AC impedance and DC polarization studies. Journal of the Electrochemical Society, 153(8), A1547.

[82] Hernández, A. M., Mogni, L., & Caneiro, A. (2010). $La_2NiO_{4+\delta}$ as cathode for SOFC: Reactivity study with YSZ and CGO electrolytes. international journal of hydrogen energy, 35(11), 6031-6036.

[83] Sayers, R., Liu, J., Rustumji, B., & Skinner, S. J. (2008). Novel K_2NiF_4-type materials for solid oxide fuel cells: compatibility with electrolytes in the intermediate temperature range. Fuel Cells, 8(5), 338-343.

[84] Zhou, X. D., Templeton, J. W., Nie, Z., Chen, H., Stevenson, J. W., & Pederson, L. R. (2012). Electrochemical performance and stability of the cathode for solid oxide fuel cells: V. high performance and stable Pr_2NiO_4 as the cathode for solid oxide fuel cells. Electrochimica Acta, 71, 44-49.

[85] Philippeau, B., Mauvy, F., Mazataud, C., Fourcade, S., & Grenier, J. C. (2013). Comparative study of electrochemical properties of mixed conducting $Ln_2NiO_{4+\delta}$ (Ln= La, Pr and Nd) and $La_{0.6}Sr_{0.4}Fe_{0.8}Co_{0.2}O_{3-\delta}$ as SOFC cathodes associated to $Ce_{0.9}Gd_{0.1}O_{2-\delta}$, $La_{0.8}Sr_{0.2}Ga_{0.8}Mg_{0.2}O_{3-\delta}$ and $La_9SrSi_6O_{26.5}$ electrolytes. Solid State Ionics, 249, 17-25.

[86] Vibhu, V., Rougier, A., Nicollet, C., Flura, A., Grenier, J. C., & Bassat, J. M. (2015). $La_{2-x}Pr_xNiO_{4+\delta}$ as suitable cathodes for metal supported SOFCs. Solid State Ionics, 278, 32-37.

[87] Wang, Y., Cheng, J., Jiang, Q., Yang, J., & Gao, J. (2011). Preparation and electrochemical performance of $Pr_2Ni_{0.6}Cu_{0.4}O_4$ cathode materials for intermediate-temperature solid oxide fuel cells. Journal of Power Sources, 196(6), 3104-3108.

[88] Nomura, T., Nishimoto, S., Kameshima, Y., & Miyake, M. (2012). Electrode properties of doped Pr_2NiO_4-based oxide cathode for intermediate-temperature SOFCs.

Journal of the Ceramic Society of Japan, 120(1407), 534-538.

[89] Yatoo, M. A., Du, Z., Yang, Z., Zhao, H., & Skinner, S. J. (2020). $La_xPr_{4-x}Ni_3O_{10-\delta}$: Mixed A-Site Cation Higher-Order Ruddlesden-Popper Phase Materials as Intermediate-Temperature Solid Oxide Fuel Cell Cathodes. Crystals, 10(6), 428.

[90] Tsai, C. Y., Aguadero, A., & Skinner, S. J. (2020). High electrical conductivity and crystal structure of the solid oxide cell electrode $Pr_4Ni_3O_{10-\delta}$. Journal of Solid State Chemistry, 289, 121533.

[91] Laffez, P., Simon, Q., Kikuchi, Y., Retoux, R., Giovannelli, F., & Yamamoto, A. (2020). Growth of polycrystalline $Pr_4Ni_3O_{10}$ thin films for intermediate temperature solid oxide fuel cell cathode by radio frequency magnetron co-sputtering. Thin Solid Films, 693, 137705.

[92] Hoffmann, M., Klingeler, R., Rout, D., Mudi, S. R., Spachmann, S., & Singh, S. (2020). Structural and physical properties of trilayer nickelates $R_4Ni_3O_{10}$ (R= La, Pr, and Nd).

[93] Tong, X., Xu, Y., Tripković, Đ., Hendriksen, P. V., Kiebach, W. R., & Chen, M. (2020). Promotion of oxygen reduction and evolution by applying a nanoengineered hybrid catalyst on cobalt free electrodes for solid oxide cells. Journal of Materials Chemistry A, 8(18), 9039-9048.

[94] Chen, Y., Chen, Y., Ding, D., Ding, Y., Choi, Y., Zhang, L., & Liu, M. (2017). A robust and active hybrid catalyst for facile oxygen reduction in solid oxide fuel cells. Energy & Environmental Science, 10(4), 964-971.

[95] Zhao, H., Li, Q., & Sun, L. (2011). Ln_2MO_4 cathode materials for solid oxide fuel cells. Science China Chemistry, 54, 898-910.

[96] Mei, W., Wang, H., Li, W., Zhou, J., Sun, X., Zhao, H., & Wang, S. (2021). Enhanced and stable strontium and cobalt free A-site deficient $La_{1-x}Ni_{0.6}Fe_{0.4}O_3$ (x= 0, 0.02, 0.04, 0.06, 0.08) cathodes for intermediate temperature solid oxide fuel cells. International Journal of Hydrogen Energy, 46(73), 36436-36444.

[97] Suzuki, T., Awano, M., Jasinski, P., Petrovsky, V., & Anderson, H. U. (2006). Composite (La, Sr) MnO_3-YSZ cathode for SOFC. Solid State Ionics, 177(19-25), 2071-2074.

[98] ZHENG, Y., Shan, G. E., Xueying, Z. H. O. U., Hong, C. H. E. N., HUANG, S., Shaorong, W. A. N. G., & Yueming, S. U. N. (2012). LSM particle size effect on the overall performance of IT-SOFC. Journal of Rare Earths, 30(12), 1240-1244.

[99] Hildenbrand, N., Boukamp, B. A., Nammensma, P., & Blank, D. H. (2011). Improved cathode/electrolyte interface of SOFC. Solid state ionics, 192(1), 12-15.

[100] Liu, J., Co, A. C., Paulson, S., & Birss, V. I. (2006). Oxygen reduction at sol–gel derived $La_{0.8}Sr_{0.2}Co_{0.8}Fe_{0.2}O_3$ cathodes. Solid State Ionics, 177(3-4), 377-387.

[101] Park, J., Zou, J., Yoon, H., Kim, G., & Chung, J. S. (2011). Electrochemical behavior of $Ba_{0.5}Sr_{0.5}Co_{0.2-x}ZnxFe_{0.8}O_{3-\delta}$ (x= 0-0.2) perovskite oxides for the cathode of solid oxide fuel cells. international journal of hydrogen energy, 36(10), 6184-6193.

[102] Vibhu, V., Rougier, A., Nicollet, C., Flura, A., Grenier, J. C., & Bassat, J. M. (2015). $La_{2-x}Pr_xNiO_{4+\delta}$ as suitable cathodes for metal supported SOFCs. Solid State Ionics, 278, 32-37.

[103] Shijie, Z., Na, L., Liping, S., Qiang, L., Lihua, H., & Hui, Z. (2022). One-pot synthesis Pr_6O_{11} decorated Pr_2CuO_4 composite cathode for solid oxide fuel cells. International Journal of Hydrogen Energy, 47(9), 6227-6236.

[104] Lyu, Y., Wang, F., Wang, D., & Jin, Z. (2020). Alternative preparation methods of thin films for solid oxide fuel cells. Materials Technology, 35(4), 212-227.

[105] Tudose, I. V., Comanescu, F., Pascariu, P., Bucur, S., Rusen, L., Iacomi, F., & Suchea, M. P. (2019). Chemical and physical methods for multifunctional nanostructured interface fabrication. Functional Nanostructured Interfaces for Environmental and Biomedical Applications, 15-26.

[106] Ugemuge, N., Parauha, Y. R., & Dhoble, S. J. (2021). Synthesis and luminescence study of silicate-based phosphors for energy-saving light-emitting diodes. In Energy Materials (pp. 445-480). Elsevier.

[107] Lee, C., & Bae, J. (2008). Fabrication and characterization of metal-supported solid oxide fuel cells. Journal of Power Sources, 176(1), 62-69.

[108] Bischof, C., Nenning, A., Malleier, A., Martetschläger, L., Gladbach, A., Schafbauer, W., Bram, M. (2019). Microstructure optimization of nickel/gadolinium-doped ceria anodes as key to significantly increasing power density of metal-supported

solid oxide fuel cells. International journal of hydrogen energy, 44(59), 31475-31487.
[109] Huang, Q. A., Oberste-Berghaus, J., Yang, D., Yick, S., Wang, Z., Wang, B., & Hui, R. (2008). Polarization analysis for metal-supported SOFCs from different fabrication processes. Journal of power sources, 177(2), 339-347.
[110] Hui, R., Berghaus, J. O., Decès-Petit, C., Qu, W., Yick, S., Legoux, J. G., & Moreau, C. (2009). High performance metal-supported solid oxide fuel cells fabricated by thermal spray. Journal of Power Sources, 191(2), 371-376.
[111] Ansar, A., Szabo, P., Arnold, J., Ilhan, Z., Soysal, D., Costa, R., & Franco, T. (2011). Metal supported solid oxide fuel cells and stacks for auxilary power units-progress, challenges and lessons learned. Ecs Transactions, 35(1), 147.

Chapter 2: Deposition and characterization of components of MS-SOFC

2.1 Introduction

This thesis aims to develop and characterize MS-SOFC by physical deposition method. It mainly includes the deposition of electrodes, electrolyte, and buffer layer by different deposition techniques. In this chapter, the APS process of the anode layer, the RMS process of the electrolyte or buffer layer, and the cathode are firstly introduced. Then different characterization techniques are presented for the analysis of morphology, structure, chemical bonding state of the materials, and single cell performance. Table 2.1 lists all raw materials used in this thesis.

Table 2.1 Raw materials involved in the experiments

Raw material	Composition/Purity	Specification	Producer
ITM	26Cr-Fe Bal.	Plane	PLANSEE SE
YSZ	$Zr_{0.92}Y_{0.08}O_{1.96}$	Powder	NEYCO
NiO	99.9 %	Powder	
8YSZ pellet	$Zr_{0.84}Y_{0.16}O_{2-\delta}$	Φ25 ×0.5 mm	
Ni target	99.9 %	Φ200 * 6 mm	AMPERE INDUSTRIE
$Ce_{90}Gd_{10}$ alloy target			
$Zr_{84}Y_{16}$ alloy target			
Pr target			

2.2 Fabrication techniques

2.2.1 Atmospheric Plasma Spraying (APS)

Thermal spraying technology uses high-temperature heat sources such as plasma jets and combustion flames to heat powder materials to a molten or semi-molten state, and then sprays the powder onto the surface of the substrate at a certain speed by means of jets, flames, or other external conditions. The powder is deposited on the substrate surface to form the coating. Since it is invented by the Germans at the beginning of the 20^{th} century, thermal spraying has developed through multiples processes:

oxyacetylene flame spraying, plasma spraying, arc spraying, detonation spraying, supersonic spraying, cold spraying technology and very low-pressure plasma spraying. Nowadays, as a practical engineering technology, thermal spraying technology is playing an important role in industrial production.

2.2.1.1 The principle of APS

APS is a thermal spraying technology that works in an atmospheric environment, and its working principle is shown in Figure 2.1. A high-intensity arc is generated between the cathode and anode of the torch by a DC power supply. The working gas (usually Ar and H_2) entering the arc chamber is ionized by the high-intensity arc to form a plasma. The powder is injected into the plasma jet at a 90° right angle through an injector, and then deposited on a surface thanks to the torch scanning face to this surface. During this process, the temperature in the plasma can reach over 10000°C, so the powder particles will be heated rapidly until they are melted or partially melted. Although the residence time of the particles in the plasma is generally very short, it is sufficient for the powder particles to be in a molten or semi-molten state when they reach the substrate surface. The heated powder particles are deposited on the substrate as a single particle unit, forming a coating with layered accumulation morphology. These particles undergo a very rapid cooling on impact with the substrate which can contribute to the formation of defects such as abundant pores and cracks in the coating.

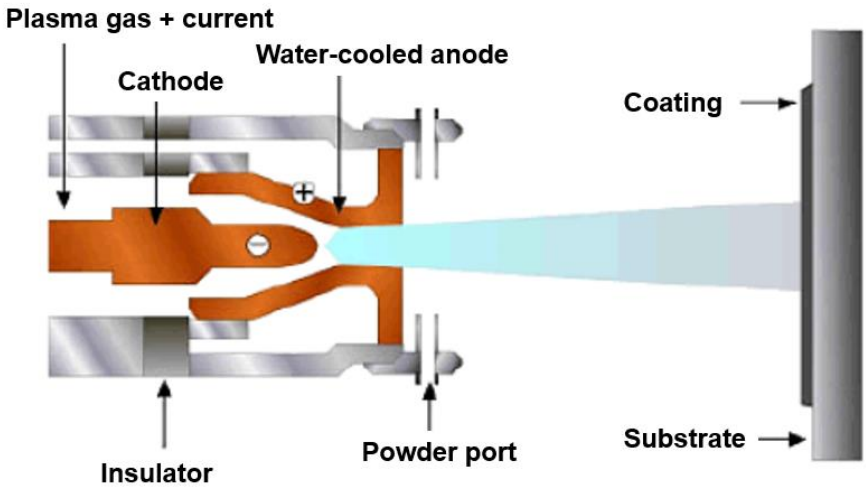

Figure 2.1: Schematic diagram of a plasma torch [1]

2.2.1.2 Deposition parameters of APS

Several factors concerning the generation of the plasma (working gas, plasma power), the powder (injector, powder size and morphology), the spraying kinematics (scanning speed, standoff distance) and the substrate (properties, surface treatments) can affect the coating deposited on the substrate.

Usually, the substrate needs to be sandblasted and cleaned with organic solvents to promote mechanical anchorage and adhesion between the coating and the substrate. In our case, the substrate has sufficient initial roughness that does not require additional post-processing. Hydrogen and argon are used as working gases to form the plasma. The composition and flow rate of the working gas have an important impact on the deposition of the coating. As a reactive gas, hydrogen can increase the thermal conductivity of the plasma, thereby improving the heat transfer to the powder particles in the plasma. Argon is considered a viscous gas that helps stabilize the plasma. The longer the powder particles stay in the plasma, the more energy they gain. The characteristics of powder particles such as particle size and melting point are also important factors affecting the coating morphology. Indeed, the increase in the size of the particles injected into the plasma can modify the microstructure of the deposit through the incorporation of less well melted particles leading to stacking faults during the coating building. Conversely, a smaller powder size can promote better particle melting and lead to a denser deposit by reducing the number or size of stacking faults.

2.2.1.3 The experimental device for APS deposition

In this thesis a F4-MB torch purchased from Oerlikon is used for the deposition of NiO-YSZ anodes. The torch is protected by a circulating water-cooling system with a nozzle outlet diameter of 6 mm. A conical cathode encased by tungsten and thorium was placed in the center of the torch. A cylindrical anode is made of copper and encased by tungsten. The working gas (H_2-Ar) enters the arc chamber controlled by the gas flow meter to form a plasma. The ignition of the plasma is controlled by a control panel as shown in Figure 2.2 (a). The torch as shown in Figure 2.2 (b) is connected to a programmable ABB robotic arm, which can be precisely scanned to ensure the

deposition of uniform thickness coatings. The robotic arm was programmed to scan the surface of the sample with the scanning conditions of a speed of 300 mm/s and a step of 5 mm. The NiO-YSZ powder is transported by the carrier gas through a feeding device as shown in Figure 2.2(c) to an injector with a diameter of 1.8 mm located at 6 mm from the torch axis. The injection direction of the powder is 90° to the plasma jet. The powder is injected into the plasma jet with a mass flow rate of 15 g/min. The distance between the substrate and the torch exit is 90 mm. Compressed air is blown from a 45° angle to the deposited coating to facilitate cooling during the deposition process.

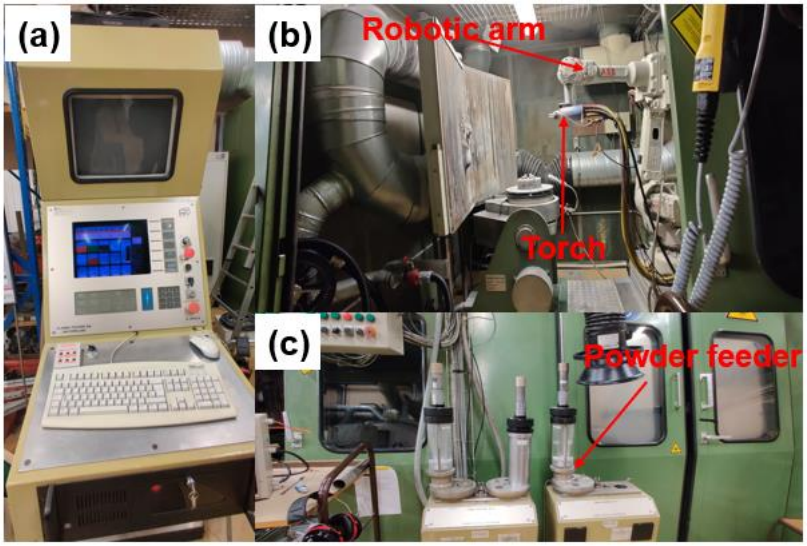

Figure 2.2 APS system: (a) control Panel, (b) spray device, (c) powder feeding device

2.2.2 Reactive Magnetron Sputtering (RMS)

Plasma-based physical vapor deposition (PVD) processes, achieved either evaporated by thermal evaporation or sputtered from the cathode target by ion bombardment, have been widely used in various industrial applications. For decades, sputter deposition has been recognized as a flexible, reliable, and effective coating technique. For sputtering deposition, the sputtering source directly affects the entire sputtering process, which undergoes from DC glow discharge sputtering discharge to magnetron sputtering discharge. In a planar configuration, the magnetron sputtering discharge is realized by adding the magnets directly behind the cathode target. Moreover, the energy of the sputtered species can be maintained while reducing the

operating pressure by the magnetron sputtering technique, which generally improves the coating properties. Therefore, magnetron sputtering technology has been the mainstay in plasma-based sputtering applications since it was developed in the 1960s and 1970s. RMS is a magnetron sputtering technology that introduces reactive gases such as oxygen and nitrogen into the chamber during the process.

2.2.2.1 Principle of RMS deposition technique

With the development of electrical technology, the progress of magnetron sputtering technology has been brought, which is mainly reflected in the sputtering source. The selection of sputtering sources for magnetron sputtering is diversified, mainly including Direct Current (DC) generator, Pulsed DC generator, Radio Frequency (RF) generator, and high-power pulsed generator etc. When using DC generator for RMS to deposit insulating coating, target poisoning is often encountered due to the coverage of the insulating coating on the target surface. In this case, a pulsed generator is introduced to avoid target poisoning. RF magnetron sputtering can deposit almost any solid coating including insulating coating. However, compared with pulsed DC magnetron sputtering, the sputtering rate of RF magnetron sputtering is lower. In addition, the application of Plasma Emission Monitoring (PEM) technology on RMS can also effectively solve the problem of target poisoning [2].

In this thesis, a pulsed DC generator is used as a sputtering source to deposit oxide coating by RMS, and its working principle is shown in Figure 2.3 illustrating the motion behavior of particles. The plasma generated by the potential difference between the magnetron cathode and the reactor used as anode. Electron ionization is initially triggered by pulsed DC generator, and the generated electrons move at a high speed under the combined action of electric and magnetic fields (**E**×**B**) and collide with argon atoms to form argon ions, finally generating plasma. In this process, the electrons generated by the pulsed DC excitation are magnetized by the magnetron because their gyration radius is much lower than the characteristic size of the magnetron, and then undergo **E**×**B** drift in the ionization region above the target surface [3]. In a circular magnetic field, electrons will perform a closed circular motion in the form of a cycloid

in the plasma region. In this case, two advantages are revealed for the ionization of argon. Firstly, the motion path of electrons is greatly prolonged, which in turn increases the collision probability of electrons and argon atoms when the average free path and reaction space remain unchanged. Secondly, the kinetic energy of the electrons gradually accumulates during the drift process, which increases the effective collision probability with the argon atoms. During the **E**×**B** drift process, high-energy electrons collide with argon atoms to produce argon ions and new electrons with weak energy, and the kinetic energy of the electrons participating in the collision is consumed. The new electrons are captured by the electric field and magnetic field together and added to the drifting electron flow to wait for the next collision. Usually, the gyration radius of ion is larger than the characteristic size of the magnetron and not be magnetized by the magnetron [4]. Therefore, the ions are not **E**×**B** drift, and their trajectory is dominated by the electric field. The generated argon ions are accelerated by the cathode potential drop and eventually bombard the metal target, causing metal atoms (M) to escape from the target. The escaping metal atoms either go straight to the substrate or collide with electrons. The metal atoms (M) running to the substrate are oxidized by oxygen on the way to form oxides deposited on the substrate or deposited directly. Metal atoms (M) collided by electrons will form metal ions (M^+) and new secondary electrons. Most metal ions (M^+) escape from the ionization region after multiple scattering elastic collisions and then undergo the same process as metal atoms (M) rushing to the substrate. A small part of the metal ions (M^+) will bombard the target under the action of the cathode potential drop to participate in the re-sputtering mechanism. This may be since these metal ions (M^+) are closer to the target surface and have lower kinetic energy so that they are easily manipulated by the cathode potential drop. Although this re-sputtering by the back-attracted target metal ions (M^+) promotes ionization, it impairs the sputtering rate. In addition, although the secondary electrons generated by each ionization collision will be re-bound by the **E**×**B** drift to facilitate the next collision, as the number of collisions increases, the electrons will gradually move out of the ionization region and the kinetic energy will decrease. Eventually, these electrons will reach the substrate under the action of an electric field **E**. Since the

electron energy at this time is very low, the temperature rise of the substrate is low.

It should be noted that the oxygen entering the ionization region may be reduced to oxygen anions (such as O^-, O^{2-}, O_2^-) because oxygen easily captures electrons. Oxygen anions may react with metal atoms (M^+) that are close to the target surface with low kinetic energy to form oxides (MO), even when pulsed power is used. If a large amount of these oxides (MO) is deposited on the target surface, it may cause target poisoning.

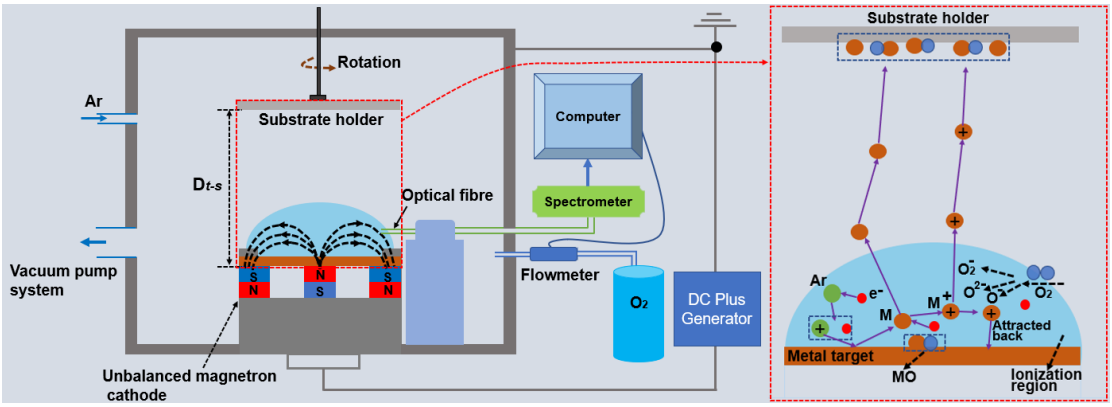

Figure 2.3: Schematic diagram of the working principle of reactive magnetron sputtering

2.2.2.2 Application of Plasma Emission Monitoring (PEM) on RMS

A typical hysteresis phenomenon is observed as shown in Figure 2.4. for the deposition of oxide coatings by Reactive Magnetron Sputtering (RMS). For a new metal target, the sputtering rate is basically unchanged with the increase of the oxygen flow rate at the beginning. As the oxygen flow rate further increases, the sputtering rate decreases, but it is not very different from the sputtering rate under pure argon. An almost metallic coating is deposited in this process and is considered a metal mode. But the sputtering rate will suddenly drop sharply when the oxygen flow rate increases to a critical value F_1. Usually, the sputtering rate R_2 currently is an order of magnitude smaller than the initial sputtering rate R_1. At this time an oxide coating is deposited and is considered an oxide mode. The reason for the decrease in sputtering rate is that the target surface is covered by metal oxide. The secondary electron emission coefficient of metal oxide is generally higher than that of metal. Therefore, a large part of the energy of the incident particles is used to excite the secondary electron emission of the metal oxide. Correspondingly, the energy the incident particles used to bombard the

metal target is reduced, resulting in a significant decrease in the sputtering rate. Starting from the oxide mode, the sputtering rate does not immediately return from R_2 to R_1 but increases slowly as the oxygen flow rate gradually decreases. This process also belongs to the oxide mode. When the oxygen flow rate decreases to a certain critical value F_2, the sputtering rate suddenly increases to R_1. Currently, the sputtering is considered to return to the metal mode. There is also a hysteresis loop between the target voltage and the oxygen flow rate like that between the sputtering rate and the oxygen flow rate. The changing trends of the two hysteresis loops are the same. Hysteresis effects are not welcomed in the RMS process. Because there are two different sputtering modes corresponding to the same oxygen flow value in the unstable region of the hysteresis loop. The specific deposition mode depends on the sputtering history experienced by the target surface.

In metal mode, a metal coating is deposited instead of the required oxide. The desired oxide coating can be deposited in oxide mode, but the deposition rate is lower. Therefore, to deposit the required oxide coating at high deposition rates, the oxygen flow rate should be fixed at the inflection point F_1 of the hysteresis loop. Usually, however, this is difficult to achieve with magnetron sputtering operating in flow-controlled mode. Because any fluctuation of oxygen partial pressure in the sputtering chamber (such as fluctuations caused by pump operation) will change the sputtering mode, and often this change is irreversible. Therefore, a fast feedback method to automatically control the oxygen flow to stabilize the reactive sputtering process is necessary. At present, there are two practical and reliable methods to achieve this goal, that is, the Plasma Emission Monitoring method and the target voltage monitoring method. Among them, the target voltage monitoring method is only suitable for the situation that there is a large difference of target voltage value between the metal mode and the oxide mode. In comparison, the scope of application of the PEM method is wider because it monitors the intensity of the emission optical from the discharge plasma.

In RMS, the emission optical position from the discharge plasma is related to the target material, gas composition, and oxide. But its emission optical intensity is related

to the RMS process. For example, in the process of depositing 8YSZ coating using $Zr_{0.84}Y_{0.16}$ alloy as the target under the condition of fixed oxygen flow rate, the oxygen partial pressure in the sputtering chamber increases because the target is covered by the oxide 8YSZ, so that the emission optical intensity of Zr at 386 nm in the discharge plasma is significantly attenuated. The PEM method automatically regulates the RMS process by monitoring the change of the spectral intensity. As a closed-loop feedback system, the PEM process usually includes optical signal acquisition, analysis, photoelectric conversion, calculation and comparison of control parameters. The equipment involved There are fiber optic probes, conducting fibers, spectrometers, controllers, etc.

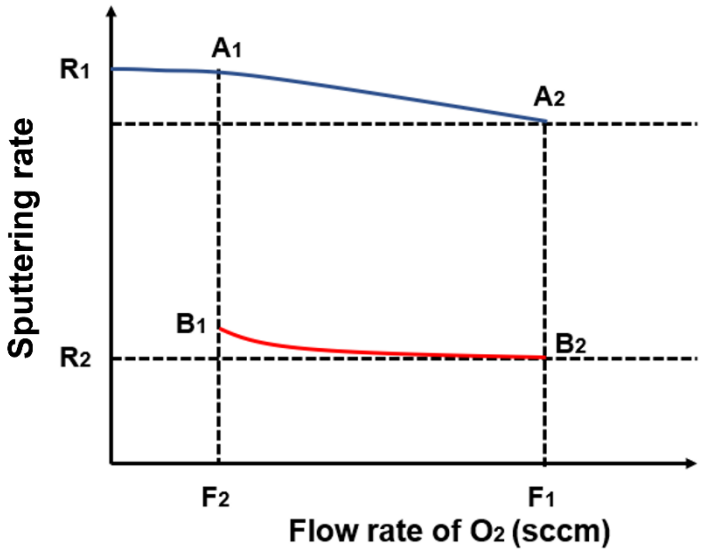

Figure 2.4: Hysteresis loops during reactive magnetron sputtering

2.2.2.3 Deposition parameters of RMS under plasma emission monitoring

To obtain the required oxide coating, some relevant deposition parameters need to be optimized. For the RMS process performed under the PEM system, the spectral intensity of the target should be considered first. As mentioned in the previous section, the PEM system regulates the sputtering process by monitoring the intensity of the emission spectrum from the discharge plasma. Therefore, the hysteresis relationship between the oxygen flow rate and the sputtering rate in Figure 2.4 can be transformed into the hysteresis relationship between the emission spectrum intensity and the oxygen flow rate as shown in Figure 2.5. In this way, the operator can more intuitively control

the sputtering process through the PEM system. The spectral signals collected from the discharge plasma under pure argon (metal mode) is defined as 100%. In the PEM system, the spectral signals can be artificially set in the scope of unstable region to achieve different sputtering processes. Therefore, the set value of the spectral signals affects the deposited coating. For the convenience of description, the set value of the spectral signal is simplified as Setpoint. It should be noted that such a hysteresis relationship is affected by the target, the gas composition in the sputtering chamber, and the operating pressure. Different target materials and gas compositions will lead to different hysteresis loops, which are mainly reflected in the position and range of the unstable region. As the deposition pressure increases, the scope of the unstable region shrinks, and the location moves toward low oxygen flow rate [5]. This change may originate from the effect of operating pressure on the particles in the sputtering chamber. In fact, the operating pressure significantly affects the kinetic energy of the particles in the sputtering chamber. The particles in the sputtering chamber have smaller average free path at higher operating pressures, which increases the probability of particle collisions. But it also leads to a decrease in the kinetic energy of the incident particles (Ar^+) due to more collisions between particles at high operating pressures. The effect of the increase of operating pressure on the coating can be intuitively reflected in the coating morphology. From the long-term research of magnetron sputtering deposition coatings by Associate Prof. P. BRIOIS, Prof. A. BILLARD et al., dense electrolyte coatings (such as YSZ [6, 7], GDC [8], LaMOx [9], etc.) can be better deposited at lower pressures (< 1 Pa), while to obtain a porous coating requires a higher pressure (usually several Pa) [5]. The morphology of the coating will develop towards the columnar crystal as the operating pressure increases. In addition, to enhance the adhesion between the coating and the substrate, it is generally considered to apply a bias power on the substrate. But some cracks appear in the coating after annealing treatment due to internal stress when an excessively high bias power is applied to the substrate [10].

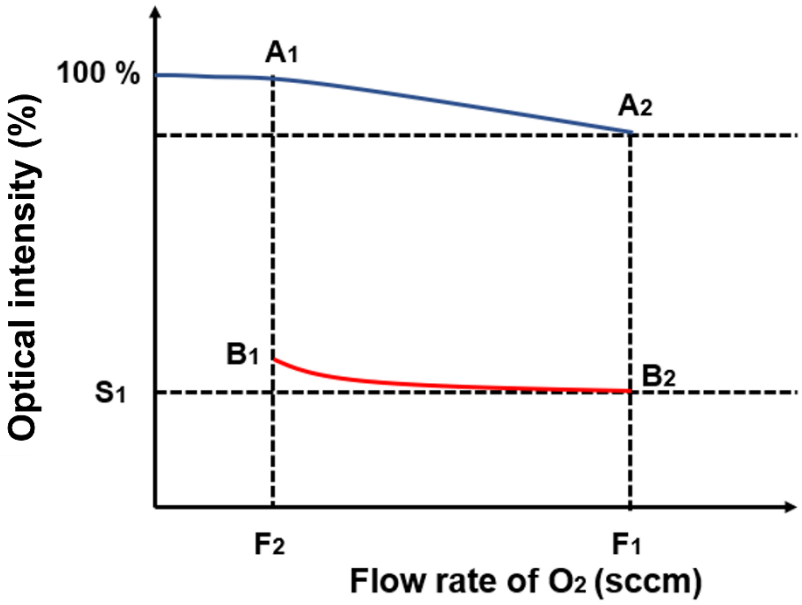

Figure 2.5: The hysteresis loop between the oxygen flow rate and the emission optical intensity of the target

2.2.2.4 The experimental device for RMS deposition

In this thesis, the 8YSZ electrolyte, GDC10 buffer layer, and Pr_2NiO_4@Pr_6O_{11} composite cathode are deposited by the RMS system as shown in Figure 2.6. The complete RMS system mainly includes sputtering chamber, vacuum system, hardware control unit, gas flow control system, pulsed DC generator and PEM system. The sputtering chamber is a cylinder with a height of 300 mm, an inner diameter of 620 mm, and a volume of about 100 L. The vacuum system consists of a main pump and a secondary turbomolecular pump, which can achieve a vacuum lower than 10^{-4} Pa. A two-channel DC Pinnacle® Plus$^+$ generator from Advanced Energy® serves as the power supply, which can adjust the pulse frequency from 5 to 350 kHz. An RF generator (CAESAR 1310 with matching box from Advanced Energy®) will be used as a bias on substrate for the deposition of the dense coatings such as 8YSZ electrolyte and GDC10 barrier layer. The substrate holder with a diameter of 610 mm is placed at a draw distance of 70 mm from the target surface (D*t-s* = 70 mm), and it can rotate at a rate of 14 Round Per Minute (RPM) driven by a motor. A pressure gauge with a display upper limit of up to 10^{-3} mBar is used to determine the vacuum in the sputtering chamber. A more accurate MKS Baratron pressure gauge is used to display the operating pressure in the deposition chamber during the deposition in real time. The sputtering chamber

allows up to four targets with a diameter of 200 mm. Each target is placed on a copper pedestal whose bottom is in contact with circulating cooling water, and a graphite sheet is placed between the target and the copper pedestal to improve electrical contact.

As an important part of this RMS system, the PEM system consists of optical fiber probes, conducting optical fiber, spectrometer, and photomultiplier to obey computer management to monitor plasma emission spectra. The fiber probe is connected to an aluminum tube with an inner diameter of 6 mm. The fiber probe and the aluminum tube are separated by a piece of glass slide to avoid signal loss due to deposition of sputtered particles on the fiber probe. The aluminum tube is placed above the ring-shape corrosive area of the required target. In this way, photons will be maximally captured due to the ring-shaped area is the main sputtering area of the required target. The captured photons are transmitted to a spectrometer equipped with a photomultiplier by optical fiber. A computer linked to the spectrometer monitors the spectral intensity through a software developed by Labview® to control the RMS process.

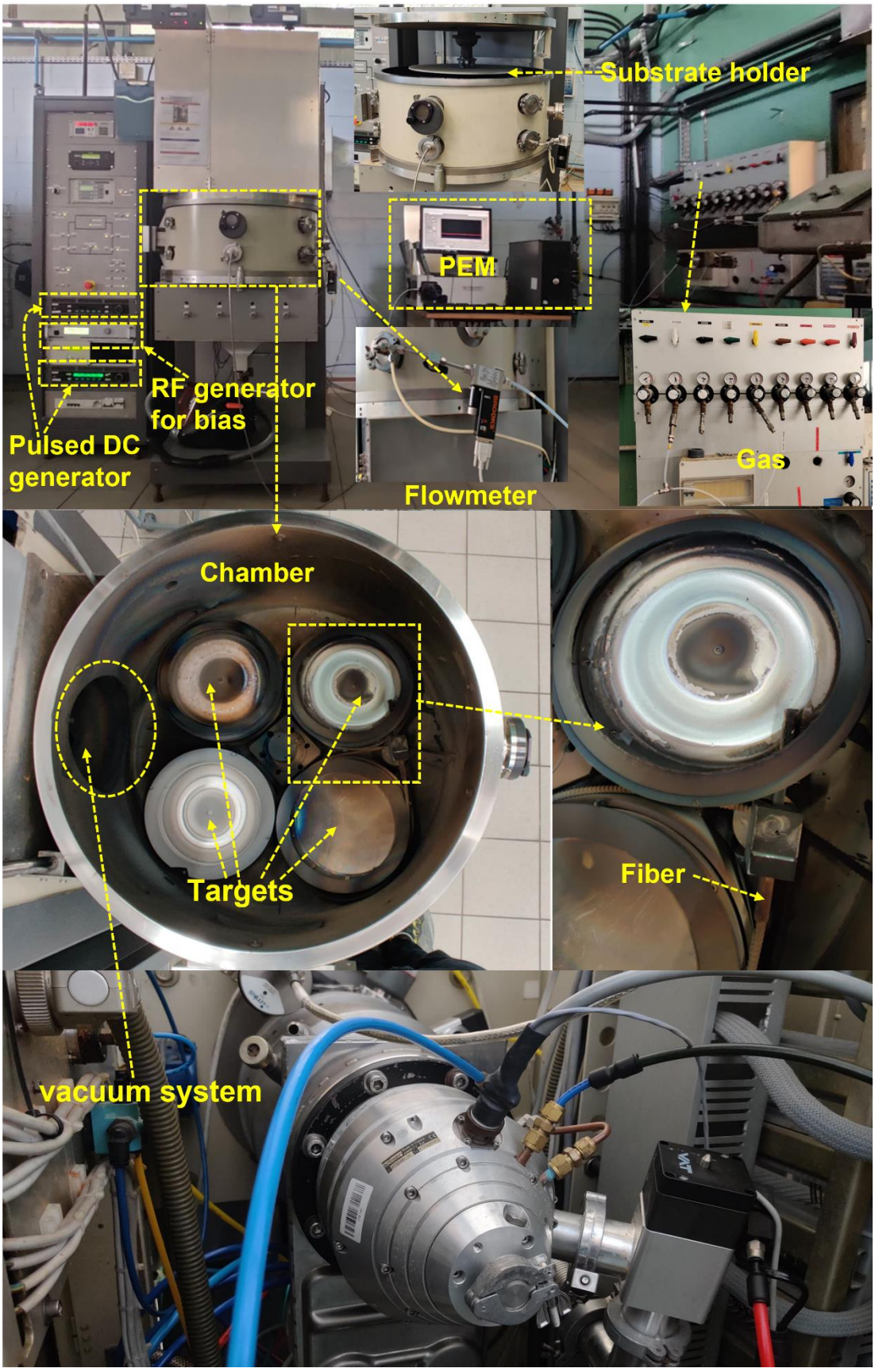

Figure 2.6: Reactive magnetron sputtering device with PEM system

2.2.3 Annealing treatments and reduction experiments

The annealing treatment of ITM alloys is carried out in a furnace under air allowing a maximum temperature of 1300°C. The rest annealing treatments involved in this thesis are carried out in a standard furnace under air from Borel company. This furnace can realize different annealing treatment processes under air, it allows a maximum temperature of 1000°C. All annealing treatments perform the same heating program in the heating stage, that is, increasing 100°C every 1h until the required temperature.

The reduction of the NiO-YSZ anode deposited by APS is carried out in a furnace heated by a resistance wire to a maximum temperature of about 780°C. The furnace is equipped with a vacuum system that consists of a main pump and a secondary turbomolecular pump, which can achieve a vacuum lower than 10^{-4} Pa. The reduction process is carried out after introducing the Ar/H_2 (50/50 sccm) mixed gas, and the vacuum in the furnace is about 1 Pa. In the heating stage, the principle of increasing 100°C every 1 h until the required temperature is followed.

2.3 Characterization techniques

In this section, some related characterization techniques and single cell performance testing techniques will be introduced.

2.3.1 Structure and microstructure

- Morphological characterization

The SEM (JEOL JSM-7800F) with nanoscale resolution is used to characterize the surface and cross-section morphology of various components in a complete single cell, including the support, anode, electrolyte, cathode, and the interface between adjacent components. A photograph of the SEM device is shown in Figure 2.7, which is equipped with an Energy Dispersive X-ray Spectroscopy (EDS) detector to measure the composition of the coatings. The phase distribution inside the coating is observed by SEM with a backscatter electron detector (BED), and the acquired images are used to quantify the porosity for porous electrode coatings (NiO-YSZ anode and cathode) by using ImageJ software. The quantitative process of coating porosity is shown in Figures

2.8 and 2.9. For the SEM-BED images under different magnifications (×1000, ×1500, and ×2000), images with magnification of ×1000 or ×1500 are selected to quantify the porosity of NiO-YSZ containing large pores. Because a larger field of view can be included at a relatively low magnification, avoiding it is possible that the images are taken at the large pores subjectively. The image with the magnification of ×2000 is used to quantify the porosity of the NiO-YSZ anode layer containing small pores. The porosity of the cathode layer is quantified using the images with the magnification of×8500. This is because the cathode layer is relatively thin, and the pores can be clearly distinguished under a larger magnification, and the distribution of pores in the cathode layer is relatively uniform. To reduce the error as much as possible, the porosity of each NiO-YSZ anode layer samples and cathode layer samples is obtained by taking the average value after analyzing 10 images.

Figure 2.7: The Scanning Electron Microscope (SEM, JEOL JSM-7800F) equipped with an Energy Dispersive X-ray Spectroscopy (EDS) [1]

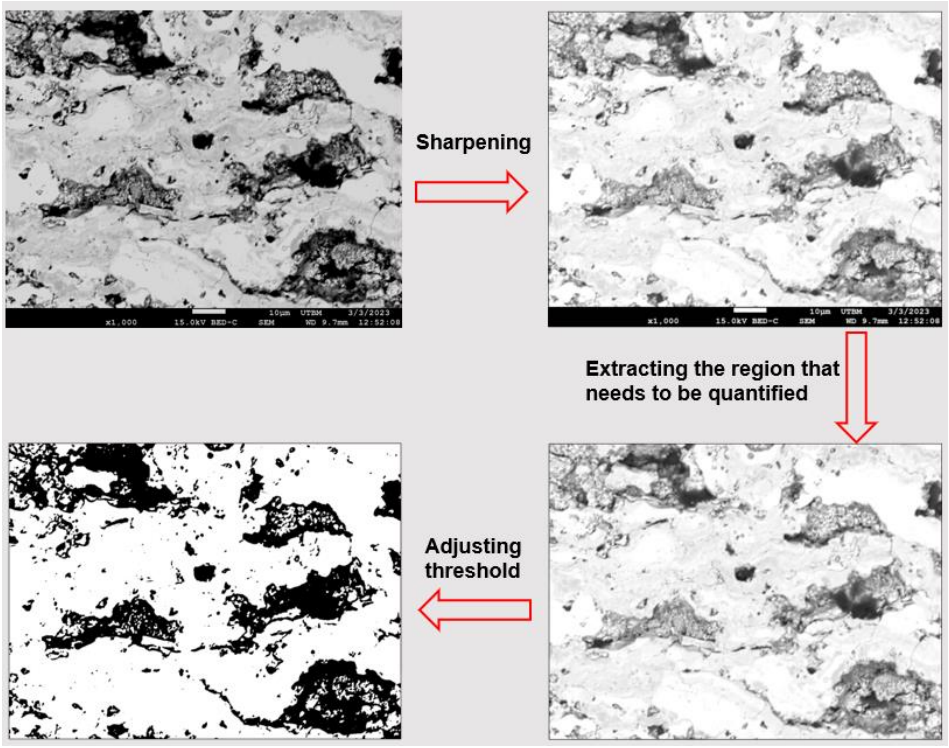

Figure 2.8 Procedure for quantifying porosity of anode layer by ImageJ software

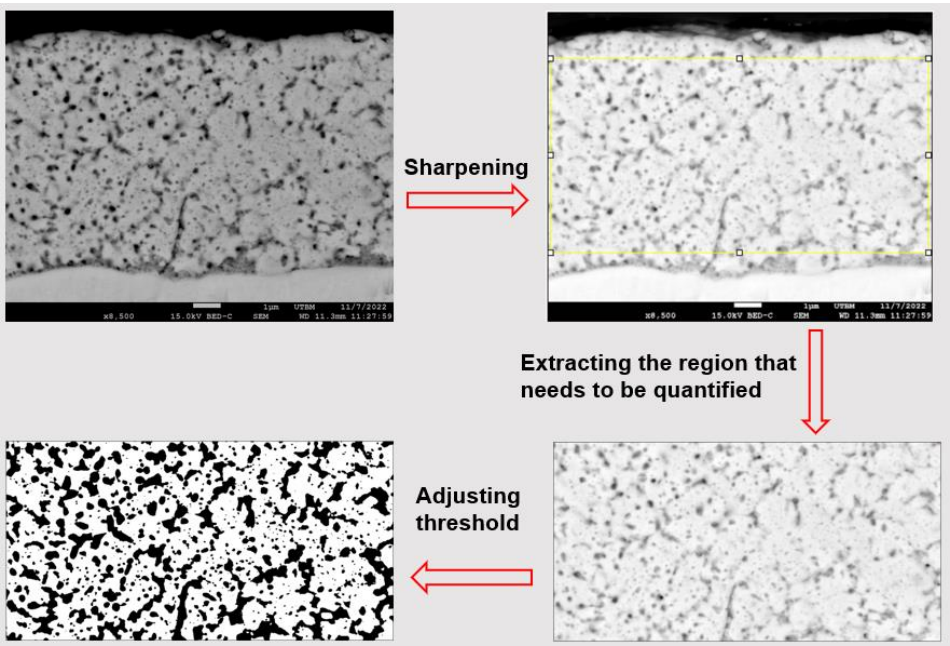

Figure 2.9: Procedure for quantifying porosity of cathode layer by ImageJ software

- Thickness measurement of coatings

Two methods are used to measure coating thickness. The thickness of the coating deposited on the glass slide is measured by a 3D Altisurf 500 device with an inductive sensor. The contact detector of 3D Altisurf 500 moves 4 mm in a straight line on the coated glass slide and crosses the coated area to reach the blank area. In this way, a step

is formed, and the calculated height with an error of 10 nm of this step is the thickness of the coating. This operation is performed three times at different positions to obtain three thickness values and then take the average as the final thickness value. After measuring the thickness of the coating, the deposition rate can be calculated to control the thickness of each component layer. For the thickness of each component layer of MS-SOFC (anode, electrolyte, buffer layer, and cathode) is determined by the built-in measurement tools in the SEM. Because the thickness of the component layer that has been deposited on the complete MS-SOFC cannot be measured by 3D Altisurf 500 device.

- Surface roughness :

The surface roughness of the single cell at each deposition stage is also realized by 3D Altisurf 500 device. The contact detector moves on the surface of the sample to scan a 7×7 mm area and collects 3735 points in total. The surface roughness information of the sample can be obtained by analyzing the scanned area. There are three parameters Ra, Rz, and Rsk that need to be paid attention because they effectively reflect the surface roughness of the sample. where Ra, Rz, Rsk represent the arithmetical mean deviation of profile, the maximum height of the profile within a sampling length, and the skewness (asymmetry) of the assessed profile, respectively [11]. A flat surface requires Ra and Rz to be as small as possible, and Rsk close to 0.

- Transmission of the coatings

The transmittance of coatings deposited on glass slides is analyzed by a Shimadzu UV-3600 UV-visible-NIR spectrophotometer controlled by UV probe 2.33 software. All measurements are performed in the visible light range from 380 nm to 780 nm.

- Powder particle Size Analysis

The particle size of the NiO-YSZ powder is evaluated by a laser diffraction size analyzer to obtain the average particle size and particle size distribution of the powder. The equipment used is a Malvern Instruments Mastersizer A2000.

- X-ray diffraction

The structure of the coating is determined using a BRUKER D8 X-ray diffraction (XRD) equipped with a LynxEye linear detector and Co Kα radiation (λ=1.78897 Å). The device is operated at a voltage of 35 keV and a current of 40 mA. The scans are carried out at room temperature in a 2θ range of 20°-90° with a scan rate of 6° min^{-1} and a scan step of 0.02°. Additionally, diffraction patterns with better signal-to-noise ratio are collected by reducing the scan rate to 0.6° min^{-1} for refinement by using the Rietveld method. The device and schematic diagram of the XRD in θ/2θ configuration are shown in Figure 2.10. According to Bragg's law, expressed as $2d_{hkl}\sin\theta = n\lambda$, where d_{hkl} is the interplanar spacing, θ is the incident angle, λ is the wavelength of the incident beam, and n is an integer, other information related to the crystalline structure of the coatings such as lattice parameters and average grain size is obtained from an XRD diffraction pattern. The lattice parameters can be calculated from the main diffraction planes by Bragg relation. The average grain size can be calculated by the Scherrer formula expressed as [12]:

$$d_{hkl} = \frac{K\lambda}{\beta\cos\theta} \qquad 2.1$$

Where β, λ, and θ refer to the line broadening at half the maximum intensity (FWHM), the X-ray wavelength, and the Bragg angle, respectively. d_{hkl}, refer to the average size of the crystalline domains in the <hkl> direction, which may be smaller or equal to the grain size. K is the Scherrer constant, which is a dimensionless shape factor with a typical value of about 0.89 but will vary with the actual shape of the crystallite.

It should be point that, in this thesis, to apply the Scherrer formula more easily, the broadening of the FWHM is attributed to the grain size and ignores the strain broadening. The K value is fixed at 0.89 and ignores the influence of the actual shape of the crystallite. In addition, in this thesis, the XRD patterns of the composite cathode coatings are also refined by the Rietveld method via using a Fullprof software. The content of each phase and the cell parameters in the composite cathode are determined by XRD refinement.

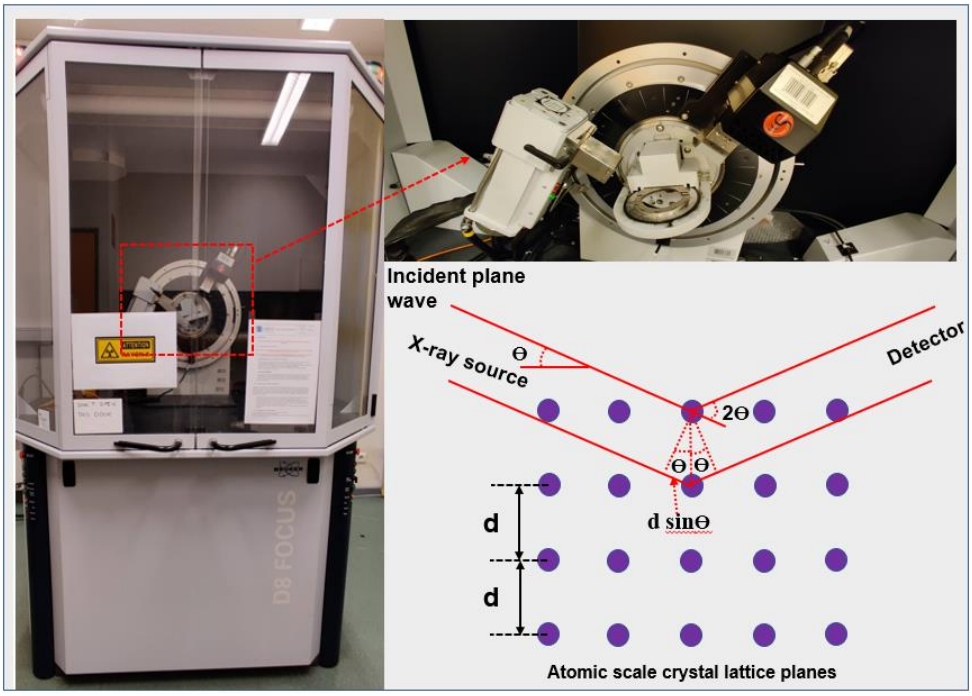

Figure 2.10: XRD equipment and schematic diagram of XRD in θ/2θ configuration

- X-ray Photoelectron Spectroscopy:

In this thesis, the chemical states, binding energies, and stoichiometric ratio of different species of elements present in the coatings are analyzed by XPS. The XPS characterization is carried out by a *K-Alpha*$^{+}$ device produced by Thermo Fisher Scientific, which operates under the high vacuum (2×10^{-7} mbar) with aluminum Kα monochromatized radiation at the 1486.7 eV X-ray photon source. The measurements of all samples are performed in constant analyzer energy mode with a pass energy of 50 eV. Charge calibration is performed based on the binding energy of the C 1s photoelectron peak at 284.8 eV. The obtained XPS spectra are interpreted by an Avantage software.

2.3.2 Electrical and electrochemical characterization

2.3.2.1 Electrical conductivity measurement

The electrical conductivity of the samples is measured according to the Figure 2.11. In order to be able to take measurements, the sample holder must be completely electrically insulated. As show in Figure 2.11, V is the voltage measured by the internal probe, while I is measured by the external probe. At this time, the resistivity of the cylindrical bulk material can be calculated by formula 2.2.

$$\rho = 2\pi s \frac{V}{I} \quad 2.2$$

where ρ, s, I and V refer to resistivity, probe spacing, applied current and measured voltage, respectively.

For thin coating samples, the thickness must be considered, and formula 2.2 is rewritten as 2.3.

$$\rho = 2\pi s t \frac{V}{I} \quad 2.3$$

where s, t, I, and V refer to probe spacing, thickness of the thin coating, applied current and measured voltage, respectively.

It must be known that the contact between the probe and the sample is also very important. Different operations may result in different contact situations as it depends on the force applied, the contact area and the roughness of the sample. Therefore, it is necessary to determine the geometry factor of the measurement unit (Figure 2.12) for each operation. For this purpose, a standardized Jandel Multiheight Probe device with well-known properties is required to correct for geometry factors before temperature-varying electrical conductivity measurements are performed in the measuring cell (Figure 2.12). At this time, it is necessary to consider the correction coefficient (C_1) related to the diameter of the sample and the correction coefficient (C_2) related to the thickness of the coating, so the formula 2.3 becomes 2.4.

$$\rho = C_1 C_2 t \frac{V}{I} \quad 2.4$$

where C_1 and C_2 refer to the correction coefficient of the sample diameter and coating thickness, respectively. (t, V, I refer to to probe spacing, thickness of the thin coating, applied current and measured voltage, respectively)

For the thin coatings deposited by magnetron sputtering to be very thin, its thickness is negligible compared to the distance (s) between the probe tips. Therefore, the factor C_2 is approximated to 1, while C_1 can be determined by drawing the calibration curve [13-14]. For alumina pellet with a diameter of 23 mm, the coefficient C_1 is 4.532. Further, the resistivity for thin coating is calculated by the formula 2.5.

$$\rho = 4.532\ R\ t \qquad 2.5$$

where R is directly output by the measuring device and t refer to the thickness of the coating.

The system used to measure the resistance of the coatings consisted of an Agilent 3458A multimeter, a furnace manufactured by Pekly, and a bracket which the samples could be placed as shown in Figure 2.12. The main body of the bracket is made of alumina to resist high temperature. Platinum wire is used to wrap four equidistant alumina grooves to form four probes. The sample (a coated alumina ceramic pellet with a diameter of 23 mm) to be measured is placed on an alumina spacer, then the probes are in contact with the coating surface and a certain pressure is applied through the spring device above the bracket. The sample is placed in the measuring cell (Figure 2.12) and the resistance is read at room temperature after 20 minutes of gas purging. It is thus possible to determine the geometry factor of the measuring unit (Figure 2.12) for each operation and to determine the electronic conductivity of the sample according to formula 2.6.

$$\sigma = \frac{1}{\rho} = \frac{1}{4.532\ t\frac{R_2}{R_1}} \qquad 2.6$$

where σ: the electrical conductivity of the coating in S/cm; R_1: the electrical resistance measured by standard equipment at room temperature; R_2: the electrical resistance measured during temperature test.

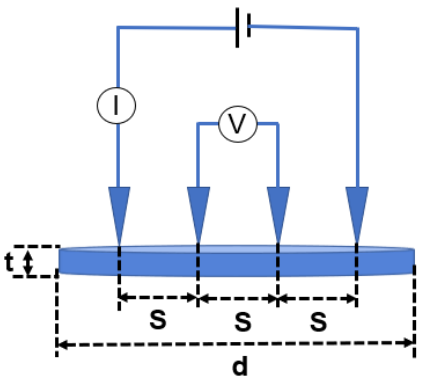

Figure 2.11: A probe arrangement for measuring electrical conductivity by four-probe method for a circular sample

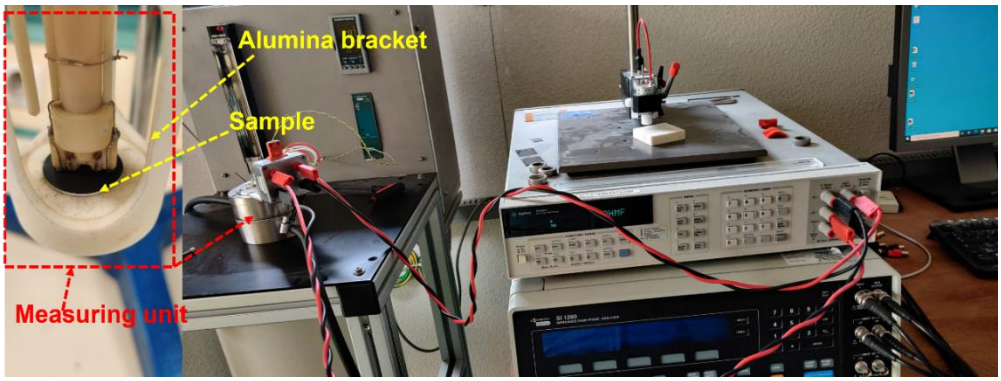

Figure 2.12: The measurement system of the electrical conductivity of the coatings

2.3.2.2 AC Electrochemical Impedance Spectroscopy (AC-EIS)

Electrochemical impedance spectroscopy (EIS) is widely used to analyze the electrochemical properties of materials. EIS can be divided into DC-EIS and AC-EIS according to the different currents used. Bauerle [16] first applied EIS technology to the analysis of the electrochemical performance of fuel cell ceramic layers. In the past few decades, EIS technology has played an important role in the field of fuel cells. For SOFC, AC-EIS is usually used to investigate the electrochemical reaction process of the cells and electrodes materials.

- The principle of AC-EIS

The working principle of AC-EIS is to apply a perturbation voltage under steady-state conditions, and then a corresponding current response is output in a certain frequency range. Different measurement objects and conditions will produce different response signals. Therefore, the electrochemical processes corresponding to different research objects and conditions are understood by analyzing these output response signals. A perturbation voltage with sine wave applied in a measurement system can be expressed as:

$$V(t) = V_0 \cdot \sin(\omega t) \quad 2.7$$

Correspondingly, a response current with sine wave is obtained as:

$$I(t) = I_0 \sin(\omega t + \theta) \quad 2.8$$

Where V_0 is the amplitude of the applied voltage in V, I_0 is the amplitude of the response current in A, ω ($\omega = 2\pi f, f$ refers to frequency in Hz) is the angular frequency in rad/s, and θ is the phase angle in °.

The impedance of the entire measurement system is expressed as:

$$Z = \frac{V_0 \cdot \sin(\omega t)}{I_0 \sin(\omega t + \theta)} = Z_0 \frac{\sin(\omega t)}{\sin(\omega t + \theta)} \quad 2.9$$

Through Euler's formula, formula 2.8 is transformed into:

$$Z = \frac{V_0 e^{j\omega t}}{I_0 e^{(j\omega t + j\theta)}} = Z_0 e^{-j\theta} = Z_0(\cos\theta + \sin\theta) = Z' - jZ'' \quad 2.10$$

Formulas 2.8 and 2.9 represent the Bode plot and Nyquist plot of the impedance diagram, respectively. The parameters related to the electrochemical process can be obtained by analyzing the impedance diagram by the Randles equivalent circuit method. Common circuit elements include resistor (R), capacitor (C), inductor (L), and constant-phase element (CPE). Different circuit elements respond differently to applied voltage disturbances.

For R, the response current and the applied voltage have the same phase. It is represented as a point on the real axis in the Nyquist plot (Figure 2.13), and the corresponding impedance can be expressed as: $Z_R = R = Z'_R;\ Z''_R = 0$

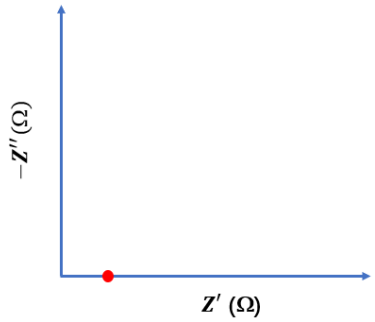

Figure 2.13: The Nyquist plot of the resistor (R)

For C, the phase of the response current is ahead of the applied voltage by $\frac{\pi}{2}$. In the Nyquist plot, it is shown as a straight line coincident with the imaginary axis in the first quadrant (Figure 2.14), and the corresponding impedance can be expressed as: $Z_C = -j\left(\frac{1}{\omega C}\right);\ Z'_C = 0;\ Z''_C = -\frac{1}{\omega C}$

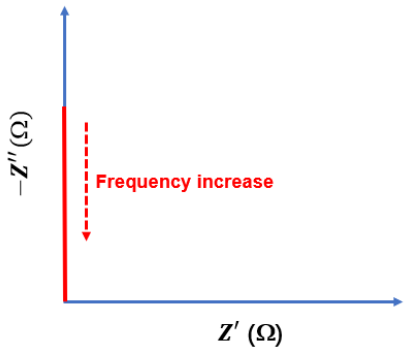

Figure 2.14: The Nyquist plot of the capacitor element (C)

For L, the phase of the response current lags the applied voltage by $\frac{\pi}{2}$. In the Nyquist plot, it appears as a straight line coincident with the imaginary axis in the fourth quadrant (Figure 2.15), and the impedance can be expressed as:$Z_L = jL\omega;\ Z_L' = 0;\ Z_L'' = L\omega$

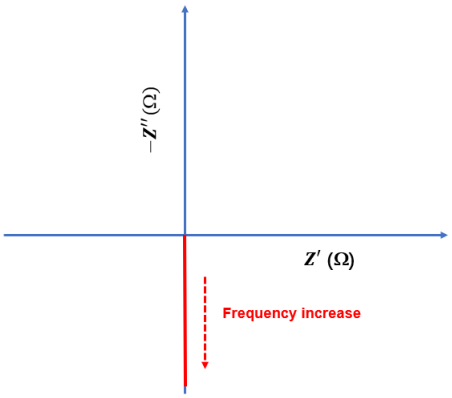

Figure 2.15: The Nyquist plot of the inductor (L)

Different equivalent circuit models can be established from the above simple circuit components. The Nyquist plot of a common equivalent circuit is shown in Figure 2.16(a), and its impedance can be expressed as:

$$Z = R_1 + \frac{1}{j\omega C + \frac{1}{R_2}} \qquad 2.11$$

Formula 2.11 can be organized as:

$$(Z' - R_1 - \frac{R_2}{2})^2 + (Z'')^2 = (\frac{R_2}{2})^2 \qquad 2.12$$

At this time, the Nyquist plot is a standard semi-circular arc with a radius of $\frac{R_2}{2}$ and its circle center of is $(R_1 + \frac{R_2}{2}, 0)$. In practice, it is almost difficult to find an electrochemical process that strictly follows R or C. In this case, CPE is proposed for

the actual electrochemical process. It combines the characteristics of R and C, and the impedance can be expressed as:

$$Z_{CPE} = \frac{1}{Y_0 j\omega^n} \qquad 2.13$$

Generally, the value of n follows the relationship of $0 < n < 1$. In particular, CPE is equivalent to R (n = 0) and C (n = 1). When the equivalent circuit shown in Figure 2.16(b) is established by replacing the capacitor C with the CPE. The semicircle in the Nyquist plot is gradually suppressed as the value of n decreases (Figure 2.16(b)).

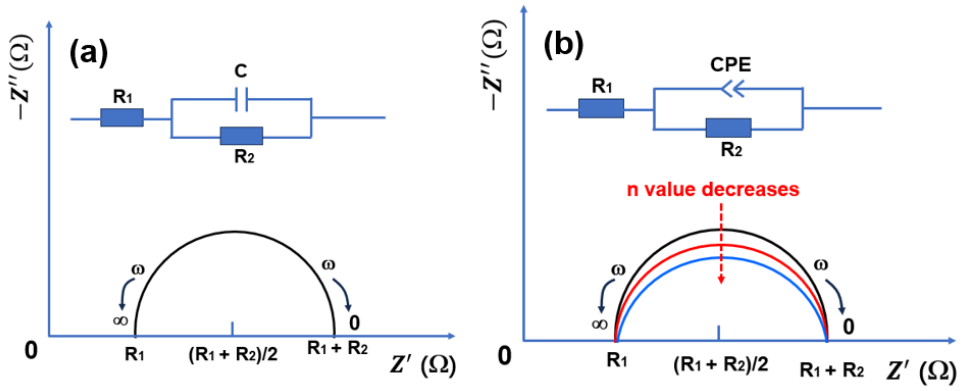

Figure 2.16: Nyquist plot of equivalent circuits: (a) $R_1(R_2//C)$; (b) $R_1(R_2//CPE)$

- Experimental device

In this thesis, a Garmy 1000E electrochemical workstation is used for AC-EIS measurement of symmetrical cells. Figure 2.17 shows the schematic diagram of the measurement. The two sides of the symmetrical cell are connected to the platinum wire electrode soldering by commercial silver paste with an area of 0.2 cm^2. Then the symmetrical cell is placed in a furnace (OTF-1200X). The measurement of impedance spectroscopy is performed between 600 and 750°C at an interval of 50°C within a frequency range of 10^{-1}-10^6 Hz under the applied voltage perturbation of 10 mV at an oxygen partial pressure of 0.2 atm. The collected EIS data are analyzed by ZView software.

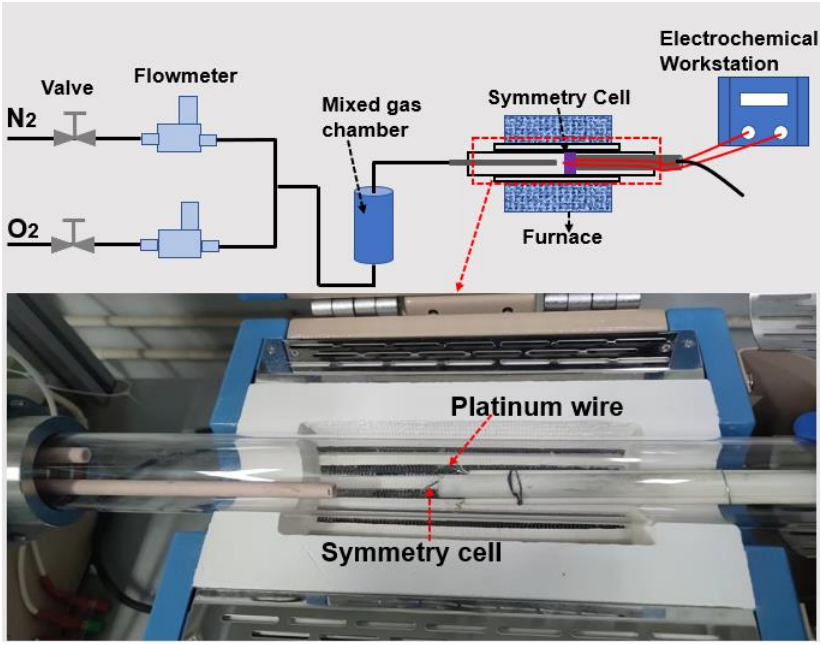

Figure 2.17: Schematic diagram of AC-EIS measurement for the symmetrical cells

2.3.2.3 Measurement of the single cells

The electrochemical performance of a SOFC is evaluated by a polarization curve (I-V curve) with the relationship between current density and voltage, as shown in Figure 2.18. Simultaneously, the I-P curve is obtained by multiplying between the current density and the corresponding voltage.

In this thesis, a CS1350 electrochemical workstation is used to collect the current-voltage discharge curve (I-V) of the MS-SOFC single cell. At the same time, the AC-EIS measurement is performed in situ. The electrochemical performance measurement system of a single cell is shown in Figure 2.19. The cathode and metal support of an MS-SOFC single cell are connected to the electrochemical workstation through platinum wires. The cell is sealed by high temperature sealant to introduce H_2 and air into the anode and cathode sides, respectively, without gas leakage. Commercial silver pastes with area of 0.2 cm^2 is coated on the cathode as the current collector layer. The sealed cell is placed in a furnace (OTF-1200X). A reduction process needs to be performed on the anode side before starting the measurement. Introduce mixed gas 5%H_2-N_2 to the anode side at a flow rate of 30 mL/min until 600°C. Then gradually increase the flow rate of H_2 until it is pure H_2 at 750°C, and the gas flow rate is increased to 60 mL/min. A heating rate of 3°C/min is used throughout the heating process. Stay

at 750°C for 3 h to facilitate the reduction of the anode layer in a pure H_2 atmosphere. It should be noted that the H_2 is first passed through the water and then enter the anode side. At the same time, air is introduced to the cathode side at a flow rate of 40 mL/min. After the open circuit voltage (OCV) stabilized, the electrochemical measurement procedure is initiated from 750°C to 600°C at an interval of 50°C. Synchronously, the measurement of EIS is also performed from 750°C to 600°C at an interval of 50°C within a frequency range of 10^{-1}-10^{6} Hz under the applied voltage perturbation of 10 mV. The stability of the MS-SOFC single cell (represented in terms of cell voltage) at 700°C with a constant current load of 0.4 A/cm^2 as a function of operation time is used to evaluate the long-term performance of the single cell.

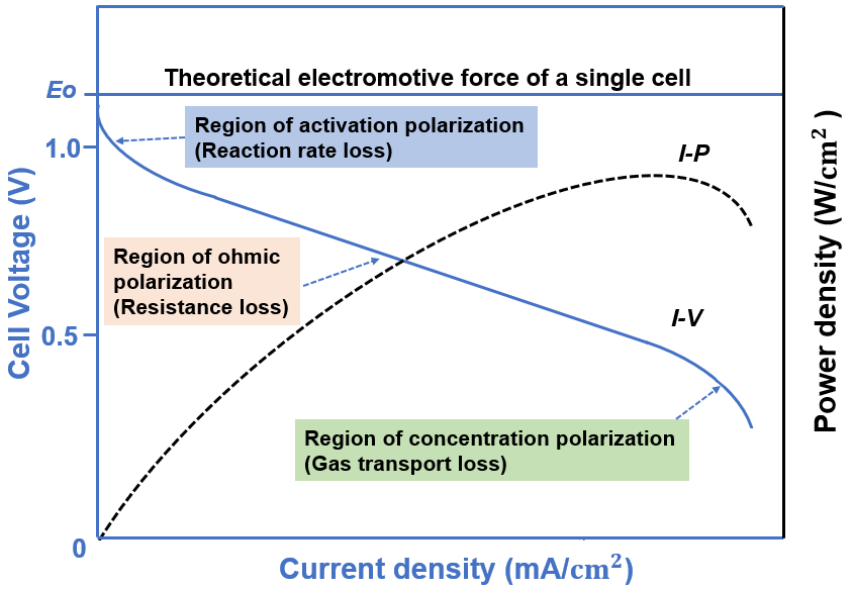

Figure 2.18: A typical I-V-P curve in a SOFC [17]

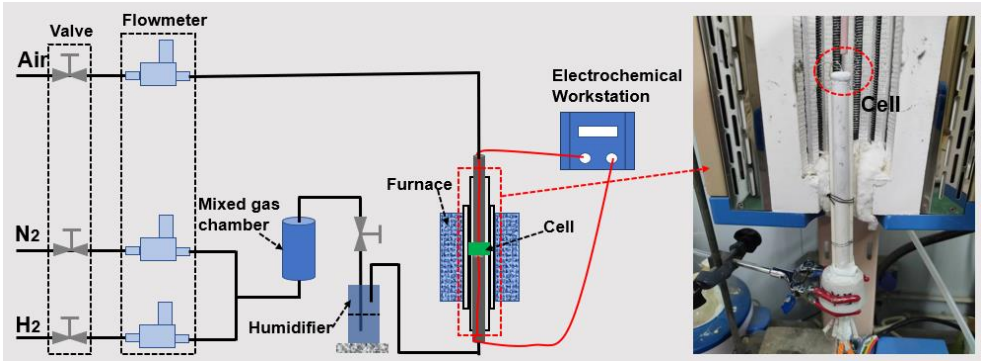

Figure 2.19: Schematic diagram of the test system for the single cell performance

2.4 References

[1] Fondard, J. (2015) Elaboration et test d'une pile à combustible IT-SOFC à support métallique poreux par l'intermédiaire de techniques de dépôt en voie sèche: projection thermique et pulvérisation cathodique magnétron. (Doctoral dissertation, Université de Technologie de Belfort-Montbeliard).

[2] Macák, K., Kouznetsov, V., Schneider, J., Helmersson, U., & Petrov, I.(2000) Ionized sputter deposition using an extremely high plasma density pulsed magnetron discharge. Journal of Vacuum Science & Technology A: Vacuum, Surfaces, and Films, 18(4), 1533-1537.

[3] Anders, A., Ni, P., & Rauch, A. (2012) Drifting localization of ionization runaway: Unraveling the nature of anomalous transport in high power impulse magnetron sputtering. Journal of Applied Physics, 111(5), 053304.

[4] Brenning, N., Lundin, D., Minea, T., Costin, C., & Vitelaru, C.(2013) Spokes and charged particle transport in HiPIMS magnetrons. Journal of Physics D: Applied Physics, 46(8), 084005.

[5] Fondard, J., Billard, A., Bertrand, G., Fourcade, S., Batocchi, P., Mauvy, F., & Briois, P. (2016) Effect of total pressure on La_2NiO_4 coatings deposited by reactive magnetron sputtering using plasma emission monitoring. Surface and Coatings Technology, 295, 29-36.

[6] Briois, P., Gourba, E., Billard, A., Ringuedé, A., & Cassir, M.(2005) Microstructure-Electrical properties relationship of YSZ thin films reactively sputter-deposited at different pressures. Ionics, 11, 301-305.

[7] Briois, P., Lapostolle, F., Demange, V., Djurado, E., & Billard, A.(2007) Structural investigations of YSZ coatings prepared by DC magnetron sputtering. Surface and Coatings Technology, 201(12), 6012-6018.

[8] Brahim, C., Ringuedé, A., Gourba, E., Cassir, M., Billard, A., & Briois, P. (2006) Electrical properties of thin bilayered YSZ/GDC SOFC electrolyte elaborated by sputtering. Journal of Power Sources, 156(1), 45-49.

[9] Briois, P., & Billard, A. (2006). A comparison of electrical properties of sputter-

deposited electrolyte coatings dedicated to intermediate temperature solid oxide fuel cells. Surface and Coatings Technology, 201(3-4), 1328-1334.

[10] Breaz, E., Aubry, E., Billard, A., Coton, N., Coquoz, P., Pappas, A., ... & Briois, P. (2017). Influence of the Bias Substrate Power on the GDC Buffer Layer. ECS Transactions, 78(1), 807.

[11] Kapłonek, W., Ungureanu, M., Nadolny, K., & Sutowski, P. (2017). Stylus profilometry in surface roughness measurements of the vertical conical mixing unit used in a food industry. Journal of Mechanical Engineering, 47(1), 1-8.

[12] Scherrer, P. (1918). Bestimmung der Grösse und der inneren Struktur von Kolloidteilchen mittels Röntgenstrahlen. Nachrichten von der Gesellschaft der Wissenschaften zu Göttingen, mathematisch-physikalische Klasse, 1918, 98-100.

[13] Schroder, D. K. (2015). Semiconductor material and device characterization. John Wiley & Sons.

[14] Weller, R. A. (2001). An algorithm for computing linear four-point probe thickness correction factors. Review of scientific instruments, 72(9), 3580-3586.

[15] Fondard, J., Billard, A., Bertrand, G., & Briois, P. (2018). $Ln_2NiO_{4+\delta}$ (Ln = La, Pr, Nd) coatings deposited by reactive magnetron sputtering as cathode material for intermediate temperature solid oxide fuel cell, Vacuum, 152, 97-108.

[16]Bauerle, J. E. (1969). Study of solid electrolyte polarization by a complex admittance method. Journal of Physics and Chemistry of Solids, 30(12), 2657-2670.

[17] Molenda, J., Świerczek, K., & Zając, W. (2007). Functional materials for the IT-SOFC. Journal of Power Sources, 173(2), 657-670.

Chapter 3: The deposition of anode functional layer, electrolyte layer and buffer layer by APS and RMS

3.1 Introduction

In this chapter, the main research content is focused on the deposition of NiO-YSZ anode functional layer, 8YSZ/GDC10 bilayer electrolyte, GDC10 buffer layer. The effect of particle size of NiO-YSZ mixed powder and Ar/H_2 gas flow rate on the porosity of NiO-YSZ coating are explored. The effect of the emission optical intensity of the targets ($Zr_{0.84}Y_{0.16}$ and $Ce_{0.90}Gd_{0.10}$) on the structure and morphology of 8YSZ and GDC10 during deposition by RMS under the control of the PEM system is investigated. The effect of the GDC10 buffer layer on preventing the interdiffusion between Cr, Ni, and Fe is investigated. In addition, the oxidation resistance of the ITM alloy in air is investigated to provide a basis for the subsequent annealing treatment of the complete cell.

3.2 Analysis of the metal support

In MS-SOFC, the metal support replaces the traditional electrode support or electrolyte support. For the metal support, its comprehensive properties including mechanical strength, CTE, stability, porosity, etc. should be considered. As mentioned in Chapter I, various metal supports have been developed for MS-SOFC. Among them, ferritic stainless-steel series are the most widely used. In this thesis, a porous support called Intermediate Temperature Metal (ITM, 26Cr-Bal. Fe) from PLANSEE SE is used to develop MS-SOFC. A plane raw ITM is cut into small pieces with a size of 2.3-3.0 × 2 × 0.1 cm^3 by a cutting machine equipped with a grinding wheel. Existing reports indicate that the ITM has a CTE (11.8 × 10^{-6} K^{-1}) matching common component materials and high creep strength to ensure structural strength at 850°C in a reducing anode atmosphere [1, 2]. In addition, the ITM exhibited long-term stability in oxidizing and reducing atmospheres at temperatures up to 850°C [2, 3]. Nevertheless, it is still necessary to investigate the properties of the ITM to provide a basis for the design of the MS-SOFC fabrication process in this thesis.

As a support, ITM should have sufficient porosity and large pore size to provide gas transmission channels. The porosity and pore size distribution of the ITM are determined by analyzing the SEM pictures of the polished ITM using ImageJ and Nano measurer 1.2 software. Figure 3.1 shows the porosity and pore size distribution of the surface and cross-section of the ITM. The porosity of the surface and cross-section of ITM are 35.5 ± 0.3 Vol.% and 35.3 ± 0.2 Vol.%, respectively. The pore diameter on the surface and cross-section are mainly in the range of 5-30 μm. The surface roughness of the substrate must be considered when depositing coatings using dry physical deposition methods. Therefore, the surface roughness of ITM should be investigated for subsequent APS deposition. The surface roughness of the ITM is determined by a 3D profilometer as show in Figure 3.2. Larger values of Ra and Rz indicate that there are many peaks and valleys on the surface of the ITM. The value of Rsk farther from 0 proves that the surface of the ITM has many deep and narrow valleys. Therefore, these peaks and valleys should be covered when depositing the anode layer by APS to facilitate the deposition of a dense electrolyte layer through RMS.

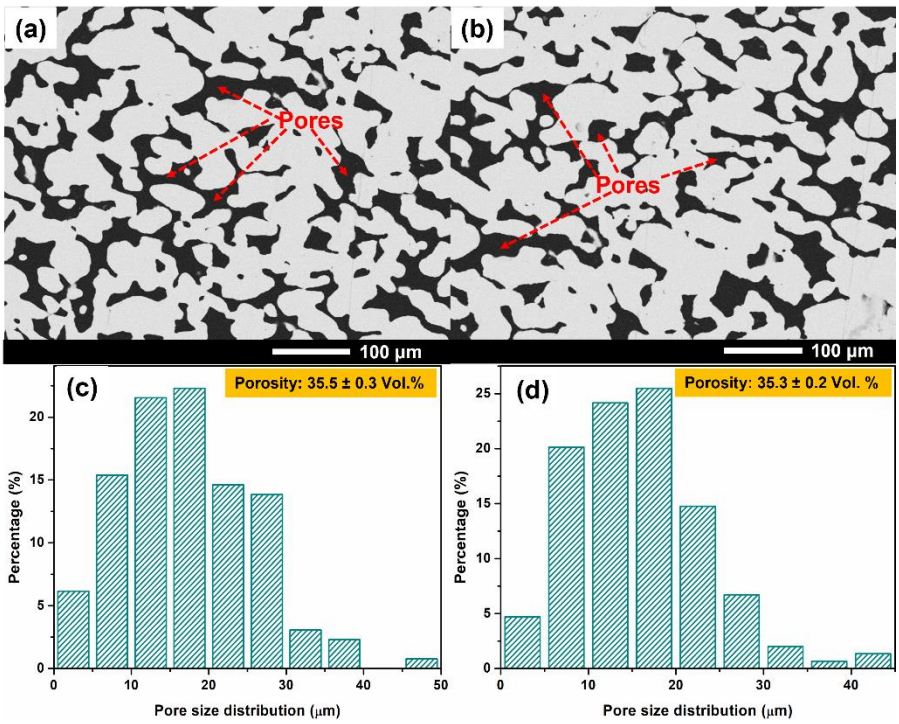

Figure 3.1: The polished metal support ITM: (a) the surface, (b) the cross-section; (c) pore size distribution and porosity of the surface, (d) pore size distribution and porosity of the cross-section

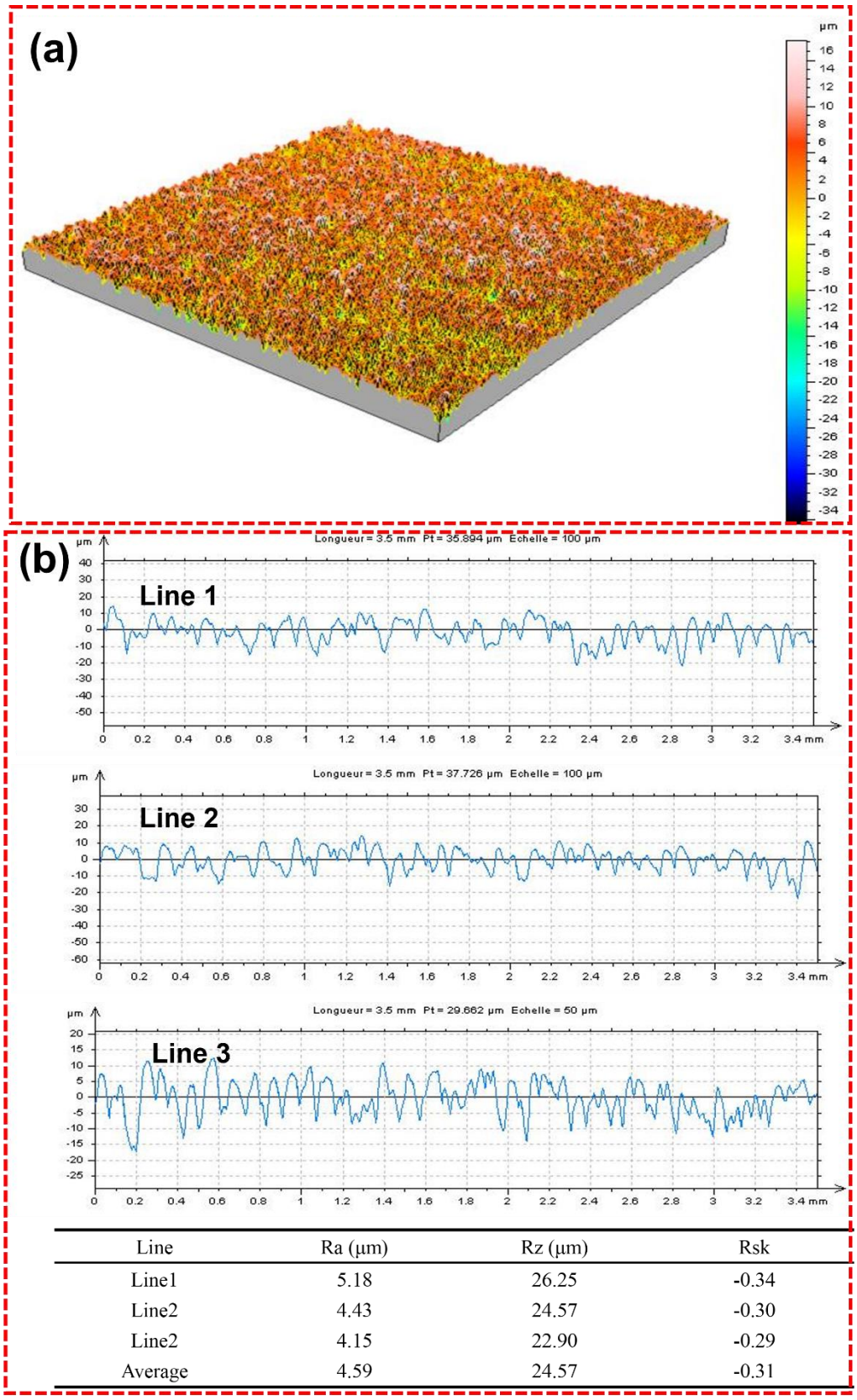

Line	Ra (µm)	Rz (µm)	Rsk
Line1	5.18	26.25	-0.34
Line2	4.43	24.57	-0.30
Line2	4.15	22.90	-0.29
Average	4.59	24.57	-0.31

Figure 3.2: (a) surface mapping of the obtained ITM support using the tactile profilometer; (b) the Ra, Rz and Rsk parameters at three different positions on the surface mapping are determined by surface analysis using the Mountain Map software.

Although MS-SOFC generally works at intermediate temperature (600-800°C), a metal support that is resistant to high-temperature in an oxidizing atmosphere is more flexible for the choice of fabrication process. For a given metal support, oxygen partial pressure, temperature, and oxidation time are the main factors affecting its oxidation resistance. In this thesis, the growth of the oxide in ITM undergoing different oxidation times (30-120 min) in the temperature range of 500-1200°C under air is investigated, and the results are shown in Figures 3.3-3.6. The XRD results show that after 120 min of oxidation, a slight peak attributed to Cr_2O_3 appears from 900°C. It is especially obvious above 1050°C and the Fe_2O_3 appears, which indicates that the Cr_2O_3 is not enough to protect the ITM. When the oxidation time is reduced to 30 min at 1000°C, the peak attributed to Cr_2O_3 weakened significantly, while the peak of Fe_2O_3 disappeared. The SEM results in Figure 3.4 show that the ITM has a good backbone at 800°C, while it can maintain the basic backbone at 1000°C, but the surface is covered with Cr_2O_3. As the temperature increased to 1100°C and 1200°C, the Cr_2O_3 covering on the ITM surface agglomerated into larger particles, resulting in the failure of the Cr_2O_3 to cover the surface of the ITM. This intensified the oxidation of the ITM. In this case, the backbone of the ITM is damaged, and obvious deformation of the sample is observed as shown in Figure 3.6. As the oxidation time decreases at 1000°C, the Cr_2O_3 on the ITM surface also decrease, which is consistent with the XRD results. Figures 3.4(f) and 3.6 show that ITM has a good backbone without deformation but is covered with a Cr_2O_3 after undergoing an annealing treatment at 1000°C for 30 min. The EDS results in Figure 3.5 show that after annealing treatment at 1000°C for 120 min, both the oxygen contents and the chromium contents on the ITM surface increase sharply, which indicates that the diffusion of chromium and the oxidation of chromium are occurred.

In summary, ITM is purchased with porous channels for gas transmission. After annealing treatment at 1000°C under air for 30 min, the surface is covered by a Cr_2O_3, but maintains a good backbone without deformation. These results suggest that the as deposited complete cell can be annealed at 1000°C for a short time (such 30 min) to promote the crystallization of the cathode layer, but a buffer layer should be deposited

on the surface of the ITM to prevent chromium from entering the anode layer through diffusion.

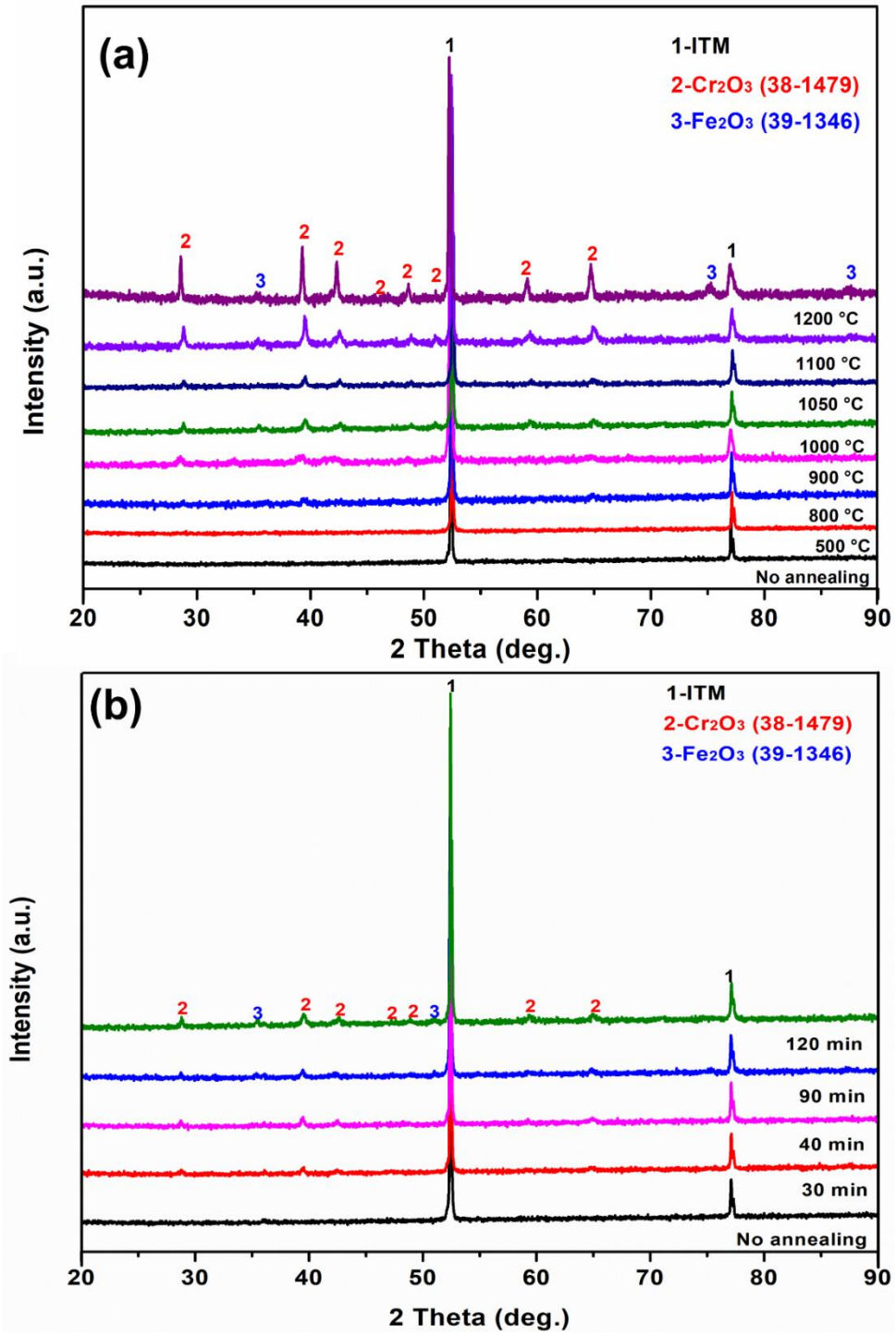

Figure 3.3: XRD patterns of ITM: (a) after annealing at different temperatures for 120min, (b) after annealing at 1000°C for different time

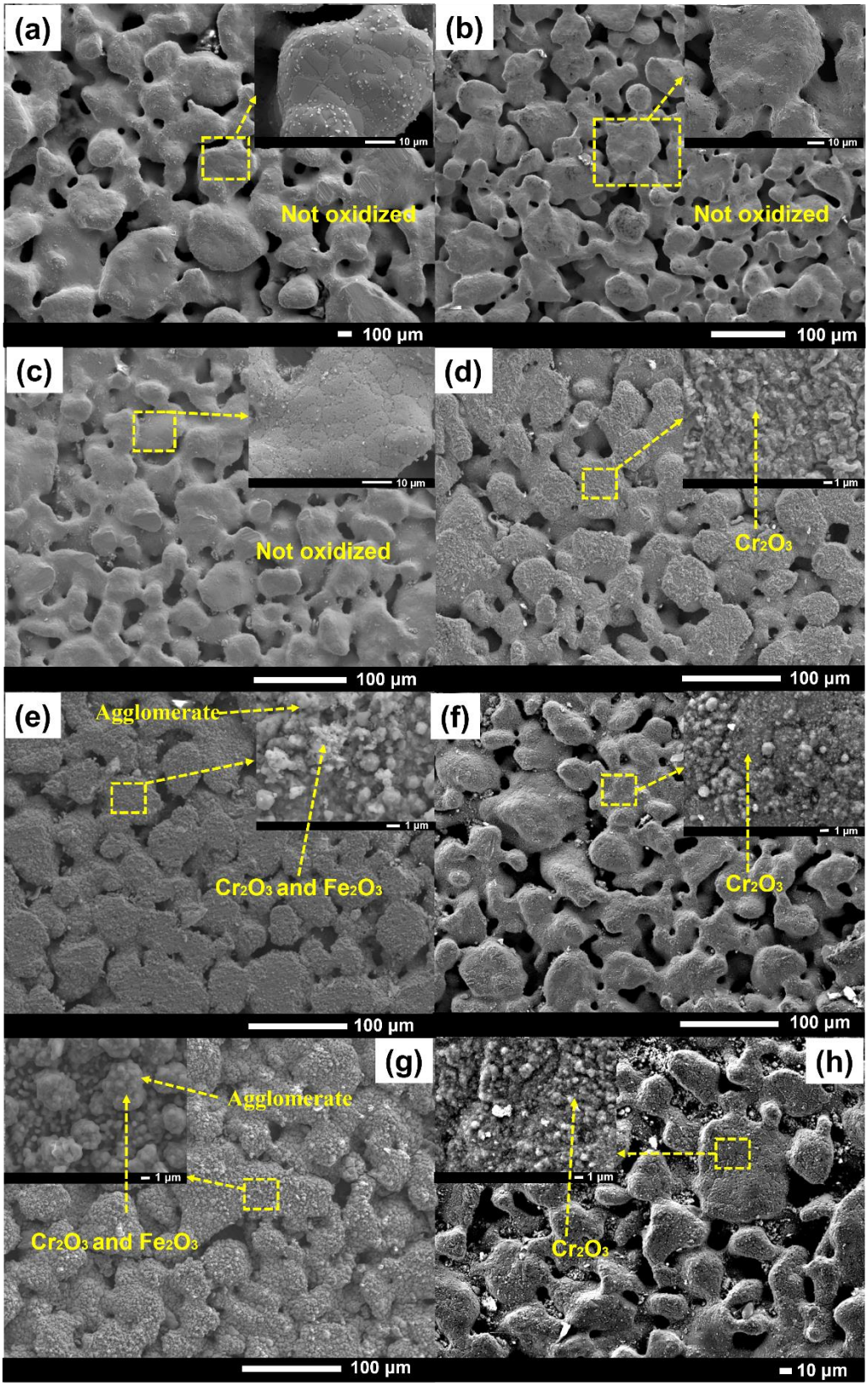

Figure 3.4: SEM images of ITM after annealing at different conditions: (a) no annealing, (b) 500°C for 120 min, (c) 800°C for 120 min, (d) 1000°C for 120 min, (e) 1100°C for 120 min, (f) 1000°C for 30 min, (g) 1200°C for 120 min, (h) 1000°C for 40 min

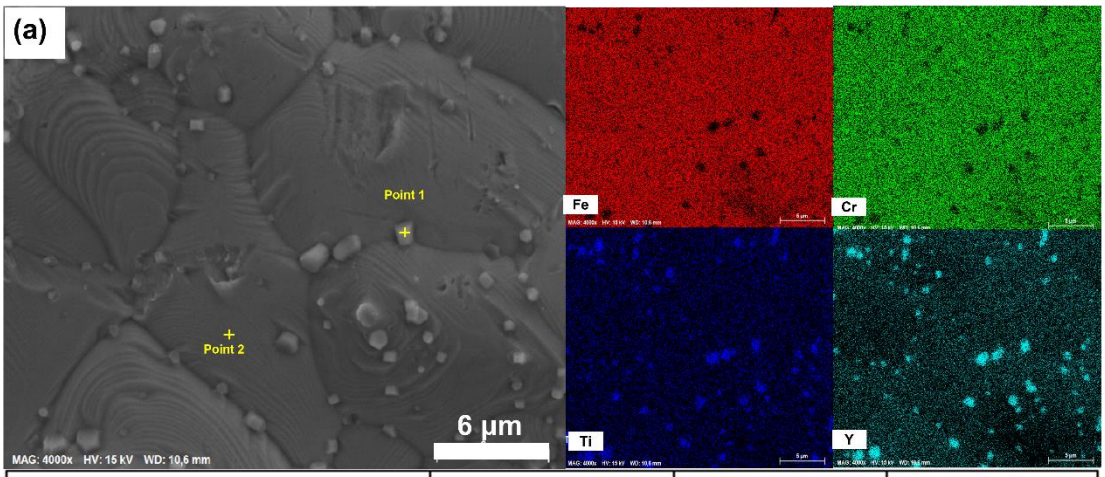

Composition (at %)	Surface	Point 1	Point 2
Fe	65.45	20.58	72.28
Cr	26.46	10.54	27.46
Ti	1.76	35.67	0.2
Y	0.71	33.21	0.06
O	5.62	–	–

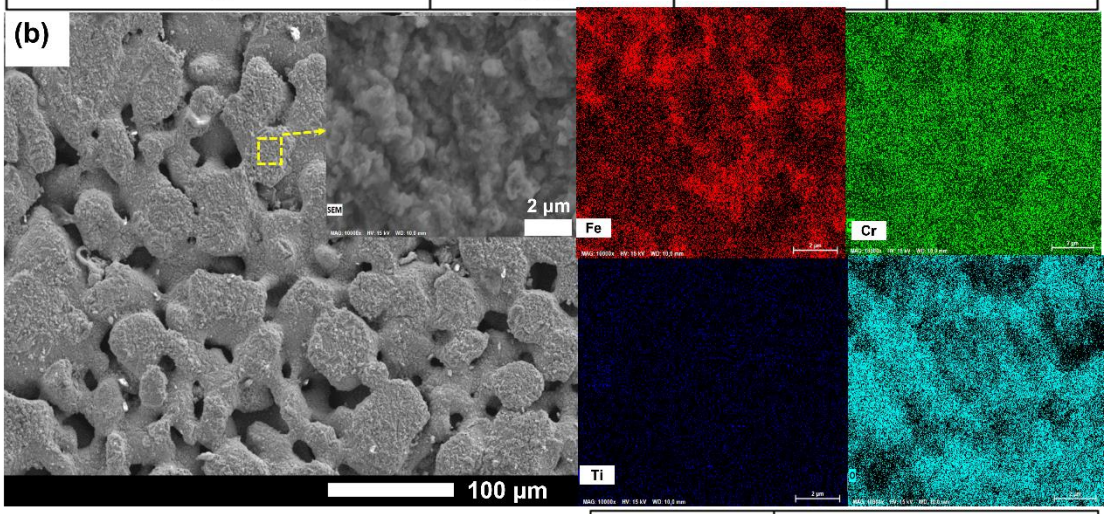

Elements	Composition (at %)
Fe	16.42
Cr	34.08
Ti	0.33
O	48.38
Other	0.79

Figure 3.5: SEM images and EDS mapping of ITM: (a) no annealing, (b) annealing at 1000°C for 120 min

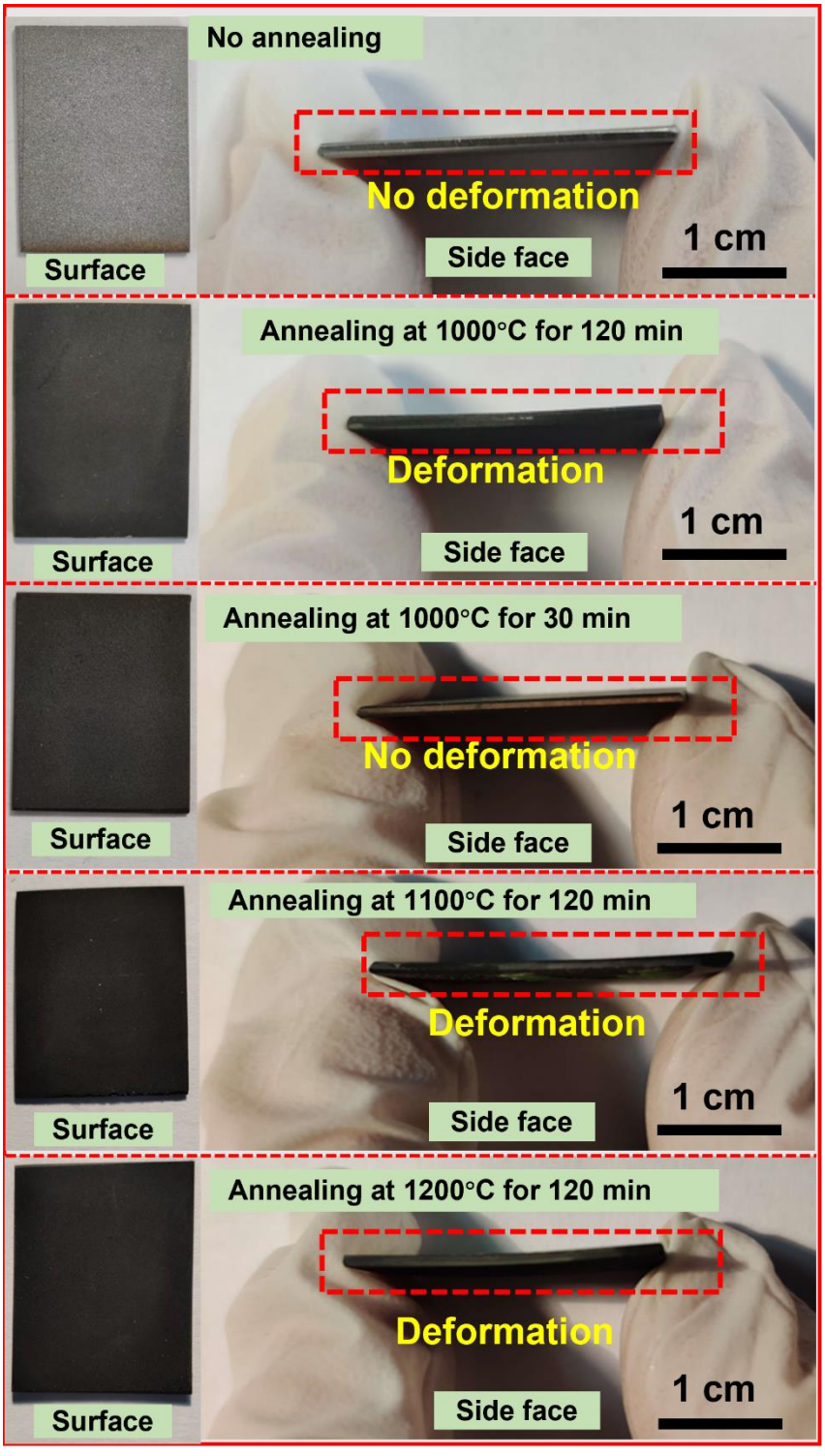

Figure 3.6: The ITM picture after annealing under different conditions

3.3 Deposition of bilayer NiO-YSZ anode by APS

Usually, powder materials are used as raw materials for APS technology. In this section, firstly, dry NiO-YSZ mixed powders are obtained by spray drying from commercial NiO and YSZ powders. Some information of commercial NiO and YSZ

powder are shown in Table 2.1. Then, the dry NiO-YSZ mixed powders are used as raw materials to deposit NiO-YSZ anode layer on ITM through APS. During this process, the effects of powder particle size and Ar/H_2 gas flow rate on the anode layer are investigated respectively.

3.3.1 Preparation of NiO-YSZ mixed powder by spray drying

The spray drying process is composed of two steps the atomization of the suspension in droplets and the drying of the atomized droplets. In this thesis, commercial NiO and YSZ powders are mixed in a beaker by magnetic stirring according to the formulation shown in Table 3.2 to obtain a suspension. PAA-NH_4 (polyacrylic acid, P90 from Coatex, France) and a polyvinyl alcohol (PVA) are used as dispersant and binder, respectively. Then, the suspension is pumped into a spray dryer from GEA Process Engineering. Finally, the NiO-YSZ powder with NiO of 65 wt. % and YSZ of 35 wt. % is obtained after atomization and drying. The obtained NiO-YSZ powder is separated in two batches at the outlet of the atomizer a distribution of finer particles and a larger one. The latter is sieved in two batches with a sieve of 63 μm. Three kinds of powder with different particle size distributions as shown in Figure 3.7 are obtained. Their median particle sizes (D_{50}) are 16.1 μm, 61.5 μm, and 65.2 μm, respectively.

From the SEM results in Figure 3.8, the particle size of NiO powder particles is bigger than that of YSZ powder. After spray drying, NiO and YSZ powder agglomerate together to form some relatively regular spherical particles. Combined with the EDS results in Figure 3.9, these spherical particles are agglomerated from NiO and YSZ powders. In addition, there is no significant difference in the particle surface for powders with different particle size distributions (Figures 3.8 (e) and (f)). The XRD results in Figure 3.10 show that there is a small amount of ZrO_2 in the YSZ ($Zr_{0.92}Y_{0.08}O_{1.96}$, tetragonal) powder. Although the tetragonal YSZ has lower ionic conductivity than the cubic structure YSZ, it has better mechanical properties when used as an anode material [4]. The XRD results also show that the NiO-YSZ powders with different particle size distributions have no obvious difference in phase.

Table 3.1: The spray drying experimental parameters

Formula				
NiO	YSZ	Distilled water	PAA-NH4	PVA
390g	210g	400g	4.0g	39.4g
Parameters				
Pressure (Pa)	Inter temperature(°C)		Outlet Temperature(°C)	
0.5	244		94-96	

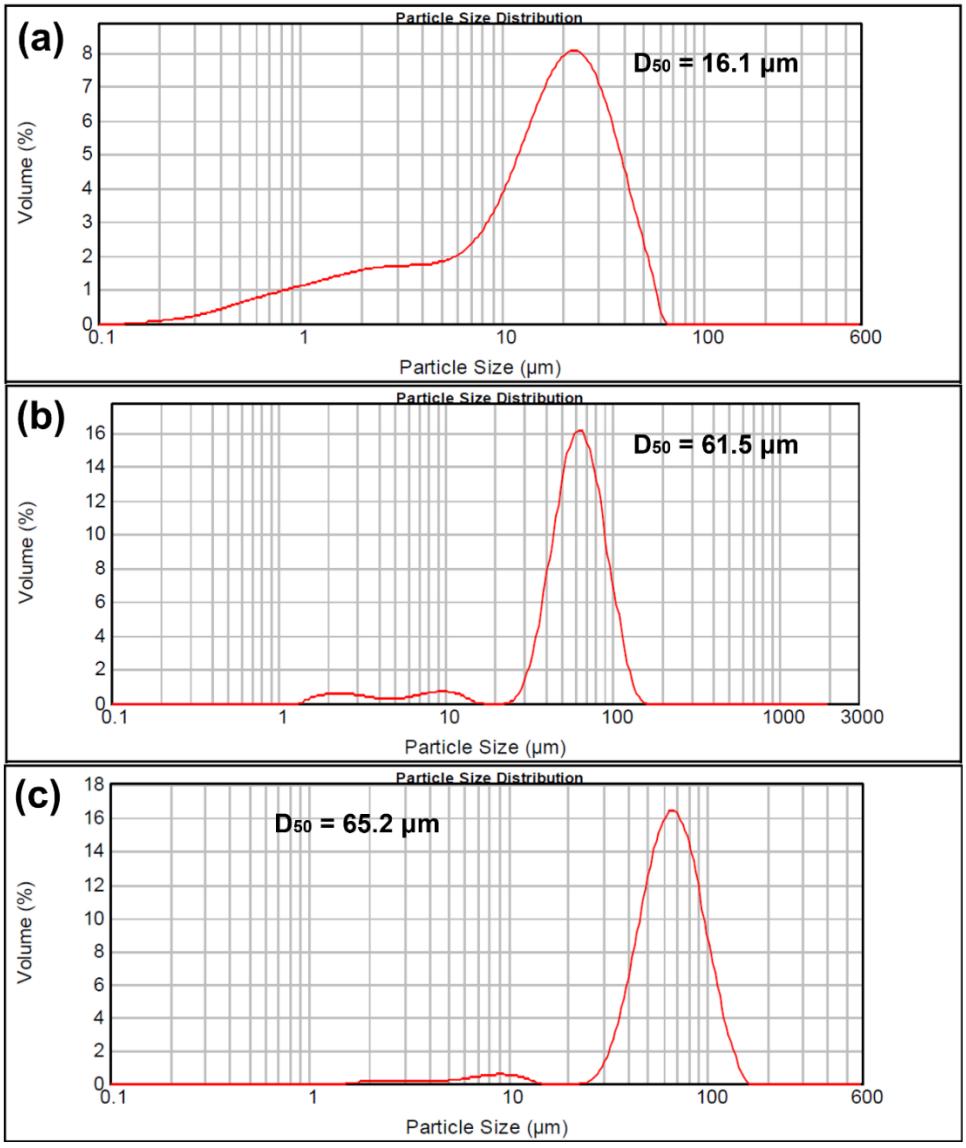

Figure 3.7: Particle size distribution of NiO-YSZ powder prepared by spray drying

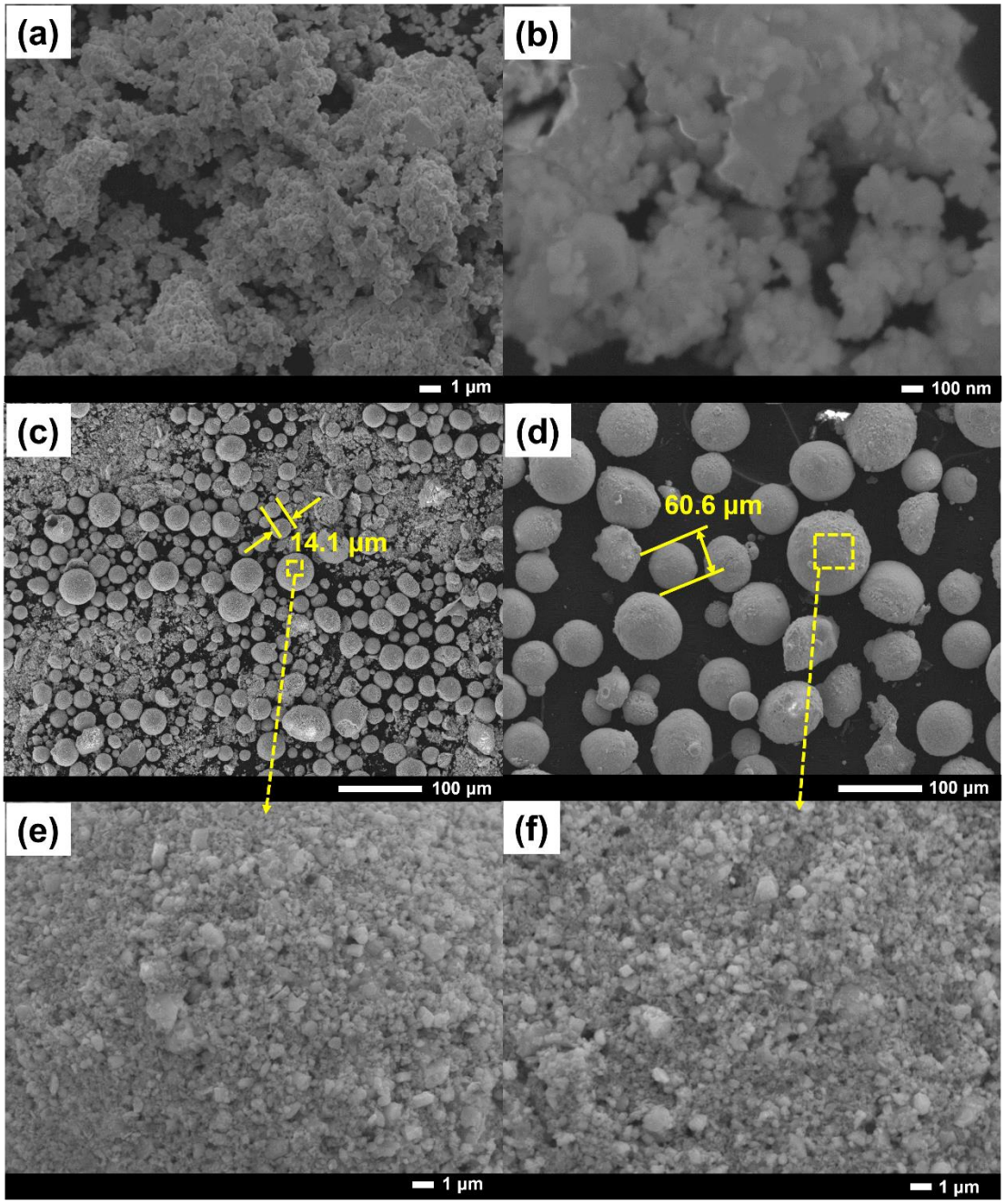

Figure 3.8: SEM observation of the different powders: (a) raw NiO powder, (b) raw YSZ powder, (c) NiO-YSZ mixed powder with D_{50} = 16.1 µm, (d) NiO-YSZ mixedpowder with D_{50} = 65.2 µm

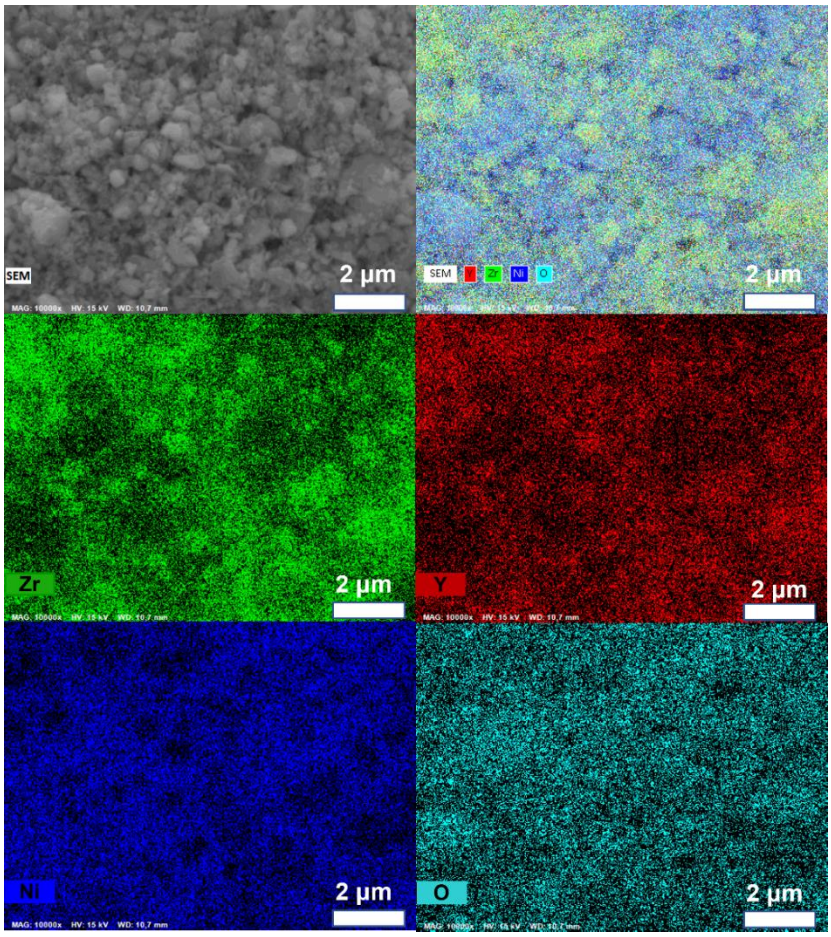

Figure 3.9: SEM observations and EDS mapping of NiO-YSZ mixed powder with D_{50} = 65.2 µm

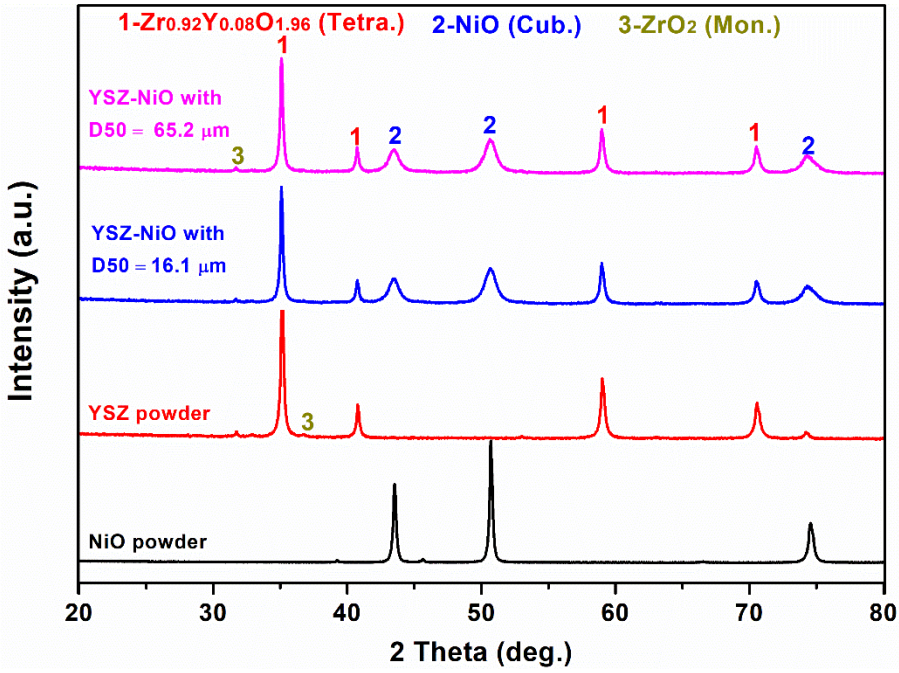

Figure 3.10: XRD of the NiO, YSZ, and two kinds of NiO-YSZ mixing powders will be used for the synthesis of anodes by APS.

3.3.2 Optimization of APS deposition parameters

An anode layer with sufficient porosity to allow gas transport is crucial for SOFC. The gas flow rate and powder particle size are important factors affecting the porosity of the NiO-YSZ anode layer deposited by APS. In this section, NiO-YSZ coatings are deposited using NiO-YSZ powders with different particle size under different Ar/H_2 flow rates. The porosity, element distribution, surface roughness, and deposition rate of the samples are evaluated. Referring to the research of J. FONDARD et al. [5], all samples are deposited under the conditions of fixed carrier gas flow rate of 3.2 L/min, nozzle scanning speed of 300 mm/s, and distance between nozzle and substrate of 90 mm.

Before depositing the NiO-YSZ anode layer on the ITM, it is necessary to optimize the APS deposition experiment to obtain suitable deposition parameters for the required NiO-YSZ anode layer. A set of deposition experiments are performed with the deposition parameters shown in Table 3.2. The effects of NiO-YSZ powder particle size and Ar/H_2 flow rate on NiO-YSZ coatings deposited on stainless steel are considered in Table 3.2. The NiO-YSZ coatings are deposited on the stainless-steel substrate that had previously been blasted with alumina powder at a pressure of 1.5 bar. The purpose of sandblasting is to improve the surface roughness of the stainless-steel substrate in order to promote mechanical anchoring of melted particles when they impact and solidify on the substrate. The blasted stainless-steel substrates need to be cleaned with alcohol and acetone successively, and then dried for APS deposition. Treating the surface of the substrate in this way is expected to enhance the adhesion of the coating to the substrate. For ease of description, the as deposited samples that are not reduced are called S1, S2, S3, S4, S5, and S6, respectively. Correspondingly, the samples after reduction are called SR1, SR2, SR3, SR4, SR5, and SR6, respectively.

Table 3.2: APS deposition parameters and reduction condition

APS experiments						
Parameters	S1	S2	S3	S4	S5	S6
Standoff distance(mm)	90	90	90	90	90	90
Carrier gas flow rate (L/min)	3.2	3.2	3.2	3.2	3.2	3.2
Current(A)	500	500	500	500	500	500
Ar gas (L/min)	50	50	50	50	35	35
H_2 gas (L/min)	3	3	3	5	8	8
Scanning step(mm)	5	5	5	5	5	5
Numbers of scanning	20	20	20	20	14	20
Scanning speed (mm/s)	300	300	300	300	300	300
NiO/YSZ (wt. %)	65/35	65/35	65/35	65/35	65/35	65/35
Powder size D_{50} (μm)	16.1	61.5	65.2	61.5	61.5	16.1
Reduction experiments						
Temperature (°C)	710					
Time (h)	3					
Ar/H_2 (sccm)	50/50					
Pressure (Pa)	1.5×10^{-2}					

As mentioned in Chapter 2, the temperature of the plasma at the nozzle can reach 10000°C, which causes NiO to face the risk of being reduced to Ni during the deposition of NiO-YSZ coating. In this way it is possible to deposit a Ni-YSZ coating on the substrate. The purpose of depositing NiO-YSZ instead of Ni-YSZ is intended to increase the porosity of the coating after undergoing reduction from NiO to Ni. Therefore, it is necessary to track the structure of the deposited NiO-YSZ coatings. The XRD pattern in Figure 3.11 shows the structure before and after reduction of the coatings deposited under different deposition parameters. For the as deposited samples, the diffraction lines on the XRD pattern correspond to the $Zr_{0.92}Y_{0.08}O_{1.96}$ (YSZ, Tetragonal), the NiO (Cubic), Ni (Cubic), and ZrO_2 (Monoclinic). ZrO_2 may come from NiO-YSZ powder. The peak assigned to Ni is considered to be from the reduction of

NiO during the deposition because NiO-YSZ powder does not contain Ni (Figure 3.10). In order, the peaks attributed to Ni in S2, S4, and S5 are more obvious. This may be attributed to two reasons. One is that the increase of the H_2 flow rate (from 5 to 8 L/min) promotes the reduction of NiO during the deposition process. The second is that the reduction of the Ar flow rate (from 50 to 35 L/min) reduces the flow rate of the plasma, which leads to a longer residence time of the NiO-YSZ powder in the plasma, thereby increases the risk of NiO to be reduced. After reduction, the peak attributed to NiO disappeared completely, which indicated that NiO is well reduced. The peak of YSZ is gradually enhanced, which may be due to the loss of NiO and/or Ni for S2, S4, and S5 in high-temperature plasma [6]. Comparing S1, S2, and S3 deposited from NiO-YSZ powders with different particle sizes, the peak assigned to YSZ has the highest intensity in S3. For the same plasma conditions, larger particle size may induce a lower melting and promote the incorporation of unmelted particle which are less affected by plasma treatment.

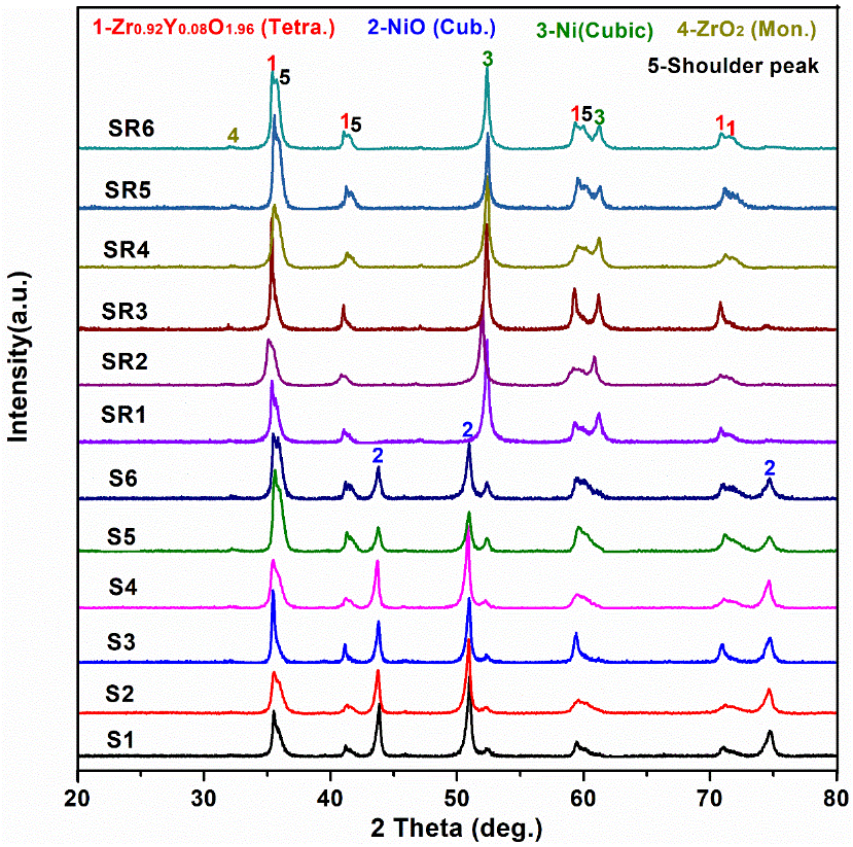

Figure 3.11: XRD patterns of NiO-YSZ anode material deposited by APS before and after reduction

The cross-section of the coating is observed by a SEM with Backscattered Electron Detector (BED). SEM pictures acquired allow to distinguish different enriched phases, pores, and cracks due to the different gray levels. The highest gray levels in the images represent pores and cracks, which are the basis for analyzing porosity using ImageJ software. For unreduced samples from S1 to S6, in addition to pores and cracks being distinguished, different phase-enriched regions such as YSZ, NiO, and Ni are also clearly identified. In each SEM-BED image, the brighter region represents the enrichment of YSZ, the darker region represents the enrichment of NiO, and the region between bright and dark represents both YSZ and NiO. Figures 3.12 and 3.13 show the global view and partial view of the cross-section of the samples. From Figures 3.12 (a)-(f), the samples deposited on the stainless steel have cracks at the interface. However, the coating deposited on ITM with the same deposition parameters as S3 adheres well to the substrate (Figure 3.12 (g)). This may be attributed to the mismatched CTE between the stainless-steel substrate and the deposited NiO-YSZ coating. The CTE of ITM is matched to that of the NiO-YSZ anode. Compared with S1, S2, and S3 in Figures 3.12 and 3.13, the larger particle size of NiO-YSZ powder resulted in larger pores in the coating. Whereas the results from S2, S4, and S5 show that the NiO-YSZ coating deposited under higher Ar/H_2 gas ratio has more large pores. The sample S6 deposited with small particle size NiO-YSZ powder under the condition of low Ar/H_2 gas ratio has fewer large pores. In addition, samples S5 and S6 deposited under high H_2 flow rate (8 L/min) observed brighter thin line-like Ni regions, which is consistent with the XRD results. For the reduced samples from SR1 to SR6 (Figure 3.14), many small pores appeared except for the pores that existed before, which may originate from the reduction of NiO. Whereas more thin line-like regions attributed to Ni appear in the reduced samples. These Ni may exist before reduction, but it is not easy to distinguish before reduction in SEM-BED images, but apparently XRD results have confirmed this point. The rest of Ni obtained after reduction is not easy to distinguish from YSZ only by SEM-BED images. To further distinguish the enriched regions of Ni and YSZ, EDS mapping analysis is performed on the reduced samples as show in Figure 3.15. From the traces of Zr and Y on the mapping images in Figure 3.15, most of the YSZ-enriched

region is distributed in the smooth region of the image. A small amount of YSZ-enriched regions are distributed in the regions where small pores appear, and these regions may be more uniformly mixed with NiO before reduction. The Ni-enriched and the YSZ-enriched regions present alternating layers, which is more obvious in the samples deposited under high H_2 flow rate and low Ar flow rate as show in Figures 3.15 (c) and (d). This may be due to higher temperature (high H_2 flow rate) and longer residence time (low Ar flow rate), which makes the powder particles easier to be melted. Furthermore, due to the large difference in the melting points of NiO (1980°C) and YSZ (2700°C), the molten NiO and YSZ are arranged alternately. But these alternating Ni-enriched region will communicate with each other in some areas, which is very important to ensure the conductivity of the anode layer. Likewise, alternating YSZ-rich regions are also connected in some regions, which is helpful to extend the TPB in the anode layer.

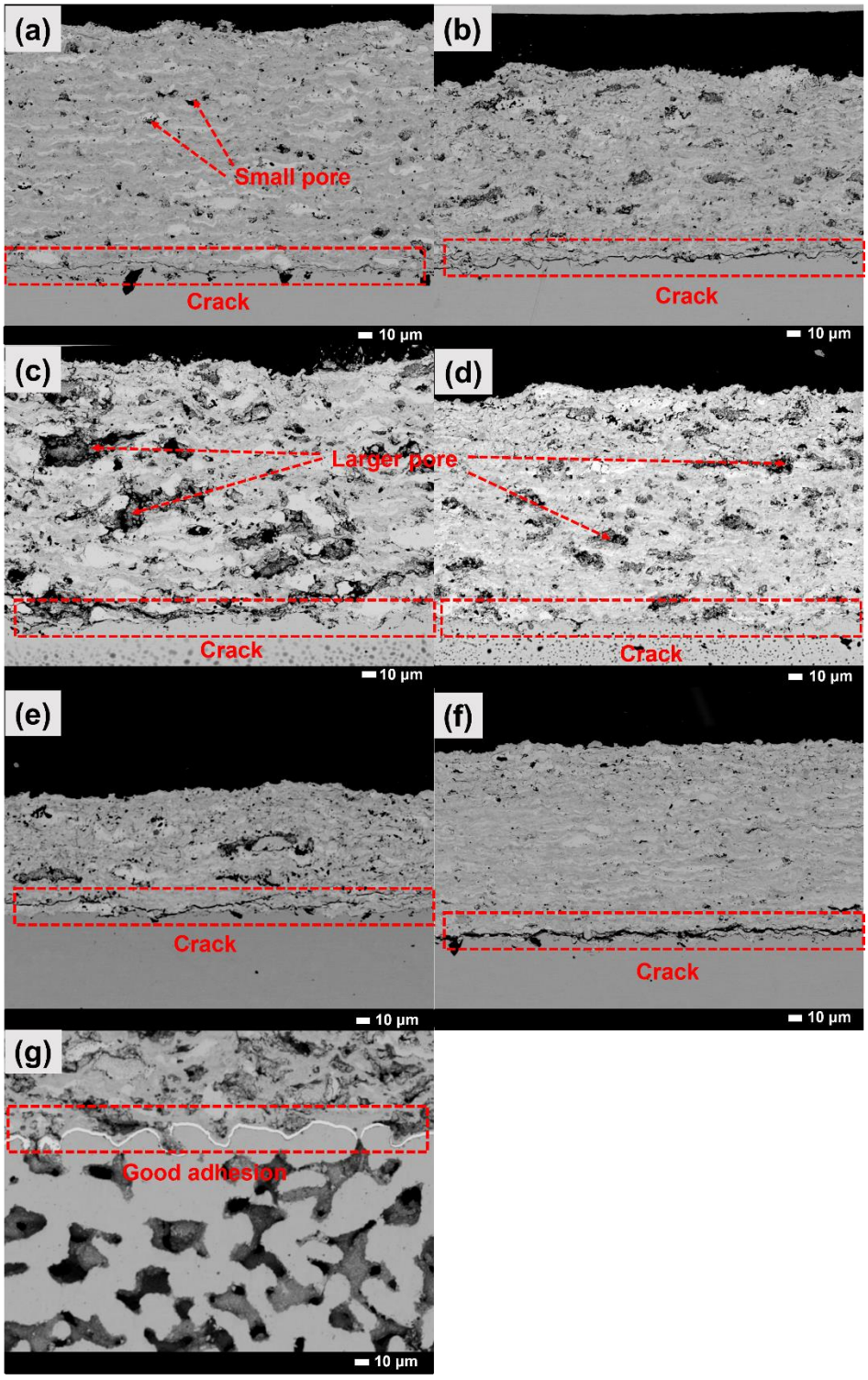

Figure 3.12: SEM-BED images of the cross-section of the deposited NiO-YSZ coatings: (a) S1 (powder size D_{50} of 16.1 µm, gas flow rate Ar/H_2 of 50/3 L/min), (b) S2 (powder size D_{50} of 61.5 µm, gas flow rate Ar/H_2 of 50/3 L/min), (c) S3 (powder size D_{50} of 65.2µm, gas flow rate Ar/H_2 of 50/3 L/min), (d) S4 (powder size D_{50} of 61.5 µm, gas flow rate Ar/H_2 of 50/5 L/min), (e) S5 (powder size D_{50} of 61.5µm, gas flow rate Ar/H_2 of 35/8 L/min), and (f) S6 (powder size D_{50} of 16.1µm, gas flow rate Ar/H_2 of 35/8 L/min) deposited on stainless steel; (g) S3 (powder size D_{50} of 65.2µm, gas flow rate Ar/H_2 of 50/3 L/min) deposited on ITM

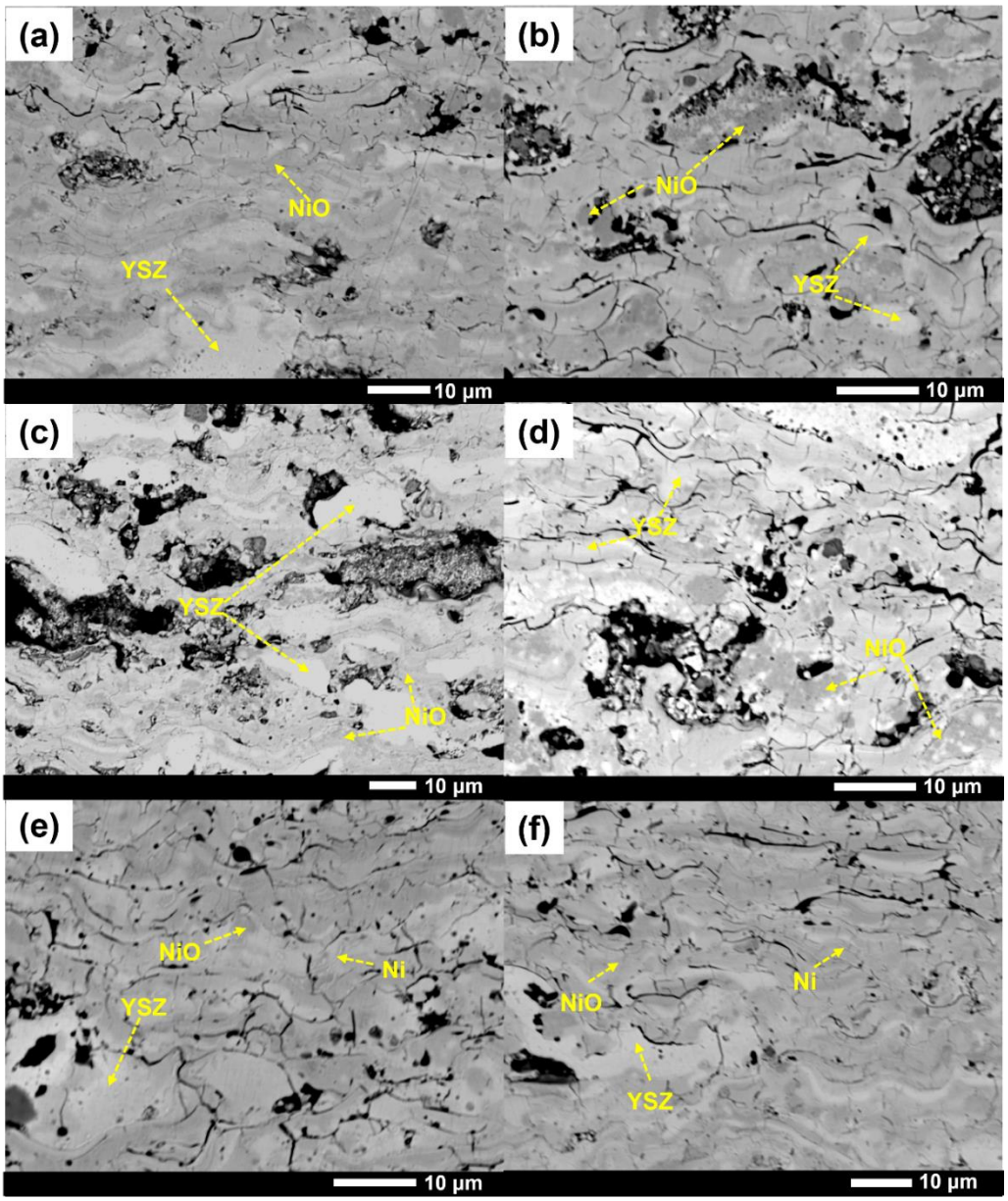

Figure 3.13: SEM-BED image of cross-section of the NiO-YSZ samples deposited by APS: (a) S1 (powder size D_{50} of 16.1 µm, gas flow rate Ar/H_2 of 50/3 L/min), (b) S2 (powder size D_{50} of 61.5 µm, gas flow rate Ar/H_2 of 50/3 L/min), (c) S3 (powder size D_{50} of 65.2µm, gas flow rate Ar/H_2 of 50/3 L/min), (d) S4 (powder size D_{50} of 61.5 µm, gas flow rate Ar/H_2 of 50/5 L/min), (e) S5 (powder size D_{50} of 61.5µm, gas flow rate Ar/H_2 of 35/8 L/min), and (f) S6 (powder size D_{50} of 16.1µm, gas flow rate Ar/H_2 of 35/8 L/min)

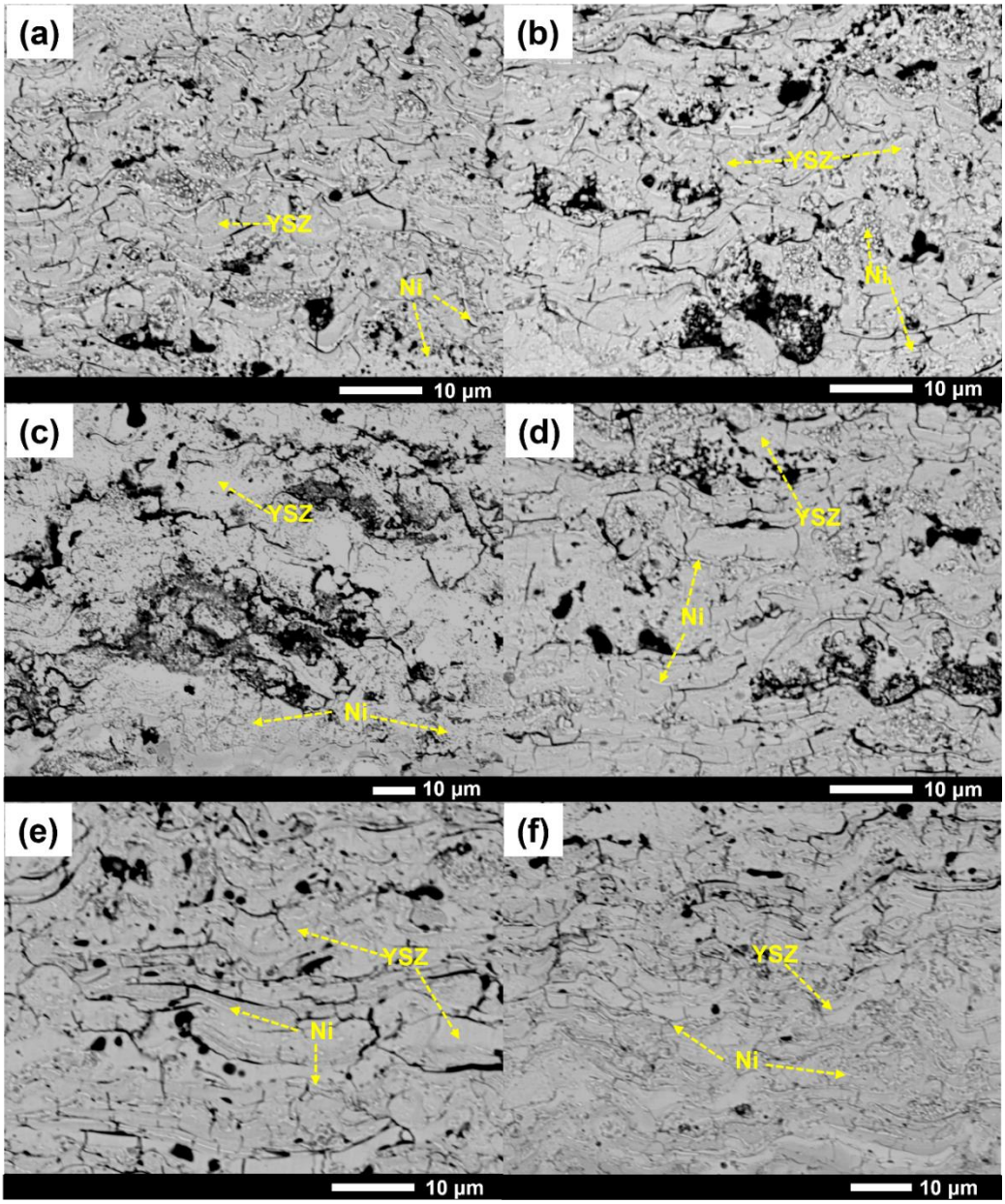

Figure 3.14: SEM-BED image of cross-section of the reduced NiO-YSZ samples deposited by APS: (a) SR1 (powder size D_{50} of 16.1 µm, gas flow rate Ar/H_2 of 50/3 L/min), (b) SR2 (powder size D_{50} of 61.5 µm, gas flow rate Ar/H_2 of 50/3 L/min), (c) SR3 (powder size D_{50} of 65.2µm, gas flow rate Ar/H_2 of 50/3 L/min), (d) SR4 (powder size D_{50} of 61.5 µm, gas flow rate Ar/H_2 of 50/5 L/min), (e) SR5 (powder size D_{50} of 61.5µm, gas flow rate Ar/H_2 of 35/8 L/min), and (f) SR6 (powder size D_{50} of 16.1µm, gas flow rate Ar/H_2 of 35/8 L/min)

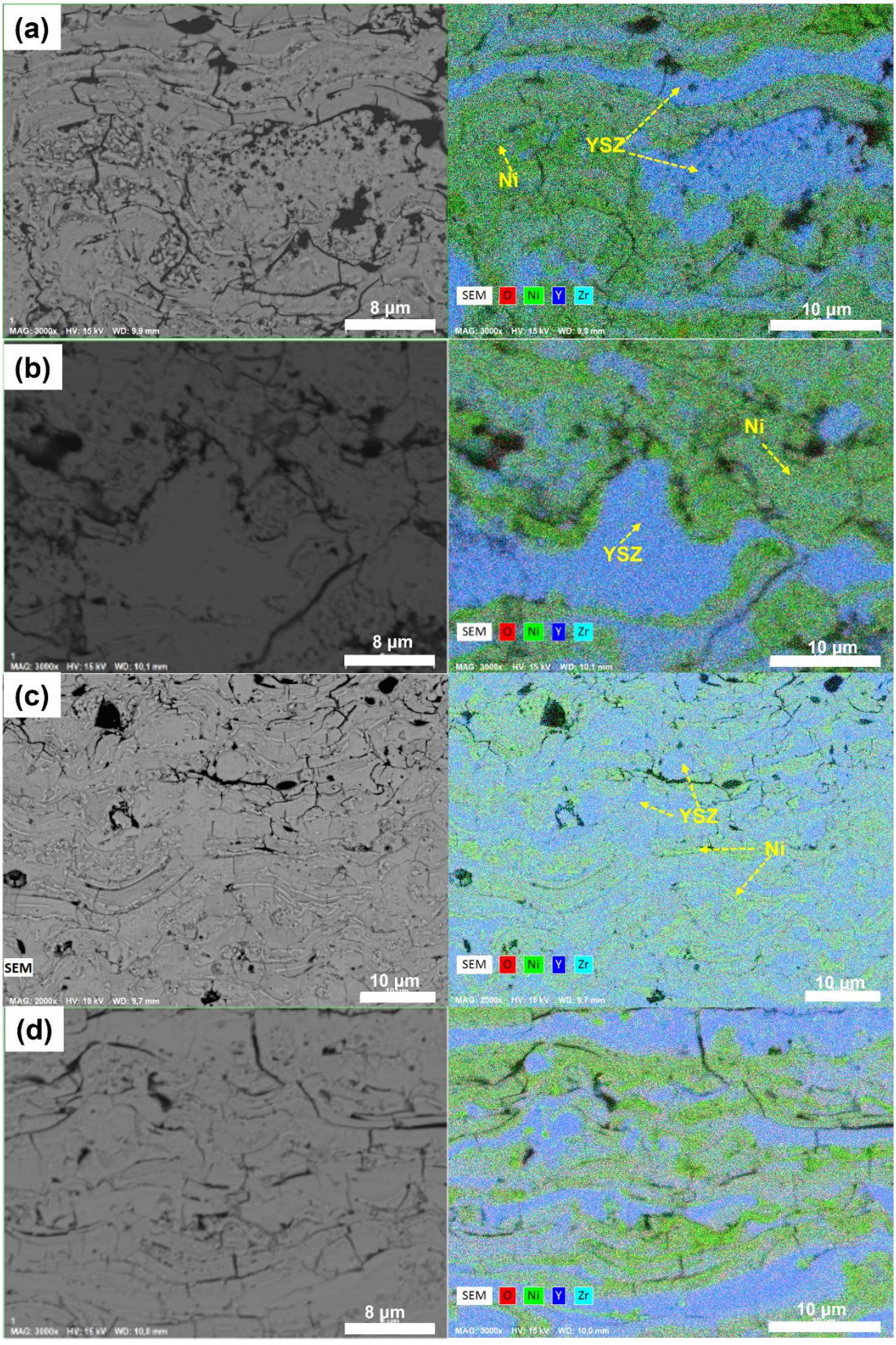

Figure 3.15: SEM-EDS results of the reduced NiO-YSZ samples deposited by APS: (a) RS1 (powder size D_{50} of 16.1 µm, gas flow rate Ar/H_2 of 50/3 L/min), (b) RS3 (powder size D_{50} of 65.2µm, gas flow rate Ar/H_2 of 50/3 L/min), (c) RS5 (powder size D_{50} of 61.5µm, gas flow rate Ar/H_2 of 35/8 L/min), (d) RS6 (powder size D_{50} of 16.1µm, gas flow rate Ar/H_2 of 35/8 L/min)

The pores in the anode layer are the key to ensure good gas transmission. Therefore, it is necessary to quantify the porosity of the deposited NiO-YSZ coating. The quantification of the porosity of the coating is achieved by using ImageJ software to analyze the SEM-BED images like Figures 3.13 and 3.14. The detailed analysis process is shown in the Chapter 2. The quantitative results of the porosity of the samples are listed in Table 3.3. Comparing the porosity of S1, S2, and S3, the porosity increases with the particle size of the NiO-YSZ powder. The porosity results from S2, S4, and S5 show that the porosity increases with the Ar/H_2 gas ratio. The porosity of the coating deposited by using NiO-YSZ powder with a D_{50} of 65.2 μm and with Ar/H_2 flow rate of 50/3 L/min reached 32.5 ± 0.5 Vol.% after reduction. This value is slightly higher than the 30 Vol.% obtained by Fondard et al [5], which may be due to the use of NiO-YSZ powder with a higher NiO content. However, the porosity of the coating deposited using the NiO-YSZ powder with a D_{50} of 16.1 μm and the Ar/H_2 flow rate of 35/8 L/min reached 16.9 ± 0.3 Vol.% after reduction.

The deposition rate of the coating is evaluated to facilitate the control of the thickness of the subsequent bilayer anode. The deposition rate in μm/scanning of the coating is defined as the thickness deposited by the torch completing one scanning procedure. Comparing the deposition rates of S1, S2, and S3 in Figure 3.16, the NiO-YSZ powder with small particle size is allowed to deposit at a higher deposition rate. However, the deposition of NiO-YSZ powder with large particle size will produce large pores and increase the thickness. This may be the reason why the deposition rate of S3 is greater than that of S2, although the particle size of the NiO-YSZ powder used to deposit S2 is smaller than that of S3. Compared to S2, S4, and S5, the high Ar/H_2 flow allows to perform deposition with a greater deposition rate.

In order to deposit dense electrolyte layers by RMS on NiO-YSZ anode coatings, the surface roughness has to be considered. Table 3.4 lists the surface roughness parameters of samples S1, S2, S3, and S6. The Ra and Rz of the coatings deposited using NiO-YSZ powder with large particle size (S3 and S2) are larger than those with small particle size powder (S1). Comparing S6 and S1, the coating deposited under low Ar/H_2 gas ratio has lower Ra and Rz. Higher Ra and Rz mean that the surface of the

coating has larger fluctuations due to higher peaks or deep valleys. The S6 sample deposited at a low Ar/H_2 ratio of 35/8 using small NiO-YSZ powder particle size with a D_{50} of 16.1 μm has lower Ra and Rz.

Based on the above experimental results, large particle size NiO-YSZ powder with D_{50} of 65.2 μm is suitable for depositing the anode layer with high porosity under high Ar/H_2 gas flow ratio (50/3 L/min). In comparison, the coating deposited using small NiO-YSZ powder particle size with D_{50} of 16.1 μm at low Ar/H_2 gas flow ratio (35/8 L/min) has fewer large pores inside and a relatively flat surface.

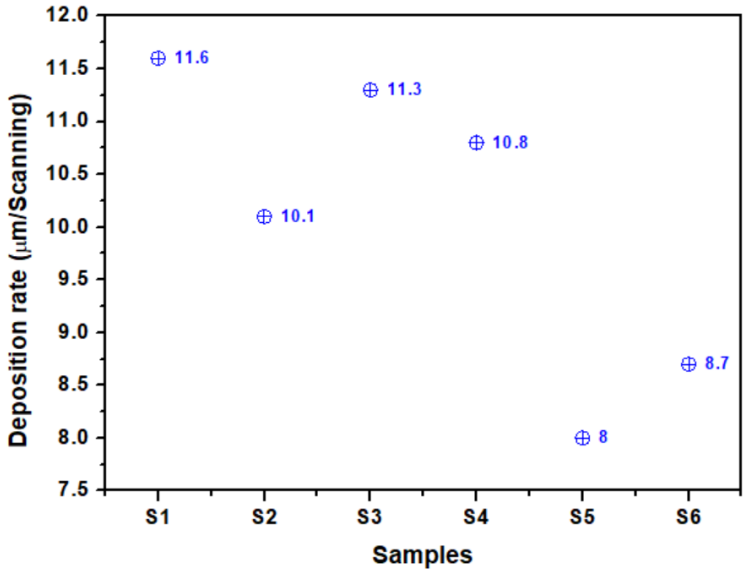

Figure 3.16: Deposition rate of the NiO-YSZ coating under different APS condition

Table 3.3: The porosity of the NiO-YSZ coatings deposited by APS under different parameters before and after reduction

Samples	Porosity (Vol. %)	Porosity increase (Vol. %)
S1	13.1 ± 0.3	5.1
SR1	18.2 ± 0.4	
S2	19.2 ± 0.3	7.2
SR2	26.4 ± 0.3	
S3	26.9 ± 0.5	5.6
SR3	32.5 ± 0.5	
S4	17.9 ± 0.5	7.3
SR4	25.2 ± 0.4	
S5	15.7 ± 0.4	7.7
SR5	23.4 ± 0.3	
S6	12.7 ± 0.2	4.2
SR6	16.9 ± 0.3	

Table 3.4: The surface roughness parameters obtained by profilometry analysis of the NiO-YSZ coatings deposited by APS on blast stainless-steel

Samples	Ra (μm)	Rz (μm)	Rsk
S1	3.39	20.91	0.08
S2	6.04	34.52	-0.25
S3	6.93	35.29	-0.14
S6	3.00	18.02	0.07

3.2.3 Deposition of bilayer anode on ITM

In this thesis, the deposited anode layer will be used as the substrate for the deposition of a dense electrolyte layer by RMS in the next stage. However, RMS deposition has high requirements on the surface flatness of the substrate. Obviously, the NiO-YSZ anode with larger pores is not suitable for a direct electrolyte deposition by RMS. Therefore, a bilayer anode design is adopted, that is, the NiO-YSZ anode with higher porosity is deposited on the ITM, and then the NiO-YSZ anode with smaller porosity is deposited to facilitate the subsequent RMS deposition. It should be noted that a GDC10 buffer layer is deposited before the deposition of the bilayer NiO-YSZ anode layer. The detailed deposition process of the GDC10 buffer layer is described in section 3.4. The deposition process of the bilayer anode is carried out according to the deposition conditions listed in Table 3.5. ITM/GDC10 substrate with a size of 2.3-3.0 × 2.0 × 0.1cm^3 is cleaned by alcohol and acetone to remove surface contamination before deposition. The sandblasting is not allowed because it will damage the GDC10 buffer layer on the ITM surface. After the APS deposition, one sample is taken to perform the reduction experiment listed in Table 3.2 to observe the porosity after reduction. The other samples are not subjected to reduction and are used for the next stage of RMS deposition. This protocol is considered to avoid the increase of the porosity of the upper anode after reduction thereby affect the RMS deposition. A high-porosity NiO-YSZ anode of about 136 μm and a low porosity NiO-YSZ anode of about 70 μm are expected to be deposited according to the deposition conditions shown in Table 3.5.

Table 3.5: APS Deposition parameters of the bilayer NiO-YSZ anode

Parameters	High porosity layer	Low porosity layer
Standoff distance(mm)	90	
Carrier gas flow rate (L/min)	3.2	
Current(A)	500	
Voltage(V)	62	66
Ar / H_2 (L/min)	50/3	35/8
Scanning Step(mm)	5	
Numbers of scanning	12	8
Scanning speed (mm/s)	300	
Mixed NiO/YSZ powder (wt. %)	65/35	
Powder size (D_{50}, μm)	65.2	16.1

As shown in Figure 3.17, the roughness of the bilayer NiO-YSZ anode deposited on ITM/GDC10 is obtained by a 3D profilometry. Ra of 4.27 μm and Rz of 23.26 μm are still relatively large, which means that there are high and low peaks and valleys on the surface. It is still not enough to meet the surface requirements for RMS deposition. Therefore, it is necessary to polish the surface to reduce the surface roughness. The polishing procedure is performed by first sandpaper grinding (600 → 800 → 1200 → 2000 mesh) then polishing use aluminum oxide polishing liquid (6 μm → 3 μm → 1μm). As shown in 3.18, the Ra and Rz of the polished sample are reduced to 0.25 μm and 2.05 μm respectively. From the collected scanning picture, the peaks and valleys on the surface of the polished sample have become smoother. From the research results of J. FONDARD [6], the NiO-YSZ surface with Ra of 0.31 μm and Rz of 3.5 μm is successfully used for RMS deposition of electrolyte layers. This shows that having a surface as shown in Figure 3.18 is sufficient for RMS deposition. Figure 3.19 is the SEM-BED images of the cross-section and surface of the polished sample. From Figure 3.19 (a), the NiO-YSZ anode layer is well adhered to the ITM/GDC10 substrate, and the GDC10 barrier layer is not damaged during the APS deposition process. The thickness of the high-porosity NiO-YSZ anode layer is about 137.2 μm, while the low-porosity NiO-YSZ is about 38.6 μm after polishing. It should be noted that the ideal situation is that the thin, low-porosity layer facilitates gas transport while providing a buffer for the high-porosity layer and the electrolyte layer. However, since the samples involved in this thesis are all manually polished, it is not easy to reduce the thickness

of the low porosity layer as much as possible without wearing the high porosity layer. In comparison, the surface roughness directly affects the deposition of the subsequent electrolyte and thus determines whether the single cell can be successfully fabricated, and a thicker low-porosity layer may only sacrifice the performance of the cell to some extent. Therefore, to ensure the smooth manufacture of subsequent single cells, such a strategy is implemented which is to reduce the thickness of the low-porosity NiO-YSZ anode layer as much as possible subject to ensuring the surface roughness. However, only samples with the surface as shown in Figure 3.18 and the thickness of the low porosity layer as shown in Figure 3.19 (a) can be obtained after efforts. It can be seen from Figure 3.19 (b) that the surface of the polished sample is flat overall, but there are still tiny pits. These pits need to be covered by a certain thickness of electrolyte layer. Figure 3.19 (c) and (d) show the partial cross-sections of the samples before and after reduction. As expected, the upper low porosity layer has fewer large sized pores. The porosity of the high porosity layer and low porosity layer of the bilayer anode before and after reduction is quantified by the analysis of SEM-BED images by ImageJ software. The obtained porosity results are listed in Table 3.6. The porosity of NiO-YSZ anode with high porosity layer is 33.1 ± 0.6 Vol.% after reduction, which is very close to the porosity (32.5 ± 0.5 Vol. %) of sample S3 deposited on stainless steel under the same conditions in the previous section. The upper low porosity NiO-YSZ anode layer has a porosity of 17.2 ± 0.4 Vol.%, which is close to that of the S6 sample (16.9 ±0.3 Vol.%) deposited on stainless-steel under the same conditions.

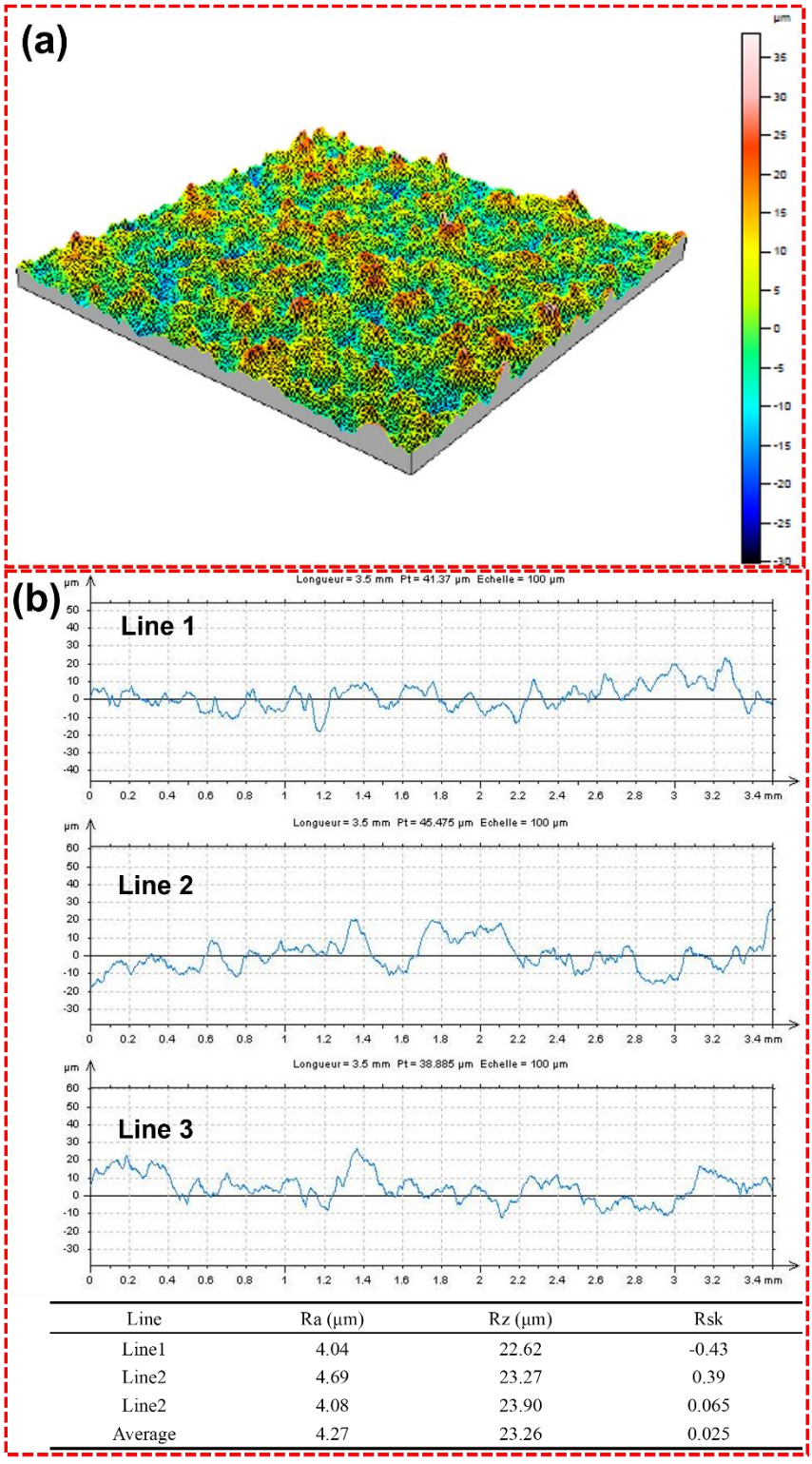

Line	Ra (µm)	Rz (µm)	Rsk
Line1	4.04	22.62	-0.43
Line2	4.69	23.27	0.39
Line2	4.08	23.90	0.065
Average	4.27	23.26	0.025

Figure 3.17: (a) surface mapping of the as deposited bilayer NiO-YSZ anode synthesized by APS on ITM/GDC10 substrate using the tactile profilometer; (b) the Ra, Rz and Rsk parameters at three different positions on the surfaceare mapping determined by surface analysis using the Mountain Map software

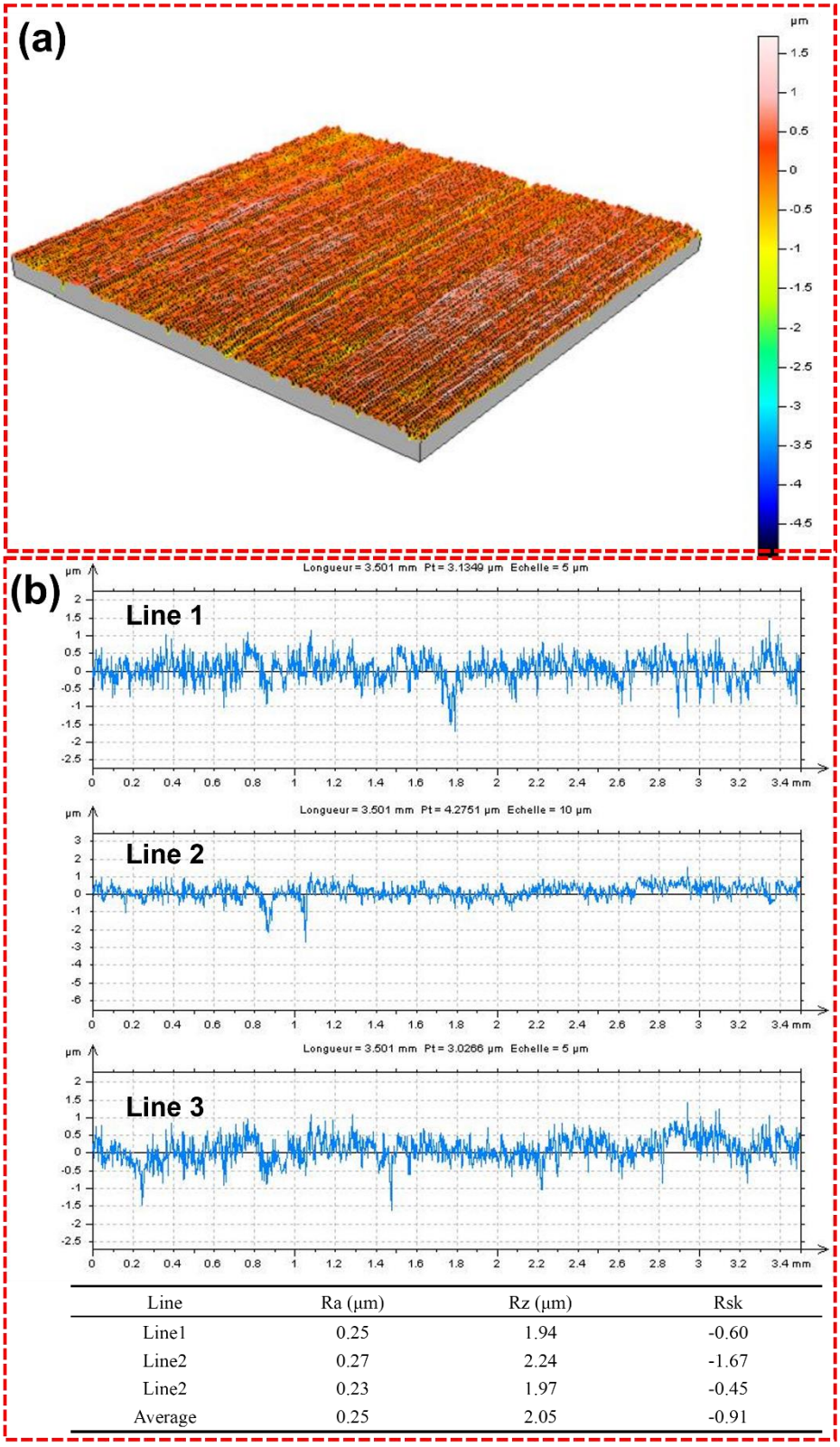

Line	Ra (µm)	Rz (µm)	Rsk
Line1	0.25	1.94	-0.60
Line2	0.27	2.24	-1.67
Line2	0.23	1.97	-0.45
Average	0.25	2.05	-0.91

Figure 3.18: (a) surface mapping of the polished bilayer NiO-YSZ anode synthesized by APS on ITM/GDC10 substrate using the tactile profilometer; (b) the Ra, Rz and Rsk parameters at three different positions on the surfaceare mapping are determined by surface analysis using the Mountain Map software

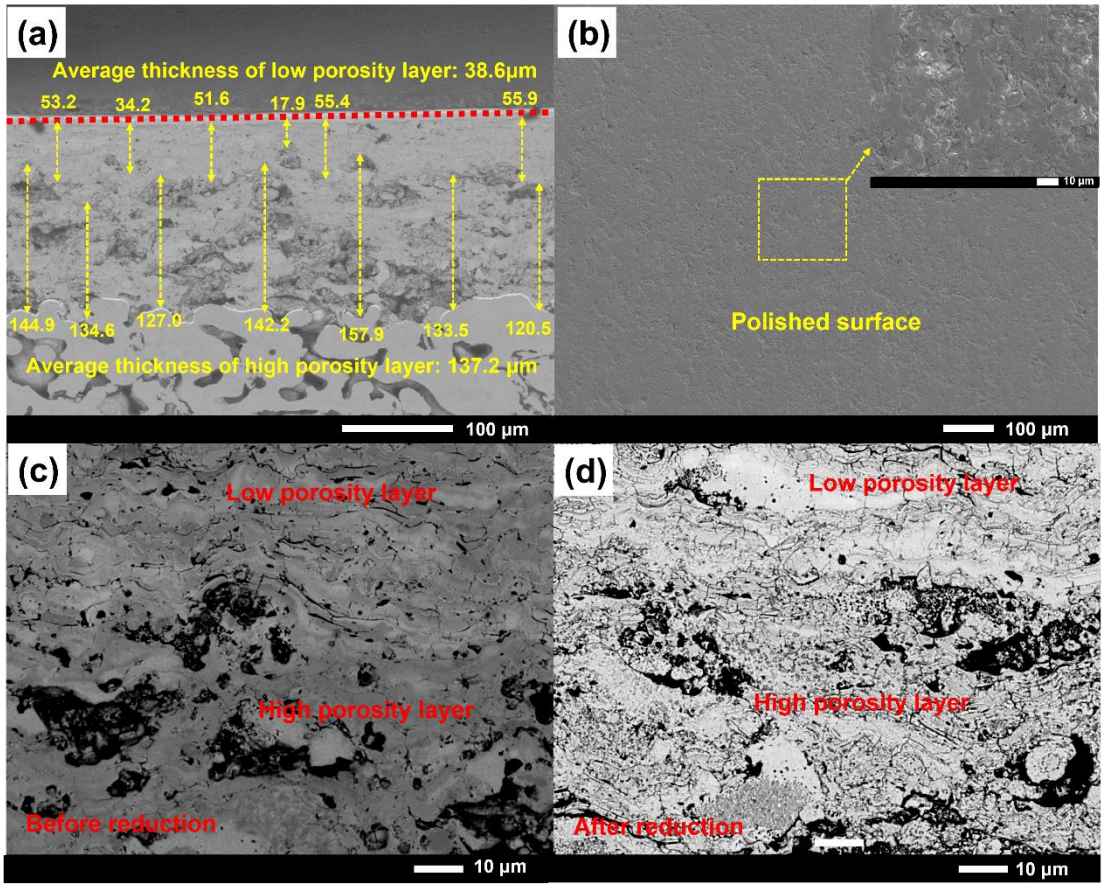

Figure 3.19: SEM-BED images of NiO-YSZ anode deposited by APS on ITM/GDC10 substrate : (a) global view of polished cross-section, (b) polished surface, (c) Partial view of polished cross-section, (d) Partial view of polished cross-section after reduction.

Table 3.6: The porosity of bilayer NiO-YSZ anode

Bilayer	Porosity (Vol.%)	Porosity increase (Vol.%)
[a]Low porosity	12.9 ± 0.3	4.3
[b]Low porosity	17.2 ± 0.4	
[a]How porosity	27.2 ± 0.4	5.9
[b]How porosity	33.1 ± 0.6	

a: before reduction, b: after reduction

3.4 Deposition of 8YSZ/GDC10 bilayer electrolyte by RMS with PEM system

8YSZ/GDC10 electrolyte is deposited by an Alcatel SCM650 sputtering chamber equipped with plasma emission monitor (PEM). Prior to this work, P. BRIOIS et al. [7], P-L. CODDET et al. [8], E. BREAZ et al. [9], and J. FONDARD et al. [5] have used this device to investigate the deposition of YSZ and GDC electrolytes. Their research results provide some solid references for the deposition of 8YSZ and GDC10

electrolytes in this section. The use of $Zr_{0.84}Y_{0.16}$ and $Ce_{0.90}Gd_{0.10}$ alloy targets allow more convenient access to homogeneous 8YSZ and GDC10 electrolytes by RMS. This is since the atomic weights between Zr (Ce) and Y (Gd), are close, resulting in the composition of the deposited coating being consistent with the target. P. BRIOIS et al [7] deposited YSZ films at pressures of 0.59 and 4.0 Pa, showing that the pores of 8YSZ films increased with the pressure. P-L. CODDET deposited a dense 8YSZ electrolyte layer in the pressure range of 0.15 to 0.2 Pa [8]. The low pressure in the chamber allows the sputtered particles to carry more energy to the substrate to promote the flow of particles and make the coating denser. The bias power applied to the substrate helps to improve the adhesion between the coating and the substrate, but too high bias power will cause cracks in the coating. E. BREAZ et al. [9] found that applying a bias power of about 80 W can improve the adhesion between GDC coating and the YSZ ceramic substrate and avoid cracks appearing in the GDC coating. J. FONDARD et al. [5] pointed out that a sufficiently thick electrolyte layer needs to be deposited to cover the defects of polished NiO-YSZ anode deposited by APS. They deposit the 8YSZ/GDC10 electrolyte layer with a total thickness of 11.3 μm with this device. It is found that the 8YSZ/GDC10 electrolyte layer well covered the NiO-YSZ anode surface without fracture or collapse due to the defects such as hills and valleys on the anode surface. In addition, the use of the PEM system relies on the acquisition of the emission optical signal intensity of the target. The emission optical signal intensity of the same target will be different under different conditions (such as the surface is oxidized or not oxidized). Therefore, it is necessary to find the appropriate emission optical intensity (Setpoint) for different target before depositing the desired coating.

In this thesis, referring to the above results, some basic deposition parameters are adopted and listed in Table 3.7. The influence of Setpoint in the PEM system on the targets is investigated. It is expected to sequentially deposit 8YSZ and GDC10 using $Zr_{0.84}Y_{0.16}$ and $Ce_{0.90}Gd_{0.10}$ alloy targets to obtain an 8YSZ/GDC10 bilayer electrolyte with a total thickness of about 11μm on this device. The GDC10 layer also acts as a buffer layer between the 8YSZ and the cathode layer.

Table 3.7: Basic RMS deposition parameters for 8YSZ and GDC10 layer

Parameters	8YSZ	GDC10
Ar flow rate (sccm)	20	20
Total pressure (Pa)	0.19-0.21	0.18-0.20
Bias (W)	25	75
D_{s-t} (mm)	70	70
Current (A)	2.5	2.5
Frequency (kHz)	50	50
T_{off} (μs)	4	4

D_{s-t} : Distance between substrate and target

3.4.1 Deposition of 8YSZ electrolyte layer

A magnetron sputtering process equipped with a PEM system is confirmed to allow greater deposition rates [6]. It realizes the control of the sputtering process by collecting the emission optical intensity of the target in real time and feeding them back to the computer with a control program developed at the laboratory. A specific emission optical intensity can be set in the control program to achieve a specific sputtering process. For an alloy target, the emission optical intensity of the host element of the alloy are usually collected.

In this thesis, the deposition stage of the 8YSZ by using $Zr_{0.84}Y_{0.16}$ alloy target is monitored based on the measurement of the emission optical intensity of the 362 nm Zr emission line on the area close up to the target. The collected information is sent to the computer to monitor the oxygen flow rate to maintain the selected optical intensity of about 4.5 % (fully oxidized target) and 100 % (in pure argon) of the Zr emission line as shown in Figure 3.20. The hysteresis loop shown in Figure 3.23 is obtained by supplying a current of 2.5 A/ pulse at 50 kHz to the target, the Ar gas flow rate is 20 sccm. Starting from a pure argon atmosphere, the deposition mode is changed from metal mode to oxide mode as gradually increasing the O_2 flow rate up to 9.7 sccm. This oxide deposition mode will switch to metal deposition mode as the O_2 flow is reduced to 5 sccm. The region where the O_2 flow rate is from 5 sccm to 10 sccm is called the unstable deposition region. Performing deposition in this region can both ensure a high deposition rate and obtain the required 8YSZ oxide. Deposition in this area is well achieved with a PEM system. But in unstable region, the deposition rate, the morphology, and oxygen stoichiometry of the coatings deposited at various Setpoints

are different. As shown in Fig. 3.21, the deposition rate of the electrolyte increases approximately linearly with the Setpoint increasing from 20 to 50 %. The deposition rate in nm/min is determined by dividing the thickness of the deposited electrolyte by the deposition time.

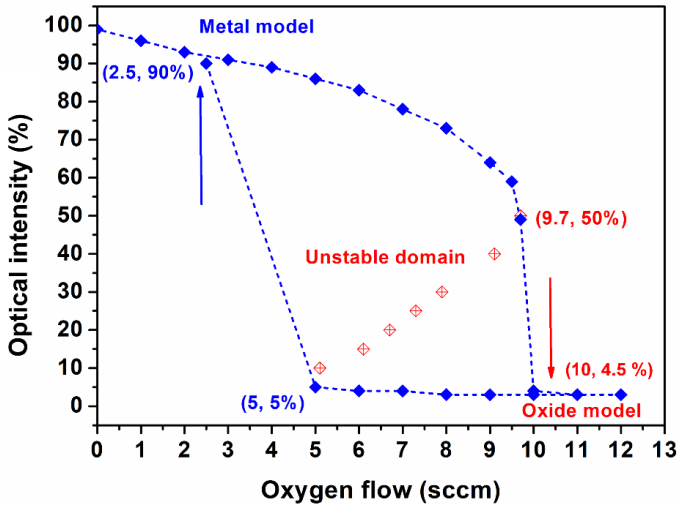

Figure 3.20: The evolution of the emission optical intensity of the $Zr_{0.84}Y_{0.16}$ target with the introduction of oxygen flow at an argon flow rate of 20 sccm (total pressure of 0.19-0.21 Pa); DC pulse generator conditions supplying on the $Zr_{0.84}Y_{0.16}$ target (current of 2.5A, frequency of 50 kHz, T_{off} of 4µs; 25W Bias applied to the substrate)

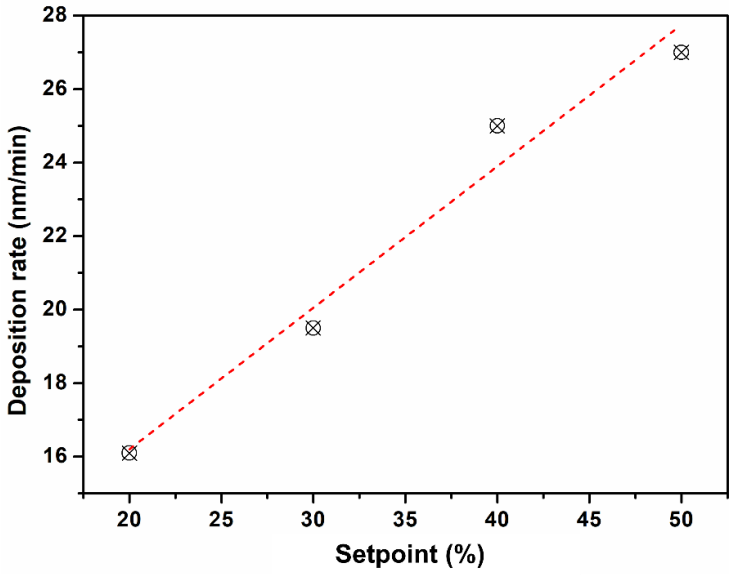

Figure 3.21: Sputtering rate of 8YSZ coatings deposited on glass substrate with different emission optical Setpoints (DC pulse generator conditions supplying on the $Zr_{0.84}Y_{0.16}$ target, current of 2.5A, frequency of 50 kHz, T_{off} of 4µs; 25W bias applied to the substrate)

The morphology of the 8YSZ coatings deposited on the silicon wafer showed obvious changes with the increase of the Setpoint. As shown in Figure 3.22, the 8YSZ

coatings deposited under the Setpoints of 20 and 30% present an obvious columnar growth. Morphology becomes nearly smooth as the Setpoint increases to 40 and 50%. The 8YSZ coatings deposited on the glass slide is characterized by XRD and spectrophotometer. As shown in Figure 3.23, the 8YSZ coatings deposited at the Setpoint of 20 and 30% have higher transmittance, which means higher oxygen stoichiometry and good crystallinity [7]. The XRD spectrum in Figure 3.24 shows that the 8YSZ coatings deposited at the Setpoint of 20 and 30% are well crystallized. Although 8YSZ deposited at the Setpoint of 20% has slightly higher transmittance compared to 30%, the deposition rate is higher at Setpoint of 30% than at Setpoint of 20%. The 8YSZ coatings deposited at the Setpoint of 40 and 50% appear to nanocrystalline and/or bad crystalline. At this time, the transmittance of 8YSZ coatings is very low (Figure 3.23), which may be related to the nanocrystalline and/or bad crystalline in the coating.

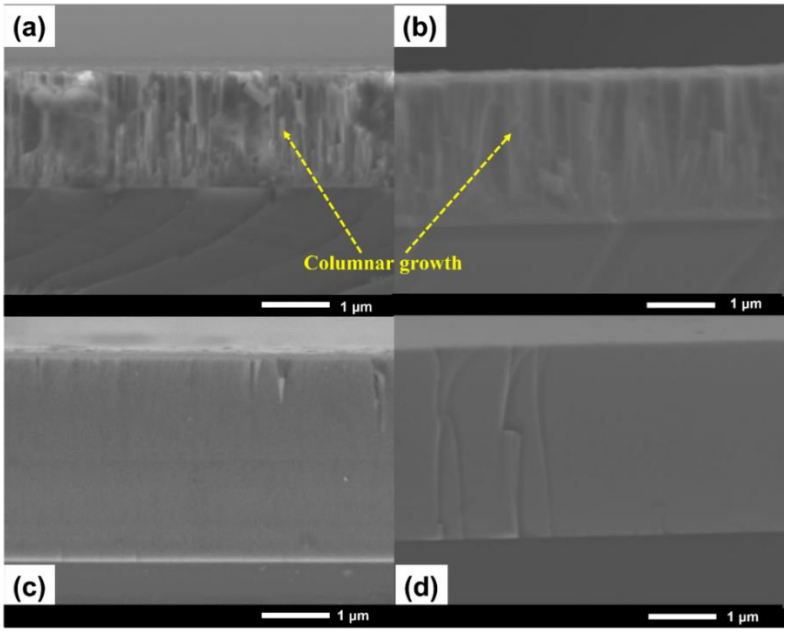

Figure 3.22: SEM images of 8YSZ coatings deposited on silicon substrate with different optical emission Setpoints (DC pulse generator conditions supplying on the $Zr_{0.84}Y_{0.16}$ target: current of 2.5A, frequency of 50 kHz, T_{off} of 4μs): (a) Setpoint 20% (average voltage of 304V, average total pressure of 0.19Pa), (b) Setpoint 30% (average voltage of 311V, average total pressure of 0.19Pa), (c) Setpoint 40% (average voltage of 319V, average total pressure of 0.20Pa), (d) Setpoint 50% (average voltage of 326V, average total pressure of 0.21Pa); 25W bias applied to the substrate

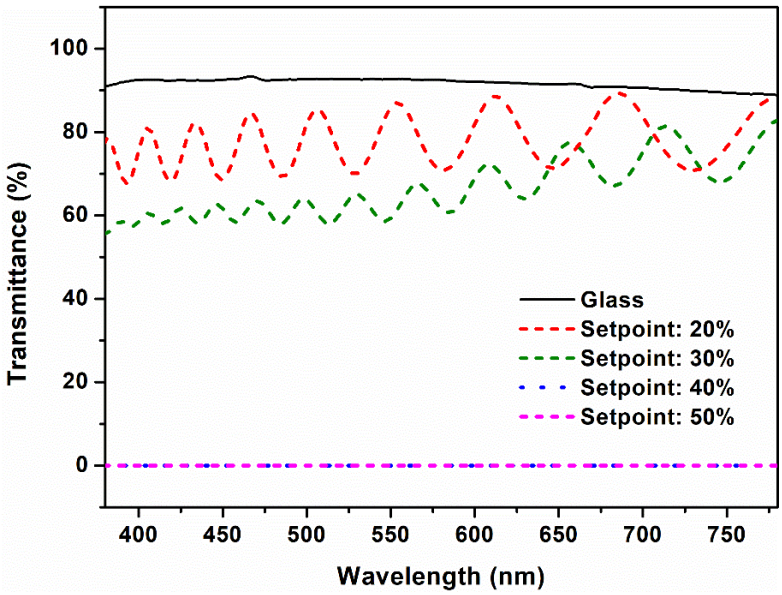

Figure 3.23: Evolution of the transmittance of the 8YSZ coatings deposited on glass substrate with different optical emission Setpoints (DC pulse generator conditions supplying on the $Zr_{0.84}Y_{0.16}$ target: current of 2.5A, frequency of 50 kHz, T_{off} of 4µs): Setpoint 20% (average voltage of 304V, average total pressure of 0.19Pa), Setpoint 30% (average voltage of 311V, average total pressure of 0.19Pa), Setpoint 40% (average voltage of 319V, average total pressure of 0.20Pa), Setpoint 50% (average voltage of 326V, average total pressure of 0.21Pa); In all experiment a 25W bias applied to the substrate

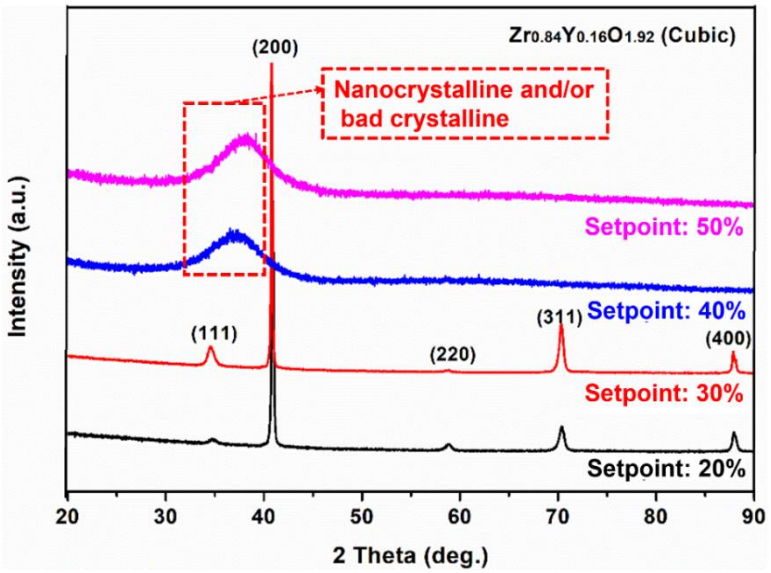

Figure 3.24: XRD patterns of the 8YSZ coatings deposited on glass substrate with different optical emission Setpoints (DC pulse generator conditions supplying on the $Zr_{0.84}Y_{0.16}$ target: current of 2.5A, frequency of 50 kHz, T_{off} of 4µs): Setpoint 20% (average voltage of 304V, average total pressure of 0.19Pa), Setpoint 30% (average voltage of 311V, average total pressure of 0.19Pa), Setpoint 40% (average voltage of 319V, average total pressure of 0.20Pa), Setpoint 50% (average voltage of 326V, average total pressure of 0.21Pa); In all experiment a 25W bias applied to the substrate

To select a suitable Setpoint to realize the deposition of 8YSZ electrolyte, the morphology of 8YSZ coatings deposited on the polished NiO-YSZ anode layer at the Setpoint of 30 and 40% is further compared. In order to check the high temperature tolerance of the 8YSZ coating, the 8YSZ electrolytes deposited on NiO-YSZ surface are performed annealing treatment at 1000°C for 2h. From Fig. 3.25 (a) and (e), the surfaces of the deposited 8YSZ coating at the Setpoint of 30 and 40% are smooth, but there are some pits caused by the NiO-YSZ anode layer. Figure 3.25 (b) and (f) show that some microcracks appeared on the surface of the 8YSZ coating deposited at the Setpoint of 40% after annealing treatment, while such microcracks are not observed in the 8YSZ coating deposited at 30%. From Fig. 3.25 (c)-(h), the 8 YSZ coating is shrunk after annealing treatment, which is consistent with the results of J. FONDARD [6]. The columnar morphology of the deposited 8YSZ coating at the Setpoint of 30% did not change significantly after annealing treatment. However, the cross-section of the deposited 8YSZ coating at the Setpoint of 40% exhibited lateral cracks and delamination after annealing treatment which is detrimental to ion conduction.

Synthetically, performing deposition at the Setpoint of 30% has a higher deposition rate compared to 20%. Although the deposition rate at 30% is lower than that at the Setpoint of 40%, the 8YSZ coating deposited at 30% has better high temperature tolerance. In fact, the 8YSZ coating deposited at the Setpoint of 40% contains less oxygen than that made at 30%. The 8YSZ coating at 40% is less tolerant with respect to temperature because too much under-stoichiometric can generate stresses during the annealing treatment, which leads to tearing of the coating. Therefore, it is optimal to perform the deposition of 8YSZ electrolyte at the Setpoint of 30% in comparison. Figure 3.25 (i) and (j) are the polished cross-sections of the 8YSZ electrolyte with a thickness of about 6.7 μm deposited on polished NiO-YSZ anode obtained after deposition for 343 min at the Setpoint of 30%. The Figure 3.25 (j) shows that the 8YSZ electrolyte covers the polished NiO-YSZ anode well, even in some areas where surface cracks exist on the NiO-YSZ anode.

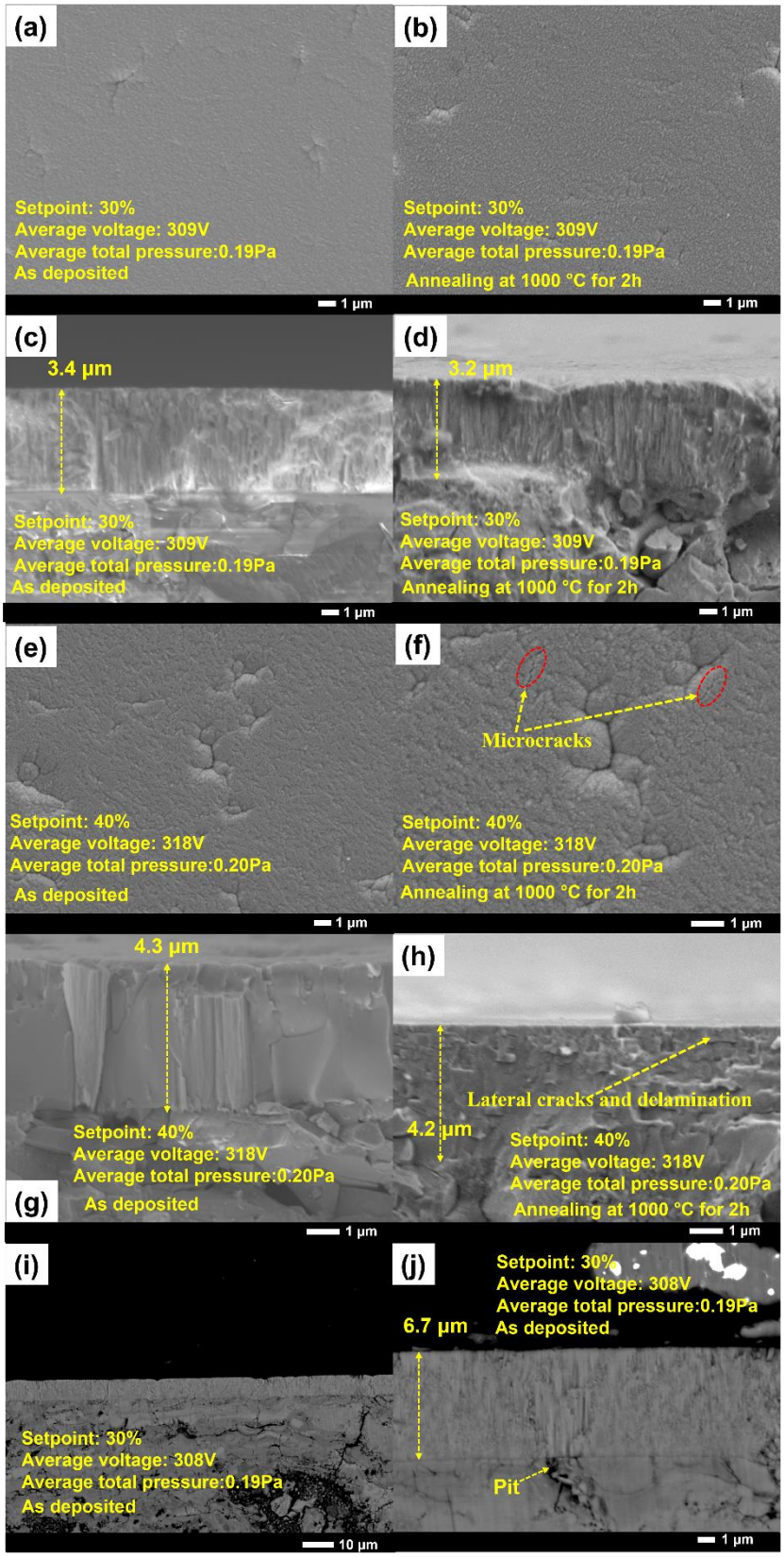

Figure 3.25: SEM images of the 8YSZ coatings deposited on polished NiO-YSZ anode with different optical emission Setpoints under the bias power of 25W: (a), (b), (e) and (f) refer to the surface; (c), (d), (g) and (h) refer to cross-section; (i) and (j) refer to the cross-section of polished 8YSZ with the thickness of 6.7 µm

3.4.2 Deposition of GDC10 as electrolyte layer and buffer layer

The deposition process of the GDC10 coatings by using $Ce_{0.90}Gd_{0.10}$ alloy target is monitored based on the measurement of the emission optical intensity of the 486 nm Ce emission line on the area close up to the target. The collected information is sent to the computer to control the oxygen flow rate to maintain the selected emission optical intensity between about 7% (fully oxidised target) and 100% (in pure argon) of the Ce emission line as shown in Figure 3.26. For the deposition process of GDC10 under the control of the PEM system, the unstable region is from the O_2 flow rate of 2 to 8 sccm. The deposition rate, morphology, structure, and transmittance of the GDC10 coating deposited in the unstable region controlled by the PEM system are investigated. Figure 3.27 shows that the deposition rate of GDC10 coating increases with the Setpoint. From Figure 3.28, the GDC10 coatings deposit at the investigated Setpoint range of 20-50% all exhibit columnar morphology. Figure 3.29 shows that the transmittance of the GDC10 coatings deposit on the glass slide decreases with the increase of the Setpoint used, which means that the oxygen stoichiometry is reduced. The transmittances of the GDC10 electrolyte deposit at the Setpoint of 20 and 30% are significantly higher than that at 40 and 50%. The XRD results of GDC10 coatings coating on a glass slide as shown in Figure 3.30 manifest that the deposited coatings have achieved a cubic structure. The FWHMs at the (111) plane of the GDC10 coatings are obtained from the XRD spectrum and the average grain size are calculated as shown in Table 3.9. The FWHM at the (111) plane of the GDC10 coating increases from 0.350 to 1.036 rad with the Setpoint from 20 to 50%. Correspondingly, the average grain size of the electrolyte decreases from 28.7 to 9.3 nm. This may be attributed to the presence of nanocrystalline grains and/or bad crystalline within the GDC10 coating. Larger grain size may be beneficial for oxygen ion conduction. Compared to deposition at the Setpoint of 20%, faster deposition can be achieved at 30%. Here, the deposition of the GDC10 electrolyte is performed at the Setpoint of 30%.

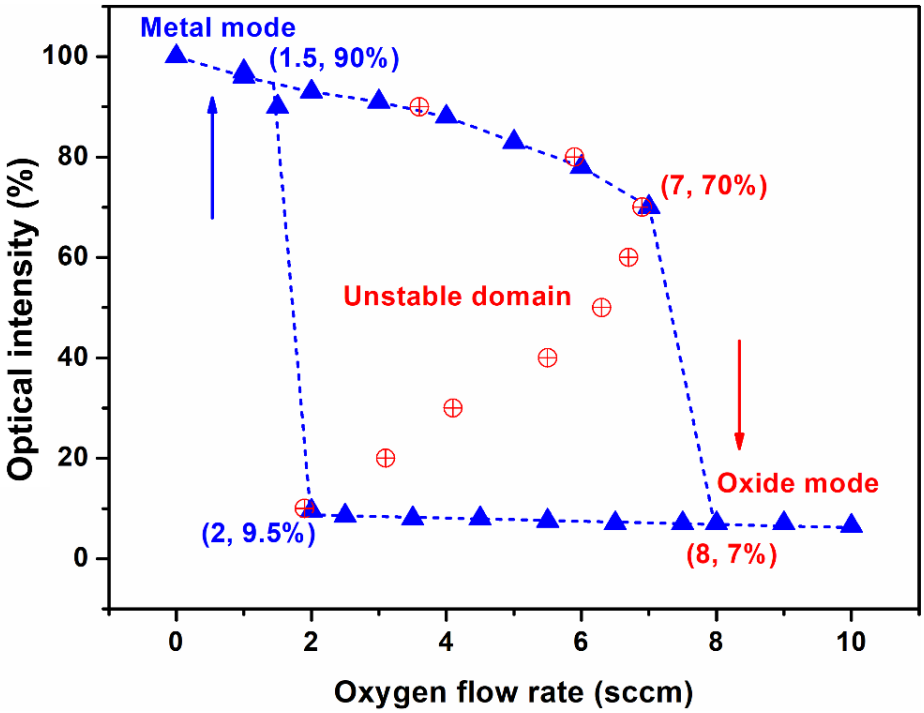

Figure 3.26: The evolution of the emission optical intensity of the $Ce_{0.90}Gd_{0.10}$ target with the introduction of oxygen flow at an argon flow rate of 20 sccm (total pressure of 0.18-0.20 Pa); DC pulse generator conditions supplying on the $Ce_{0.9}Gd_{0.1}$ target: current of 2.5A, frequency of 50 kHz, T_{off} of 4µs; 75W bias applied to the substrate

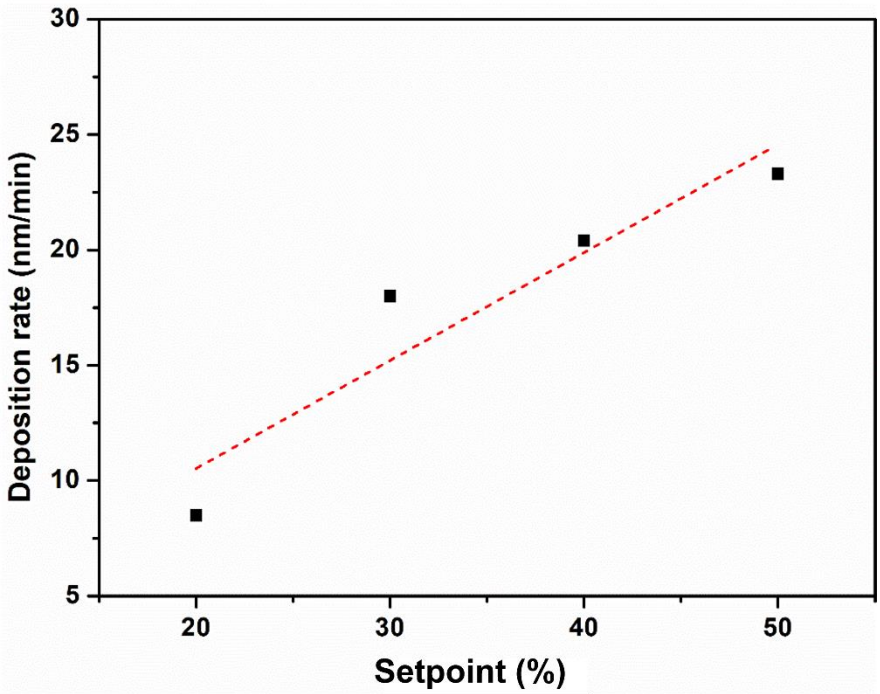

Figure 3.27: Sputtering rate of GDC10 coatings deposited on glass substrate with different optical emission Setpoints; DC pulse generator conditions supplying on the $Ce_{0.90}Gd_{0.10}$ target: current of 2.5A, frequency of 50 kHz, T_{off} of 4µs; 75W bias applied to the substrate

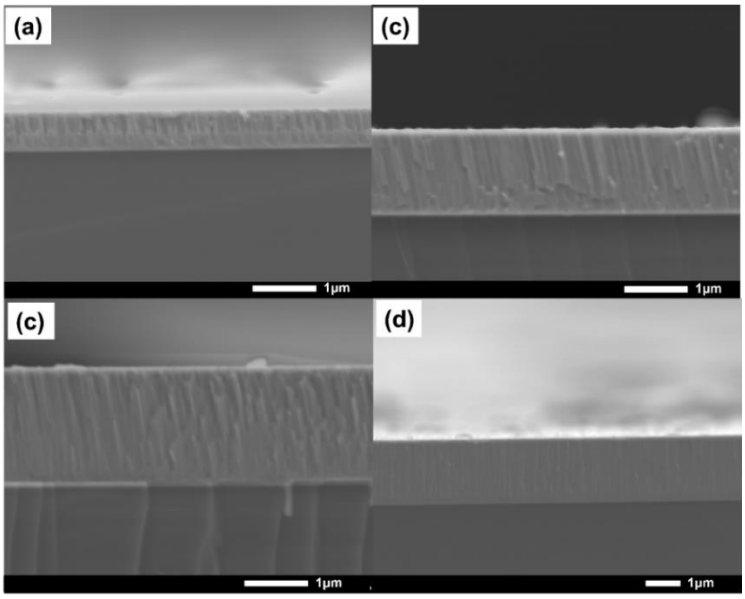

Figure 3.28: SEM images of GDC10 coatings deposited on silicon with different optical emission Setpoints (DC pulse generator conditions supplying on the $Ce_{0.90}Gd_{0.10}$ target: current of 2.5A, frequency of 50 kHz, T_{off} of 4µs): (a) Setpoint 20% (average voltage of 196V, average total pressure of 0.18Pa); (b) Setpoint 30% (average voltage of 229V, average total pressure of 0.19Pa); (c) Setpoint 40% (average voltage of 252V, average total pressure of 0.20Pa); (d) Setpoint 50% (average voltage of 267V, average total pressure of 0.20Pa); In all case a 75W bias applied to the substrate

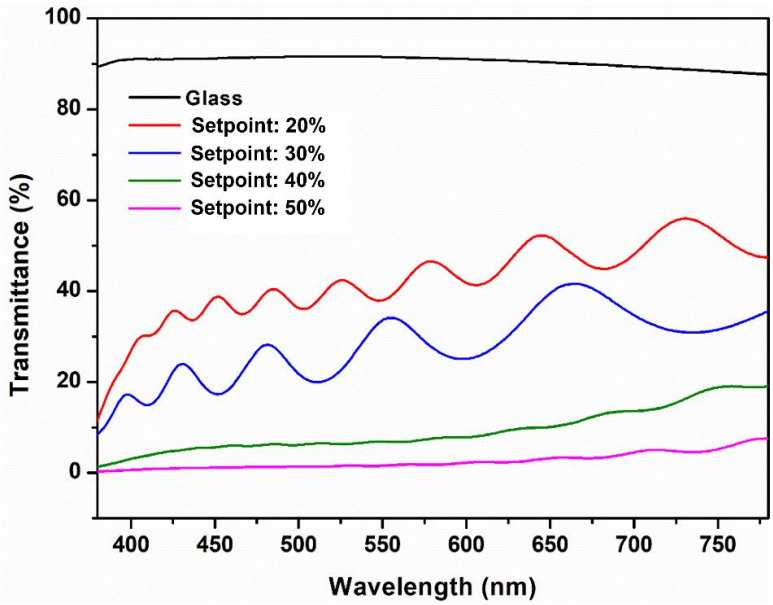

Figure 3.29: transmittance evolution of GDC10 coatings deposited on glass substrate with different optical emission Setpoints (DC pulse generator conditions supplying on the $Ce_{0.90}Gd_{0.10}$ target: current of 2.5A, frequency of 50 kHz, T_{off} of 4µs): Setpoint 20% (average voltage of 196V, average total pressure of 0.18Pa); Setpoint 30% (average voltage of 229V, average total pressure of 0.19Pa); Setpoint 40% (average voltage of 252V, average total pressure of 0.20Pa); Setpoint 50% (average voltage of 267V, average total pressure of 0.20Pa); In all case a 75W bias applied to the substrate

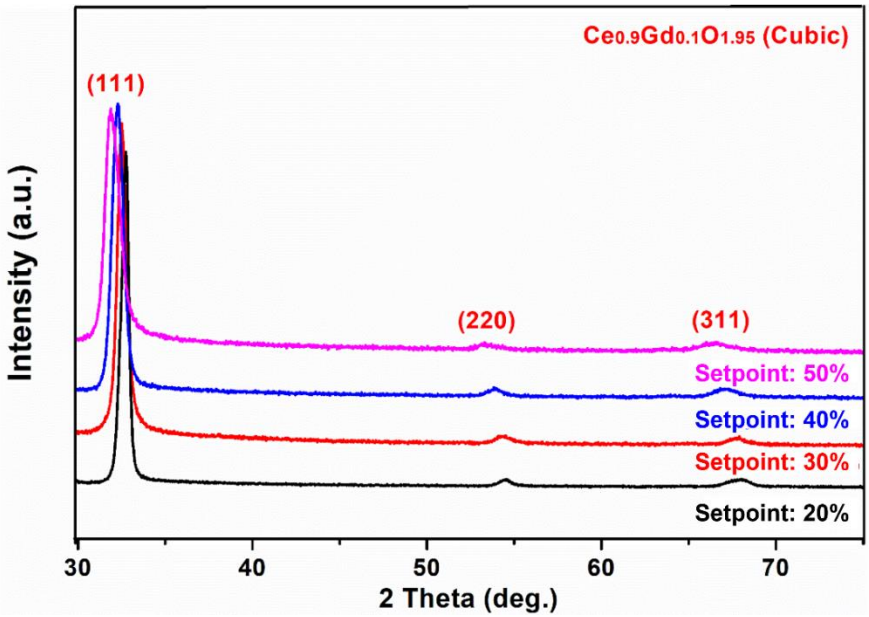

Figure 3.30: XRD of GDC10 coatings deposited on glass substrate with different optical emission Setpoints (DC pulse generator conditions supplying on the $Ce_{0.90}Gd_{0.10}$ target: current of 2.5A, frequency of 50 kHz, T_{off} of 4µs): Setpoint 20% (average voltage of 196V, average total pressure of 0.18Pa); Setpoint 30% (average voltage of 229V, average total pressure of 0.19Pa); Setpoint 40% (average voltage of 252V, average total pressure of 0.20Pa); Setpoint 50% (average voltage of 267V, average total pressure of 0.20Pa); In all experiment a 75W bias applied to the substrate

Table 3.8: Full width at half maximum (FWHM) of the (111) plane and grain size obtained from XRD pattern of GDC10 deposited with different optical emission Setpoints

Setpoint	20%	30%	40%	50%
FWHM (rad)	0.350	0.495	0.745	1.036
Crystallite (Å)	287	198	130	93

3.4.2.1 Deposition of GDC10 as electrolyte layer

The deposition process takes 228 min to obtain a GDC10 electrolyte layer with a thickness of about 4.1µm on 8YSZ electrolyte surface. A "half-cell" with the ITM/GDC10/NiO-YSZ/8YSZ/GDC10 configuration is thus obtained before depositing the cathode layer in the next step. Such "half-cells" are annealed at 500°C for 2 h to remove possible stresses in the electrolyte. Figure 3.31 shows the cross-section and surface morphology of the annealed "half-cell". From Figures 3.31 (a), (b), (g), and (h) show a good adhesion between GDC10 and 8YSZ layers. This is beneficial for the ion conduction of the electrolyte. However, the adhesion between 8YSZ electrolyte and NiO-YSZ seem weaker in comparison. It is obvious that the 8YSZ/GDC10 electrolyte layer and the NiO-YSZ anode layer in the cross-section are not in the same plane after

being broken artificially for SEM observing as shown in Figure 3.31 (a). Figure 3.31 (d) shows that the surface of GDC10 deposited on 8YSZ has no microcracks in a larger field of view. There are some pits which may be affected by the NiO-YSZ anode surface. From 3.31 (c), partial magnification of the surface shows granular growth derived from columnar growth. Further, the cross-section of the polished half-cell is shown in Figures 3.31(e)-(f). The 8YSZ/GDC10 bilayer electrolyte in most areas of the half-cell is intact as shown in Fig. 3.31(f). However, microcracks appeared in 8YSZ layer at local areas, especially where there are pits on the NiO-YSZ anode surface, as shown in Figure 3.31(g). Microcracks also appear in GDC10 when the pits on the NiO-YSZ anode surface are larger as shown in Figure 3.31(h). The EDS mapping of Figure 3.32 confirms that the layers in the "half-cell" are in the correct position. Figure 3.33 presents the XRD patterns of different layers indicating that the correct coatings are deposited at each layer.

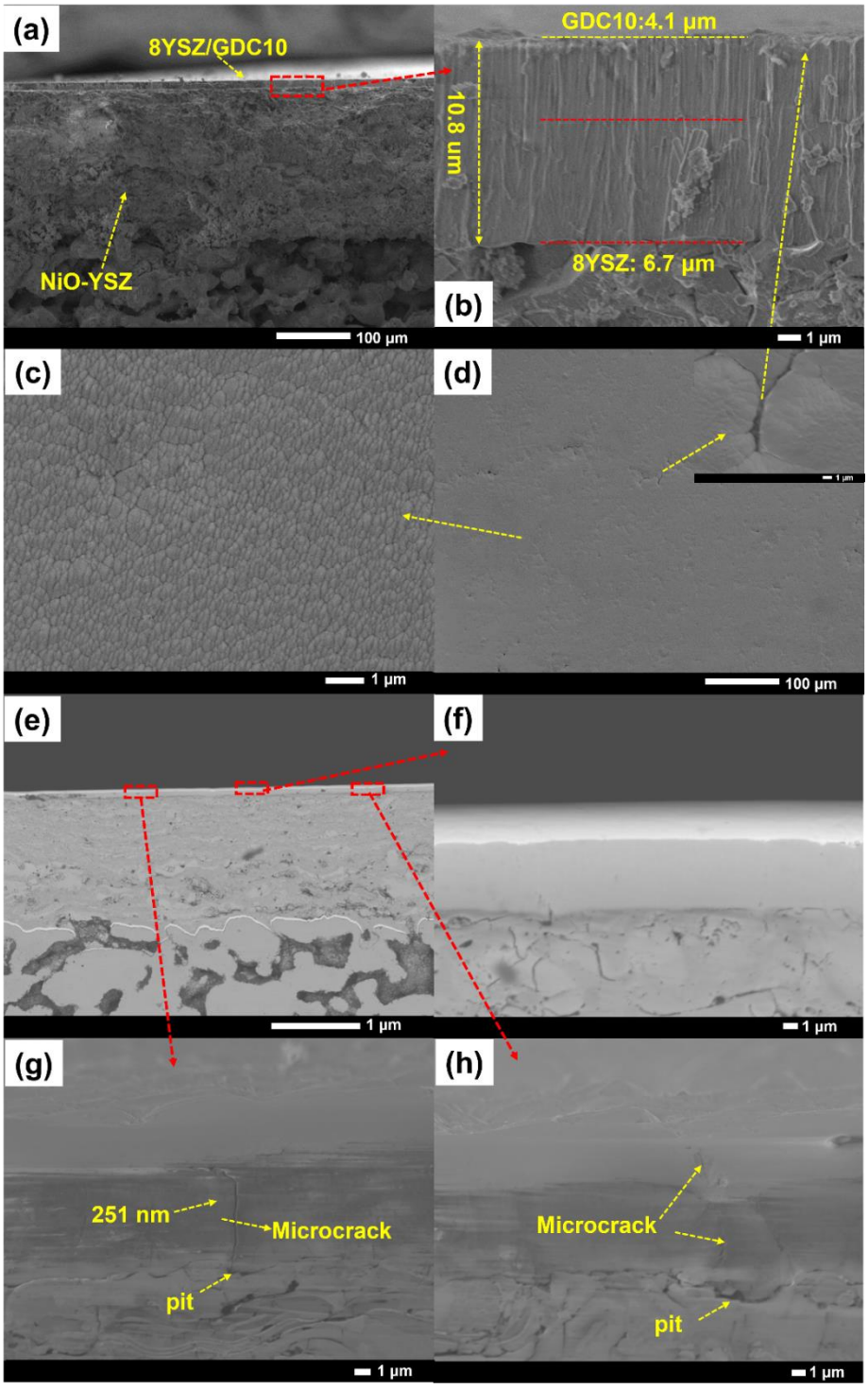

Figure 3.31: SEM images of GDC10 deposited on ITM/GDC10/NiO-YSZ/8YSZ after annealing at 500°C for 2h (DC pulse generator conditions supplying on the $Ce_{0.90}Gd_{0.10}$ target: current of 2.5A, frequency of 50 kHz, T_{off} of 4µs; Setpoint 30%, average voltage of 222V, average total pressure of 0.20Pa): (a) cross section of the global field of view; (b) the cross-section of bilayer electrolyte 8YSZ/GDC10 deposited on NiO-YSZ anode layer; (c) & (d) the surface of GDC10 deposited on 8YSZ layer; (e), (f), (g), and (h) are the polished cross-section of GDC10 deposited on 8YSZ layer; 75W bias applied to the substrate

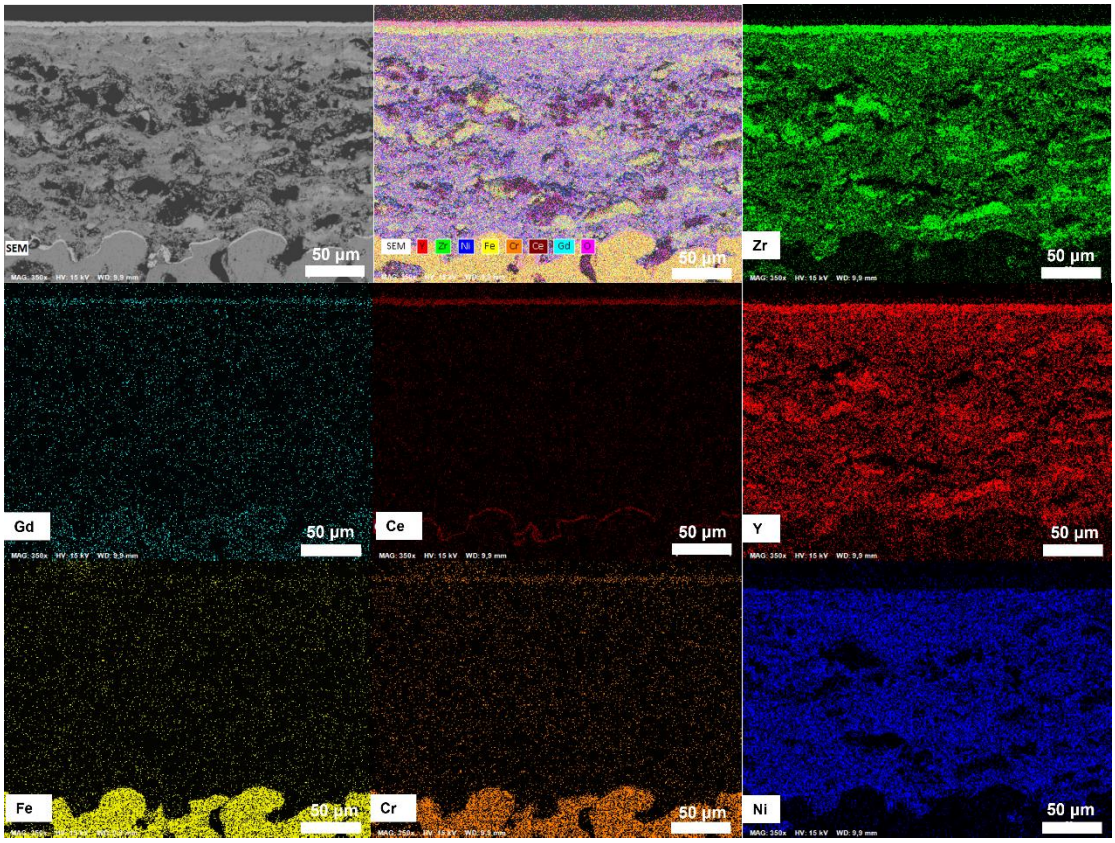

Figure 3.32: SEM-EDS mapping of the cross-section of ITM/GDC10/NiO-YSZ/8YSZ/GDC10

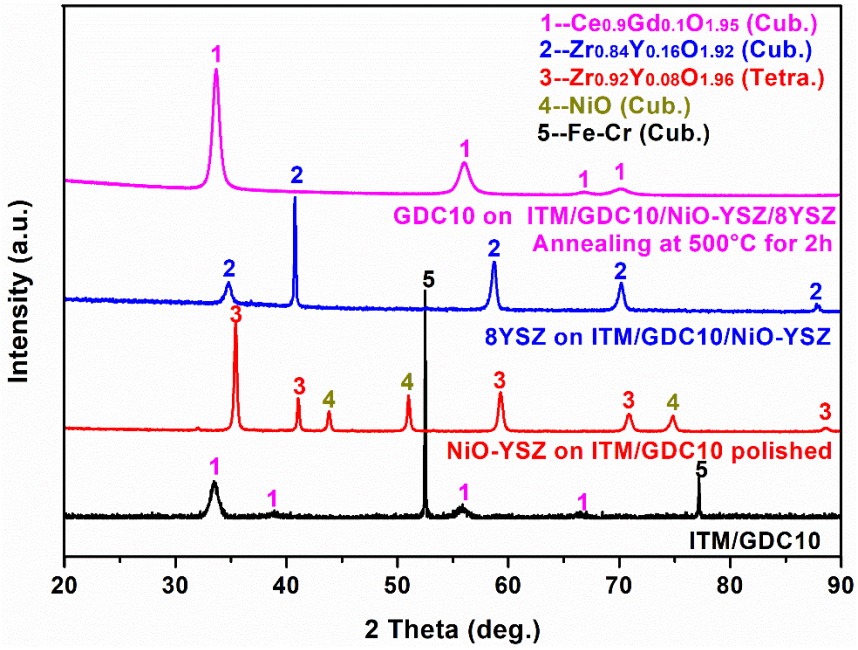

Figure 3.33: XRD after deposition of different layers of the half-cell

3.4.2.2 Deposition of GDC10 as buffer layer between the ITM and NiO-YSZ anode

Using ITM with higher Cr content as a support inevitably encounters Cr diffusion not only during the fabrication process (such as annealing) of MS-SOFC but also during

operation. Besides, Ni in the Ni-YSZ anode will also diffuse into the ITM, which leads to the transformation of ferrite to austenite. After this transformation, the high temperature oxidation resistance of the ITM is reduced, while the CET is greatly increased. Therefore, it is necessary to deposit a buffer layer between the ITM and the Ni-YSZ anode layer to prevent the interdiffusion of Cr and Ni. At present, the research interest on the diffusion barrier layer mainly focuses on $(Co, Mn)_3O_4$ spinel type [10, 11], $LaCrO_3$ perovskite type [12], and doped or undoped CeO_2 [13, 14] materials. Among them, GDC is considered to be a good option because it has a CTE matching that of the ITM and Ni-YSZ anode, and also has electronic conductivity under reducing atmosphere [14]. The GDC does not react chemically with the components of the anode and the metal support. In this thesis, GDC10 is selected as the barrier layer deposited by RMS.

According to the section 3.2, the surface of the ITM is highly roughened. For such ITM surface, there are some areas on the surface that cannot be reached by directional deposition method such as sputtering. If a very thick layer of GDC10 (>25 μm), according to the Rz of the ITM surface is 24.57 μm, is continuously deposited as, it can completely cover the surface of the ITM as shown in Figure 3.34 (c). The advantage of GDC10 completely covering the ITM surface is that it can prevent Cr from entering the NiO-YSZ anode either through evaporation or diffusion. However, too thick buffer layer will lead to greater interfacial resistance and affect the anode reaction. Depositing a thin layer of GDC10 as show in Figure 3.34 (b) can prevent the diffusion between Fe, Cr, and Ni.

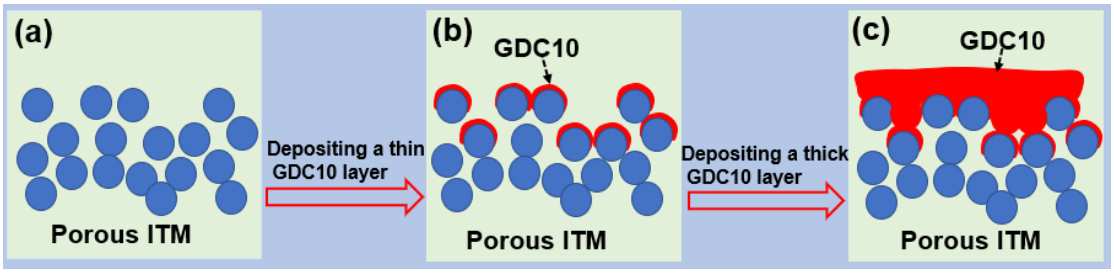

Figure 3.34: Schematic of the deposition of the GDC10 buffer layer via RMS

After referring to the work of J. FONDARD [6], a thin GDC10 buffer layer with a thickness of about 2.2 μm is deposited on the ITM surface by RMS under the control

of the PEM system in this thesis. It takes 123 min to deposit the GDC10 buffer layer using the same parameters as for the GDC10 electrolyte. Figure 3.35 shows the morphology of ITM covered with GDC10 buffer layer. Figure 3.35 (a) and (b) show that the GDC10 buffer layer covers the flat areas and peaks of the ITM surface well. From Figures 3.35(c)-(d), the coverage of GDC10 coating is not ideal in those deep and narrow valleys, because the sputtered particles cannot reach those areas. These results are consistent with expectations for the case of depositing a thin layer of GDC10 as a layer. In addition, Figure 3.35 (e) also shows that the GDC10 buffer layer is well adhere to the ITM surface.

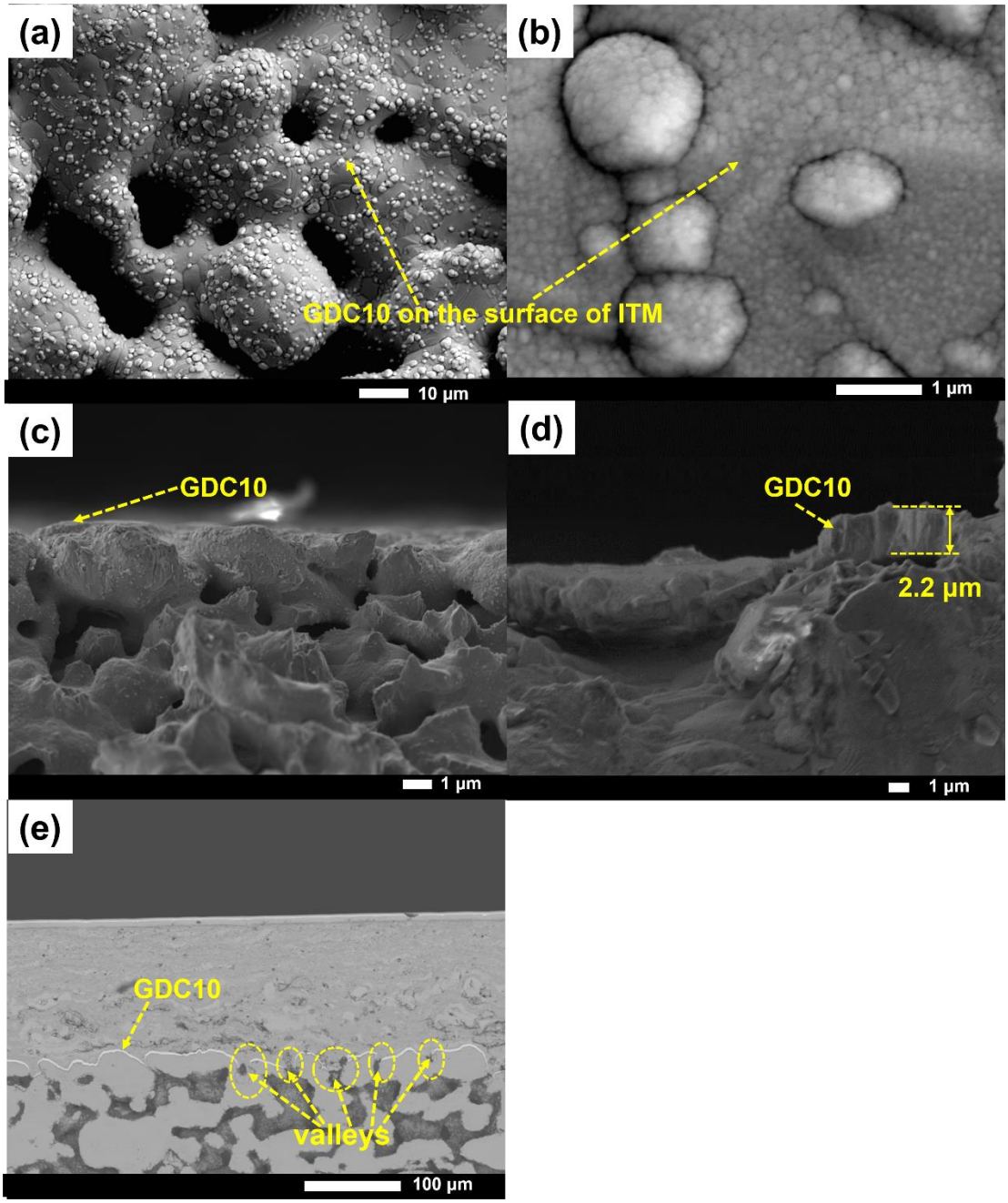

Figure 3.35: SEM observation of morphology of GDC10 layer deposited by RMS on ITM substrate (DC pulse generator conditions supplying on the $Ce_{0.90}Gd_{0.10}$ target: current of 2.5A, frequency of 50 kHz, T_{off} of 4µs; Setpoint 30%, average voltage of 223V; average total pressure of 0.20Pa): (a) & (b) surface, (c) & (d) cross-section, (e) polished cross-section

To examine the effect of the GDC10 buffer layer on preventing the interdiffusion of Cr and Ni, a long-term annealing experiment is performed. Specifically, the ITM/GDC10/NiO-YSZ sample is placed in a furnace operating under air atmosphere at intermediate temperature (750°C) for 72 h. After annealing treatment, the cross-section of the sample is polished, and then the diffusion of Fe, Cr, Ni, Zr, and Y at the

interface is tracked through SEM-EDS. As a comparison, the sample that did not undergo long-term annealing treatment are also observed. From the observations shown in Fig. 3.36, no obvious diffusion of Fe, Zr, and Y are observed. This indicates that Fe, Zr, and Y are stable in their respective positions even exposed to air for a long time (72 h) at 750°C. After annealing treatment, Ni diffused towards the interface. However, no trace of Ni is found in the ITM bulk. Compared with Ni, the enrichment of Cr on the interface is more obvious, and it has crossed the interface (Figure 3.36b). This may be attributed to the faster diffusion rate of Cr. From Figure 3.36 (b), although Cr is enriched at the interface, it does not cross the GDC10 buffer layer to enter the NiO-YSZ anode bulk. This indicate that the GDC10 buffer layer can effectively prevent the interdiffusion between Cr and Ni. In addition, Figure 3.37 shows that some valley regions on the ITM surface are also covered by GDC10 buffer layer to prevent the interdiffusion of Cr and Ni.

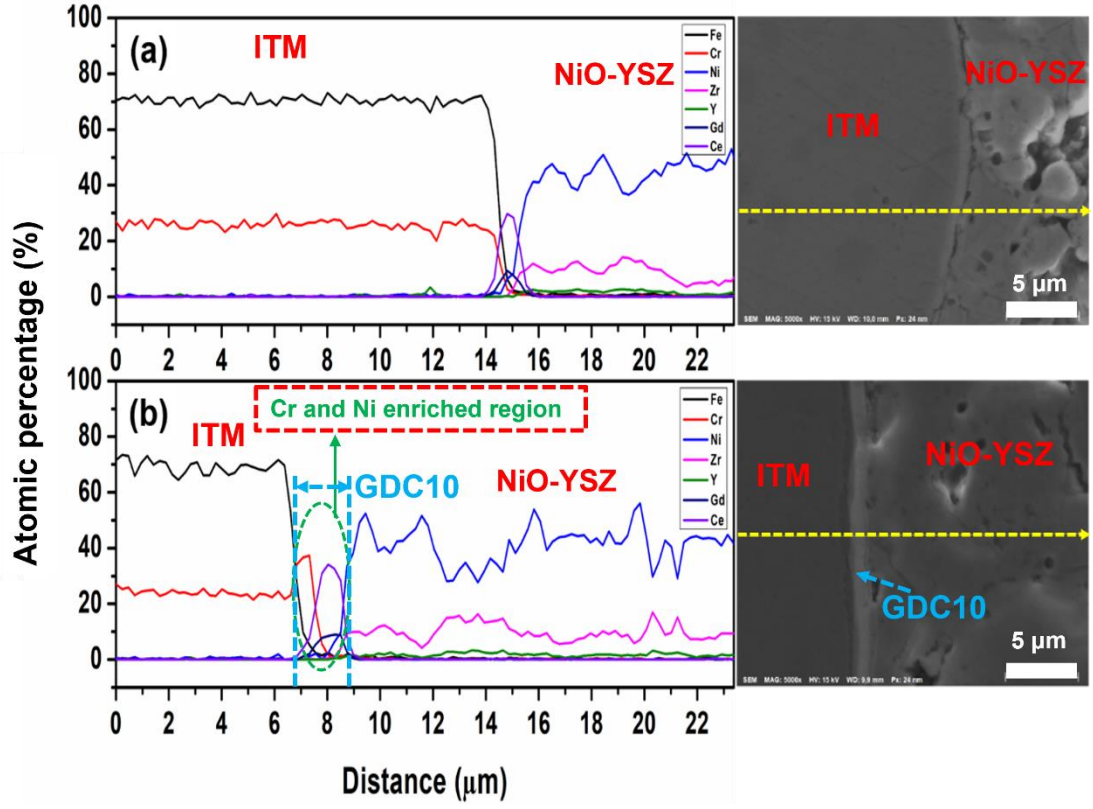

Figure 3.36: SEM observation and EDS profile of NiO-YSZ anode layer deposited by APS on ITM substrate with GDC10 buffer layer realized by RMS: (a) before annealing, (b) after annealing at 750°C for 72h under static air

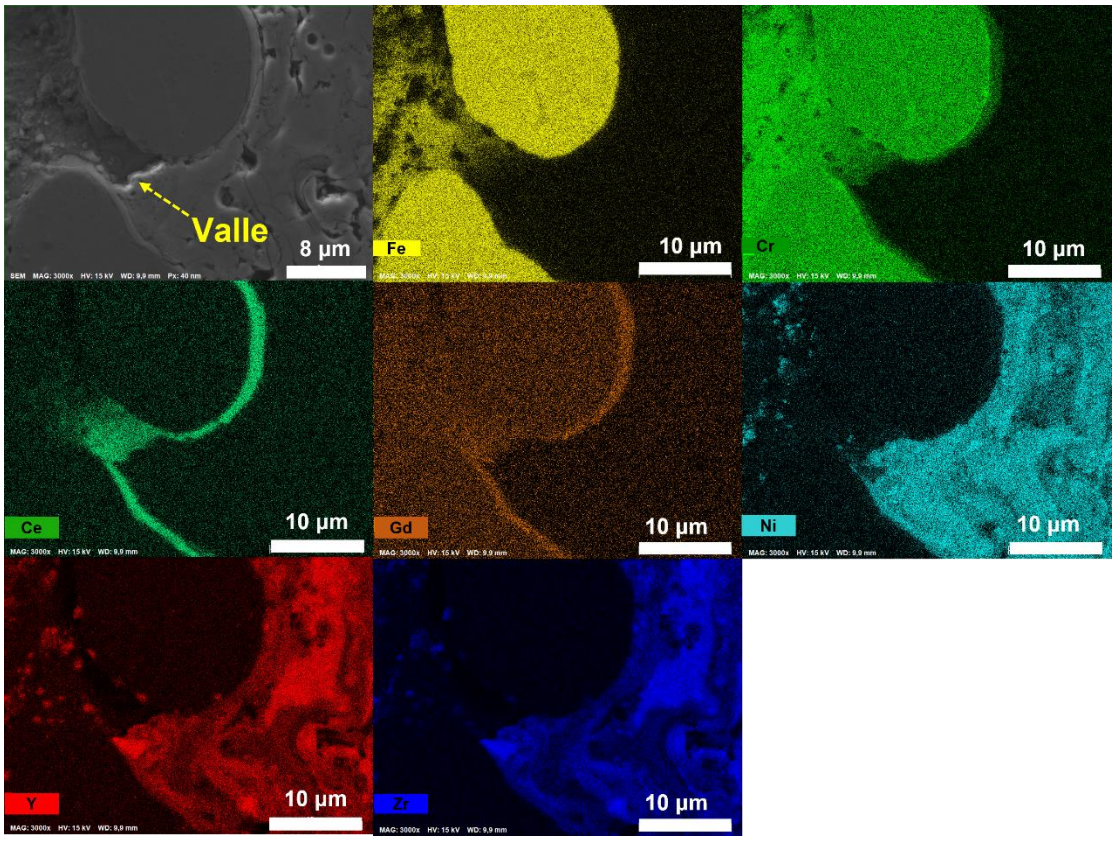

Figure 3.37: EDS mapping of cross-section of the NiO-YSZ deposited on ITM with GDC10 buffer layer after annealing treatment at 750°C for 72h under static air

3.5 Conclusion

In this chapter, a "half-cell" with ITM/GDC10/NiO-YSZ/8YSZ/GDC10 configuration is successfully fabricated by APS and RMS for the fabrication of a complete single cell. In this configuration, the GDC10 layer with the thickness of about 2.2 µm located between the ITM and the NiO-YSZ anode acts as a buffer layer to prevent the interdiffusion between Ni and Cr. The deposited NiO-YSZ anode with porosity gradient consists of upper (low porosity) and lower (high porosity) layers. 8YSZ/GDC10 with the thickness of about 10.8 µm acts as the bilayer electrolyte of MS-SOFC, while GDC10 also acts as a buffer layer to prevent possible cathode diffusion into the 8YSZ electrolyte. After investigation, the following conclusions are drawn:

(a) Annealing treatment experiments of ITM alloy in air revealed its high temperature tolerance. This alloy can withstand annealing treatment at 500°C for 120min without damage, but the surface is slightly oxidized at 900°C for

120 min. Such oxidation becomes more serious as the temperature increases. The sample is heavily deformed and oxidized after annealing at over 1000°C for 120 min. However, the degree of oxidation is significantly weakened, and no surface curvature appeared after annealing at 1000°C for 30 min.

(b) The large particle size of NiO-YSZ powder will lead to large-sized pores in the NiO-YSZ coating deposited by APS, which is beneficial to increase the porosity of the NiO-YSZ coating. The large flow of H_2 leads to the reduction of NiO during the deposition process, which is unfavorable for increasing the porosity of NiO-YSZ coating. Finally, a lower NiO-YSZ anode layer with high porosity of 33.1 ± 0.6 Vol.% (after reduction) and a thickness of about 137.2 μm is deposited on ITM/GDC10. The upper low porosity NiO-YSZ anode layer with a porosity of 17.2 ± 0.4 Vol.% (after reduction) and a thickness of about 70 μm is deposited on the high porosity NiO-YSZ anode layer. Then the upper NiO-YSZ anode layer is polished to flatten the surface in order to accommodate the deposition of the electrolyte layer by RMS, and the thickness is reduced to about 38.6 μm.

(c) The 8YSZ with the thickness of 3.4 μm deposited on the polished NiO-YSZ anode at the optical emission Setpoint of 30% can withstand the annealing treatment at 1000°C for 2h without damage. GDC10 layer with the thickness of about 4.1μm deposited on 8YSZ layer (about 6.7μm) at the optical emission Setpoint of 30% to form the "half-cell" with the configuration of ITM/GDC10/NiO-YSZ/8YSZ/GDC10. Overall, the "half-cell" can remain intact after annealing treatment at 500°C for 2h, but some microcracks appear in local areas. The result of long-term annealing treatment on the ITM/GDC10/NiO-YSZ samples show that GDC10 buffer layer successful prevents the interdiffusion between Cr and Ni.

3.6 References

[1] Tabernig, B., Franco, T., Venskutonis, A., Kestler, H., & Sigl, L. S. (2011). Properties of a P/M FeCr alloy as interconnect material for solid oxide fuel cells.

Proceedings, EURO PM.

[2] Haydn, M., Ortner, K., Franco, T., Menzler, N. H., Venskutonis, A., & Sigl, L. S. (2013). Development of metal supported solid oxide fuel cells based on powder metallurgical manufacturing route. Powder Metallurgy, 56(5), 382-387.

[3] Menzler, N. H., Sebold, D., Sohn, Y. J., & Zischke, S. (2020). Post-test characterization of a solid oxide fuel cell after more than 10 years of stack testing. Journal of Power Sources, 478, 228770.

[4] Song, X., Ding, Y., Zhang, J., Jiang, C., Liu, Z., Lin, C., & Zeng, Y. (2023). Thermophysical and mechanical properties of cubic, tetragonal and monoclinic ZrO_2. Journal of Materials Research and Technology.

[5] Fondard, J., Bertrand, P., Billard, A., Fourcade, S., Batocchi, P., Mauvy, F., & Briois, P. (2017). Manufacturing and testing of a metal supported Ni-YSZ/YSZ/La_2NiO_4 IT-SOFC synthesized by physical surface deposition processes. Solid State Ionics, 310, 10-23.

[6] Fondard, J. (2015) Elaboration et test d'une pile à combustible IT-SOFC à support métallique poreux par l'intermédiaire de techniques de dépôt en voie sèche: projection thermique et pulvérisation cathodique magnétron. (Doctoral dissertation, Université de Technologie de Belfort-Montbeliard).

[7] Briois, P., Gourba, E., Billard, A., Ringuedé, A., & Cassir, M. (2005). Microstructure-Electrical properties relationship of YSZ thin films reactively sputter-deposited at different pressures. Ionics, 11, 301-305.

[8] Coddet, P., Pera, M. C., & Billard, A. (2011). Planar solid oxide fuel cell: Electrolyte deposited by reactive magnetron sputtering and cell test. Fuel Cells, 11(2), 158-164.

[9] Breaz, E., Aubry, E., Billard, A., Coton, N., Coquoz, P., Pappas, A., & Briois, P. (2017). Influence of the Bias Substrate Power on the GDC Buffer Layer. ECS Transactions, 78(1), 807.

[10] Wei, W., Chen, W., Ivey, & D. G. (2009). Oxidation resistance and electrical properties of anodically electrodeposited Mn-Co oxide coatings for solid oxide fuel cell interconnect applications. Journal of Power Sources, 186(2), 428-434.

[11] Jin, Y., Sheng, J., Hao, G., Guo, M., Hao, W., Yang, Z., & Peng, S. (2022). Highly

dense (Mn, Co) 3O4 spinel protective coating derived from Mn-Co metal precursors for SOFC interconnect applications. International Journal of Hydrogen Energy, 47(29), 13960-13968.

[12] Jeong, H., Roehrens, D., & Bram, M. (2020). Facile route for reactive coating of $LaCrO_3$ on high-chromium steels as protective layer for solid oxide fuel cell applications. Materials Letters, 258, 126794.

[13] Brandner, M., Bram, M., Froitzheim, J., Buchkremer, H. P., & Stöver, D. (2008). Electrically conductive diffusion barrier layers for metal-supported SOFC. Solid state ionics, 179(27-32), 1501-1504.

[14] Bischof, C., Nenning, A., Malleier, A., Martetschläger, L., Gladbach, A., Schafbauer, W., & Bram, M. (2019). Microstructure optimization of nickel/gadolinium-doped ceria anodes as key to significantly increasing power density of metal-supported solid oxide fuel cells. International journal of hydrogen energy, 44(59), 31475-31487.

Chapter 4: Composite Pr_2NiO_4@Pr_6O_{11} (PPNO) and Pr_2NiO_4 (PNO) cathode deposited by RMS at high pressure for MS-SOFC

4.1 Introduction

Recently, the rare earth nickelate compounds (Ln_2NiO_4, Ln = La, Pr, Nd) with the Ruddlesden-Popper ($(AO)(ABO_3)_m$, m = 1) structure have attracted interest as IT-SOFC cathodes due to their excellent Mixed Ionic and Electronic Conduction (MIEC) properties [1-5]. These cathode materials with MIEC properties allow the Oxygen Reduction Reaction (ORR) sites extend to the bulk instead of limited to the Triple-Phase Boundary (TPB), reducing electrode polarization. Of note is that Pr_2NiO_4 exhibits the highest oxygen diffusion among related rare earth nickelate compounds at intermediate temperatures, which favors the ORR process [5-6]. Moreover, investigations have shown that the Pr_6O_{11} oxide exhibits promising on ORR at cathode since the significantly accelerated oxygen surface exchange kinetics [7-9]. By consulting the literature, there is no research report on the composite cathode of Pr_6O_{11} and Pr_2NiO_4. Considering the possible synergistic effect of these two phases, the ORR process of the Pr_2NiO_4 cathode can be enhanced by the formation of composite.

In this chapter, it mainly focusses on the deposition of Pr_2NiO_4@Pr_6O_{11} (PPNO) composite and Pr_2NiO_4 (PNO) cathode by RMS. The complete MS-SOFC single cells with the configuration of ITM/GDC10/YSZ-NiO/8YSZ/GDC10/PPNO2 and PNO are fabricated. The performance of the single cell is evaluated by I-V measurement as well as EIS. The long-term performance test of the ITM/GDC10/YSZ-NiO/8YSZ/GDC10/PPNO2 single cell is evaluated.

4.2 The deposition and characterization of PPNO and PNO cathodes by RMS

PPNO and PNO cathode coatings are realized by co-sputtering Pr and Ni targets in an Alcatel SCM650 sputtering chamber equipped with a PEM system. J. FONDARD

et al. [10] investigated the effect of deposition pressure on the morphology evolution of La_2NiO_4 cathode coatings by using this device. They found that deposition under high pressure favored the formation of abundant pores in the coating. In this section, PPNO and PNO cathode coatings are deposited under the control of a PEM system at a high pressure of about 2.0 Pa. The deposition process is performed by adjusting the emission optical intensity (Setpoint) of Pr target with a fixed current supply of 2.5 A/ pulsed at 50 kHz. On this basis, the atomic ratio of Pr/Ni is adjusted by controlling the power apply on the Ni target. As the first part of this work, the deposition process of Pr-Ni-O coatings are investigated to provide a reference for the deposition of PPNO and PNO cathode coatings. Then the morphology, structure, electrical and electrochemical properties of the PPNO and PNO cathode coatings are studied.

4.2.1 The deposition of Pr-Ni-O coatings

Here, the deposition process of the Pr-Ni-O coatings by using Pr and Ni targets are monitored based on the measurement of the emission optical intensity of Pr (422nm) target on the area close up to the target. The collected information is sent to the computer to control the oxygen flow rate to maintain the selected emission optical intensity between about 25% (fully oxidized target) and 100% (in pure argon) as shown in Figure 4.1. Starting from a pure argon atmosphere, the deposition mode is changed from metallic mode to oxide mode as gradually increasing the flow rate of O_2 to 7 sccm. This oxide deposition mode will switch to metal deposition mode as the O_2 flow is reduced to 3.2 sccm. The region where the O_2 flow rate is from 3.2 to 7 sccm is called the unstable deposition region for the Pr-Ni-O coating. The voltage change on the Ni target is also recorded synchronously as the O_2 flow rate at a fixed power of 111W. The hysteresis loop presented by the voltage change on the Ni target with the oxygen flow rate is similar to the relationship between the emission optical intensity of the Pr target and the oxygen flow rate. Their unstable deposition regions basically overlap as shown in Figure 4.1 by these two hysteresis loops.

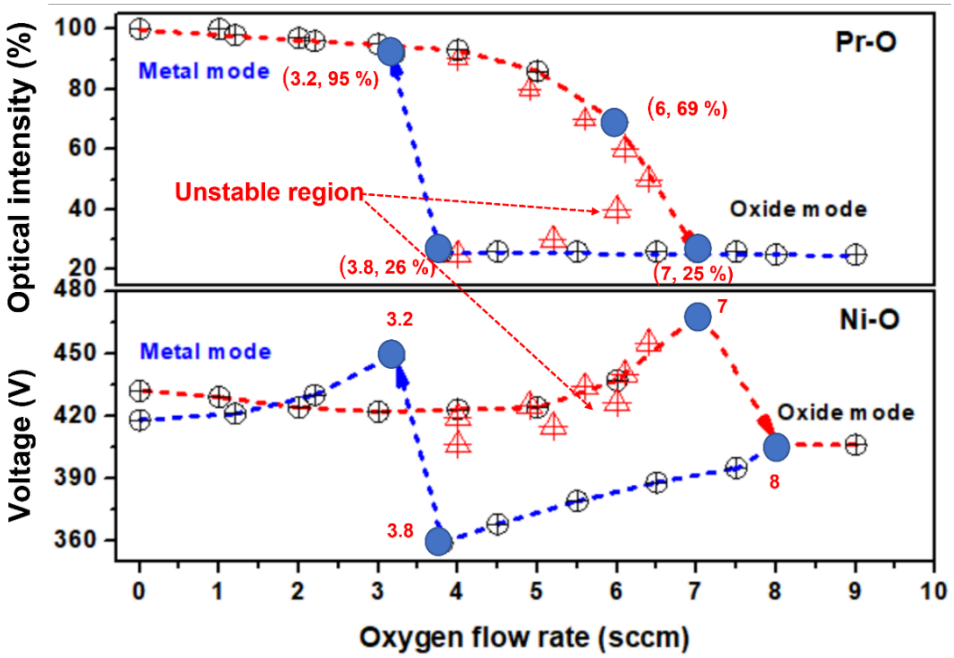

Figure 4.1: The evolution of the emission optical intensity of the Pr (422nm) target and the voltage of Ni target with the introduction of oxygen flow (DC pulse generator conditions supplying on the Pr target: current of 2.5A, frequency of 50 kHz, T_{off} of 4μs; DC pulse generator conditions supplying on the Ni target: power of 111W, frequency of 50 kHz, T_{off} of 4μs; total pressure of 1.97-2.02Pa)

To select a suitable emission optical intensity (Setpoint) on Pr target for depositing Pr-Ni-O coatings, the deposition rate and the structure of the obtained coatings at different Setpoints are investigated. Some basic parameters of depositing Pr-Ni-O coating are listed in Table 4.1 and 4.2. The optical emission Setpoints on Pr target is adjusted to 50, 60, and 70% while the applied power of the Ni target is fixed 111W. From Figure 4.2(a), the deposition rate of the coating increases linearly with the selected Setpoint on Pr target. Besides, from Figure 4.2 (b), the atomic ratio of Pr/Ni increases with the Setpoint on the Pr target, which should be attributed to the increase of the power applied to the Pr target as shown Table 4.2. From the XRD patterns in Figure 4.3, the coatings deposited at the optical emission Setpoint of 50 and 60% on Pr target are PrO_x with nanocrystalline and/or bad crystalline. The coating deposited at the optical emission Setpoint of 70% on Pr target mainly contains cubic Pr_6O_{11} and a small amount of NiO and metal Pr. Although there is a small amount of metal Pr in the coating deposited at the optical emission Setpoint of 70% compared to 50 and 60%, there are obvious advantages in the deposition rate and the crystallinity of the coating.

Table 4.1: The RMS deposition parameters of Pr-Ni-O coatings

Parameters	Pr target	Ni target
Ar flow rate (sccm)	200	
O_2 flow rate (sccm)	3.8-7.0	
Total pressure (Pa)	1.97-2.02	
D_{s-t} (mm)	70	
Frequency (kHz)	50	
T_{off} (μs)	4	
Voltage (V)	203-235	390-479
Current (A)	2.5	0.23-0.35
Power (W)	510-630	111-160
Setpoint (%)	50-70	–

D_{s-t}: Distance between substrate and target

Table 4.2: Sputtering parameters for Pr-Ni-O coatings with different Setpoints

Setpoint	Pr target			Ni target		
(%)	Voltage (V)	Current (A)	Power (W)	Voltage (V)	Current (A)	Power (W)
50	203-205	2.5	510-512	445-451	0.25-0.28	111
60	210-212	2.5	526-530	478-479	0.23	111
70	243-252	2.5	608-630	430-453	0.24-0.26	111

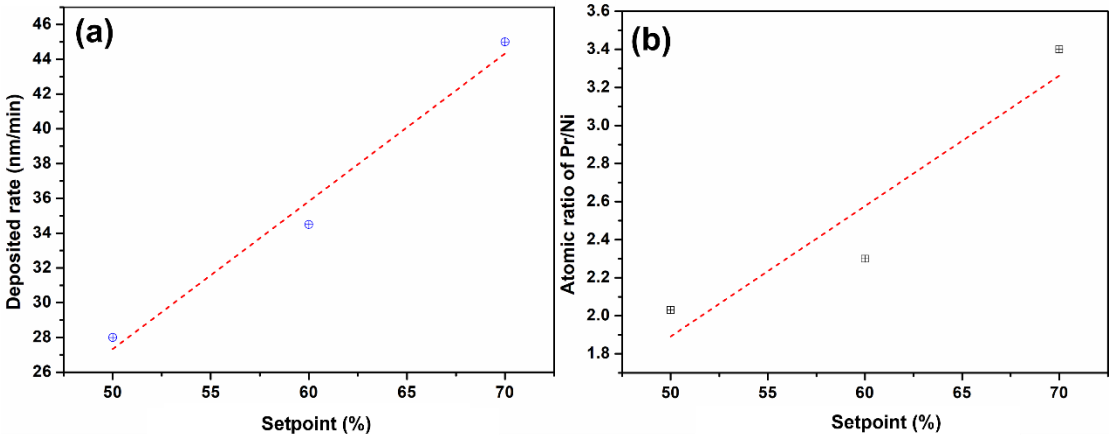

Figure 4.2: (a) Deposition rate and (b) atomic ratio of Pr/Ni as a function of optical emission Setpoint on Pr target (DC pulse generator conditions supplying on the Pr and Ni target: Intensity regulation mode at 2.5 A applied on Pr Target, Power regulation mode at 111 W on Ni target in all targets a DC pulse at frequency of 50 kHz, T_{off} of 4μs are applied)

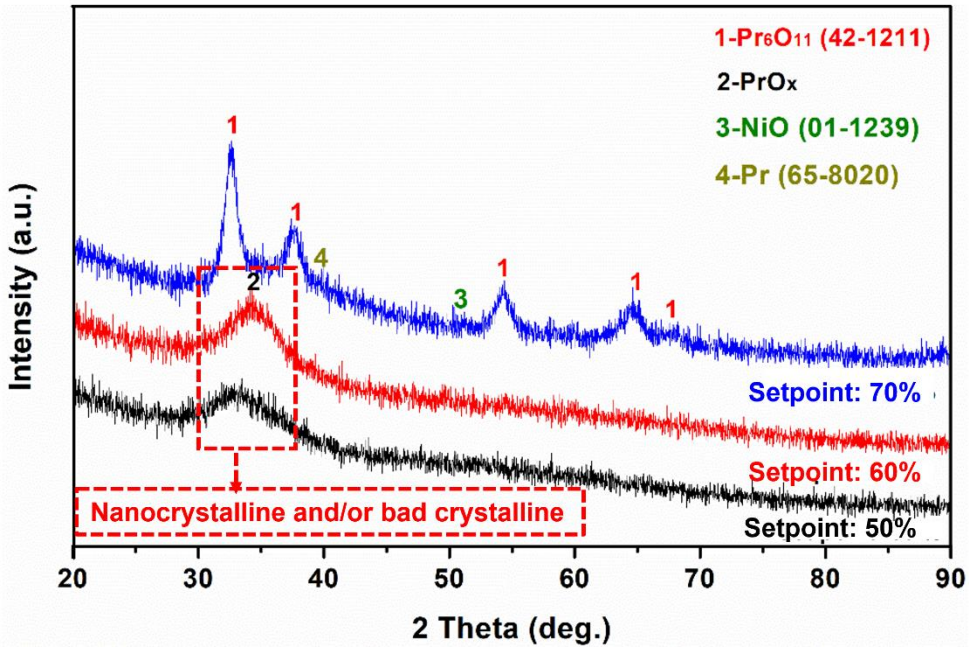

Figure 4.3: XRD patterns of Pr-Ni-O coatings deposited on glass slides with different optical emission Setpoints on Pr target (DC pulse generator conditions supplying on the Pr and Ni target: Intensity regulation mode at 2.5 A applied on Pr Target, Power regulation mode at 111 W on Ni target in all targets a DC pulse at frequency of 50 kHz, T_{off} of 4µs are applied)

Next attempts are made to deposit Pr-Ni-O coatings with different atomic ratio of Pr/Ni at the optical emission Setpoint of 70% on Pr target by adjusting the power applied to the Ni target. The atomic ratio of Pr/Ni in the coating is determined by the EDS spectrum of a typical Pr-Ni-O coating as shown in Figure 4.4. From Figure 4.5, the atomic ratio of Pr/Ni (surface of coatings) decreases approximately linearly with the increase of the power applied to the Ni target. Simultaneously, the deposition rate exhibits an approximately linear increase with increasing power applied to the Ni target.

These coatings with different atomic ratio of Pr/Ni after annealing treatment at 1000°C for 30 min are characterized by XRD. The XRD pattern in Figure 4.6 shows that Pr_2NiO_4 and Pr_6O_{11} appear in the coating with high atomic ratio of Pr/Ni (6.1 and 3.4). The coating with low Pr/Ni atomic ratio (1.4) has mainly phase of Pr_6O_{11}, and a small amount of nickel oxides (NiO and Ni_2O_3). The Pr_6O_{11} and $Pr_4Ni_3O_{9.85}$ appeared in the coating with the Pr/Ni atomic ratio of 2.0. The Pr_6O_{11} and $Pr_4Ni_3O_{9.85}$ may originate from the decomposition of Pr_2NiO_4. When the Pr/Ni atomic ratio is 1.6, the main phase in the coating is Pr_2NiO_4, but there are traces of NiO, which may be due to the lack of Pr. Therefore, coatings with higher atomic ratio of Pr/Ni should be deposited

in order to obtain composite coating (PPNO) containing Pr_2NiO_4 and Pr_6O_{11}. Comparing the XRD patterns of Pr/Ni atomic ratios of 3.4 and 6.1, the content of Pr_6O_{11} and Pr_2NiO_4 in PPNO coating can be adjusted by controlling the Pr/Ni atomic ratio. To deposit PNO cathode coating, the Pr/Ni atomic ratio should be controlled between 1.6 and 2.0. The cross-sections of coatings with different Pr/Ni atomic ratios deposited on alumina pellet after annealing treatment at 1000°C for 30min are observed. The annealed coatings showed a porous morphology, and it seemed that the coatings with high Pr/Ni atomic ratios (3.4 and 6.1) are more porous than those with low Pr/Ni atomic ratios (1.4 and 2.0). Based on the above experimental results, choosing the optical emission Setpoint of 70% on Pr target is appropriate for the deposition of PPNO and PNO cathodes.

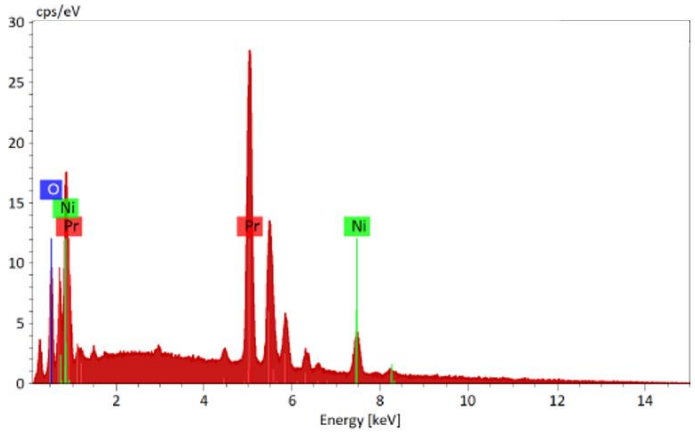

Figure 4.4: A typical EDS spectrum of the Pr-Ni-O coating

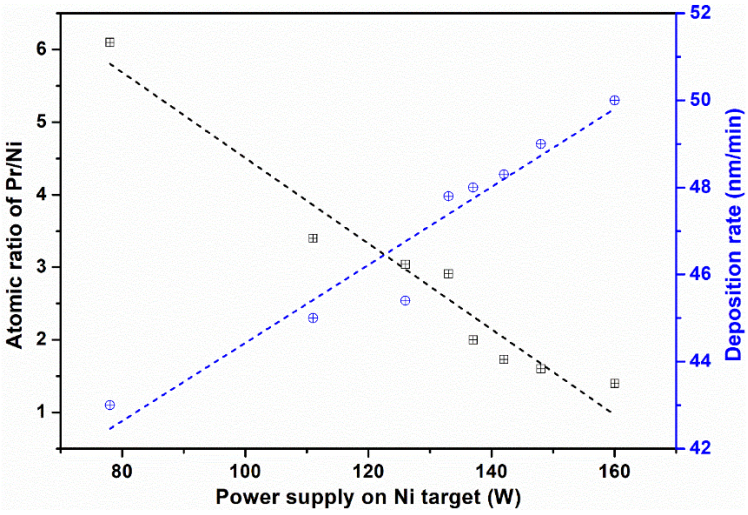

Figure 4.5: Deposition rate and Pr/Ni atomic ratio of the Pr-Ni-O coating deposited with different powers on the Ni target (DC pulse generator conditions supplying on the Pr and Ni target: frequency of 50 kHz, T_{off} of 4µs, Intensity regulation mode at 2.5 A applied on Pr Target)

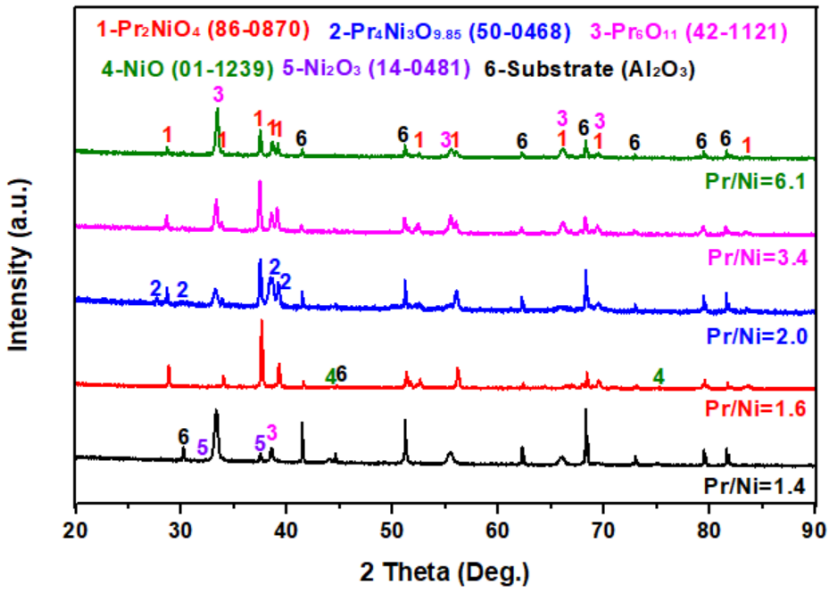

Figure 4.6: XRD of Pr-Ni-O coatings deposited on alumina pellet with different atomic ratios after annealing treatment at 1000°C for 30 min (DC pulse generator conditions supplying on the Pr and Ni target: frequency of 50 kHz, T_{off} of 4µs; Optical emission Setpoint 70% on Pr target): Pr/Ni = 1.4, 160 W on Ni target; Pr/Ni = 1.6, 148 W on Ni target; Pr/Ni = 2.0, 137 W on Ni target; Pr/Ni = 3.4, 111 W on Ni target; Pr/Ni = 6.1, 78 W on Ni target

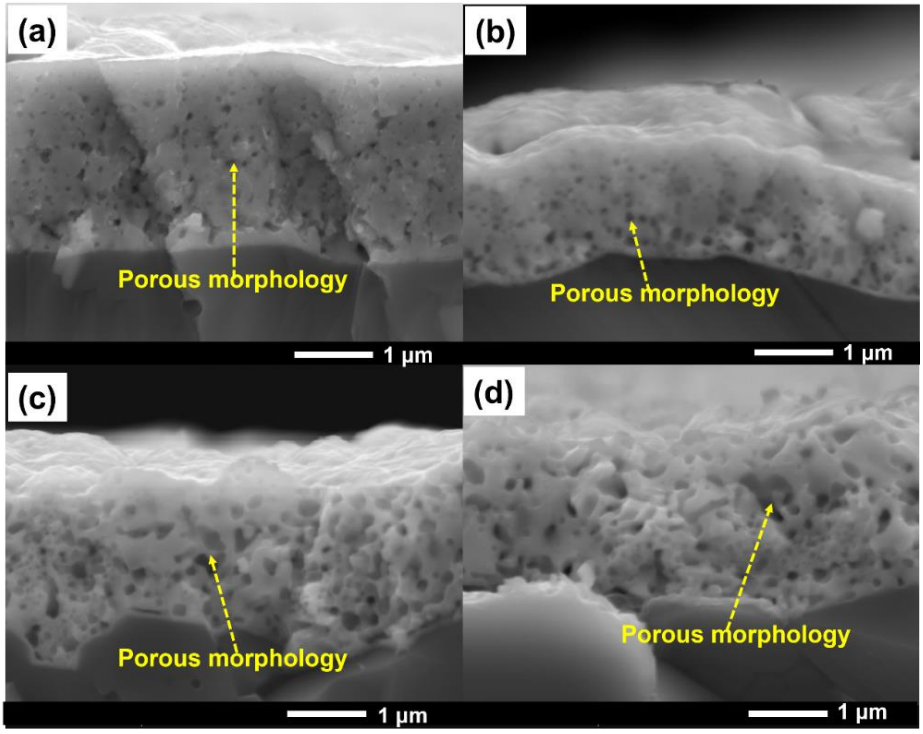

Figure 4.7: SEM images of Pr-Ni-O coatings deposited on alumina pellet with different atomic ratios after annealing treatment at 1000°C for 30 min (DC pulse generator conditions supplying on the Pr and Ni target: frequency of 50 kHz, T_{off} of 4µs; Setpoint 70% on Pr target): (a) Pr/Ni = 1.4, 160 W on Ni target; (b) Pr/Ni = 2.0, 137 W on Ni target; (c) Pr/Ni = 3.4, 111 W on Ni target; (d) Pr/Ni = 6.1, 78 W on Ni target

4.2.2 The deposition of Pr_2NiO_4@Pr_6O_{11}(PPNO) and Pr_2NiO_4(PNO) cathodes

As mentioned above that PPNO and PNO coatings can be achieved by depositing Pr-Ni-O coatings with high Pr/Ni atomic ratio and low Pr/Ni atomic ratio, respectively. Here, the PPNO1, PPNO2, and PNO coatings are deposited at the otpical emission Setpoint of 70% on Pr target. The deposition parameters are listed in Table 4.3. The structural and morphology evolution of PPNO1 coating subjected to different annealing treatments are observed. PPNO2 and PNO are used as the cathode to characterize the electrical and electrochemical properties.

Table 4.3: The deposition parameters to deposit PPNO and PNO coatings

Deposition parameters		PPNO1	PPNO2	PNO
Ar flow rate (sccm)			200	
O_2 flow rate (sccm)		4.8-5.3	4.9-5.2	4.9-5.3
Total pressure (Pa)			1.9-2.1	
Drawing distance(mm)			70	
Frequency (kHz)			50	
T_{off} (μs)			4	
Pr target	Setpoint (%)		70	
	Current (A)		2.5	
Ni target	Power (W)	126	133	142
Deposition time (min)		130	140	170

4.2.2.1 Pr_2NiO_4@Pr_6O_{11} (PPNO)

The composition of the PPNO coatings after undergoing different annealing treatments are analyzed by EDS as shown in Table 4.4. The surface (cross-section) composition results show that the Pr/Ni atomic ratio of the PPNO1 coating increased from 2.45 ± 0.05 (2.26 ± 0.05) to 3.06 ± 0.09 (2.36 ± 0.02) after annealing at 1000°C for 30min. At this annealing treatment stage (1000°C for 30min), more Pr_6O_{11} phases formed firstly on the surface during the temperature rise due to the possible temperature gradient between the surface and bulk of the coating. Because of this, the Pr/Ni atomic ratio on the surface of the coating is higher than that in the bulk (cross-section). However, the Pr/Ni atomic ratio increases both on the surface and cross-section of the PPNO1 coating after annealing, which may be due to the loss of part of Ni during annealing treatment. From Figures 4.8 (a) and (b), no obvious diffusion of Pr and Ni is

observed at the interface of GDC10 and PPNO1 after annealing treatment at 1000°C for 30 min compared with as deposited coating. Therefore, the loss of Ni may be through evaporation in the form of NO_x during annealing treatment. After performing annealing treatment under condition of 1000°C/30 min and after 750°C/50h, the Pr/Ni atomic ratio of the PPNO1 surface increased from 3.06 ± 0.09 to 3.21 ± 0.09, while the Pr/Ni atomic ratio in the cross-section did not change significantly (2.36 ± 0.02 *v.s.* 2.44 ± 0.02). During this process, the increase of the Pr/Ni atomic ratio on the PPNO1 surface may be due to the migration of Pr_6O_{11} to the surface, while Ni is unlikely to be lost in the form of NiO_x due to the already formed Pr_2NiO_4 phase. In addition, no significant diffusion of Pr and Ni is observed at the interface of GDC10 and PPNO1 as compared to the coating annealing at 1000°C for 30 min (Figures 4.8 (b) and (c)). The Pr/Ni atomic ratio of PPNO2 coating has the same variation trend as that of PPNO1 coating (Table 4.4).

Table 4.4 The composition of the PPNO coatings after different annealing treatments

Samples		Elements (at. %)		Atomic ratio
		Pr	Ni	Pr/Ni
PPNO1	As deposited	71.01±0.44	28.99±0.44	2.45±0.05
Surface	1000 °C for 30min	75.35±0.52	24.65±0.52	3.06±0.09
	1000 °C-30min-750 °C-50 h	76.22±0.52	23.78±0.52	3.21±0.09
PPNO1	As deposited	69.31±0.47	30.69±0.47	2.26±0.05
Cross-section	1000 °C for 30min	70.24±0.18	29.76±0.18	2.36±0.02
	1000 °C-30min-750 °C 50 h	70.89±0.19	29.11±0.19	2.44±0.02
PPNO2	As deposited	69.10±0.37	30.90±0.37	2.24±0.04
Surface	1000 °C for 30min	74.40±0.64	25.60±0.64	2.91±0.09
	1000 °C-30min-750 °C-50 h	75.12±0.52	24.88±0.52	3.02±0.08
PPNO2	As deposited	68.01±0.33	31.99±0.33	2.13±0.03
Cross-section	1000 °C for 30min	69.68±0.12	30.32±0.12	2.30±0.01
	1000 °C-30min-750 °C 50 h	70.23±0.23	29.77±0.23	2.36±0.02

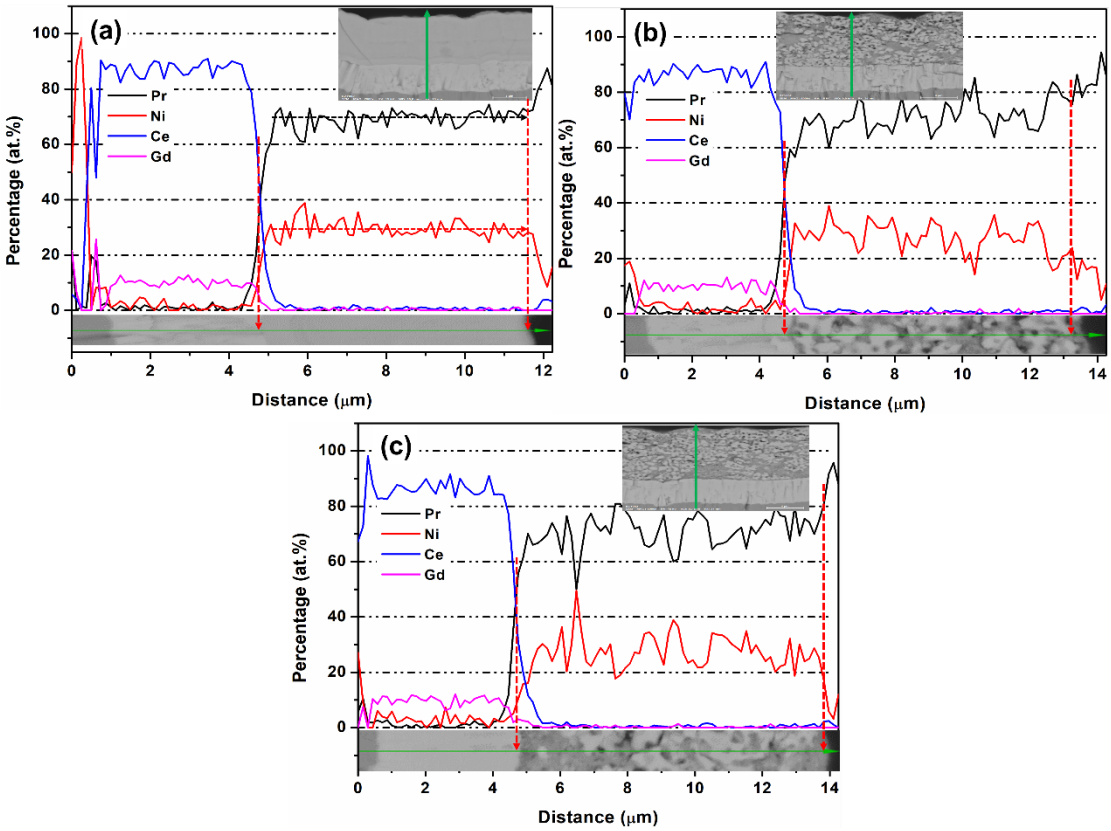

Figure 4.8: The SEM-EDS profile of the cross-section of the PPNO1 coatings: (a) as deposited, (b) annealing at 1000°C for 30 min, (c) 1000°C/30 min and after 750°C/50 h

The XRD pattern in Figure 4.9 demonstrates the structural changes in the PPNO1 coating with increasing annealing temperature. Pr_6O_{11} exists in the as deposited coating and NiO and PrO_x appear successively as the annealing treatment temperature increases to 950°C. After annealing treatment at 950°C, traces of Pr_2NiO_4 phase appeared. After annealing treatment at 1000°C, a typical composite coating material with two phases of Pr_2NiO_4 and Pr_6O_{11} is formed. When PPNO1 coating crystallizes towards Pr_2NiO_4, the electrical resistance of the coating gradually decreases dure to the electronic conductivity of Pr_6O_{11} oxide is much lower than that of Pr_2NiO_4. This structural evolution is consistent with the change in the electrical resistance of the coating. The PPNO1 coating that has been annealed at 1000°C is placed in a furnace under air atmosphere for 50 h at 750°C (1000°C/30min and after750°C/50 h) to check the stability of the coating. The XRD pattern of the PPNO1 coating after annealing for 50 h shows that the peak intensity attributed to Pr_6O_{11} is relatively enhanced, which may mean that the content of Pr_6O_{11} phase on the coating surface increases. Vibhu [11] investigated the decomposition of Pr_2NiO_4 powder at 700 and 800°C for one week

under air. The results showed that most of the Pr_2NiO_4 powders are decomposed into $Pr_4Ni_3O_{10+\delta}$, $PrNiO_{3-\delta}$ (major phase), and Pr_6O_{11} at 700°C, while the Pr_2NiO_4 powder is completely decomposed into $Pr_4Ni_3O_{10+\delta}$, $PrNiO_{3-\delta}$, and Pr_6O_{11} at 800°C. Therefore, the increase in the content of Pr_6O_{11} phase may be due to migration rather than decomposition of Pr_2NiO_4 since no $Pr_4Ni_3O_{10-\delta}$ and perovskite $PrNiO_{3-\delta}$ in the XRD pattern. In addition, the crystallite size of both phases (Pr_2NiO_4 and Pr_6O_{11}) in PPNO1 coating increases with the increase of annealing temperature as listed in Table 4.5. After annealing for 50 h, the crystallite size of both phases also increased.

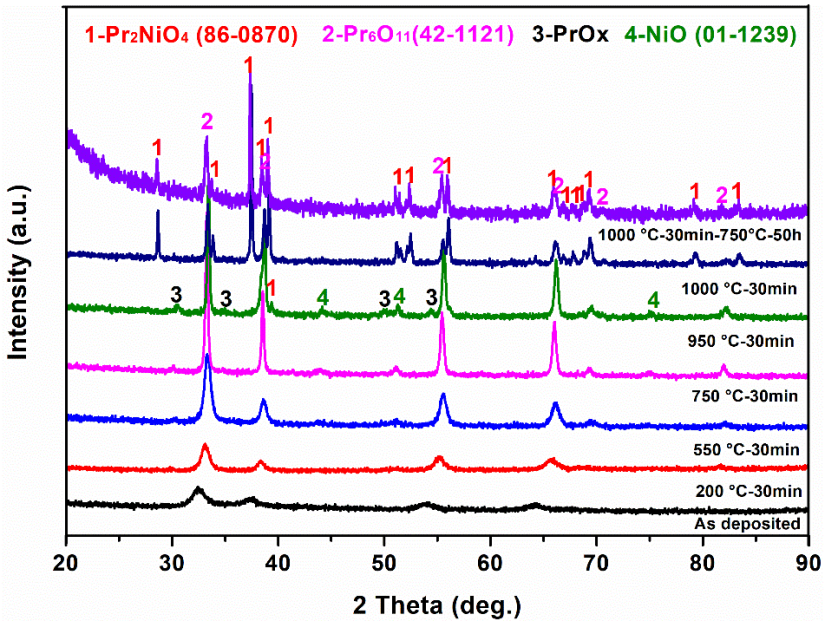

Figure 4.9: XRD patterns of the PPNO1 cathode coating deposited on alumina pellet after various annealing treatments in air

Table 4.5: The crystallite size of the PPNO1 coatings deposited on alumina pellet as function of the annealing temperature.

Temperature (°C)	Crystallite size (nm)	
	Pr_2NiO_4	Pr_6O_{11}
As deposited	–	7.8
200	–	10.3
550	–	12.7
750	–	32.6
950	62.3	40.6
1000	87.9	44.9
1000/30 min and after 750/50 h	96.3	46.1

Figure 4.10 (a) shows the XRD pattern of Pr_2NiO_4 and Pr_6O_{11} in PPNO2 coating

after annealing treatment at 1000°C for 30 min. Like PPNO1, the peak intensity assigned to Pr_6O_{11} in PPNO2 is relatively enhanced after annealing treatment at 750°C for 50h but no $Pr_4Ni_3O_{10-\delta}$ and perovskite $PrNiO_{3-\delta}$. The XRD results show that the PPNO (PPNO1 and PPNO2) material may has certain stability (Figures 4.8 and 4.10). The XRD pattern of PPNO2 subjected to annealing treatment at 1000°C for 30 min are refined by FullProf software as shown in Figure 4.10 (b) and Table 4.6. The refinement results showed that the content of Pr_6O_{11} phase in the PPNO2 coating accounted for 37.09 wt.%. The PPNO2 coating is used as the cathode of the complete single cell.

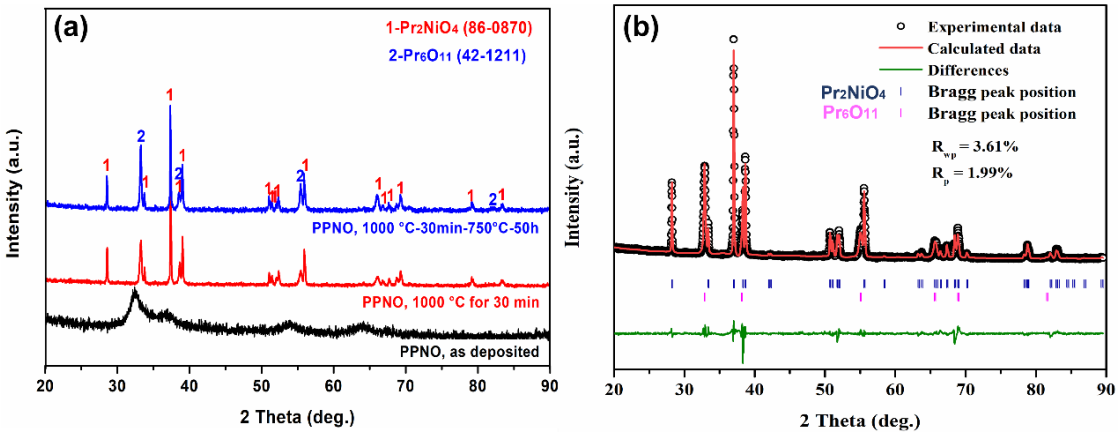

Figure 4.10 XRD patterns of the PPNO2 coating deposited on alumina plate after various annealing treatments in air (a); refined XRD patterns of PPNO2 coating after annealing at 1000°C for 30min (b)

Table 4.6 Structural parameters of the PPNO2 coating after annealing at 1000°C for 30min obtained from Rietveld refinement

Structural parameters	PPNO2	
	Pr_2NiO_4	Pr_6O_{11}
Percentage (wt.%)	62.91	37.09
a (Å)	5.453	5.479
b (Å)	5.453	5.479
c (Å)	12.453	5.479
Vol. ($Å^3$)	370.293	164.477
Space group	Fmmm	Fm -3m

As a cathode coating, the porous morphology facilitates the diffusion of oxygen. Figure 4.11 demonstrates the morphology evolution of the PPNO1 coating with annealing treatment. Initially, the as deposited PPNO1 coating looks dense (Figures 4.11 (a) and (d)). After annealing treatment at 950°C for 30 min, a distinct porous (macro pores) morphology is formed as shown in Figures 4.11 (i) and (j). The formation

of the porous morphology of the PPNO1 coating may have go through three stages. In the first stage, the atomic-scale defects of the as deposited coating are eliminated to form micro (nano) pores as the annealing treatment proceeds (until 750°C). Then micro(nano) pores are aggregated into macro pores at 950°C in the second stage (Figures 4.11 (i) and (j)). These two stages are accompanied by volume expansion of the coating, probably due to the formation of micro(nano) pores (Table 4.7). In the third stage, macro pores are aggregated into large pores at 1000°C. At the same time, small particles of Pr_6O_{11}-enriched form typical large particles of Pr_2NiO_4-enriched (Figures 4.11 (k) and (l)). This stage is accompanied by volume shrinkage, probably due to the aggregation of small particles into larger ones (Table 4.7). Correspondingly, the porosity of the coating decreased from 44.8 ± 0.3 Vol. % (at 950°C) to 42.9 ± 0.2 Vol.% (at 1000°C). After undergoing a long-term annealing treatment (1000°C/30min-and after 750°C/50h), PPNO1 maintains the porous morphology and has not significantly change in porosity (Table 4.7), which shows the stability of the morphology. However, it seems that more small particles of Pr_6O_{11} migrate to the surface, which may be the reason for the increase of the Pr/Ni atomic ratio of the surface as show in Table 4.5. A similar porous morphology is also observed in the PPNO2 coating as shown in Figure 4.12. The thickness of PPNO2 coating increased from 6.7 ± 0.1 to 8.1± 0.1 μm after annealing at 1000°C for 30 min, while the porosity is 43.9 ± 0.5 Vol. %. After annealing for 50h (1000°C/30min-and after 750°C/50 h), the thickness of PPNO2 coating increased from 8.1 ± 0.1 to 8.4 ± 0.2 μm and the porosity slight decrease to 42.6 ± 0.4 Vol.%.

It can be considered that the Pr_6O_{11} and Pr_2NiO_4 phases are enriched on small and large particles, respectively, which can be confirmed by the XRD pattern (Figures 4.8 and 4.10) and the EDS results (Figures 4.13-4.14). On the one hand, the XRD results have confirmed that the PPNO1 and PPNO2 coatings both contain Pr_2NiO_4 and Pr_6O_{11} after annealing treatment (1000°C for 30 min and 1000°C/30min-and after 750°C/50 h). On the other hand, the Pr/Ni atomic ratio in small particles is much larger than that in large particles (Figure 4.13). This indicates that Ni is enriched in the large particles, while Pr is more enriched in the small particles. The mapping results in Figure 4.14 (b)

and (c) also confirms this point.

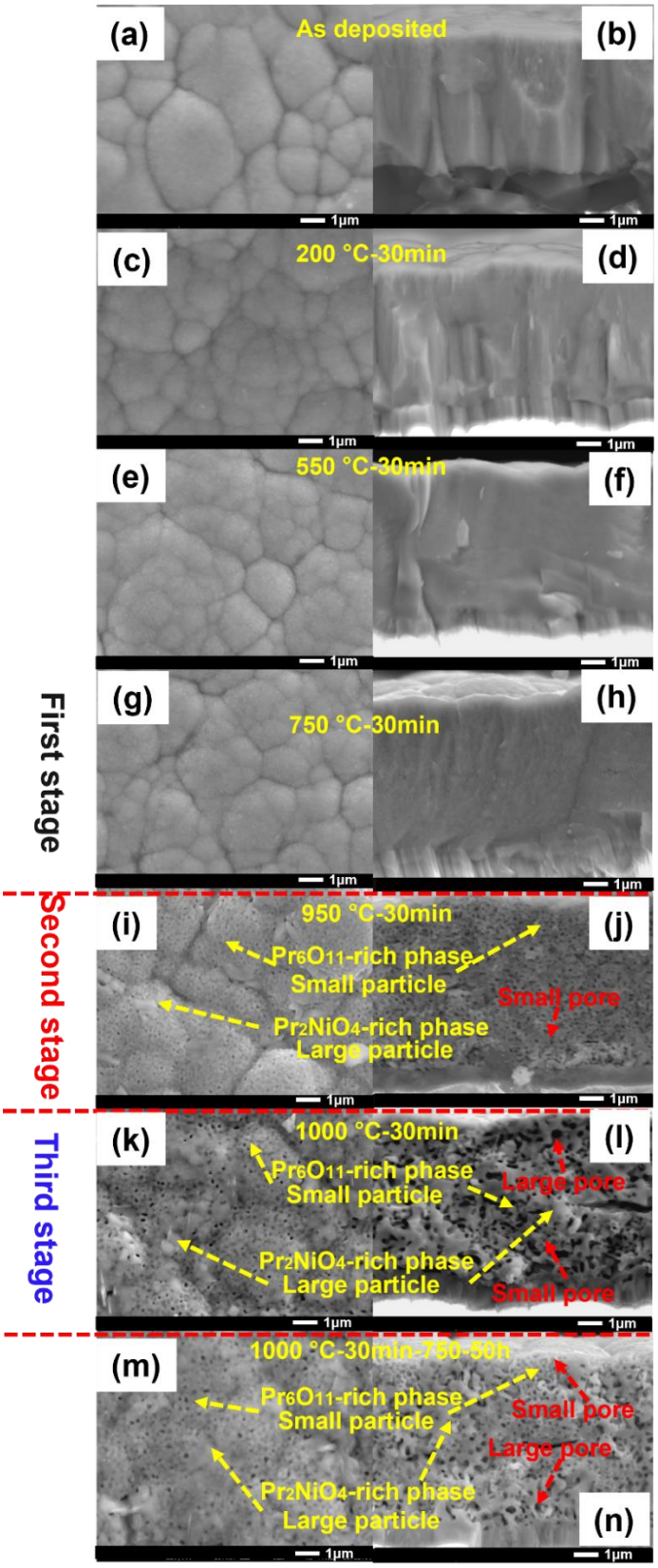

Figure 4.11: SEM images of the PPNO1 coatings deposited on GDC10 layer after various annealing treatments: (a), (c), (e), (g), (i), (k), and (m) refer to the surface; (b), (d), (f), (h), (j), (l), and (n) refer to the cross-section

Table 4.7: The porosity and thickness of the PPNO coatings as function of the annealing temperature

Samples	Temperature (°C)	Cross-section porosity (Vol.%)	Thickness (µm)
PPNO1	As deposited		5.9 ± 0.2
	200	–	6.0 ± 0.1
	550	–	6.5 ± 0.2
	750	–	6.6 ± 0.2
	950	44.8 ± 0.3	7.5 ± 0.2
	1000	42.9 ± 0.2	6.9 ± 0.1
	1000°C/30min-and after 750°C/50 h	42.1 ± 0.3	7.2 ± 0.1
PPNO2	As deposited	–	6.7 ± 0.1
	1000	43.9 ±0.5	8.1 ± 0.1
	1000°C/30min-and after 750°C/50 h	42.6 ± 0.4	8.4 ± 0.2

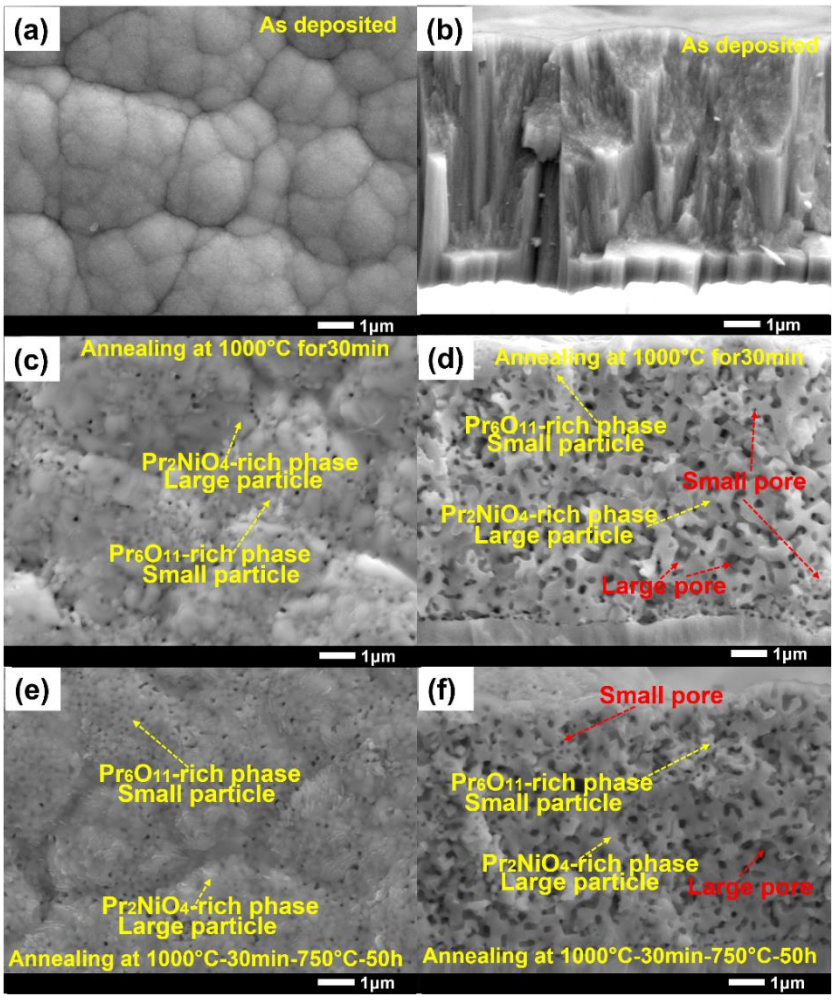

Figure 4.12: SEM observation of the PPNO2 cathode coatings deposited on GDC10 layer after various annealing treatments: (a), (c), and (e) refer to the surface; (b), (d), and (f) refer to the cross-section

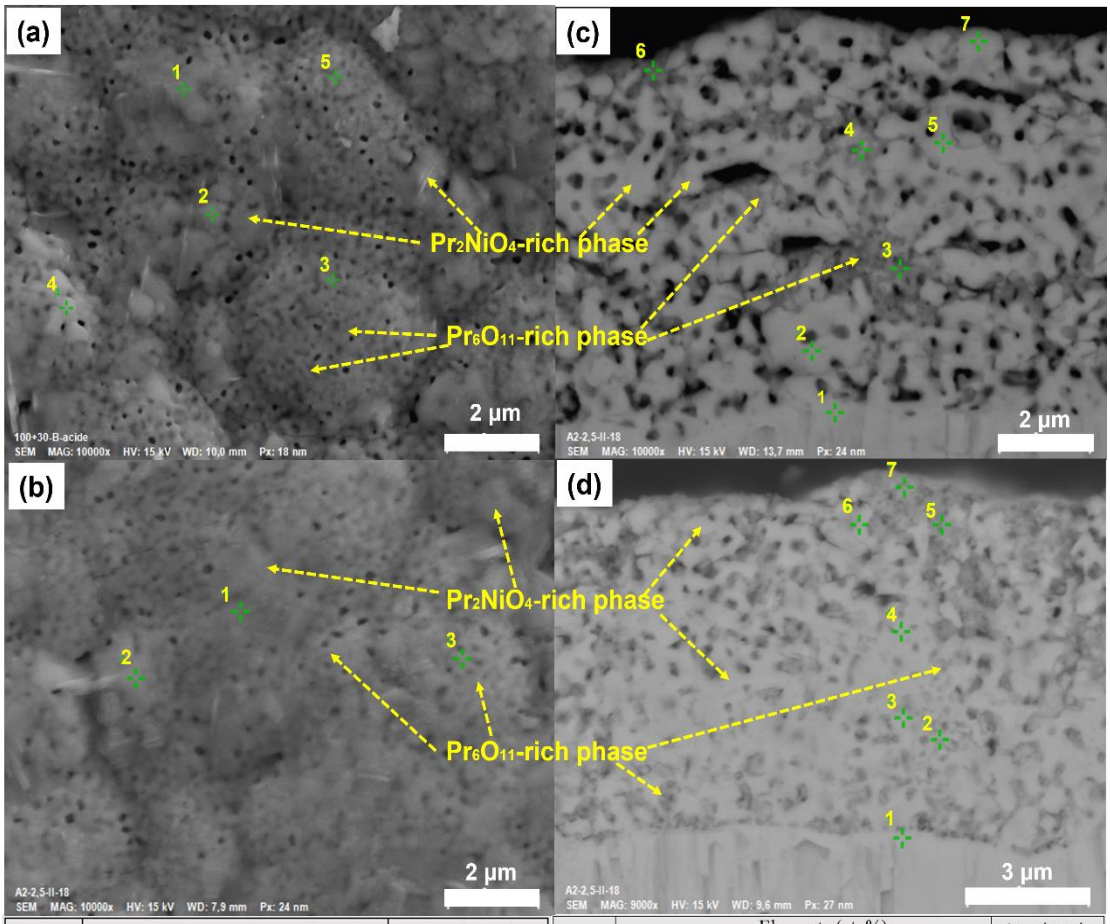

Point From (a)	Elements (at. %)			Atomic ratio
	Pr	Ni	O	Pr/Ni
1	25.13	13.04	61.82	1.93
2	28.19	13.35	58.46	2.11
3	28.97	8.68	62.35	3.33
4	24.53	12.25	63.22	2.00
5	25.89	9.20	64.91	2.81

Point From (b)	Elements (at. %)			Atomic ratio
	Pr	Ni	O	Pr/Ni
1	30.17	13.89	55.94	2.17
2	25.96	12.66	61.38	2.05
3	29.96	5.54	64.50	5.41

Point From (c)	Elements (at. %)					Atomic ratio
	Pr	Ni	O	Ce	Gd	Pr/Ni
1	4.29	1.18	65.39	26.05	3.09	3.64
2	25.11	12.75	61.90	0.24	0.00	1.97
3	24.44	8.68	66.70	0.18	0.00	2.82
4	30.73	8.69	60.42	0.16	0.00	3.54
5	27.09	13.88	59.03	0.00	0.00	1.95
6	34.95	5.96	58.89	0.20	0.00	5.86
7	26.01	13.35	60.56	0.08	0.00	1.95

Point From (d)	Elements (at. %)					Atomic ratio
	Pr	Ni	O	Ce	Gd	Pr/Ni
1	6.09	1.51	65.94	23.93	2.53	4.03
2	32.02	9.97	57.72	0.28	0.00	3.2
3	27.40	13.44	58.97	0.21	0.00	2.03
4	28.98	13.48	57.55	0.00	0.00	2.15
5	32.53	5.40	61.90	0.17	0.00	6.02
6	26.27	13.07	60.51	0.15	0.00	2.01
7	32.76	9.47	57.49	0.28	0.00	3.45

Figure 4.13: The SEM-EDS results of the PPNO1 cathode coatings: (a) and (b) refer to surface of the coating annealing at 1000°C for 30 min and 1000°C/30 min-and after 750°C/50h, respectively; (c) and (d) refer to cross-section of the coating annealing at 1000°C for 30min and 1000°C/30 min-and after 750°C/50h, respectively

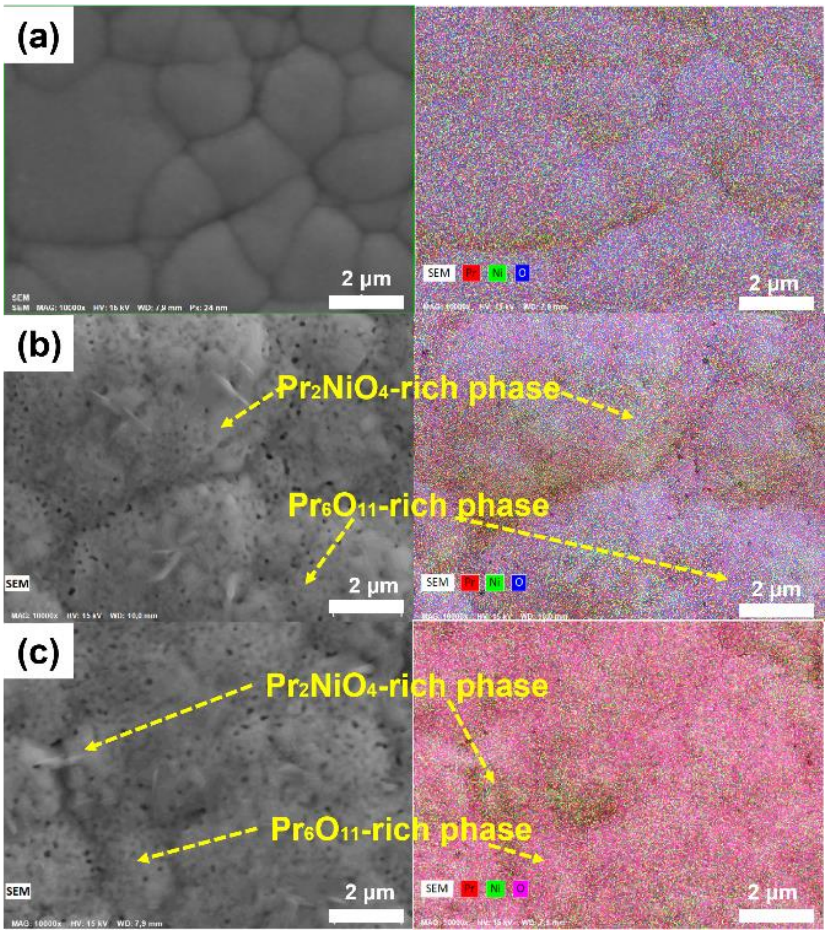

Figure 4.14: The SEM-EDS mapping of the PPNO1 cathode coatings surface after different annealing treatments: (a) as deposited, (b) annealing at 1000°C for 30 min, (c) 1000°C/30min-and after 750°C/50 h

4.2.2.2 Pr_2NiO_4 (PNO)

The surface (cross-section) composition results show that the Pr/Ni atomic ratio of the PNO coating increased from 1.61 ± 0.02 (1.51 ± 0.02) to 1.73 ± 0.02 (1.57 ± 0.01) after annealing at 1000°C for 30min (Table 4.8). This change trend is similar to that of PPNO coating. Like PPNO1, no obvious diffusion of Pr and Ni is observed at the interface of GDC10 and PNO coating after annealing treatment in contrast to as deposited coating (Figures 4.15 (c)-(e)). However, after annealing treatment at 1000°C for 30 min, Pr_2NiO_4 is formed mainly with a trace amount of NiO and without Pr_6O_{11} due to the low Pr/Ni atomic ratio (Figure 4.16 (a)). After annealing for 50h (1000°C/30min-and after 750°C/50 h), the Pr/Ni atomic ratio on the surface and cross-section of PNO does not change significantly, which may be due to the absence of Pr_6O_{11} migration. However, a small amount of $Pr_4Ni_3O_{9.85}$ and Pr_6O_{11} appeared in the

PNO coating after annealing for 50h (1000°C/30min-and after 750°C/50 h), which may be derived from the decomposition of Pr_2NiO_4. The XRD patterns of PNO subjected to annealing treatment at 1000°C for 30 min are refined by FullProf software. For this PNO coatings, a single Pr_2NiO_4 phase refinement is performed while ignoring traces of NiO. The refinement results are shown in Figure 4.16 (b) and Table 4.9. Compared with PPNO2 (Figure 10 (b) and Table 4.6), the unit cell volume of Pr_2NiO_4 phase in PNO is 373.865 $Å^3$ greater than that in PPNO2 of 370.293 $Å^3$. This may be related to the less lattice oxygen of PPNO2 result in the reduction of the unit cell volume (Figure 4.18 and Table 4.11). This result is consistent with the report of Zhao et al [12] that the presence of Pr_6O_{11} suppressing the coarsening of Pr_2NiO_4 grains.

Table 4.8 The composition of PNO coating with annealing treatment

PNO	Annealing Treatment	Elements (at. %)		Atomic ratio
		Pr	Ni	Pr/Ni
Surface	As deposited	61.71±0.27	38.29±0.28	1.61±0.02
	1000 °C for 30min	63.36±0.20	36.64±0.20	1.73±0.02
	1000°C/30min-and after 750°C/50 h	63.69±0.53	36.31±0.53	1.75±0.04
Cross-section	As deposited	60.12±0.28	39.88±0.28	1.51±0.02
	1000 °C for 30min	61.14±0.10	38.86±0.10	1.57±0.01
	1000°C/30min-and after 750°C/50 h	61.36±0.16	38.64±0.16	1.59±0.01

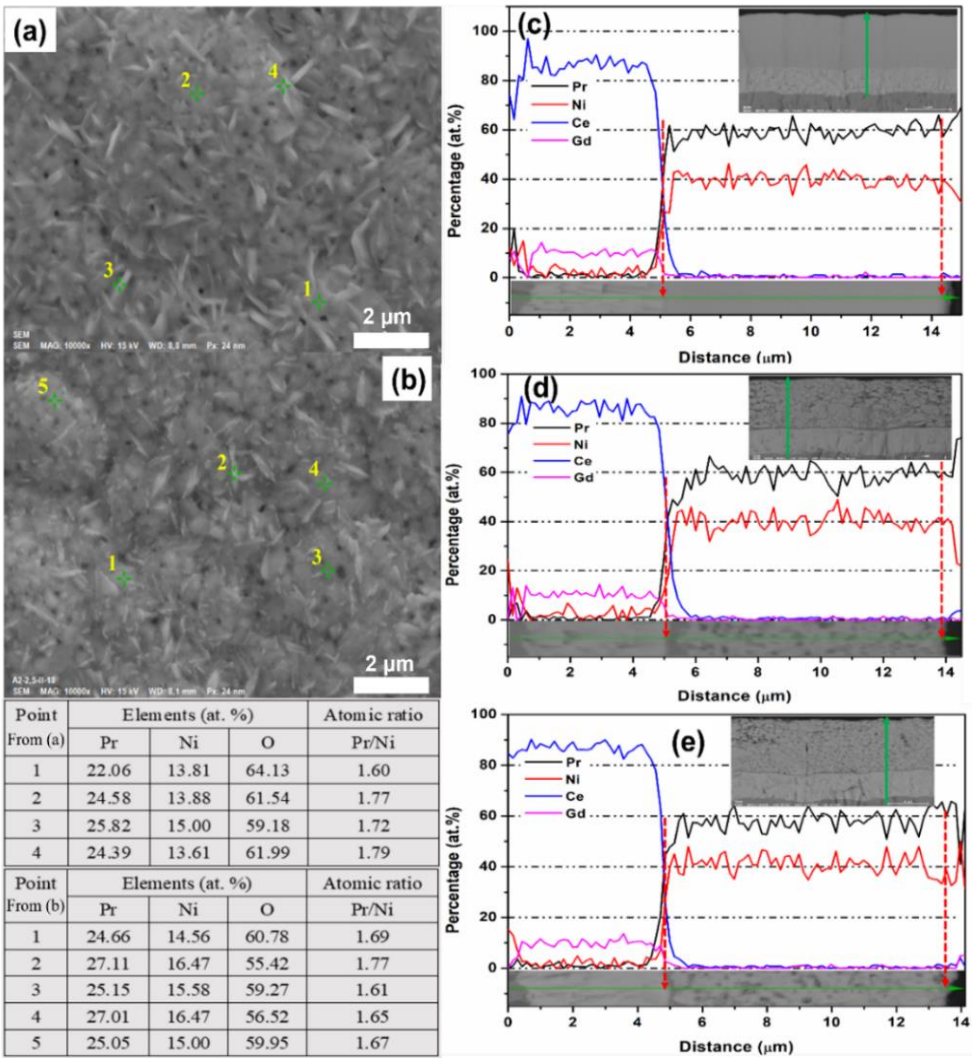

Point From (a)	Elements (at. %)			Atomic ratio
	Pr	Ni	O	Pr/Ni
1	22.06	13.81	64.13	1.60
2	24.58	13.88	61.54	1.77
3	25.82	15.00	59.18	1.72
4	24.39	13.61	61.99	1.79

Point From (b)	Elements (at. %)			Atomic ratio
	Pr	Ni	O	Pr/Ni
1	24.66	14.56	60.78	1.69
2	27.11	16.47	55.42	1.77
3	25.15	15.58	59.27	1.61
4	27.01	16.47	56.52	1.65
5	25.05	15.00	59.95	1.67

Figure 4.15 SEM-EDS results of the PNO coatings deposited on GDC10 layer: (a) and (b) refer to the surface of PNO coating after annealing at 1000°C for 30 min and 1000°C/30min-and after 750°C/50 h, respectively; (c), (d) and (e) refer to the cross-section of the as deposited PNO coating, after annealing at 1000°C for 30 min and 1000°C/30min-and after 750°C/50 h, respectively

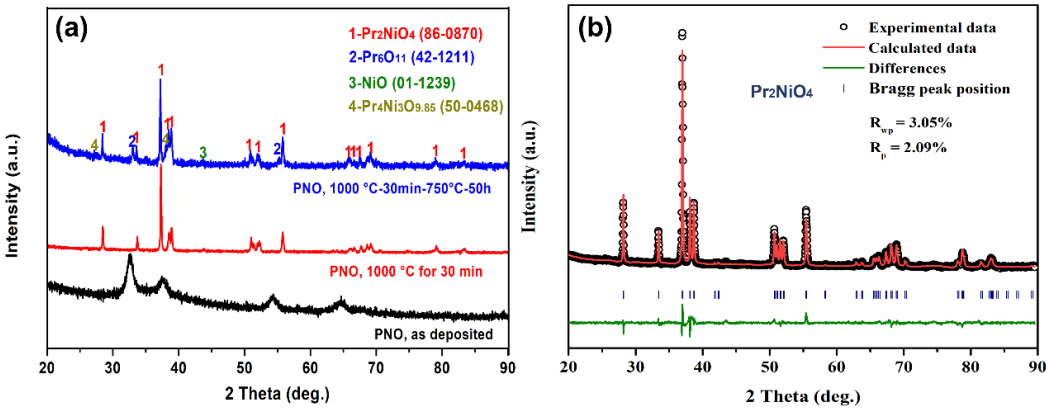

Figure 4.16: XRD of the PNO cathode coating deposited on alumina pellet after various annealing treatments under air (a); refined XRD of PNO cathode coating after annealing at 1000°C for 30min (b)

Table 4.9: Structural parameters of the PNO cathode coating obtained after Rietveld refinement.

Structural parameters	(Pr_2NiO_4) PNO
a (Å)	5.481
b (Å)	5.481
c (Å)	12.445
Vol. ($Å^3$)	373.865
Space group	Fmmm

The morphology of PNO cathode coatings is shown in Figure 4.17. The as deposited PNO cathode coating appears to be dense as shown in Figures 4.17 (a) and (b). The porous morphology is formed after annealing at 1000°C for 30 min (Figures 4.17 (c) and (d)). It can be clearly seen that the porous morphology of PNO is different from that of PPNO (Figures 4.11 and 4.12). This difference may come from the third stage of porous morphology formation. In the third stage, all small particles of Pr_6O_{11}-enriched are aggregated into large particles of Pr_2NiO_4-enriched accompanied by volume shrinkage in PNO. Accordingly, all Pr_6O_{11}-enriched particles disappeared. Therefore, only bulky particles are observed in PNO. Furthermore, it seems that PNO has smaller pores compared to PPNO2, which may be the reason of the lower porosity of PNO (31.3 ± 0.4 Vol. %) than PPNO2 (43.9 ± 0.5 Vol. %). After annealing for 50h (1000°C/30min-and after 750°C/50 h there is no major change in morphology (the thickness and porosity) of PNO. The EDS results of the PNO (Figures 4.15 (a) and (b)) show that the Pr/Ni atomic ratio of each point on the surface has no obvious difference, which may be related to its single phase (P_2NiO_4).

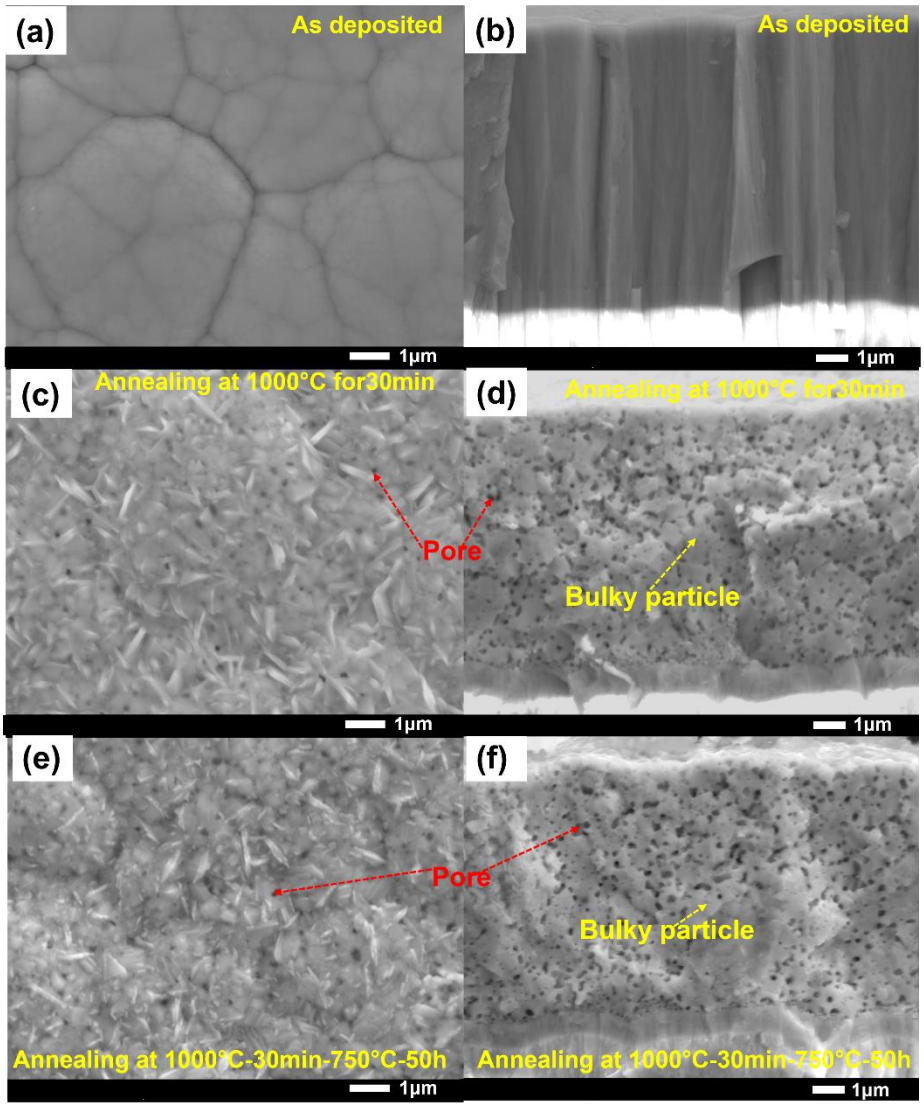

Figure 4.17: SEM images of the PNO cathode coatings deposited on GDC10 layer after various annealing treatments: (a), (c), and (e) refer to the surface; (b), (d), and (f) refer to the cross-section.

Table 4.10: The cross-section porosity and thickness of the PNO cathode coating

Samples	Thickness (μm)			Cross-section porosity (Vol.%)	
	As deposited	1000°C	1000°C/30min-and after 750°C/50 h	1000°C	1000°C/30min-and after 750°C/50 h
PNO	8.9 ± 0.1	8.5 ± 0.2	8.4 ± 0.2	31.3 ± 0.4	31.2 ± 0.4

For the cathode of SOFC, the oxygen adsorption capacity of the material is an important factor affecting the ORR activity. Here, the XPS of O1s of PPNO2 and PNO after annealing at 1000°C for 30 min are collected to confirm the surface oxygen species (Figure 4.18). Four distinct peaks are observed from the XPS spectra of the O1s orbital. The peak at low binding energy of about 528.2 eV is considered to belong to, $O_{lattice}$, while the peaks at high binding energy (529.7, 531.2, and 532.5 eV) belong to $O_{surface}$,

represents O^{2-}, O^{-}, and O_2^{-}, respectively [13, 14]. A larger $O_{surface}/O_{lattice}$ ratio means stronger oxygen adsorption ability on material surface, which helps to promote ORR activity [15, 16]. The percentage of peak areas assigned to $O_{lattice}$ and $O_{surface}$ in PPNO2 and PNO are shown in Table 4.11. Obviously, PPNO2 has larger $O_{surface}/O_{lattice}$ ratio (7.15) than that of PNO (4.76). Additionally, oxides lose lattice oxygen at high temperatures, resulting in the additional oxygen vacancies [12]. More oxygen vacancies are helpful for the ORR process occurring at cathode.

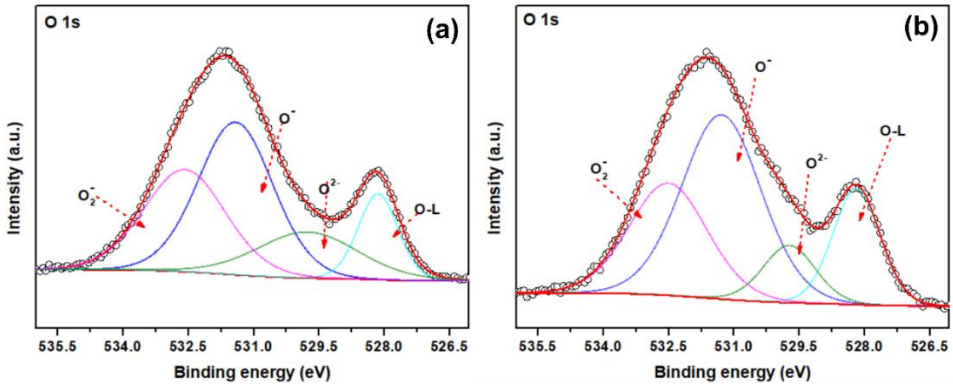

Figure 4.18: XPS patterns of the PPNO2 and PNO coatings after annealing at 1000 °C for 30 min: (a) PPNO2, (b) PNO

Table 4.11: The percentages of oxygen species of PPNO2 and PNO coatings after annealing at 1000 °C for 30 min

Oxygen species	PPNO2	PNO
$O_{surface}$ (%)	87.73	82.65
$O_{lattice}$ (%)	12.27	17.35
$O_{surface}$/ $O_{lattice}$	7.15	4.76

In summary, PPNO coatings can be obtained by depositing the Pr-Ni-O coating with a high Pr/Ni atomic ratio of 3.06 ± 0.09 and 2.91 ± 0.09 after annealing at 1000°C for 30min, while PNO coating realized by depositing the Pr-Ni-O coating with a low Pr/Ni atomic ratio of 1.73 ± 0.02 after annealing at 1000°C for 30min. A distinct porous morphology in PPNO coating can be realized after annealing treatment at least 950°C for 30 min. Although the coating has the highest porosity of 44.8 ± 0.4 Vol.% after annealing treatment at 950°C, it is not the desired PPNO coating with Pr_2NiO_4 and Pr_6O_{11}. The porosity of PPNO (PPNO1 of 42.9 ± 0.2 Vol. % and PPNO2 of 43.9 ± 0.5 Vol. %) coating is much higher than that of PNO (31.3 ± 0.4 Vol. %) coating after

annealing treatment at 1000°C for 30 min.

4.2.2.3 Electrical and Electrochemical Characterization

From the discussion in the previous section, the porous PPNO2 composite and PNO cathode are confirmed to be prepared by RMS followed by annealing treatment at 1000°C for 30 min. Here, the PPNO2 composite (8.1 μm) and PNO (8.5 μm) cathode coatings are deposited on both sides of the 8YSZ ceramic plate with a diameter of 25 mm and a thickness of 0.5 mm for the measurement of AC-EIS. PPNO2 and PNO coating deposited on alumina ceramic plate is used to measure electrical conductivity. As shown in Figure 4.19 (a), both PPNO2 and PNO exhibit semiconducting conduction behavior in the temperature range from 300 to 900°C. In the whole temperature range, the conductivity of PNO is higher than that of PPNO2, which indicates that the introduction of Pr_6O_{11} reduces the electronic conductivity. It is well known that Pr_6O_{11} is a poor electron conductor, and the electron conduction channel is blocked after adding Pr_6O_{11} [17]. The maximum conductivity of the deposited PPNO2 coating is about 87 S/cm at 700°C, while that of PNO coating is about 109 S/cm at 650°C. This maximum value is in the area of use of the IT-SOFCs. Compared with the literature listed in Table 4.12, the electronic conductivity of the PNO cathode deposited in this work is close to that of the literature, but higher than that of La_2NiO_4 cathode. There are few reports on the electrical conductivity of PPNO composites. Compared with Pr_2CuO_4@Pr_6O_{11}, the deposited PPNO2 materials have obvious advantages in electrical conductivity. In addition, the activation energy calculated by the Arrhenius formula (Equation 4.1) are similar values (Figure 4.19 (b)). This may indicate that the introduction of Pr_6O_{11} did not change the carrier transport mechanism in the PPNO2 material.

$$\sigma(T) = \frac{A}{T}\exp\left(-\frac{E_a}{kT}\right) \quad 4.1$$

Where T, and k, A, and Ea refer to the absolute temperature, Boltzmann's constant, a pre-exponential factor, and activation energy, respectively.

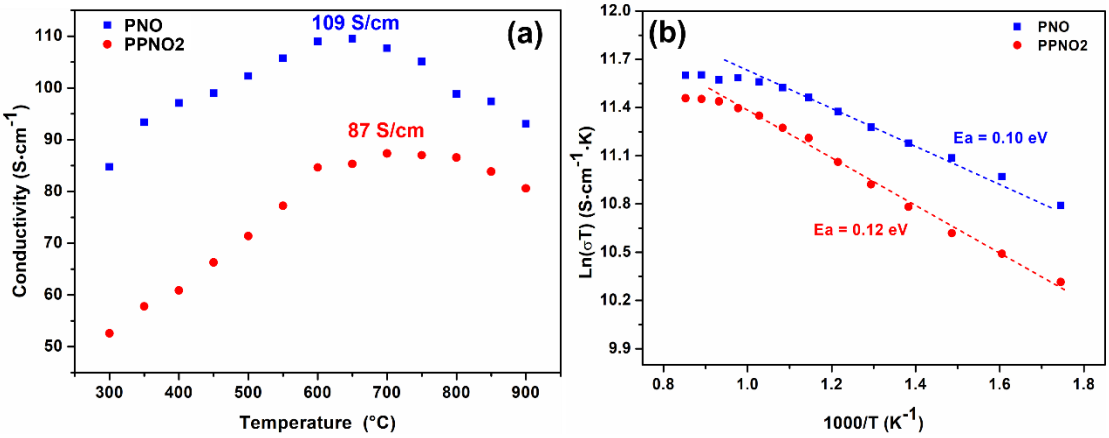

Figure 4.19: Conductivity (a) and Arrhenius curves (b) of PNO and PPNO2 coatings deposited on alumina pellet measured by four-probe method under air from 300 to 900°C

Table 4.12 The electronic conductivity of some cathode materials reported in the literature

	Maximum conductivity (S/cm)	Temperature (°C)	Ref.
Pr_2NiO_4	119	600	[18]
Pr_2NiO_4	106	450	[19]
$Pr_{1.5}La_{0.5}NiO_4$	110	600	[20]
La_2NiO_4	50	600	[20]
Pr_2CuO_4	95	700	[12]
Pr_2CuO_4@Pr_6O_{11}	39	700	[12]

The electrochemical performances of PPNO2 and PNO cathodes are evaluated by analyzing the AC-EIS of PPNO2/8YSZ/PPNO2 and PNO/8YSZ/PNO symmetric cells, respectively. The collected impedance diagram is fitted by selecting an appropriate equivalent circuit model through ZView software. Figures 4.20 and 4.21 correspond to the Nyquist plots of PPNO2/8YSZ/PPNO2 and PNO/8YSZ/PNO symmetrical cells in the temperature range of 600-750°C with a step of 50°C, respectively. From Figure 4.20, for the PPNO2 cathode, the $LR_1(CPE_1//R_2)(CPE_2//R_3)$ equivalent circuit model is considered for fitting the Nyquist plot. The Nyquist plot of the PNO cathode presents typical two semicircles as shown in Figure 4.21. The Nyquist plots are fitted by the equivalent circuit of $LR_1(CPE_1//R_2)(CPE_2//R_3)$. After fitting the impedance diagram with the ZView software, the resistances attributed to different contributions are used to calculate the polarization resistance (R_p) of the cathode material, which reflects the electrochemical performance of the cathode material. On the basis of the fitted data and using relations formula 4.2, the mean capacitance of each contribution from semicircle

have been calculated.

$$C = R^{((1-n)/n)} \times CPE^{1/n} \qquad 4.2$$

The Schouler-type representation is adopted for plotting the capacitive effect (C). of each contribution *v.s.* reciprocal temperature [21, 22]. Such plotting is considered to provide a reference for interpreting a given impedance diagram. Typical Arrhenius plots are shown in Figure 4.22. For the Nyquist plots of the PPNO2 cathode at 600°C (Figure 4.20 and 4.22), the lower capacitance (10^{-9} F) from R_2 is attributed to the response of the electrolyte [23]. Therefore, R_2 and R_1 are combined, excluded from R_p, that is, $R_p = R_3$ as shown in Figure 4.20. From 700 °C to 750°C, the capacitance corresponding to the first semicircle increases (10^{-5}-10^{-3} F), which is attributed to the electrode response [24-25]. In this case, $R_p = R_2+R_3$, and R_1 is a response from the electrolyte. Whereas for the PNO electrode, the capacitances response from R_2 and R_3 are 10^{-4} F and 10^{-2} F, respectively, which is attributed to the response of the electrode [23, 25]. Likewise, R_1 is attributed to the response of the electrolyte for PNO. In this case, for PNO electrode, $R_p = R_2+R_3$ at temperature from 600 to 750°C. Finally, the R_p of PPNO2 and PNO cathodes are listed in Table 4.13. Correspondingly, the Arrhenius plot is shown in Figure 4.23.

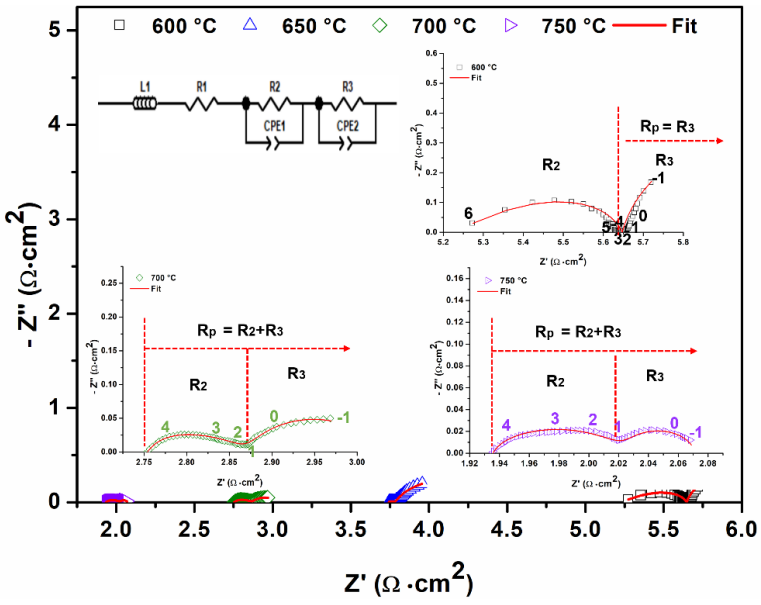

Figure 4.20: The EIS measurement of PPNO2/8YSZ/PPNO2 symmetric cell at different temperature in the oxygen partial pressure of 0.2 atm with the applied voltage perturbation of 10 mV

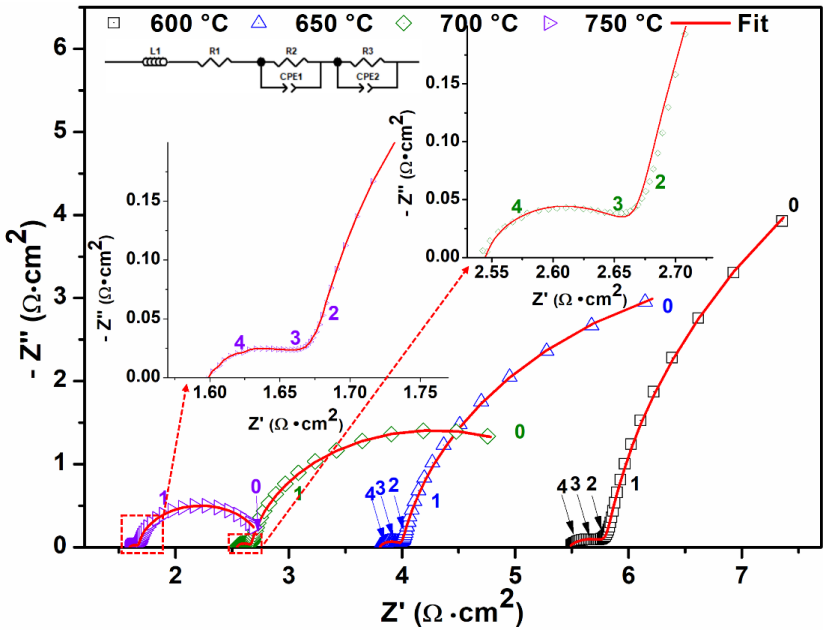

Figure 4.21: The EIS measurement of PNO/8YSZ/PNO symmetric cell at different temperature in the oxygen partial pressure of 0.2 atm with the applied voltage perturbation of 10 mV

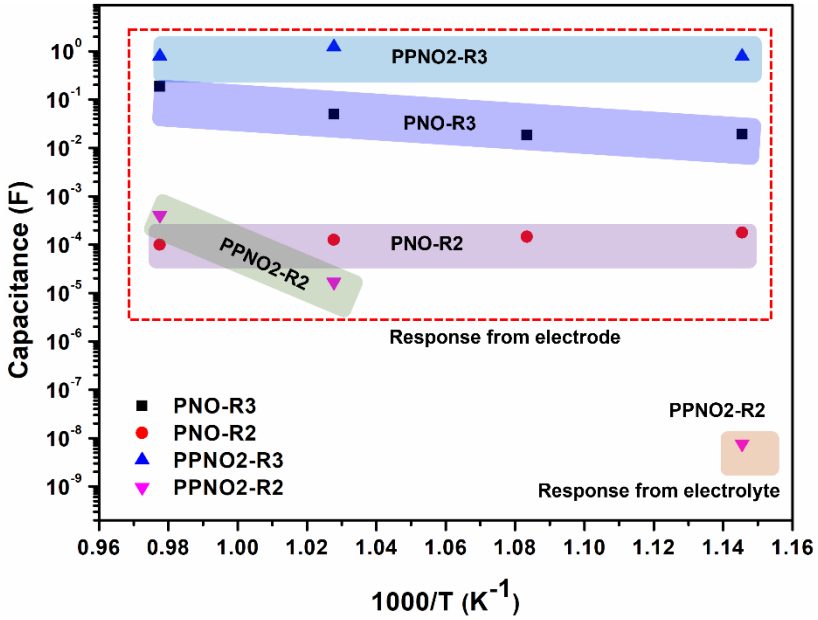

Figure 4.22: The Arrhenius plots of the capacitances for PPNO2 and PNO cathodes

The R_p and activation energy (E_a) of the PPNO2 cathode is much lower than that of the PNO at the temperature range o from 600-750°C, which shows the obvious advantage of PPNO cathode. Compared with the PNO cathode, the PPNO2 cathode with higher porosity and higher $O_{surface}/O_{lattice}$ ratio may be the reason for its lower polarization resistance [26]. Additionally, there have been some reports indicating that Pr_6O_{11} can significantly accelerate the oxygen surface exchange kinetics [7, 9]. This may also be the reason for the R_p of PPNO2 is lower than that of PNO. Table 4.13 also

lists some reports on PNO and Pr_6O_{11} modified cathodes. The R_p of the deposited PNO cathode is higher than that reported in the literature. Only at a higher temperature of 750°C, its Rp of 0.84 $\Omega \cdot cm^2$ is close to that reported by J. FONDARD et al. of 0.8 $\Omega \cdot cm^2$ [27]. This may be related to the morphology of the deposited PNO cathode. However, the deposited PPNO2 exhibited favorable competitiveness with low R_p of 0.07 $\Omega \cdot cm^2$ at 750°C. This may be attributed to the introduction of Pr_6O_{11}, which seems to have an important contribution in promoting the cathode ORR activity [7-9].

Table 4.13: The polarization resistances (R_p) of PPNO2 and PNO cathodes

R_p ($\Omega \cdot cm^2$) of Symmetry cells	Temperature (°C)			
	600	650	700	750
PNO/8YSZ/PNO	11.53	5.45	2.36	0.84
PPNO2/8YSZ/PPNO2	0.43	–	0.16	0.07
PNO/GDC/PNO			0.18 [2]	
PNO/GDC/PNO	0.83 [28]			
PNO/YSZ/YDC/PNO	0.32[29]			
PNO/GDC/PNO	0.36[30]			
PNO/LSGM/PNO	1.19[30]			
PNO/YSZ/PNO				0.8[27]
PNO/YSZ/PNO				0.18[31]
PPCO/GDC/PPCO				0.07[12]

PPCO: $Pr_2CuO_4@Pr_6O_{11}$

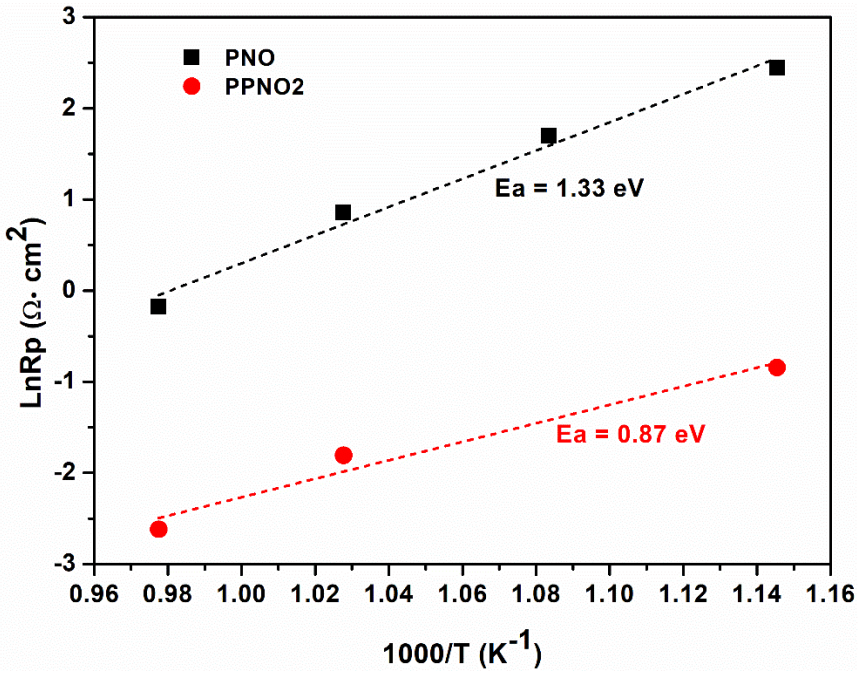

Figure 4.23: Arrhenius plots of polarization resistance (R_p) for PNO and PPNO2 cathodes

4.3 Fabrication and characterization of single cells

4.3.1 Fabrication of single cells

J. FONDARD [32] developed a MS-SOFC with ITM/GDC/Ni-YSZ/YSZ/LNO configuration, in which the LNO cathode deposited by RMS is in-situ crystallized during cell testing. However, the maximum power density of this cell is only 60 mW/cm^2 at 700°C. KIM et al. also reported that the cathode obtained by in-situ sintering has higher polarization resistance than that co-sintering [33, 34]. Therefore, annealing treatment of cathodes deposited by RMS instead of in-situ crystallization during the cell testing is considered in this thesis to improve the crystallinity and the porosity. Based on the investigation of the oxidation behavior of ITM in air in Chapter 3, an annealing treatment at 1000°C for 30min is performed for the fabrication of MS-SOFC single cell as shown in Figure 4.24. The fabrication of the MS-SOFC sequentially undergoes the deposition of the GDC10 buffer layer by RMS, the deposition of the NiO-YSZ bilayer anode by APS, the deposition of the 8YSZ/GDC10 bilayer electrolyte by RMS, and the deposition of the cathode layer (PPNO2 and PNO) by RMS. It should be noted that the NiO-YSZ, 8YSZ and GDC10 layer have been completed in Chapter 3, while the PPNO2 and PNO cathodes are deposited according to the deposition parameters given in Table 4.3. Among them, annealing treatment is performed at 500°C for 2h after the deposition of GDC10 electrolyte layer. Based on the above investigation on the PPNO2 cathode coating, the deposited PPNO2 coating has good electrochemical performance after annealing treatment at 1000°C for 30 min. Therefore, the complete single cell with configuration of ITM/GDC/Ni-YSZ/YSZ/GDC10/PPNO2 (named MS/PPNO2) and ITM/GDC/Ni-YSZ/YSZ/GDC10/PNO (named MS/PNO) are annealed at 1000°C for 30 min to obtain better cathode performance. However, the single cell is slightly deformed after annealing treatment. In order to meet the cell size requirements of the measuring device, the cells are manually worn down to small size of 1.1×1.1×0.1 cm^3.

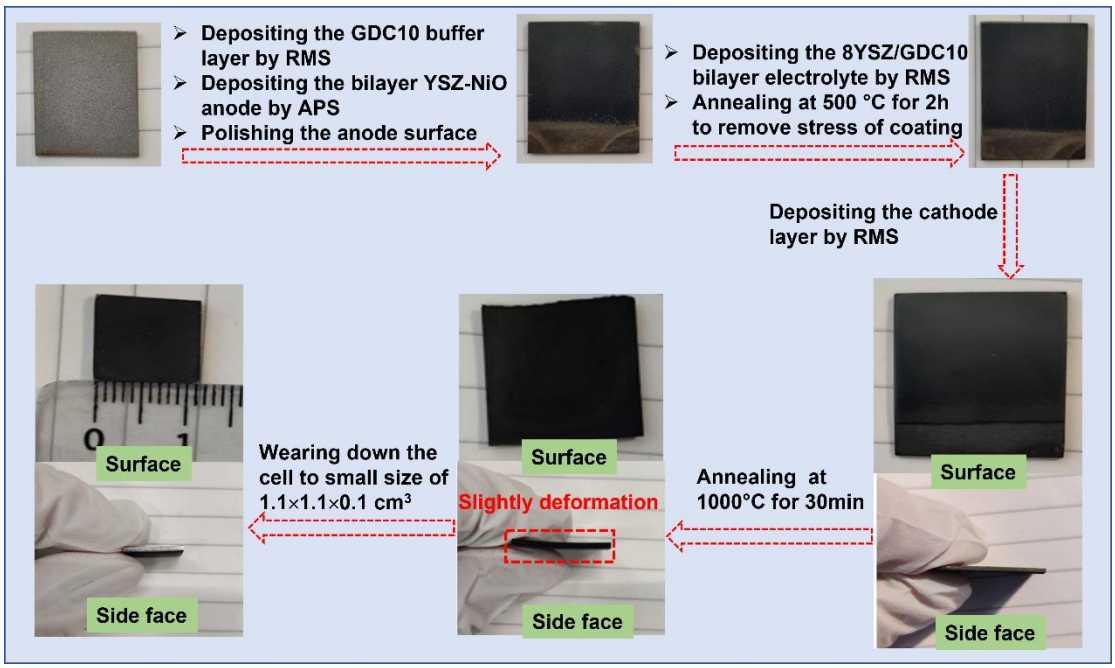

Figure 4.24: Fabrication process of MS-SOFC single cell

4.3.2 Characterization of single cells

The characterization of a complete single cell is performed according to the procedure shown in Figure 4.25. The discharge curve (I-V) measurements at variable temperature from 750 to 600°C are performed for MS/PPNO2 and MS/PNO single cells. Then a long-term performance test of MS/PPNO2 single cell with a constant current density of 0.4 A/cm^2 at 700°C for 63h is performed. It should be pointed out that it is cooled to room temperature after the I-V measurement for MS/PPNO2, and then the long-term performance test is measured after the temperature is raised to 700°C at a heating rate of 3°C/min. This can be considered as the MS/PPNO2 single cell has undergone a thermal cycle. The measurement results are shown in Figures 4.26-4.27 and Tables 4.14-4.15.

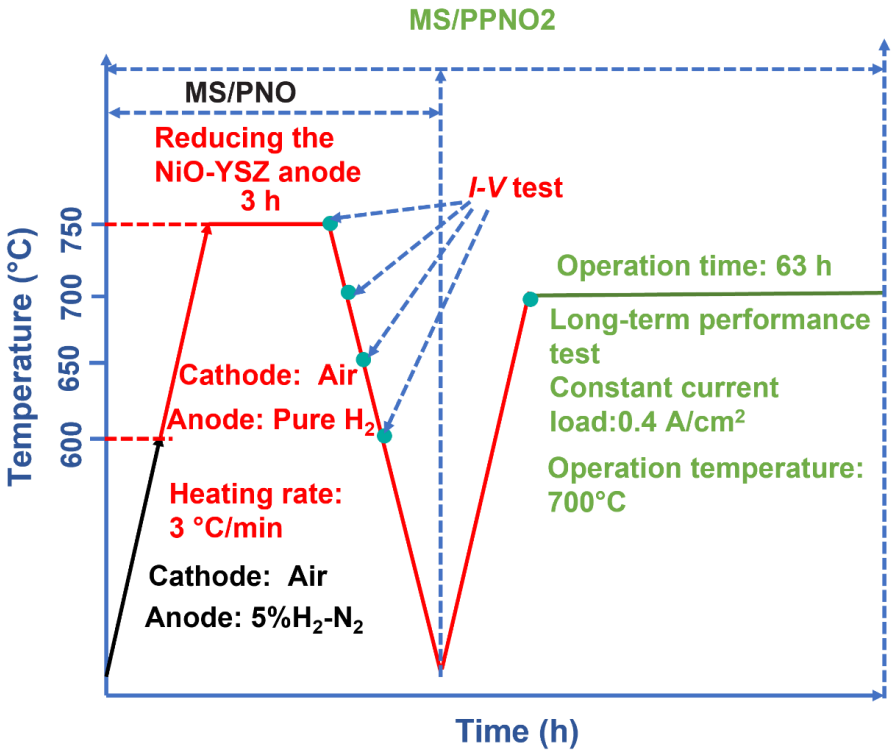

Figure 4.25: Schematic diagram of the characterization procedure for the complete single cells

As shown in Figure 4.26 and Table 4.14, the OCV of MS/PPNO2 decreases with increasing temperature, from 0.968 V at 600°C to 0.941 V at 750°C. The maximum power density (P_{max}) increases from 390 mW·cm^{-2} at 600°C to 1010 mW·cm^{-2} at 750°C with increasing temperature. Comparing the literature listed in Table 4.16, it seems that this does not show a disadvantage in terms of OCV values. However, the OCV of MS/PPNO2 is still low compared to the relatively higher values of 1.082 V [33], 1.058 V [35], and 1.06 V [36]. The P_{max} of MS/PPNO2 is competitive compared with that in Table 4.16. The reason for the lower OCV of MS/PPNO2 may be the internal defects of the cell. It can be seen from Figure 4.28 that some microcracks exist in the 8YSZ electrolyte. These microcracks are generated during annealing treatment. The stability of the MS/PPNO2 (represented in terms of cell voltage) at 700°C with a constant current load of 0.4 A/cm^2 as a function of operation time is used to evaluate the long-term performance of the single cell. After operation for 63 h, the voltage of MS/PPNO2 decreased from 0.75 V to 0.72 V as shown in Table 4.15, which shows that the cell has long-term performance. However, during the long-term test, the cell voltage first decreases and then increases slowly, and there are many noises (Figure 4.27). This may

be caused by the accumulation of water inside the cell. As shown in Figure 4.29, the ITM support in the cell is extruded during the cutting process, which causing the collapse of porous channels in the local area. As shown in Table 4.15, after a thermal cycle, the voltage of the cell at 700°C decreased by 0.09 V, which may indicate that the thermal resistance of the single cell should be improved.

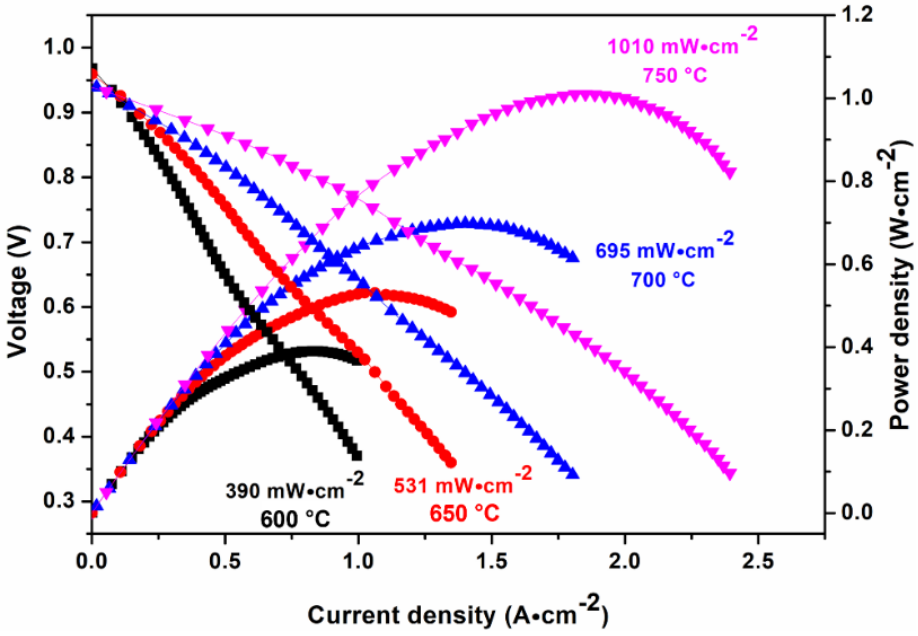

Figure 4.26: I-V-P curves of the MS/PPNO2 single cell at various temperatures

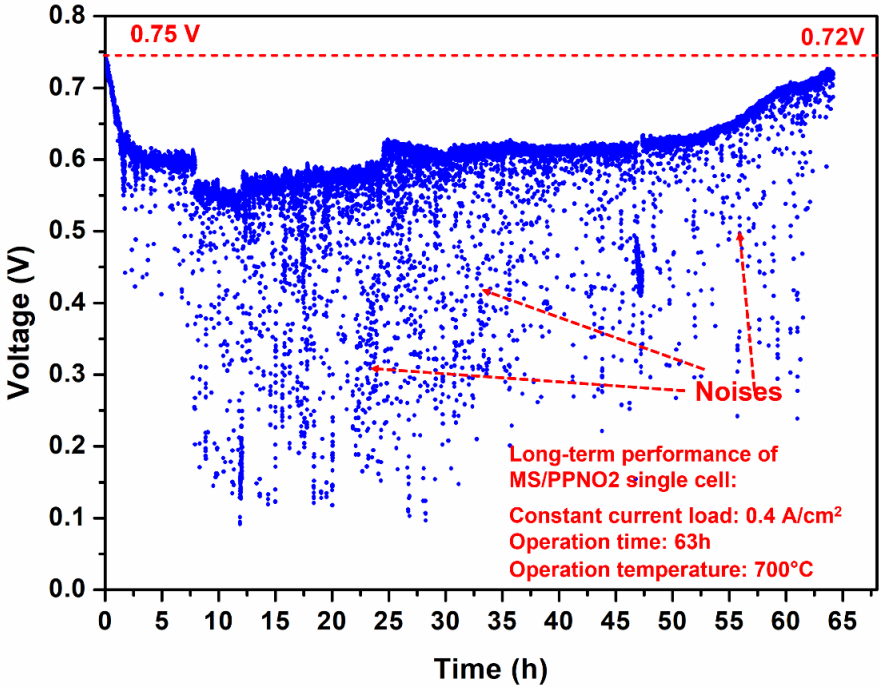

Figure 4.27: The long-term performance of the MS/PPNO2 single cell under a constant current density of 0.4 A·cm^{-2} for 63 h

Table 4.14: The OCV of the MS/PPNO2 single cell at various temperatures

Cells	OCV (V)			
	750°C	700°C	650°C	600°C
MS/PPNO2	0.941	0.939	0.960	0.968

Table 4.15: The voltage of MS/PPNO2 single cell undergoing different processes

	Initial	Cycle I	Stability test for 63h	Decrease1[a]	Decrease2[b]
Voltage (V)	0.84	0.75	0.72	0.09	0.03
Current ($A \cdot cm^2$)	0.4	0.4	0.4	–	–

a: from Initial to Cycle I; b: from Cycle I to after long-term test

Table 4.16: Performance of some reported MS-SOFC

Cell configuration	OCV (V)	P_{max} (mW/cm^2)	Ref.
STS430/Ni-YSZ/8YSZ/GDC/BSCF	1.082, 3%H_2O-H_2	310 at 700°C	[33]
STS430/Ni-YSZ/8YSZ/LSCM	1.10, Dry H_2	30 at 700°C	[37]
ITM/GDC20/Ni-GDC10/8YSZ/GDC20/LSCF	1.12, Dry H_2	903 at 700°C	[38]
SS430/Ni-SDC/ScSZ/GDC/SSC-GDC	0.98, 3%H_2O-H_2	140 at 600°C	[39]
ITM/GDC20/NiO-YSZ/8YSZ/GDC20/LNO	0.9, 5%H_2O-H_2	76 at 700°C	[40]
HastelloyX/NiO-SDC/SDC/SSCo	0.82, Dry H_2	560 at 700°C	[41]
ITM/NiO-YSZ/YSZ/LSCF	1.058, 5%H_2O-H_2	360 at 700°C	[42]
Fe22Cr/Ni-YSZ/ScYSZ/LSC	1.06, 2%H_2O-H_2	780 at 700°C	[36]

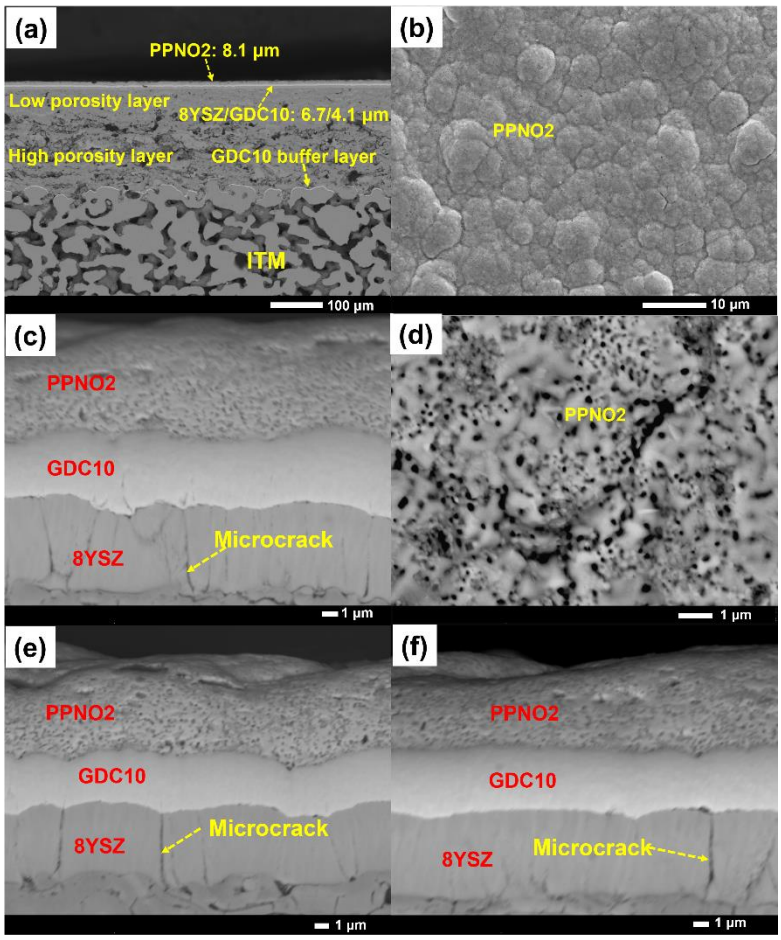

Figure 4.28: SEM observation of the MS/PPNO2 single cell: (a) polished cross section under larger field of view; (b) and (d) refer to the surface of cell; (c), (e), and (f) refer to the local polished cross-section

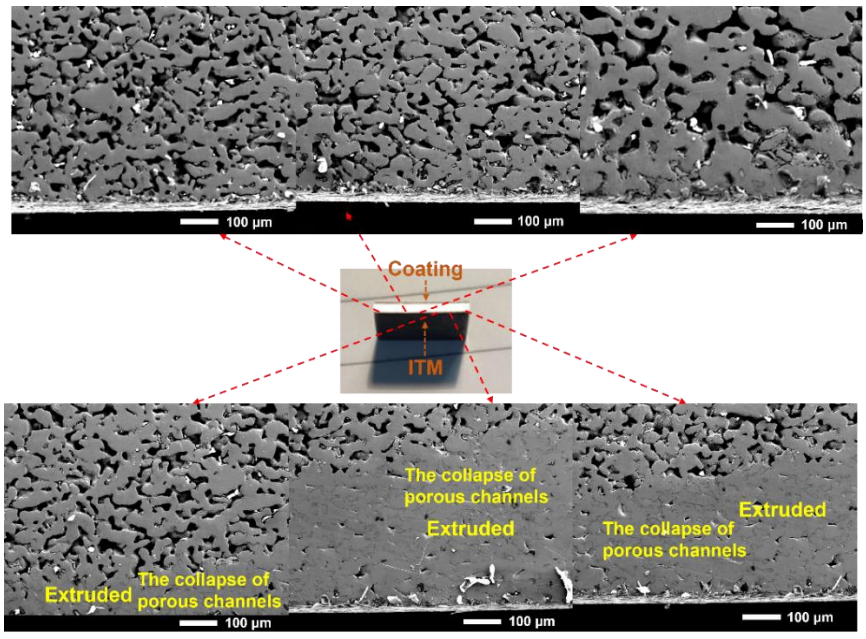

Figure 4.29: SEM observation of the ITM support of the MS/PPNO2 single cell

As shown in Figure 4.30 and Table 4.17, the P_{max} of MS/PNO increases from 133 $mW \cdot cm^{-2}$ at 600°C to 326 $mW \cdot cm^{-2}$ at 750°C. The OCV of MS/PNO decreases from 0.840V at 600°C to 0.817V at 750°C. Although this OCV is within 0.8-1.5V of the most feasible fuel cell reversible voltage range considered by O'HAYRE et al. [43], the OCV of MS/PNO is still low for SOFC. Compared with MS/PPNO2, the OCV and P_{max} of MS/PNO are lower, which may be attributed to two aspects. On the one hand, it is due to the internal defects of the cell. As shown in Figure 4.31, it seems to have more serious microcracks in the electrolyte than in that of MS/PPNO2. Especially when there are pits on the NiO-YSZ surface, the deposited electrolyte layer may be severely fractured as shown in Figure 4.31 (f). Although MS/PNO and MS/PPNO2 are deposited under the same conditions except for the cathode layer, differences may occur when manually polishing the surface of the NiO-YSZ anode layer. On the other hand, it is due to the difference in the cathode layer. After the analysis of the symmetrical cells PPNO2/8YSZ/PPNO2 and PNO/8YSZ/PNO, the advantages of the PPNO2 cathode in terms of electrochemical performance have been confirmed.

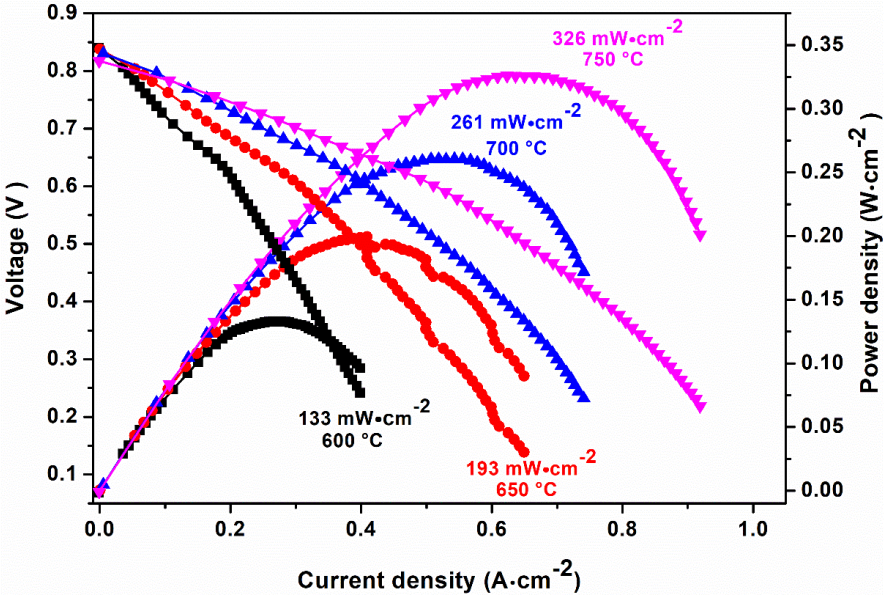

Figure 4.30: I-V-P curves of the MS/PNO single cell at various temperatures

Table 4.17: The OCV of the MS/PNO single cell at various temperatures

Cells	OCV (V)			
	750°C	700°C	650°C	600°C
MS/PNO	0.817	0.830	0.838	0.840

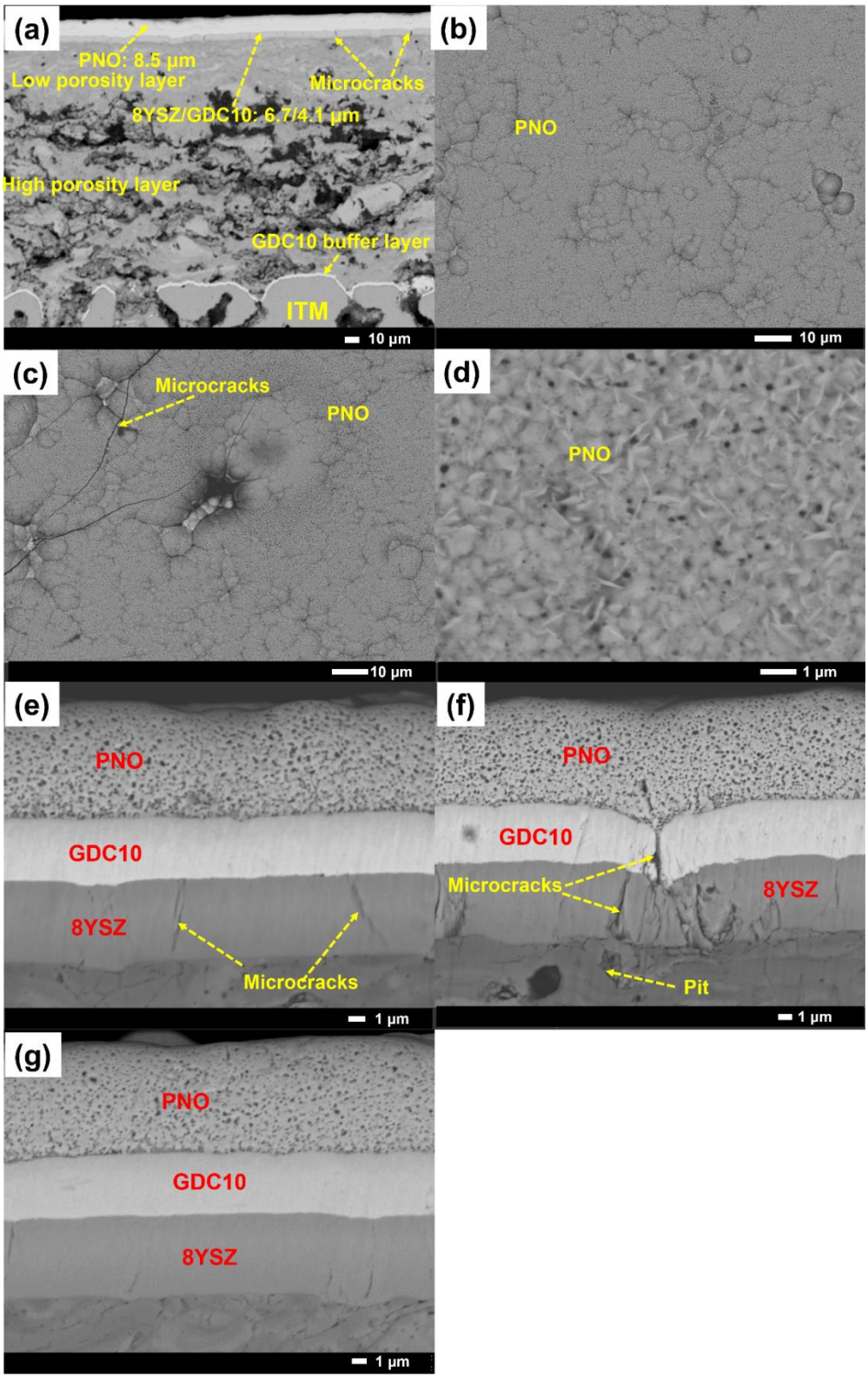

Figure 4.31: SEM observation of the MS/PNO single cell: (a) polished cross section under larger field of view; (b), (c), and (d) refer to the surface of cell; (e), (f), and (g) refer to the local polished cross-section

Electrochemical impedance diagrams of single cells are collected at different temperatures. Figures 4.32 and 4.33 are the Nyquist plots of MS/PPNO2 and MS/PNO at different temperatures, respectively. It can be seen that there are three responses on the Nyquist plots of the single cell. For the convenience of fitting, $R_1(CPE_1//R_2)(CPE_2//R_3)(CPE_3//R_4)$ equivalent circuit is used to fit all Nyquist plots by ZView software. The resistances of different response regions obtained after fitting are listed in Table 4.18. Usually, the response frequency of the electrolyte of the single cell is in the high frequency region of 10^5-10^6 Hz [44]. In addition, there may also be contact resistance in the high frequency region when measuring the impedance diagram of a single cell. Therefore, R_1 in Figures 4.32 and 4.33 should include electrolyte resistance and possible contact resistance. R_1 is also called ohmic resistance (R_{ohm}) in a single cell. From Table 4.18, the R_1 in MS/PPNO2 is significantly smaller than that in MS/PNO from 650°C to 750°C. This appears to be due to the more severe microcracking of the electrolyte in the MS/PNO mentioned above. An increase in temperature may lead to the intensification of microcracks in the electrolyte. Therefore, the R_1 of the two single cells is relatively close at a lower temperature (600°C), and the gap of R_1 becomes larger as the temperature increases (650-750°C). To further confirm the assignment of the responses from R_2, R_3, and R_4, the relaxation frequency and capacitance are calculated according to formulas 4.2 and 4.3.

$$f_r = \frac{1}{2\pi(R\times CPE)^{1/n}} \qquad 4.3$$

Figure 4.34 (a) shows that the capacitance from the R_2, R_3 and R_4 responses are all high (10^{-3}-10^0 F), which should be attributed to the electrode response [25]. According to the investigation on the single cells with the configuration of ITM/GDC/Ni-YSZ/8YSZ/GDC/LNO and Ni-YSZ/8YSZ/GDC/LNO from J. FONDARD [40], the low frequency (LF) regions (10^0 Hz) correspond to the anode layer response at 700 °C. For MS/PPNO2 and MS/PNO cells, Figure 4.34 (b) shows that the response from R_4 has a relaxation frequency of 10^{-1}-10^1 Hz (low frequency, LF), which is in the same order as the result of J. FONDARD. Therefore, here, R_4 is attributed to the cathode layer response for MS/PPNO2 and MS/PNO single cells. The

responses from R_2 and R_3, with relaxation frequency of 10^1-10^4 Hz (middle frequency, MF), are attributed to the anode layer response.

It can be seen from Table 4.18 that the $R_{MF} = R_2+R_3$ of the two cells are relatively close at the temperature from 650°C to 750°C. This also verifies that the polarization resistance in the middle frequency region is attributed to the response of the anode layer, since the anode layer is the same for both cells. While the resistance (R_4) of MS/PPNO2 is much lower than that of MS/PNO at temperatures from 600°C to 750°C in the LF region, which indicates that the activity of PPNO2 cathode has obvious advantages compared with PNO in the single cells. This result is consistent with that of the symmetrical cells. Similarly, the R_p and ASR of MS/PPNO2 is smaller than that of MS/PNO, which is mainly due to the contribution of the cathode layer.

In summary, the performance of MS/PPNO2 is much better than that of MS/PNO. This may be attributed to the PPNO2 cathode with better electrochemical performance and fewer internal defects.

Table 4.18: The resistances attributed to different response regions from the EIS diagram of the single cells

Cells	Temperature (°C)	R ($\Omega \cdot cm^2$)						
		R_1 (R_{ohm})	R_2	R_3	R_2+R_3 (R_{MF})	R_4 (R_{LF})	R_p	ASR
MS/PNO	600	0.116	0.015	0.107	0.122	0.880	1.002	1.118
	650	0.086	0.017	0.077	0.094	0.548	0.642	0.728
	700	0.066	0.014	0.060	0.074	0.295	0.369	0.435
	750	0.051	0.022	0.028	0.05	0.216	0.266	0.317
MS/PPNO2	600	0.118	0.032	0.070	0.102	0.241	0.343	0.461
	650	0.076	0.028	0.060	0.088	0.144	0.232	0.308
	700	0.049	0.022	0.048	0.070	0.100	0.170	0.219
	750	0.036	0.015	0.033	0.048	0.060	0.108	0.144

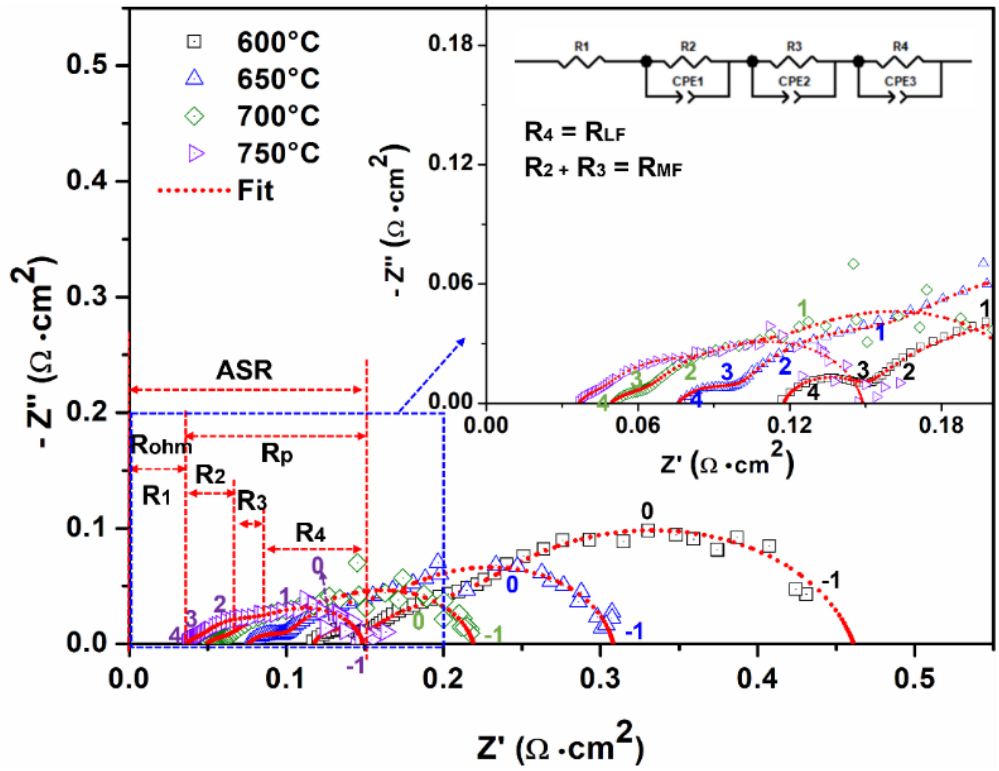

Figure 4.32: EIS measurement of the MS/PPNO2 single cell at various temperatures within a frequency range of 10^{-1}-10^{6} Hz at the applied voltage perturbation of 10 mV under air

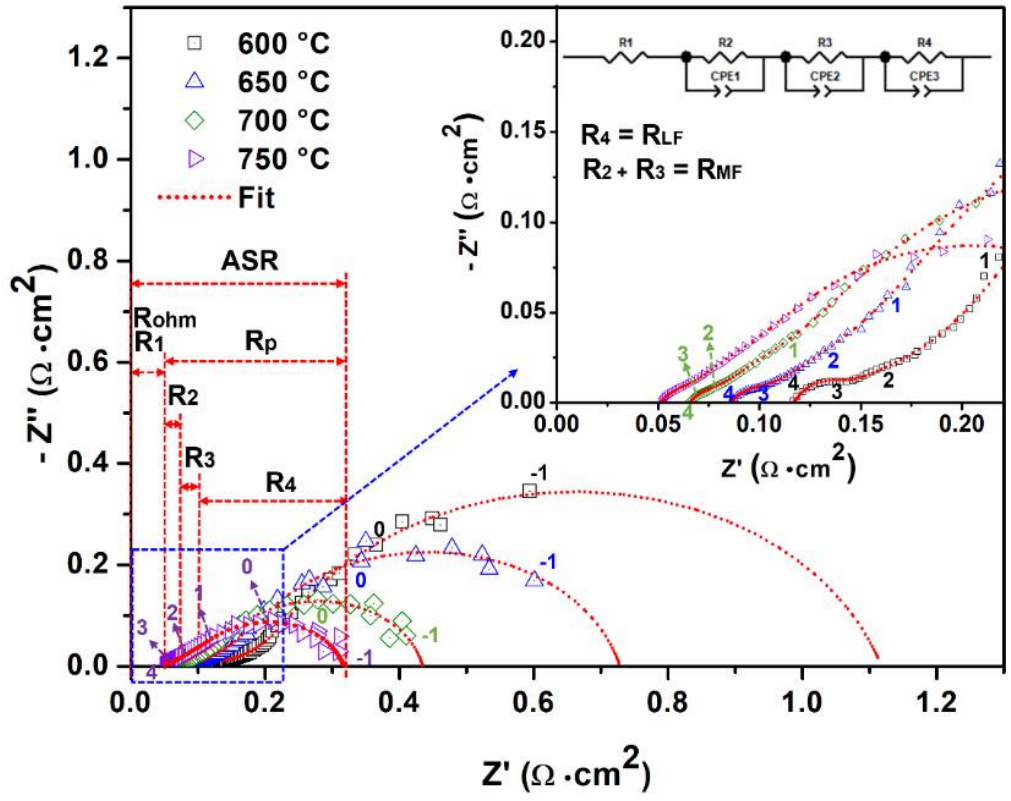

Figure 4.33: EIS measurement of the MS/PNO single cell at various temperatures within a frequency range of 10^{-1}-10^{6} Hz at the applied voltage perturbation of 10 mV under air

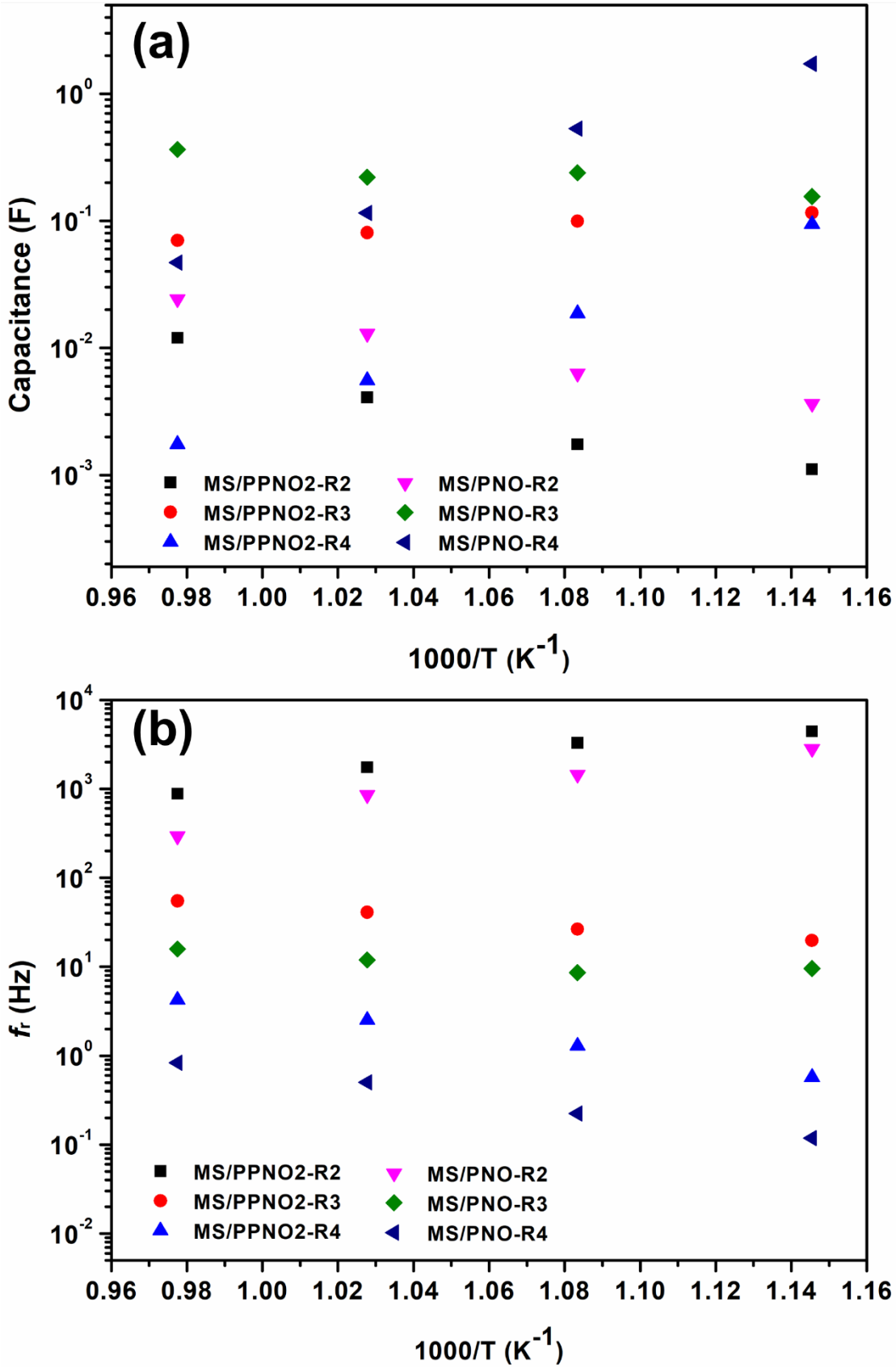

Figure 4.34: The corresponding relaxation frequency and capacitance calculated according to the fitting result of EIS spectrum of single cells (MS/PPNO2 and MS/PNO) by a ZView software: (a) capacitance; (b) relaxation frequency

4.4 Conclusion

In this chapter, PPNO2 and PNO cathode coatings are deposited by RMS. The structure and morphology evolution of PPNO1 deposited by RMS as a function of annealing treatment temperature are investigated. The electrical and electrochemical properties of PPNO2 and PNO cathodes are characterized. The MS/PPNO2 and MS/PNO are fabricated and characterized. The main conclusions are as follows:

(a) The Pr-Ni-O coating with high Pr/Ni atomic ratio of 3.06 ± 0.09 and 2.91 ± 0.09 deposited by RMS after annealing at 1000°C for 30min formed a porous morphology with Pr_2NiO_4 and Pr_6O_{11} (PPNO). The deposited Pr-Ni-O coating with low Pr/Ni atomic ratio of 1.73 ± 0.02 formed a porous morphology with Pr_2NiO_4 (PNO) phase after annealing treatment at 1000°C for 30 min. After annealing treatment at 750°C for 50 h, PPNO showed a more stable structure compared to PNO. In addition, both PPNO and PNO showed stable porous morphology.

(b) Compared with PPNO2 (87 S/cm at 700°C), PNO has a better electronic conductivity of 109 S/cm at 650°C. At 750°C, the R_p of PNO cathode is 0.84 $\Omega \cdot cm^2$, while that of PPNO is 0.07 $\Omega \cdot cm^2$. This indicate that PPNO2 has obvious advantages in electrochemical performance, which may be derived from better morphology and the promotion of Pr_6O_{11} on the ORR of the cathode.

(c) MS/PPNO2 complete cell has better cell performance, and its maximum P_{max} and OCV are 1010 $mW \cdot cm^{-2}$ and 0.941V at 750°C, respectively. However, the P_{max} and OCV of MS/PNO are only 326 $mW \cdot cm^{-2}$ and 0.817 V at 750°C, respectively. The difference in performance between MS/PPNO2 and MS/PNO cell is due to the electrochemical activity of the cathode (PPNO2 *v.s* PNO) and the influence of microcracks in the electrolyte layer. The MS/PPNO2 single cell exhibits interesting long-term performance.

4.5 References

[1] Mauvy, F., Lalanne, C., Bassat, J. M., Grenier, J. C., Zhao, H., Dordor, P., & Stevens,

P. (2005). Oxygen reduction on porous $Ln_2NiO_{4+\delta}$ electrodes. Journal of the European Ceramic Society, 25(12), 2669-2672.

[2] Han, Z., Bai, J., Chen, X., Zhu, X., & Zhou, D. (2021). Novel cobalt-free $Pr_2Ni_{1-x}Nb_xO_4$ (x= 0, 0.05, 0.10, and 0.15) perovskite as the cathode material for IT-SOFC. International Journal of Hydrogen Energy, 46(21), 11894-11907.

[3] Sadykov, V. A., Pikalova, E. Y., Kolchugin, A. A., Fetisov, A. V., Sadovskaya, E. M., Filonova, E. A., & Pikalov, S. M. (2020). Transport properties of Ca-doped Ln_2NiO_4 for intermediate temperature solid oxide fuel cells cathodes and catalytic membranes for hydrogen production. International Journal of Hydrogen Energy, 45(25), 13625-13642.

[4] Sharma, R. K., Burriel, M., Dessemond, L., Bassatc, J. M., & Djurado, E. Design of interfaces in efficient Ln_2NiO_4 (Ln ¼ La, Pr) cathodes for SOFC applications.

[5] Deronzier, E., Chartier, T., & Geffroy, P. M. (2021). Oxygen semi-permeation properties of $Ba_{1-x}Sr_xFeO_{3-\delta}$ perovskite membranes. Solid State Ionics, 361, 115560.

[6] Nomura, T., Nishimoto, S., Kameshima, Y., & Miyake, M. (2012). Electrode properties of doped Pr_2NiO_4-based oxide cathode for intermediate-temperature SOFCs. Journal of the Ceramic Society of Japan, 120(1407), 534-538.

[7] Tong, X., Xu, Y., Tripković, Đ., Hendriksen, P. V., Kiebach, W. R., & Chen, M. (2020). Promotion of oxygen reduction and evolution by applying a nanoengineered hybrid catalyst on cobalt free electrodes for solid oxide cells. Journal of Materials Chemistry A, 8(18), 9039-9048.

[8] Gu, Y., Zhang, Y., Zheng, Y., Chen, H., Ge, L., & Guo, L. (2019). $PrBaMn_2O_{5+\delta}$ with praseodymium oxide nano-catalyst as electrode for symmetrical solid oxide fuel cells. Applied Catalysis B: Environmental, 257, 117868.

[9] Chen, Y., Chen, Y., Ding, D., Ding, Y., Choi, Y., Zhang, L., & Liu, M. (2017). A robust and active hybrid catalyst for facile oxygen reduction in solid oxide fuel cells. Energy & Environmental Science, 10(4), 964-971.

[10] Fondard, J., Billard, A., Bertrand, G., Fourcade, S., Batocchi, P., Mauvy, F., & Briois, P. (2016). Effect of total pressure on La_2NiO_4 coatings deposited by reactive magnetron sputtering using plasma emission monitoring. Surface and Coatings

Technology, 295, 29-36.

[11]Vibhu, V. (2016) Stability and ageing studies of praseodymium-based nickelates as cathodes for Solid Oxide Fuel Cells, Université de Bordeaux.

[12] Shijie, Z., Na, L., Liping, S., Qiang, L., Lihua, H., & Hui, Z. (2022). One-pot synthesis Pr_6O_{11} decorated Pr_2CuO_4 composite cathode for solid oxide fuel cells. International Journal of Hydrogen Energy, 47(9), 6227-6236.

[13] Liu, L., Zhou, X., Wang, Y., Li, S., Yin, R., Guo, P., & Li, B. (2017). Composite ceramic cathode $La_{0.9}Ca_{0.1}Fe_{0.9}Nb_{0.1}O_{3-\delta}/Sc_{0.2}Zr_{0.8}O_{2-\delta}$ towards efficient carbon dioxide electrolysis in zirconia-based high temperature electrolyser. International Journal of Hydrogen Energy, 42(22), 14905-14915.

[14] Tao, Z. T., Jiang, Y. M., Lei, L., & Chen, F. (2019). $Pr_{0.5}Ba_{0.5}Co_{0.7}Fe_{0.25}Nb_{0.05}O_{3-\delta}$ as air electrode for solid oxide steam electrolysis cells. International Journal of Hydrogen Energy, 44(42), 23539-23546.

[15] Sun, Q., Sun, L., Dou, Y., Li, Q., Li, N., Huo, L., & Zhao, H. (2021). Insights into the oxygen reduction reaction on Cu-doped $SrFeO_{3-\delta}$ cathode for solid oxide fuel cells. Journal of Power Sources, 497, 229877.

[16] Li, H., Su, C., Wang, C., & Lü, Z. (2020). Electrochemical performance evaluation of $FeCo_2O_4$ spinel composite cathode for solid oxide fuel cells. Journal of Alloys and Compounds, 829, 154493.

[17] Nicollet, C., Flura, A., Vibhu, V., Rougier, A., Bassat, J. M., & Grenier, J. C. (2016). An innovative efficient oxygen electrode for SOFC: Pr_6O_{11} infiltrated into Gd-doped ceria backbone. international journal of hydrogen energy, 41(34), 15538-15544.

[18] Vibhu, V., Flura, A., Nicollet, C., Fourcade, S., Penin, N., Bassat, J. M., & Pouchard, M. (2018). Characterization of $PrNiO_{3-\delta}$ as oxygen electrode for SOFCs. Solid State Sciences, 81, 26-31.

[19] Boehm, E., Bassat, J. M., Dordor, P., Mauvy, F., Grenier, J. C., & Stevens, P. (2005). Oxygen diffusion and transport properties in non-stoichiometric $Ln_{2-x}NiO_{4+\delta}$ oxides. Solid State Ionics, 176(37-38), 2717-2725.

[20] Vibhu, V., Rougier, A., Nicollet, C., Flura, A., Grenier, J. C., & Bassat, J. M. (2015). $La_{2-x}PrxNiO_{4+\delta}$ as suitable cathodes for metal supported SOFCs. Solid State Ionics, 278,

32-37.

[21] Schouler, E. J. L., & Kleitz, M. (1987). Electrocatalysis and inductive effects at the gas, Pt/stabilized zirconia interface. Journal of the Electrochemical Society, 134(5), 1045.

[22] Schouler, E. J. L., Mesbahi, N., & Vitter, G. (1983). In situ study of the sintering process of yttria stabilized zirconia by impedance spectroscopy. Solid State Ionics, 9, 989-996.

[23] Adler, S. B. (1998). Mechanism and kinetics of oxygen reduction on porous $La_{1-x}Sr_xCoO_{3-\delta}$ electrodes. Solid State Ionics, 111(1-2), 125-134.

[24] Mauvy, F., Lalanne, C., Bassat, J. M., Grenier, J. C., Zhao, H., Huo, L., & Stevens, P. (2006). Electrode properties of $Ln_2NiO_{4+\delta}$ (Ln= La, Nd, Pr): AC impedance and DC polarization studies. Journal of the Electrochemical Society, 153(8), A1547.

[25] Dailly, J., Fourcade, S., Largeteau, A., Mauvy, F., Grenier, J. C., & Marrony, M. (2010). Perovskite and A_2MO_4-type oxides as new cathode materials for protonic solid oxide fuel cells. Electrochimica Acta, 55(20), 5847-5853.

[26] Zhang, W., Zhang, L., Guan, K., Zhang, X., Meng, J., Wang, H., & Meng, J. (2020). Effective promotion of oxygen reduction activity by rare earth doping in simple perovskite cathodes for intermediate-temperature solid oxide fuel cells. Journal of Power Sources, 446, 227360.

[27] Fondard, J., Billard, A., Bertrand, G., Briois, P. (2018). $Ln_2NiO_{4+\delta}$ (Ln= La, Pr, Nd) coatings deposited by reactive magnetron sputtering as cathode material for intermediate temperature solid oxide fuel cell, 152, 97-108.

[28] Sharma, R.K., Khamidy, N.I., marc Bassat, J., Djurado, E.J.E.T. (2017). $La_{2-x}Pr_xNiO_{4+\delta}$-Based Efficient SOFC Cathodes: Effect of Microstructure, Composition and Architecture, 78, 581.

[29] Ferchaud, C., Grenier, J. C., Zhang-Steenwinkel, Y., Van Tuel, M. M., Van Berkel, F. P., & Bassat, J. M. (2011). High performance praseodymium nickelate oxide cathode for low temperature solid oxide fuel cell. Journal of Power Sources, 196(4), 1872-1879.

[30] Philippeau, B., Mauvy, F., Mazataud, C., Fourcade, S., & Grenier, J. C. (2013). Comparative study of electrochemical properties of mixed conducting $Ln_2NiO_{4+\delta}$ (Ln=

La, Pr and Nd) and $La_{0.6}Sr_{0.4}Fe_{0.8}Co_{0.2}O_{3-\delta}$ as SOFC cathodes associated to $Ce_{0.9}Gd_{0.1}O_{2-\delta}$, $La_{0.8}Sr_{0.2}Ga_{0.8}Mg_{0.2}O_{3-\delta}$ and $La_9Sr_1Si_6O_{26.5}$ electrolytes. Solid State Ionics, 249, 17-25.

[31] Ogier, T., Chauveau, F., Bassat, J. M., Mauvy, F., Grenier, J. C., Mougin, J., & Petitjean, M. (2011). Enhanced Performances of $Ln_2NiO_{4+\delta}$/CGO Multilayered Anodes for High Temperature Steam Electrolysis (HTSE). ECS Transactions, 35(1), 1817.

[32] Fondard, J., Bertrand, P., Billard, A., Fourcade, S., Batocchi, P., Mauvy, F., & Briois, P. (2017). Manufacturing and testing of a metal supported Ni-YSZ/YSZ/La_2NiO_4 IT-SOFC synthesized by physical surface deposition processes. Solid State Ionics, 310, 10-23.

[33] Kim, Y. M., Kim-Lohsoontorn, P., & Bae, J. (2010). Effect of unsintered gadolinium-doped ceria buffer layer on performance of metal-supported solid oxide fuel cells using unsintered barium strontium cobalt ferrite cathode. Journal of Power Sources, 195(19), 6420-6427.

[34] Huang, Q. A., Wang, B., Qu, W., & Hui, R. (2009). Impedance diagnosis of metal-supported SOFCs with SDC as electrolyte. Journal of Power Sources, 191(2), 297-303.

[35] Vaßen, R., Hathiramani, D., Mertens, J., Haanappel, V. A. C., & Vinke, I. C. (2007). Manufacturing of high performance solid oxide fuel cells (SOFCs) with atmospheric plasma spraying (APS). Surface and Coatings Technology, 202(3), 499-508.

[36] Nielsen, J., Persson, Å. H., Muhl, T. T., & Brodersen, K. (2018). Towards high power density metal supported solid oxide fuel cell for mobile applications. Journal of The Electrochemical Society, 165(2), F90.

[37] Lee, C., & Bae, J. (2008). Fabrication and characterization of metal-supported solid oxide fuel cells. Journal of Power Sources, 176(1), 62-69.

[38] Bischof, C., Nenning, A., Malleier, A., Martetschläger, L., Gladbach, A., Schafbauer, W., & Bram, M. (2019). Microstructure optimization of nickel/gadolinium-doped ceria anodes as key to significantly increasing power density of metal-supported solid oxide fuel cells. International journal of hydrogen energy, 44(59), 31475-31487.

[39] Huang, Q. A., Oberste-Berghaus, J., Yang, D., Yick, S., Wang, Z., Wang, B., & Hui, R. (2008). Polarization analysis for metal-supported SOFCs from different fabrication

processes. Journal of power sources, 177(2), 339-347.

[40] Fondard, J. (2015) Elaboration et test d'une pile à combustible IT-SOFC à support métallique poreux par l'intermédiaire de techniques de dépôt en voie sèche: projection thermique et pulvérisation cathodique magnétron. (Doctoral dissertation, Université de Technologie de Belfort-Montbeliard).

[41] Hui, R., Berghaus, J. O., Decès-Petit, C., Qu, W., Yick, S., Legoux, J. G., & Moreau, C. (2009). High performance metal-supported solid oxide fuel cells fabricated by thermal spray. Journal of Power Sources, 191(2), 371-376.

[42] Marcano, D., Mauer, G., Vaßen, R., & Weber, A. (2017). Manufacturing of high performance solid oxide fuel cells (SOFCs) with atmospheric plasma spraying (APS) and plasma spray-physical vapor deposition (PS-PVD). Surface and coatings technology, 318, 170-177.

[43] O'hayre, R., Cha, S. W., Colella, W., & Prinz, F. B. (2016). Fuel cell fundamentals. John Wiley & Sons.

[44] Briois, P., & Billard, A. (2006). A comparison of electrical properties of sputter-deposited electrolyte coatings dedicated to intermediate temperature solid oxide fuel cells. Surface and Coatings Technology, 201(3-4), 1328-1334.

Chapter 5: Conclusions and perspectives

5.1 Conclusions

In this thesis, a MS-SOFC exhibiting competitive performance is fabricated by all physical deposition method. The whole fabrication process includes the deposition of bilayer NiO-YSZ anode by APS, the deposition of bilayer 8YSZ/GDC10 electrolyte by RMS, the deposition of GDC10 buffer layer by RMS, and the deposition of cathodes (PPNO2 and PNO) by RMS. There are mainly the following conclusions:

(a) Porous Pr_2NiO_4@Pr_6O_{11} (PPNO) and Pr_2NiO_4 (PNO) are successfully synthesized by RMS followed by subsequent annealing treatment at 1000°C for 30 min. The R_p of the PPNO2 cathode is much lower than that of the PNO cathode. At 750°C, the R_p of the PPNO2 cathode is 0.07 $\Omega \cdot cm^2$, while that of the PNO cathode is 0.84 $\Omega \cdot cm^2$. This indicates that the electrochemical activity of the PPNO2 cathode is higher than that of the PNO cathode, which may be because of Pr_6O_{11} on the promotion of ORR occurs at the cathode. Although the PPNO cathode coating deposited by RMS remained stable in structure and porous morphology after annealing treatment at 750°C for 50 h in air, the stability of the PPNO cathode in the more complex environments (such as longer annealing time, different oxygen partial pressures) has not been clarified. Therefore, the more comprehensive properties of PPNO cathode materials still need to be further investigated.

(b) The maximum power density of MS/PPNO2 single cell can reach 1010 $mW \cdot cm^2$ at 750°C. The voltage of the MS/PPNO2 single cell dropped only about 0.03V after long-term performance test at 700°C for 63h, which indicates that the MS/PPNO2 single cell exhibits interesting long-term performance. However, the voltage drop of the MS/PPNO2 cell is relatively large (about 0.09 V) after a thermal cycle, which indicates that the thermal resistance of the cell needs to be improved.

(c) A dense and thin (about 10.8μm) 8YSZ/GDC10 bilayer electrolyte is successfully deposited by RMS on the polished NiO-YSZ anode layer.

However, some microcracks appeared in the electrolyte layer after two annealing treatments (500°C for 2h and 1000°C for 30min). The existence of microcracks may be the reason for the low OCV of MS/PPNO2 cell.

(d) Bilayer NiO-YSZ anode with porosity gradient is realized on preformed ITM plane by APS. Although the upper layer (low porosity) surface of the bilayer NiO-YSZ anode is carefully polished by hand, there are still some pits on the surface, which may be one of the reasons for the internal defects (microcracks) of the 8YSZ/GDC10 electrolyte layer deposited by RMS.

(e) The thin GDC10 buffer layer (about 2.2 μm) deposited by RMS between ITM and NiO-YSZ anode layer can effectively prevent interdiffusion between Fe, Cr, and Ni.

5.2 Perspectives

MS-SOFC is one of the most promising development directions for SOFC commercialization dure to its significant advantages in cost and durability. Exploring new fabricating processes to solve the preparation problems of high-performance electrodes and electrolytes, reducing fabricating costs, improving cell performance and long-term stability is one of the current development trends of MS-SOFC. Combined with the investigation of this thesis, follow-up research can be carried out in the following aspects:

(a) Establish a set of standards for the fabrication of MS-SOFC by physical deposition methods. Specifically, the corresponding assessment indicators are proposed at each deposition stage to ensure that cells with as few internal defects as possible.

(b) The deposition of electrolyte by RMS should be further investigated, which can focus on further reducing the electrolyte thickness as well as eliminating internal microcracks in the electrolyte layer caused by annealing treatment.

(c) The deposition of NiO-YSZ anode with a pore gradient should be further optimized to obtain a suitable surface with low roughness for direct deposition of dense electrolyte layers by magnetron sputtering.

(d) The cathode materials should be further developed by magnetron sputtering, with the aim of finding cathode materials that can be annealed at lower temperatures or without annealing treatment to obtain porous morphology and requested structure.

SPIM

Titre: Développement de piles à combustible à oxyde solide sur support métallique (MS-SOFC) par pulvérisation de plasma atmosphérique(APS) et technique de pulvérisation de magnétron réactif (RMS)

Mots clés: MS-SOFC, APS, RMS, anode NiO-YSZ, cathode composite PPNO

Résumé: L'énergie et l'environnement sont des enjeux majeurs du développement social. Les piles à combustible à oxyde solide (SOFC) est un dispositif de conversion d'énergie hautement efficace, qui est l'un des candidats prometteurs pour atténuer la crise énergétique et environnementale. Le principal problème des SOFC est qu'ils fonctionnent à des températures élevées (800-1000°C), ce qui limite leur application commerciale plus large. Abaisser la température de fonctionnement à des températures intermédiaires (600-800°C) ou même inférieures peut apporter des avantages significatifs aux SOFC en termes de coût et de durée de vie. Cependant, cela oblige des développements afin de relever le défi de limiter la dégradation des performances due à la chute de température.

Dans cette thèse, une SOFC à support métallique poreux (MS-SOFC) est fabriquée par APS et RMS. La couche d'anode NiO-YSZ est déposée sur le support métallique poreux ITM par APS. Une couche tampon barrière GDC10 est insérée entre l'ITM et l'anode NiO-YSZ pour empêcher l'interdiffusion entre le Cr, Fe présent dans l'ITM vers l'anode et le Ni de l'anode vers l'ITM. Une couche d'électrolyte 8YSZ/GDC10mince et dense d'une épaisseur d'environ 10,8 µm est déposée par RMS afin de réduire la perte ohmique due à une température de fonctionnement plus basse. Enfin, Un composite PPNO hautement électrochimiquement actif est synthétisé par RMS pour la couche cathodique.

Title: Development of Metal Supported Solid Oxide Fuel Cell (MS-SOFC) by Atmospheric Plasma Spraying (APS) and Reactive Magnetron Sputtering (RMS) Technique

Keywords: MS-SOFC, APS, RMS, NiO-YSZ anode, PPNO composite cathode

Abstract: Energy and environmental are major challenges to social development. SOFC is a highly efficient energy conversion device, which is one of the promising candidates to alleviate the energy and environmental crisis. The main problem of conventional SOFC is that they work at high temperatures (800-1000°C), which limits their wider commercial application. Lowering the operating temperature to intermediate temperatures (600-800°C) or even lower can bring significant benefits to SOFC in terms of cost and lifetime. However, this makes SOFCs face the challenge of performance degradation due to temperature drop.

In this thesis, metal-supported SOFC (MS-SOFC) is fabricated by APS and RMS. A thin and dense 8YSZ/GDC10 electrolyte layer with thickness of about 10.8µm is deposited by RMS in order to reduce ohmic loss due to lower operating temperature. A highly electrochemically active PPNO composite is synthesized by RMS for the cathode layer. The NiO-YSZ anode layer is deposited on the metal support ITM by APS. A GDC10 buffer layer is deposited between the ITM and the NiO-YSZ anode to prevent the interdiffusion between Cr, Fe, and Ni.

UBFC UNIVERSITÉ BOURGOGNE FRANCHE-COMTÉ

Université Bourgogne Franche-Comté
32, avenue de l'Observatoire
25000 Besançon